# Application of $^{19}$F MRI for *in vivo* detection of biological processes

Dissertation zur Erlangung des

naturwissenschaftlichen Doktorgrades

der Bayerischen Julius-Maximilians-Universität Würzburg

vorgelegt von

**Thomas Christian Basse-Lüsebrink**

aus Regensburg

Würzburg 2012

Eingereicht am: _____

bei der Fakultät für Physik und Astronomie

1. Gutachter: Prof. Dr. rer. nat. Peter M. Jakob

2. Gutachter: Prof. Dr. med. Dr. rer. nat. Wolfgang R. Bauer

der Dissertation

1. Prüfer: Prof. Dr. rer. nat. Peter M. Jakob

2. Prüfer: Prof. Dr. med. Dr. rer. nat. Wolfgang R. Bauer

3. Prüfer: _____

im Promotionskolloquium

Tag des Promotionskolloquiums: _____

Doktorurkunde ausgehändigt am: _____

# Contents

# Abbreviations

In this work the following abbreviations are used (alphabetic order):

- af: **A**cceleration **F**actor
- BALL: **B**iochemical **AL**gorithms **L**ibrary
- BS: **B**loch-**S**iegert
- BS-CPMG-TSE: **BS**-based **CPMG-TSE** method
- BS-FLASH: **BS**-based **FLASH** method
- BS-SE: **BS**-based **S**pin-**E**cho method
- CPMG: **C**arr **P**urcell **M**eiboom **G**ill
- CS: **C**ompressed **S**ensing
- CSA: **C**ompressed **S**ensing **A**veraging
- CSI: **C**hemical **S**hift **I**maging
- CS-TSE-CSI: **CS** accelerated **TSE CSI**
- CT: **C**omputer **T**omography
- EPI: **E**cho **P**lanar **I**maging
- FDA: **F**ood and **D**rug **A**dministration
- FID: **F**ree **I**nduction **D**ecay
- FISP: **F**ast **I**maging with **S**teady state **P**recession
- FLASH: **F**ast **L**ow **A**ngle **SH**ot
- FOV: **F**ield-**o**f-**V**iew
- GD: **G**a**D**olinium
- GFM: **G**ado**F**luorine **M**
- $G_P$: **P**hase encoding **G**radient
- $G_R$: **R**ead encoding **G**radient
- $G_S$: **S**lice encoding **G**radient
- i.v.: **I**ntra**V**enously
- IRSF: **I**nversion **R**ecovery **S**napshot **F**LASH
- IUPAC: **I**nternational **U**nion of **P**ure and **A**pplied **C**hemistry
- kc: **K**-space **C**enter
- mIP: **M**inimum **I**ntensity **P**rojection
- Mn: **M**anga**N**ese
- MPS: **M**ononuclear **P**hagocyte **S**ystem
- MR: **M**agnetic **R**esonance

- MRI: **M**agnetic **R**esonance **I**maging
- MRT: **M**agnet**R**esonanz**T**omographie
- MTX: **Ma**a**T**ri**X**
- NA: **N**umber of **A**verages
- NMR: **N**uclear **M**agnetic **R**esonance
- MRS: **M**agnetic **R**esonance **S**pectroscopy
- MSE: **M**ulti **S**pin-**E**cho
- PEO-PPO-PEO: **P**oly(**E**thylene **O**xide)-**P**oly(**P**ropylene **O**xide)-**P**oly(**E**thylene **O**xide)
- PFC: **P**er**F**luoro**C**arbon
- PFOB: **P**er**F**luoro**O**ctyl**B**romide
- PFPE: **P**er**F**luoro**P**oly**E**ther
- PF15C: **P**er**F**luoro-**15**-**C**rown-ether
- PNS: **P**eripheral **N**ervous **S**ystem
- $pO_2$: **P**artial Pressure of **O**xygen
- ppm: **P**arts **P**er **M**illion
- PSF: **P**oint **S**pread **F**unction
- PT: **P**hoto**T**hrombosis
- RARE: **R**apid **A**cquisition **R**elaxation **E**nhancement
- Res: **RE**Solution
- RF: **R**adio **F**requency
- RMSE: **R**oot **M**ean **S**quare **E**rror
- ROI: **R**egion **o**f **I**nterest
- SAR: **S**pecific **A**bsorption **R**ate
- SB: **S**pectral **B**andwidth
- SFA: **S**ingularity **F**unction **A**nalysis
- SNR: **S**ignal to **N**oise **R**atio
- SOS: **S**um-**o**f-**S**quares
- SP: **S**pectral **P**oints
- SPIO: **S**uper **P**aramagnetic **I**ron **O**xide
- ST: **S**lice **T**hickness
- subaf: **SUB** **A**cceleration **F**actor
- $T_{AQ}$: **A**c**Q**uisition **T**ime
- TE: **E**cho **T**ime
- $T_{exp}$: **E**xperiment **T**ime
- TF: **T**urbo**F**actor
- TFA: **T**ri**F**luoro**A**cid
- TIE: **I**nter **E**cho **T**ime
- TR: **R**epetition **T**ime

- TrueFISP: **TRUE F**ast **I**maging with **S**teady state **P**recession
- TSE: **T**urbo-**S**pin-**E**cho
- $T_{1w}$: $\mathbf{T}_1$-**W**eighted
- $T_{2w}$: $\mathbf{T}_2$-**W**eighted
- $T^*_{2w}$: $\mathbf{T}^*_2$-**W**eighted

# Declaration

Figures of the present work were prepared with MATLAB® (The MathWorks Inc., Natick, USA) and CorelDRAW® X4 and X6 (Corel Corporation, Ottawa, Canada) if not otherwise indicated.

All animal experiments presented in this work were performed according to institutional guidelines and were approved by the Ethics Committee for Animal Welfare of the University of Würzburg, Germany. Furthermore, all MR measurements were performed on a horizontal 7T Bruker Biospec (Bruker BioSpin GmbH, Reinstetten, Germany) small animal scanner at room temperature.

# 1 Introduction

Since the discovery of **M**agnetic **R**esonance **S**pectroscopy (MRS) in 1946 [1, 2] remarkable developments in this field have occurred. In 1973, Lauterbur introduced the idea of **M**agnetic **R**esoncance **I**maging (MRI) using magnetic field gradients and a back projection technique to enable spatial encoding of the **M**agnetic **R**esoncance (MR) signal [3]. In subsequent years, several fundamental principles were developed and applied to MRI. For example, Ernst et al. proposed the concept of fourier-encoded MRI [4], which was performed in 1980 by Edelstein et al. [5] and is currently the most commonly used imaging technique for MRI. The first fast imaging methods were introduced in 1977 by Mansfield (**E**cho **P**lanar **I**maging (EPI) [6], and in 1986 by Hennig et al. (**R**apid **A**cquisition **R**elaxation **E**nhancement RARE) [7], Haase et al. (**F**ast **L**ow **A**ngle **SH**ot FLASH) [8] and Oppelt et al. (**TRUE F**ast **I**maging with **S**teady State **P**recession TrueFISP) [9]. Due to all the dedicated focus on this field, MRI became one of the most important diagnostic modalities in medicine.

With the help of the unique tissue contrast and multiple quantitative parameters accessible through MRI, radiologists can investigate a variety of different medical conditions. Additionally, using contrast agents with MRI can help clarify certain medical questions by altering the contrast of surrounding tissue. Contrast agents were used even in the first MRI paper. Thus, Lauterbur showed in 1973 that changing the $T_1$ relaxation time of the proton signal from $H_2O$ through **M**anga**N**ese (Mn) ions leads to a different MR image signal strength than using pure $H_2O$ [3]. Although Mn-based $T_1$ contrast agents still exist, the most common $T_1$ contrast agents are nowadays **G**a**D**olinium (GD) chelates.

Cell tracking is one of the possible applications of $T_1$ contrast agents. For example, labeling cells with GD contrast agents to identify the cells in $\mathbf{T_1}$-**W**eighted ($T_{1w}$) MR images has been proposed [10, 11]. Alternatively, **S**uper **P**aramagnetic **I**ron **O**xide (SPIO) contrast agents can also be used for cell tracking. However, instead of a positive contrast as provided by $T_1$ contrast agents, SPIO labeled cells provide a negative contrast in $\mathbf{T_2}$-**W**eighted ($T_{2w}$) and $\mathbf{T_2^*}$-**W**eighted ($T_{2w}^*$) MRI due to dephasing of the surrounding proton spins and shortening of the $T_2$ relaxation constant [12–15]. One major limitation of contrast agents, however, is that they only work by changing the proton signal. Thus, in specific measurements situations other effects can lead to a similar contrast in the MR image, leaving the detectability of cells labeled with a contrast agents ambiguous [14, 16–19]. Furthermore, signal behavior alteration can limit the assessment of functional parameters in $^1$H MRI when using contrast agents.

Recently, the MR community regained great interest in $^{19}$F MRI due to its potential to provide unambiguous cell tracking [16, 20, 21]. Since no endogenous fluorine background signal can be observed with standard $^{19}$F MRI unambiguous cell tracking of fluorine labeled cells is possible. In general, $^{19}$F compounds exhibit their own signal and therefore act as markers and not as contrast agents. Thus, $^{19}$F markers are measured directly. The hardware, however, must allow acquisition of the MR signal at both the $^{19}$F and the $^1$H resonance frequencies. This is necessary since additional $^1$H background scans are normally required to enable the localization of the fluorine image into the anatomical

context. Moreover, due to the often low concentration of the $^{19}$F marker at the **R**egion **o**f **I**nterest (ROI), long scan times and/or low resolved images must usually be taken into account when performing $^{19}$F MRI.

The present work centers on the field of $^{19}$F MRI and concentrates on three major aspects. First, the applicability of $^{19}$F MRI to the field of experimental neurology was investigated. Thus, with the help of $^{19}$F MRI, early stages of vessel occlusion in ongoing thrombosis were visualized in mice. Furthermore, the inflammation in the peripheral nervous system of rats was investigated with $^{19}$F MRI. Second, since the successful application of **C**ompressed **S**ensing (CS) to $^{19}$ MRI could be recently shown [22–24], a further investigation of this reconstruction technique applied to $^{19}$F is discussed. Third, fast and quantitative $^{1}$H $B_1^+$ mapping is covered, specifically regarding how future $B_1^+$ mapping methods might allow for fast, quantitative $^{19}$F MRI in even inhomogeneous coil setups.

The work is structured as follows: after the introduction, Chapter 2 presents the basic physical principles of MRI. Chapter 3 deals with the basic principles underlying $^{19}$F MRI. Furthermore, the fluorine markers used in this study, their basic properties and two common $^{19}$F quantification procedures are presented. In Chapter 4, after discussing basic principles underlying MR sequences, the commonly used $^{1}$H/$^{19}$F MRI sequences in this work are presented. Furthermore, exemplary sequence-specific artifacts are discussed. Chapter 5 presents the two animal models investigated in the present work. Chapter 6 investigates how the principle of CS can be applied to a specific $^{19}$F sequence and, furthermore, how it can be used to reduce spike artifacts in CS-accelerated $^{19}$F MR images. Chapter 7 deals with the fast acquisition of $^{1}$H $B_1^+$ maps using **B**loch-**S**iegert-based (BS) spin-echo-based sequences. Thus, a novel, fast **T**urbo-**S**pin-**E**cho (TSE) method is presented and the possible translation and application to $^{19}$F MRI is discussed. A further discussion and conclusion of the whole thesis is given in Chapter 8 followed by a German Version in Chapter 9 and an appendix in Chapter 10.

# 2 Basics of MRI

The understanding of MRI has increased dramatically over the years, leading to the existence of several dedicated publications dealing with the physical principles of MRI. Therefore, this work will only briefly describe the basic principles underlying MRI. The interested reader is thus directed to literature dealing in more detail with MRI (e.g., [25, 26]).

The remarks in the present chapter follow the descriptions in [25–31].

## 2.1 Physical principles of MRI

Whether or not MRS/MRI can be performed using a certain atomic species is determined by the magnetic properties of the specific nuclei. Therefore, only nuclei with a nonvanishing nuclear spin (**S**) are MRS/MRI "active" and can thus be detected. An overview of different atomic species including the spin quantum numbers ($I$), that define **S** is presented in Table 2.1.

**Table 2.1:** *Nuclear properties of different isotopes. Values obtained from [27–29]. I is the spin quantum number, $\gamma$ is the gyromagnetic ratio of the specific isotope and N/A stands for not applicable.*

| *Isotope* | *I* | *$\gamma/2\pi$ [MHz/T]* | *Natural Abundance* | *Relative Sensitivity [%]* |
|---|---|---|---|---|
| $^{1}$H | 1/2 | 42.58 | 99.99 | 1.00 |
| $^{2}$H | 1 | 6.54 | 0.02 | $9.56 \times 10^{-3}$ |
| $^{12}$C | 0 | N/A | 98.90 | 0.00 |
| $^{13}$C | 1/2 | 10.71 | 1.11 | $1.59 \times 10^{-2}$ |
| $^{14}$N | 1 | 3.08 | 99.63 | $1.01 \times 10^{-3}$ |
| $^{15}$N | 1/2 | 4.31 | 0.37 | $1.04 \times 10^{-3}$ |
| $^{16}$O | 0 | N/A | 99.96 | 0.00 |
| $^{17}$O | 5/2 | 5.77 | 0.04 | $2.91 \times 10^{-2}$ |
| $^{19}$F | 1/2 | 40.05 | 100.00 | 0.83 |
| $^{23}$Na | 3/2 | 11.26 | 100.00 | $9.25 \times 10^{-2}$ |
| $^{31}$P | 1/2 | 17.23 | 100.00 | $6.63 \times 10^{-2}$ |

As provided in Table 2.1, both isotopes ($^{1}$H & $^{19}$F ) investigated in the present work have $I = 1/2$.

The relation between the gyromagentic ratio ($\gamma$) and **S** of the regarded nuclei defines the magnetic moment ($\boldsymbol{\mu}$):

$$\boldsymbol{\mu} = \gamma \mathbf{S} \tag{2.1}$$

According to quantum mechanics, only certain eigenstates are allowed for **S** and thus also for the magnetic moment:

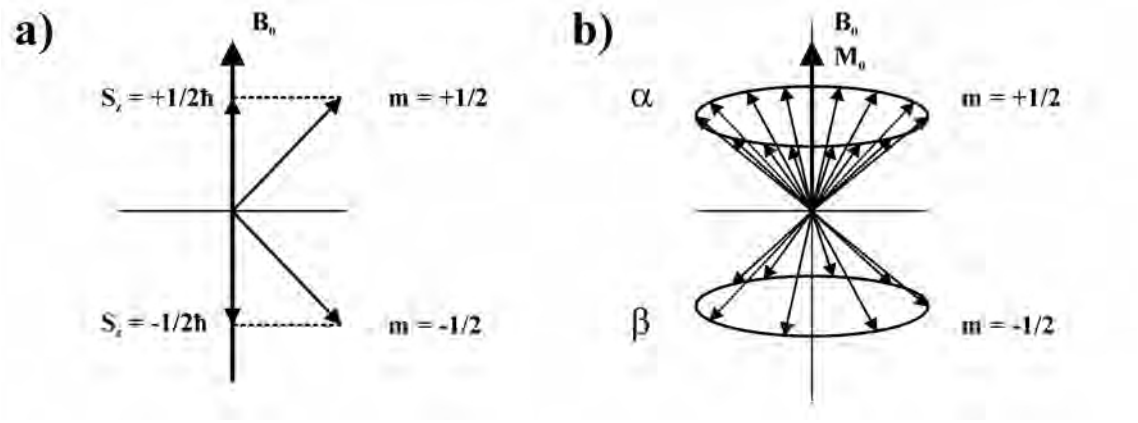


**Figure 2.1:** *a) Sketch illustrating the two eigenstates possible for a nuclei with $I = 1/2$ in a magnetic field $B_0$. b) Sketch showing the different populations of the two energy levels for $I = 1/2$ isotopes. The figure is based on two figures of Reference [28].*

$$\mu = \gamma\sqrt{I(I+1)}\hbar \tag{2.2}$$

The $\gamma$ is a nuclei specific constant (Table 2.1). Thus, isotopes with a **S** of zero have also a $\mu$ of zero.

If a nuclei is placed inside a magnetic field $\mathbf{B}_0$, the following applies for the z-component of the spin **S**:

$$S_z = m\hbar \tag{2.3}$$

with $m$ being the magnetic quantum number that can have $2(I+1)$ values (m=-$I$,-$I$+1,...$I$). Thus, for a nuclei with $I = 1/2$, two eigenstates are possible (cf. Figure 2.1a).

In the semi-classical model, the nuclei-dipoles are precessing around the direction of the main magnetic field (z-axis). Their precession frequency is the so-called Larmor frequency ($\omega_0$):

$$\omega_0 = \gamma B_0 \tag{2.4}$$

One important fact is that, due to different energy states, the different eigenstates are unequally populated. For $I = 1/2$ nuclei, the Boltzmann distribution gives the following relation for the thermal equilibrium:

$$\frac{N_\beta}{N_\alpha} = e^{\frac{\Delta E}{k_B T}} = e^{\frac{\gamma\hbar B_0}{k_B T}} \tag{2.5}$$

with $N_{\alpha/\beta}$ being the number of nuclei in the lower/higher energy level, $\Delta E$ the energy difference of the two eigenstates, $k_B$ the Boltzmann constant, and $T$ the temperature.

Figure 2.1b illustrates the distribution of the nuclei in the two eigenstates. Since $N_\alpha > N_\beta$, a macroscopic magnetization ($\mathbf{M_0}$) results in the direction of $\mathbf{B_0}$. Thereby, $\mathbf{M_0}$ is the summation of all magnetic moments:

$$\mathbf{M_0} = \frac{N\gamma^2\hbar^2 I(I+1)}{3k_B T}\mathbf{B_0} \tag{2.6}$$

It is important to note that $\mathbf{M_0}$ has only a longitudinal component (direction of $\mathbf{B_0}$) since the components perpendicular to $\mathbf{B_0}$ are equally distributed. Thus, when the summation of all magnetic moments ($\mathbf{M_0}$) is regarded, transversal magnetization does not occur. Furthermore, the difference of the population of the two energy levels at room temperature is in the **P**arts **P**er **M**illion (ppm) range and thus very small. Nevertheless, the density of protons in tissue is so large that measurable MR signal can be detected.

Since global magnetization behaves similar to classical momenta, classical physics are used to describe its behavior in the following.

## 2.2 Bloch equation

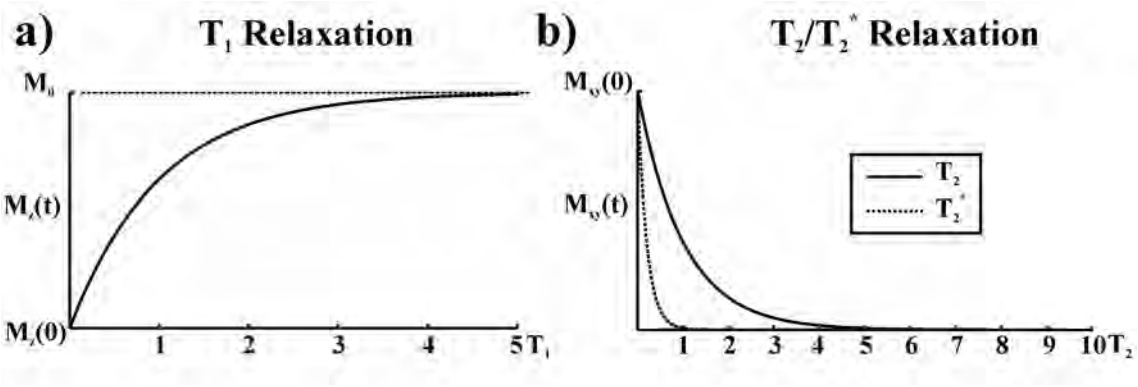


**Figure 2.2:** *Figure displaying the magnetization behavior during relaxation. a) $T_1$ relaxation. b) $T_2/T_2^*$ relaxation. The parameters for calculation were $T_2$ = 1/2 $T_1$ and $T_2^*$ = 1/5 $T_2$. The figure is based on a figure of Reference [26].*

The following uses the so-called Bloch equation to describe the magnetization behavior in a constant external field $\mathbf{B}_0$. For simplicity, it is assumed that the external field $\mathbf{B}_0$ only consists of a z-component. Furthermore, all relationships are described in a rotating coordinate system [32], the so-called rotating frame. Contrary to the static laboratory system, the rotating frame is assumed to precess with $\omega_0$ around $\mathbf{B}_0$. Thus, vectors precessing with $\omega_0$ around $\mathbf{B}_0$ are static in regard to the rotating frame.

For a constant external field $\mathbf{B}_0$ the different relaxation processes can be described by the so-called Bloch equation:

$$\frac{d\mathbf{M}}{dt} = \gamma\mathbf{M}\times\mathbf{B}_0 + \frac{1}{T_1}\left(M_0 - M_L\right)\mathbf{e}_z - \frac{1}{T_2}\mathbf{M}_T \tag{2.7}$$

with $\mathbf{M}$ being the magnetization vector, $T_1$ the spin-lattice relaxation time, $T_2$ the spin-spin relaxation time, $M_L$ the longitudinal magnetization component, and $\mathbf{e_z}$ the unit vector in z-direction. Furthermore, $\mathbf{M}_T = M_x\mathbf{e}_x + M_y\mathbf{e}_y$ with $M_{x,y}$ being the x and y components of the magnetization vector and $\mathbf{e_{x,y}}$ the unit vectors in the x,y-direction.

The $T_1$ relaxation describes the relaxation of $M_L$, which can be derived from Equation 2.7:

$$\frac{dM_L}{dt} = \frac{1}{T_1}(M_0 - M_L) \tag{2.8}$$

The $T_1$ relaxation is due to the interaction of the spin system with its surrounding. Importantly, the $T_1$ constant is different for multiple tissues and thus one important contributor to the contrast in a MR image. When Equation 2.8 is solved (e.g., for a single excitation) an exponential relationship is found:

$$M_L(t) = M_L(0)e^{\frac{-t}{T_1}} + M_0(1 - e^{\frac{-t}{T_1}}) \tag{2.9}$$

with $M_L(0)$ being the longitudinal magnetization component directly after excitation. The resulting relaxation curve from Equation 2.9 is plotted in Figure 2.2a.

The $T_2$ relaxation describes the relaxation of $\mathbf{M}_T$, which can be derived from Equation 2.7. Both components are given by:

$$\begin{aligned} \frac{dM_x}{dt} &= \omega_0 M_y - \frac{M_x}{T_2} \\ \frac{dM_y}{dt} &= -\omega_0 M_x - \frac{M_y}{T_2} \end{aligned} \tag{2.10}$$

The $T_2$ relaxation is due to a dephasing effect of the spin ensemble. Regarded over time, spins at different probe positions experience different magnetic fields due to microscopic field fluctuations. Therefore, a dephasing effect occurs that reduces the transversal $\mathbf{M}_T$ magnetization. The solution for Equation 2.10 gives:

$$M_T(t) = M_T(0)e^{\frac{-t}{T_2}} \tag{2.11}$$

with $M_T(0)$ being the transversal magnetization component directly after the excitation. The resulting $T_2$ relaxation curve from Equation 2.11 is plotted in Figure 2.2b. In general, $T_2$ relaxation time constants are shorter than $T_1$ relaxation constants.

Furthermore, the spin system can additionally dephase in the transversal plane due to local inhomogeneities of the external magnetic field. Similar to $T_2$ relaxation, the locally diverse magnetic fields cause the local spins to precess with different frequencies at different probe positions. Thus, the spins dephase with time and the global magnetization relaxes faster than the $T_2$ value. The relaxation constant describing this effect is called $T_2^{'}$. Unlike $T_2$ relaxation, this relaxation mechanism is compensate for by using so-called spin-echo experiments. Thus, spin-echo experiments mainly experience $T_2$ relaxation. However, so-called gradient-echo experiments suffer from a combination of $T_2$ and $T_2^{'}$ relaxation labeled $T_2^*$ relaxation:

$$\frac{1}{T_2^*} = \frac{1}{T_2} + \frac{1}{T_2^{'}} \tag{2.12}$$

The resulting $T_2^*$ relaxation curve from Equation 2.12 plugged into Equation 2.11 is plotted in Figure 2.2b.

Gradient and spin-echo experiments are explained in greater detail in Chapter 4. Furthermore, the effect of relaxation on different MR sequences is regarded in more detail in Chapter 4.

## 2.3 The MR signal

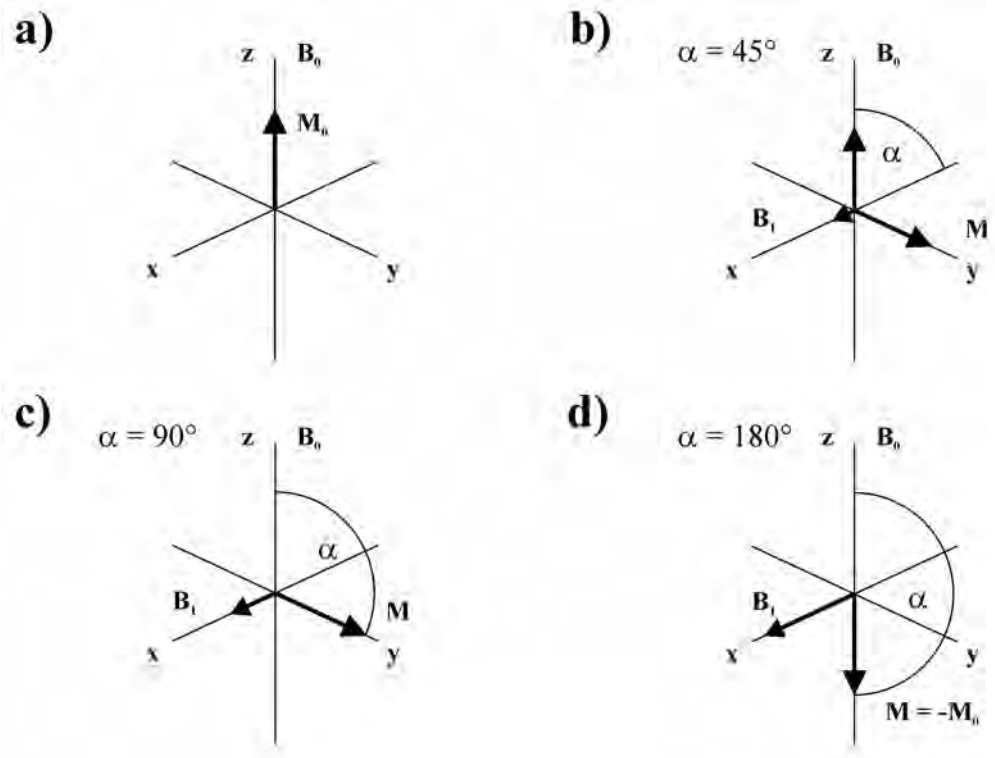


**Figure 2.3:** *Sketch demonstrating different magnetization vectors following a RF pulse with the same duration but different $B_1$ magnitude. The coordinate system is precessing with $\omega_0$ (rotating frame). a) Magnetization state before excitation. b) Magnetization after a $\alpha = 45°$ pulse was applied. The resulting magnetization vector has a longitudinal and transversal component. c) Magnetization after a $\alpha = 90°$ pulse was applied. The resulting magnetization vector has only a transversal component. d) Magnetization after a $\alpha = 180°$ pulse was applied. The resulting magnetization vector has only a -z component. The figure is based on a figure of Reference [28].*

As mentioned in Section 2.1, the summation of nuclear moments results in a global magnetization that can be treated like a classical magnetization vector. Furthermore, the Bloch equation (Equation 2.7) discussed in Section 2.2 shows that a transversal magnetization component precesses around the direction of the external magnetic field with $\omega_0$. As discussed below, this allows induction of a measurable signal in a receiver coil. With thermal equilibrium, however, only a longitudinal magnetization component $M_0$ in the direction of the external field $\mathbf{B_0}$ exists. To introduce a measurable signal, the magnetization vector must be tipped into the transversal plane (cf. Figure 2.3). Therefore, a **R**adio **F**requency (RF) pulse consisting of a rotating magnetic field pulse is normally applied. When relaxation is ignored, Equation 2.7 can be written as:

$$\frac{d\mathbf{M}}{dt} = \gamma \mathbf{M} \times \mathbf{B}_{eff} \tag{2.13}$$

with $\mathbf{B}_{eff}$ being the effective magnetic field:

$$\mathbf{B}_{eff} = \frac{1}{\gamma} \left[ (\omega_0 - \omega)\, \mathbf{e}_z + \omega_1 \mathbf{e}_x \right] \tag{2.14}$$

with $\omega$ being the RF laboratory frequency and $\omega_1$ the spin precessing frequency generated by the RF pulse. When the RF pulse is applied on-resonant $\omega = \omega_0$, Equation 2.14 simplifies to:

$$\mathbf{B}_{eff} = \frac{1}{\gamma}\omega_1 \mathbf{e}_x \tag{2.15}$$

and thus Equation 2.13 can be used to describe the effect of the on-resonant RF pulse on the magnetization vector:

$$\frac{d\mathbf{M}}{dt} = \mathbf{M} \times \omega_1 \mathbf{e}_x \tag{2.16}$$

Normally the RF pulse is applied for a certain duration ($t_\alpha$). The angle between the $B_0$/z-direction and the resulting magnetization vector $M$ is the so-called flip angle $\alpha$ (cf. Figures 2.3b–d). The flip angle $\alpha$ fulfills the following relationship:

$$\alpha = \gamma B_1 t_\alpha \tag{2.17}$$

Thus, $\alpha$ is directly proportional to the magnitude $B_1$ and $t_\alpha$ of the RF pulse. Figures 2.3b–d shows the effective magnetization vector after a RF pulse with the same duration but different magnitudes. An transversal component ($\mathbf{M_T}$) of the magnetization is introduced in Figure 2.3b and c. This magnetization precesses with $\omega_0$ around $B_0$ and thus induces a measurable signal into the MR coil [33]:

$$U_{ind} = -\frac{d}{dt}\int \mathbf{B_1^*}(\mathbf{r})\mathbf{M_T}(\mathbf{r})\ \mathrm{dV} \tag{2.18}$$

with $U_{ind}$ being the induced electric potential, $\mathbf{B_1^*}(\mathbf{r})$ the fictive magnitude of the magnetic field generated by a unit current in the coil at position r, and dV as the volume element of the integrated probe. According to the principle of reciprocity [33], $B_1^*(r)$ can be used for this equation since the induced potential from a specific place in the probe is proportional to the $B_1$ field introduced by the coil at this place.

In Figure 2.3d, the complete magnetization is inverted and no $\mathbf{M_T}$ exists. Thus, no signal can be measured. However, the change of the magnetization vector introduced by the RF pulse relaxes towards the original state when no additional RF pulses are applied.

# 3 $^{19}$F MRI

Four years after the introduction of MRI in 1973 [3], $^{19}$F MRI was presented for the first time [34]. Even at this early stage, the imaging potential of **P**er**F**luoro**C**arbon (PFC) compounds by $^{19}$F MRI was already acknowledged [34]. Emulsified PFC compounds were investigated as potential blood substitutes since the early 1960s [35] and thus a wide variety of PFC compounds are currently available as potential $^{19}$F MRI markers [36, 37]. With the rise of $^{19}$F MRI, PFC compounds often served as markers to measure different *in vivo* physiological parameters such as the **P**artial Pressure of **O**xygen ($pO_2$) [36, 38, 39]. Furthermore, since the intravenous injection of PFC emulsions leads to the uptake of PFC compounds by phagocytes [40–42], $^{19}$F imaging of PFC labeled macrophages was performed [21, 43]. Recently, it was shown by Ahrens et al. that cells can be labeled *ex vivo* with PFC emulsions and tracked *in vivo* by $^{19}$F MRI [16]. Taken together, these findings lead to great interest in cellular $^{19}$F MRI. Thus, the applicability of PFC emulsions to serve as a cell marker has been shown in several studies since then [20, 21, 37, 44–49].

This chapter is intended as an overview of the basic principles underlying $^{19}$F MRI. Furthermore, a description of the PFC $^{19}$F MRI markers used and their basic properties is provided. A more general description of different $^{19}$F MRI markers can be found in [36]. A more detailed description concentrating on PFC compounds used as cellular $^{19}$F MRI markers is provided in [37]. Furthermore, for the interested reader, several review papers exist dealing with different aspects of $^{19}$F MRI [18, 19, 36, 37, 42, 50].

## 3.1 Theory of $^{19}$F MRI

This section is intended to give an overview of the basic definitions and physical principles underlying $^{19}$F MRI.

### 3.1.1 Sensitivity of the $^{19}$F nucleus

**Table 3.2:** *Nuclear properties of $^{1}H$ and $^{19}F$. Values obtained from [27–29]. I is the spin quantum number and $\gamma$ the gyromagnetic ratio.*

| *Isotope* | *I* | $\gamma/2\pi$ *[MHz/T]* | *Natural Abundance* | *Relative Sensitivity [%]* |
|---|---|---|---|---|
| $^{1}$H | 1/2 | 42.58 | 99.99 | 1.00 |
| $^{19}$F | 1/2 | 40.05 | 100.00 | 0.83 |

Table 3.2 presents an extract of Table 2.1. It concentrates on the two isotopes focused on in the present work: $^{1}$H and $^{19}$F. As mentioned before, both nuclei have $I = 1/2$ and thus the same basic physical principles apply. Furthermore, the $\gamma$ of both nuclei differs by only 6%. Thus, in comparison to $^{1}$H, a high relative sensitivity for $^{19}$F is also given. Since the spin value is the same for $^{1}$H and $^{19}$F, the relative sensitivity depends only on the magnetic moment of the regarded nucleus [27]. According to [27], the ratio of the signal intensities ($S_{^{19}F}$,$S_{^{1}H}$) is given as:

$$\frac{S_{^{19}F}}{S_{^{1}H}} = \frac{(\mu_{^{19}F})^3 B_0{}^{\frac{3}{2}}}{(\mu_{^{1}H})^3 B_0{}^{\frac{3}{2}}} = \frac{(\mu_{^{19}F})^3}{(\mu_{^{1}H})^3} \tag{3.1}$$

Inserting Equation 2.1 in Equation 3.1 leads to:

$$\frac{S_{^{19}F}}{S_{^{1}H}} = \frac{(\gamma_{^{19}F})^3}{(\gamma_{^{1}H})^3} = \frac{(40.05\ MHz/T)^3}{(42.58\ MHz/T)^3} \approx 0.83 \tag{3.2}$$

As pointed out in [50], the relative **S**ignal to **N**oise **R**atio (SNR) in $^{19}$F has an even higher value if the noise is dominated by the sample. In this case, the noise increases linearly with the frequency and therefore the following relation is applicable:

$$\frac{SNR_{^{19}F}}{SNR_{^{1}H}} = \frac{(\gamma_{^{19}F})^2}{(\gamma_{^{1}H})^2} \approx 0.89 \tag{3.3}$$

These virtues and a natural abundance of 100% make $^{19}$F an interesting target for MRI. Furthermore, the low amounts of endogenous fluorine ($\approx 0.0066$ mol/L compared to $^{1}$H $\approx$ 99 mol/L or $^{31}$P $\approx 0.35$ mol/L) [51] in tissue make $^{19}$F a particularly interesting candidate for an unambiguous marker without a natural background signal [16, 52].

### 3.1.2 SNR considerations regarding $^{19}$F MRI

This section follows Reference [53], which also provides a more detailed explanation of the following issues.

Since $^{19}$F MR imaging often suffers from low signal strength, the noise influence on the signal should be considered [44, 53].

In general, the $SNR$ is defined as follows:

$$SNR = \frac{S}{\sigma} \tag{3.4}$$

with $S$ being the signal intensity in the absence of noise and $\sigma$ the standard deviation of the noise of the real and imaginary part of the images. Normally the $S$ of magnitude images is regarded. In this case, however, the noise distribution is no longer Gaussian but Rician [53]. Thus, the measured signal intensity in the magnitude images ($S_m$) is $\neq S$ and Equation 3.4 will provide incorrect results. However, as shown in [53], the mean $S_m$ can be approximated as:

$$S_m = \sqrt{S^2 + \sigma^2} \tag{3.5}$$

As seen from Equation 3.5, if $S \gg \sigma$ this effect can be neglected. For $S$ only $> \sigma$, which is often the case for $^{19}$F MR, the Rician influence on $S_m$ often cannot be ignored. However, for low $SNR$, Equation 3.5 can be rewritten to provide an approximated mean $S$ [53]:

$$S = \sqrt{|S_m^2 - \sigma^2|} \tag{3.6}$$

Thus, Equation 3.4 can be rewritten for low signal strengths:

$$SNR = \frac{\sqrt{|S_m^2 - \sigma^2|}}{\sigma} \tag{3.7}$$

Although Equation 3.7 does not provide a Gaussian distribution, it has been shown that Equation 3.7 can be used for $SNR$ calculation when $SNR \geq 2$ [53].

### 3.1.3 Chemical shift

The present section follows References [27, 28].

To maximize the $^{19}$F signal, the molecules used as $^{19}$F markers normally have multiple $^{19}$F atoms. The different $^{19}$F atoms of those molecules often experience a different chemical environment and thus, the $^{19}$F atoms do not experience the same effective magnetic field. In more detail, Equation 2.4 must be rewritten for a specific atom of the regarded molecule thus:

$$\omega_0 = \gamma B_0(1 - \sigma) \tag{3.8}$$

with $\sigma$ being the so-called shielding constant. The shielding effect is based on the electron density surrounding the regarded nucleus.

As consequence markers with $^{19}$F nuclei bound in different chemical environments exhibit multiple resonance frequencies. This effect is called the chemical shift and actually enables the structural classification of different molecules by MRS that is widely used in chemistry.

This property combined with the fact that the chemical shift covers a range of $\approx$ 300 ppm for fluorine molecules (compared to $\approx$ 12 ppm for $^1$H) [36, 54], however, make $^{19}$F MRI of molecules with chemically unequal atoms challenging [52, 55–57]. Thus, special or modified imaging sequences must be used for multi-resonant $^{19}$F molecules [52, 58]. A practical example of *in vivo* imaging of a multi-resonant $^{19}$F molecule is provided in Chapter 5.

The chemical shift ($\delta$) of a specific resonance line is defined by:

$$\delta = \frac{\nu_{Substance} - \nu_{Reference}}{\nu_{Reference}} \tag{3.9}$$

with $\nu_{Substance}$ being the frequency of the specific resonance line and $\nu_{Reference}$ the frequency of a reference. Thus, $\delta$ has no unit but is normally given in ppm.

### 3.1.4 J-Coupling

Besides the chemical shift of the differently bound $^{19}$F nuclei, the so-called J-coupling (indirect spin-spin coupling) can influence the sensitivity of $^{19}$F MRI [52, 55, 56]. However, J-coupling is a phenomena that only occurs in multi-resonant $^{19}$F-molecules such as **P**er**F**luoro**O**ctyl**B**romide (PFOB). This section describes the basic properties of J-coupling and follows the descriptions in [27, 28, 52, 55, 56].

The origin of J-coupling lies in a magnetic interaction between different nuclei. This interaction applies not directly over space but indirectly over the electrons of the chemical bonds. The basic principles of J-coupling are best demonstrated on a simple AX spin

system. Thus, the magnetic moment of the nucleus A weakly magnetizes the bonding electrons. Therefore, in an external field $B_0$, the neighbor nucleus X will, depending on the spin state of nucleus A, experience an effective magnetic field $B_{eff}$ different from $B_0$. For example, if nucleus A has a spin of $I = 1/2$ it can occupy two approximately equiprobable spin-states. As a consequence, not only one resonance line is observed in a spectrum for nucleus X but two lines with the same intensity. The difference between those two resonance lines is defined as the so-called scalar coupling constant $J_{AX}$. Importantly, $J_{AX}$ is $B_0$ independent and is thus given in Hz. An overview of typical fluorine scalar coupling constants is given in Table 3.3.

**Table 3.3:** *Values for different fluorine scalar coupling constants. Values obtained from [36].*

| *Number of bonds* | *Label* | *J [Hz]* |
|---|---|---|
| 2 | $^2J_{FF}$ | 200-800 |
| 3 | $^3J_{FF}$ | <1 |
| 4 | $^4J_{FF}$ | 1-20 |
| 5 | $^5J_{FF}$ | 0-40 |
| 6 | $^6J_{FF}$ | 0-40 |

In general, a simple relationship for the resonance line splitting is given for $I = 1/2$ nuclei. Thus, single resonance lines (assuming spin coupling does not occur), will split into $n + 1$ resonance lines when spin coupling with a neighboring group appears. Hereby, $n$ is the number of chemically equivalent nuclei from the coupling group. The generalized formula for the number of resonance lines is: $2nI + 1$.

A practical example is found by looking at a $CF_3$ end-group of a linear PFC molecule. If the $CF_3$ end-group is regarded by itself, only one resonance line would theoretically be present in the MRS spectrum since all atoms are chemically equivalent. If, however, a $CF_2$ group neighbors a $CF_3$ group J-coupling takes place. This is a so-called $A_3X_2$ system because two fluorine atoms are present in the $CF_2$ group and three in the $CF_3$. According to the relationship of the resonance line splitting, a triplet for the $CF_3$ and a quartet for the $CF_2$ is present in the spectrum. In the following, only the $CF_3$ is regarded.

Please note that since a minimum of 3 bonds are normally between the chemically different fluorine nuclei in a PFC molecule this structure can often not be resolved using a standard MRI spectrometer. This is due to low $J$ constants (Table 3.3). The resonance line splitting due to J-coupling can be resolved with MRS spectrometers and can be used for molecule characterization.

Although no chemical shift problems are to be expected from J-coupling in $^{19}$F MRI of PFC compounds, another effect can be observed in spin-echo sequences. Equation 3.10 gives the signal of a coupled $CF_3$ group for a spin-echo sequence dependent on the **E**cho **T**ime ($TE$).

$$S(TE) = \frac{1 + cos(2\pi JTE)}{2}\, e^{\frac{-TE}{T_2}} \tag{3.10}$$

Thus, no pure $T_2$ decay can be observed for the $CF_3$ group when a spin-echo sequence is used for measurement (cf. Figure 3.4a).

This effect arises from signal cancellation at specific $TE$ time points due to the different $CF_3$ resonance lines. It is important to know that the relative intensity of the resonance lines after splitting behaves like binomial-coefficients. Thus, for a $CF_3$ group with a coupling $CF_2$ group ($n = 2$), the following intensity pattern is given:

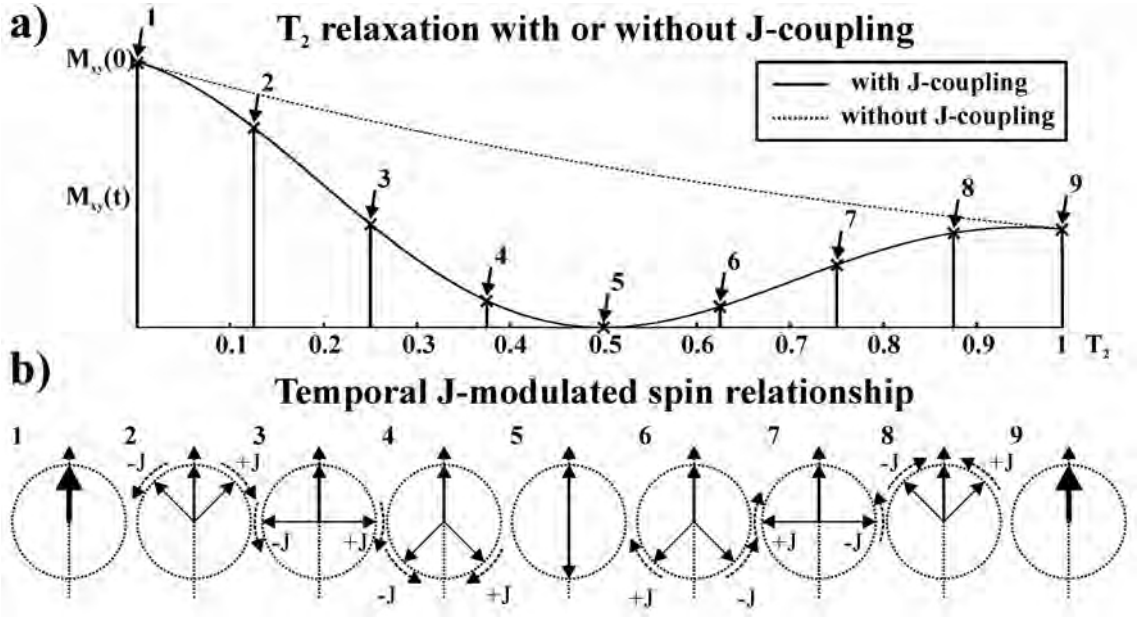


**Figure 3.4:** *a) Simulation showing the influence of J-coupling on a $CF_3$ resonance signal during the $T_2$ decay according to Equation 3.10. Chosen parameters: $J$ = 10 Hz and $T_2$ = 100 ms. b) Magnetization vectors of the different spin states at different temporal points.*

$$1 : \frac{n}{1} : \frac{n(n-1)}{2 \cdot 1} = 1 : 2 : 1 \tag{3.11}$$

Thus, the two outer resonance lines with $f_0 \pm J$ have only half the intensity of the resonance line at $f_0$ ($f_0$ = middle frequency of the $CF_3$ group). Since the two outer spin ensembles precess with $f_0 \pm J$, signal cancellation appears at $TE = 1/2J$ ( cf. Figure 3.4b).

Methods to cancel the J-modulation in spin-echo-based $^{19}$F MR imaging of specific resonance lines are presented in References [52, 55, 56]. Spin-echo sequences are explained in more detail in Section 4.2.2.

## 3.2 $^{19}$F substances

All 2D structural formulas of the presented molecules were drawn with the program BKchem version 0.13.0 written by Beda Kosata [59]. All 3D structural formulas were drawn using the **B**iochemical **AL**gorithms **L**ibrary (BALL) [60, 61].

### 3.2.1 Trifluoroacid (TFA)

As with "most biomedical applications" [36], the official $^{19}$F MRS/MRI reference standard of the **I**nternational **U**nion of **P**ure and **A**pplied **C**hemistry (IUPAC), fluorotrichloromethane, was impractical for the present work. Instead, **Tri**-**F**luoro-**A**cid (TFA) was used as the $^{19}$F reference substance.

TFA was chosen as reference substance on the basis of its single resonance peak ($\approx$ -76.5 ppm). This peak is due to its three chemically equivalent fluorine atoms which is close to the resonances of several PFC compounds. Furthermore, TFA is a water soluble liquid acid

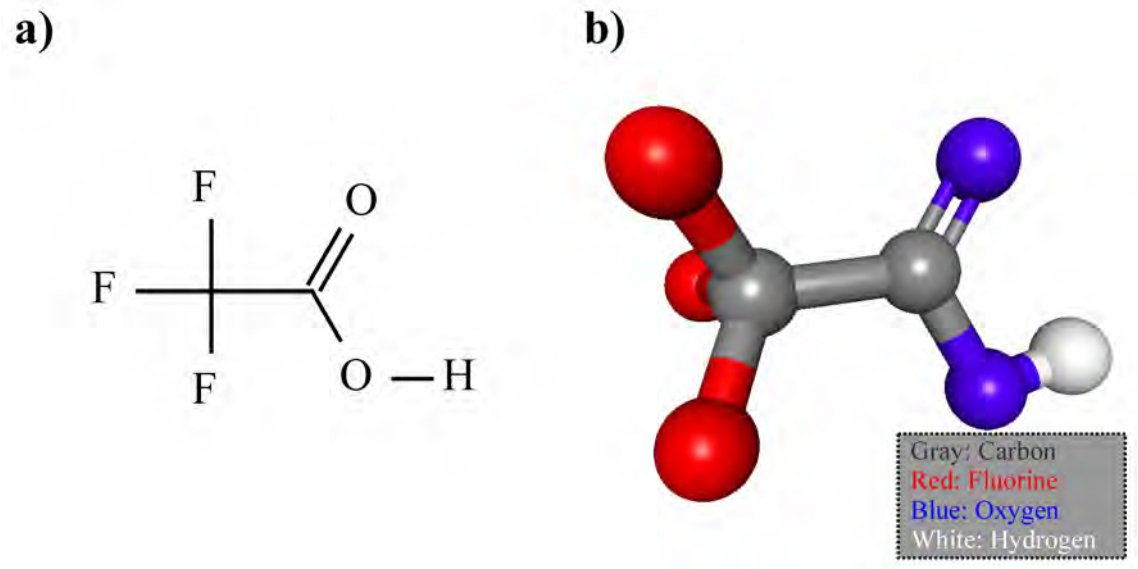


**Figure 3.5:** *a) 2D structural formula of TFA. b) 3D structural formula of TFA.*

with a molecular weight of 114.02 g/mol [62]. Thus, different concentrations of fluorine spins can be easily obtained by diluting TFA in water. The 2D and 3D structural formulas of TFA are shown in 3.5.

### 3.2.2 Perfluorocarbons (PFC)

Only PFC compounds were used for *in vivo* $^{19}$F MRI in the present work. The following describes some of the basic chemical and MR properties of PFC compounds before presenting in detail the PFC compounds used in the present work. An overview of multiple PFC compounds can be found in [36, 37].

PFC compounds are linear or cyclic carbon molecules with all protons substituted in most cases by fluorine atoms [63]. This is often performed through direct fluorination [37, 64, 65]. A basic example is hexafluoro benzene, in which all protons of the benzene molecule are substituted by fluorine atoms (cf. Figure 3.6). PFC compounds are thermally and chemically very stable [37, 66, 67] because, combined with other PFC inherent properties, the fluorine-carbon bond is the most stable single bond found in organic chemistry. Consequently, PFC compounds are biologically inert and thus remain unmetabolized in the organism [37, 63, 66–68]. Furthermore, PFC compounds are hydrophobic since the fluorinated chains inherit a large surface and the fluorine atoms show a low polarizability [67]. Interestingly, PFC compounds often also show lipophobic behavior [29, 37, 46, 67]. Therefore, PFC compounds cannot be dissolved in standard solvents and are normally emulsified before *in vivo* application [29, 36, 63, 66, 67, 69].

PFC emulsions are produced by adding a surfactant and water & buffer to the PFC compound. Emulsion are mainly produced through sonification [37, 44, 46] or microfluidization [37, 45]. This process creates so-called PFC nanoemulsions [37]. Normally PFC nanoemulsions show a distribution of the particle diameters between 20–500 nm [37]. Typically, current PFC nanoemulsions have a PFC content between 10% and 40% Volume/Volume (v/v) [16, 20].

Historically, the first PFC emulsion approved for human application by the **F**ood

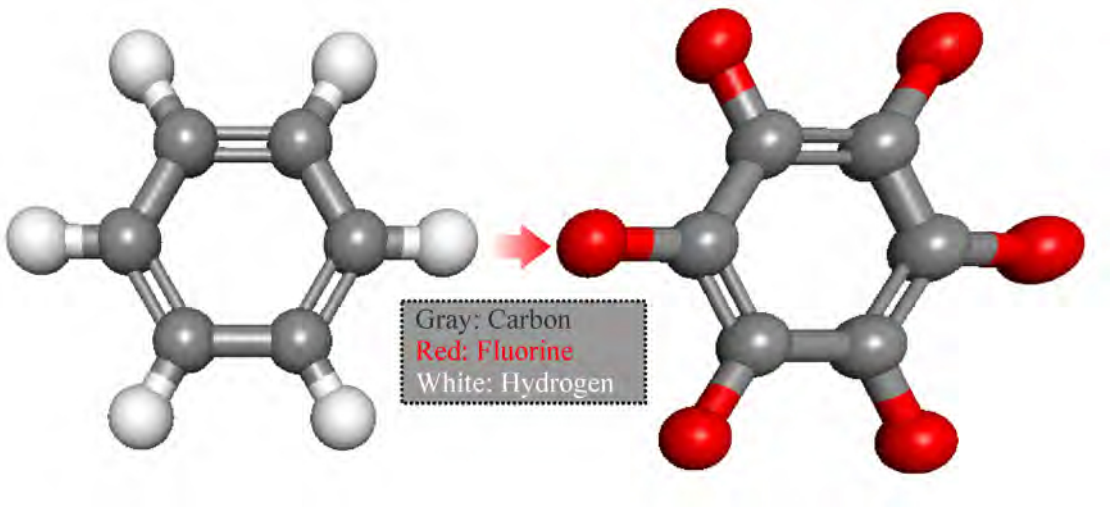


**Figure 3.6:** *To form a PFC out of benzene (left), all the protons are substituted by fluorine atoms (right)*

and **D**rug **A**dministration (FDA) as a blood-substitute used a "**P**oly(**E**thylene **O**xide)-**P**oly(**P**ropylene **O**xide)-**P**oly(**E**thylene **O**xide) (PEO-PPO-PEO) triblock non-ionic copolymer" [37] (Pluronic-F68®, BASF, Ludwigshafen am Rhein, Germany) as the PFC emulsion surfactant; however, the surfactant had correlating side-effects [69]. Pluronic-F68® is still used as a surfactant for PFC nanoemulsions used in pre-clinical research [37, 45]. A recently proposed approach using a different non-toxic polymer for PFC encapsulation showed that the particles can be created with a range of diameters (200–2000 nm) [70]. Thus, successful cell labeling was also possible using the obtained nanoparticles [70, 71]. Alternatively, phospholipids are often used as a surfactant in PFC emulsions [20, 37]. Egg yolk phospholipids, for example, have been used in the preparation of blood-substitute PFC nanoemulsions meant for human application [69, 72]. However, to the knowledge of the author, no FDA approved PFC emulsions are available for human application to date [73]. Thus, in general, PFC emulsions are currently used for pre-clinical research.

Not only can PFC compounds be emulsified, they can also be encapsulated using alternative techniques. For example, PFC loaded alginate capsules have been proposed as a mean of delivery [74]. Since, however, the diameter of those capsules are normally in the range of mm [74], cell labeling with those particles is currently not possible.

The *in vivo* biodynamics of emulsions (e.g., **I**ntra**V**enously (i.v.) applied PFC emulsions) depends on the PFC compound used [36]. In general, the PFC emulsions are cleared from the bloodstream by macrophage activity and thus mainly embedded into organs of the **M**ononuclear **P**hagocyte **S**ystem (MPS) (e.g., the spleen and liver) [36, 37, 47, 67–69, 75]. The half-life of the PFC emulsion in the blood stream is normally in the range of several hours [36, 68, 69, 75]. Other than $^{19}F$ signal found in the organs of the MPS, signal can often be detected in other organs, especially the lungs [47, 68, 75]. This is because the PFC compounds are exhaled in a slow process through the lungs [37, 67, 69, 72].

As mentioned above, PFC emulsions have been investigated as potential blood-substitutes since the early 1960s [35, 37]. This is due to their ability to coordinate high amounts of oxygen [38]. Importantly, the concentration of oxygen in the PFC emulsion correlates linearly with the $pO_2$ in its surrounding [63, 69, 76]. Contrary to hemoglobin, in which the

oxygen is bound, the oxygen is physically dissolved in PFC emulsions [63, 67]. This feature is due to the low interactions (i.e. low van der Waals interactions) in the PFC molecules [67]. Since the binding of the oxygen is only physical PFC emulsions have a quicker release than oxygen bound to hemoglobin [63].

As mentioned, the concentration of the physically dissolved oxygen in the PFC emulsions correlates linearly with the $pO_2$ in its surrounding, obeying Henry's law [38, 66, 76]. Since oxygen is paramagnetic, it influences the relaxation times of the PFC molecules in its proximity [38, 39]. According to Dardzinsk et al., the $T_1$ and $T_2$ relaxation times of a PFC molecule obey the following equations [39]:

$$\frac{1}{T_1} = A_1 + B_1 \cdot pO_2 + C_1 \cdot T \tag{3.12}$$

$$\frac{1}{T_2} = A_2 + B_2 \cdot pO_2 + C_2 \cdot T \tag{3.13}$$

Thereby, $A_{1/2}$, $B_{1/2}$ and $C_{1/2}$ are constants and $T$ the temperature. Thus, with the help of PFC emulsions the $pO_2$ can be measured *in vivo* by MR relaxometry [36, 38, 39]. However, a certain temperature dependence must be taken into account as shown in Equations 3.12 and 3.13.

Besides measuring $pO_2$, the MR community gained further interest in PFC emulsions when it was shown that different types of cells can be labeled with PFC emulsions *in* and *ex vivo* [16, 20, 21, 37, 43–47]. Current detection limits are reported to be in the range of $10^{15}$–$10^{16}$ fluorine spins per voxel at high field strength [18–21]. Cells are normally labeled with $10^{11}$–$10^{13}$ fluorine spins [18–21]. This has translated to an *in vitro* detection limit of 200–6000 PFC labeled cells per voxel [18–21]. Furthermore, the visualization of $4\times10^6$ cells in 7 min on a human scanner working at 1.5 T field strength has been reported [18, 20]. Additionally, first clinical trials concentrating on visualizing the delivery of a PFC labeled cell vaccine for the treatment of colorectal cancer were started in 2011 [77].

In addition to MRI further applications of certain PFC compounds were shown for ultrasound, radiography and **C**omputer **T**omography (CT) [72, 78–81], making them also targets of multi-modality imaging [82, 83].

### Perfluoro-15-crown-ether (PF15C)

Figure 3.7 shows the structural formulas of **P**er**F**luoro-**15**-**C**rown-ether (PF15C). Due to the chemically equivalently bonds of the fluorine atoms, the PF15C spectrum exhibits only one resonance line corresponding to 20 fluorine atoms (cf. Figure 3.10a) [37, 39]. In principle, different perfluoro crown ethers exist with only a single resonance line; however, other than PF15C, their behavior is incompatible with biomedical applications [84]. Due to the simple spectrum of PF15C, no specialized MRI sequences must be applied to suppress chemical shift artifacts [37, 39].

Furthermore, PF15C shows a relative long $T_2$ time (dependent on specific parameters such as $pO_2$, Equation 3.13), which makes it especially interesting for MRI using multiple echoes [39]. Thus, PF15C is often used in $^{19}$F MRI cell tracking studies [16, 20, 43, 47]. Moreover, due to its high potential to coordinate oxygen and the strong dependency of the PF15C $T_{1/2}$ relaxation times on the $pO_2$, PF15C is a good candidate for *in vivo*

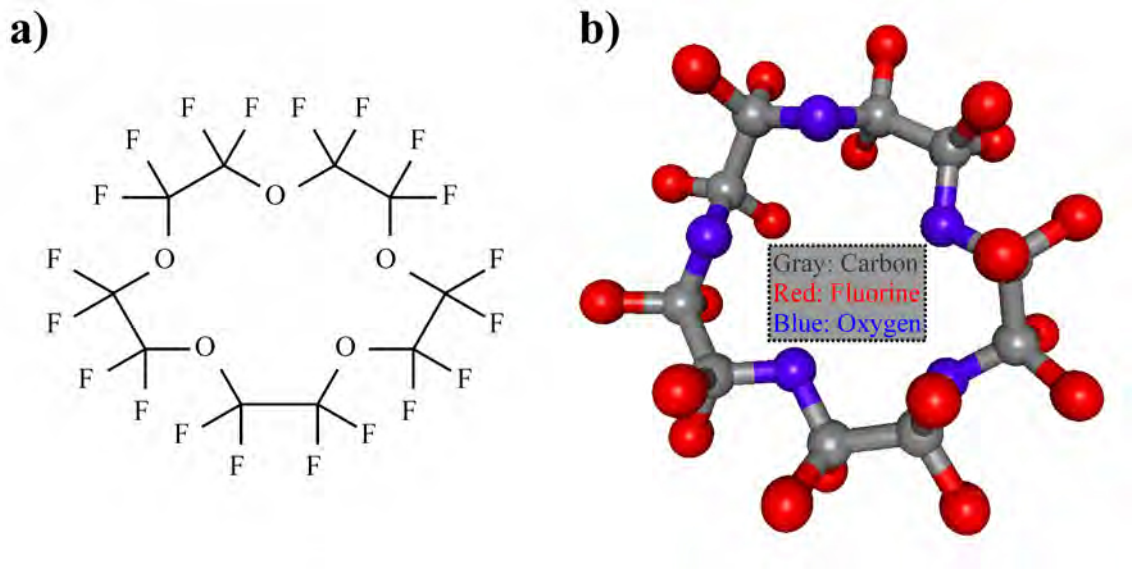


**Figure 3.7:** *a) 2D structural formula of PF15C. b) 3D structural formula of PF15C.*

oxygenation studies [37, 39].

### Perfluorooctylbromide (PFOB)

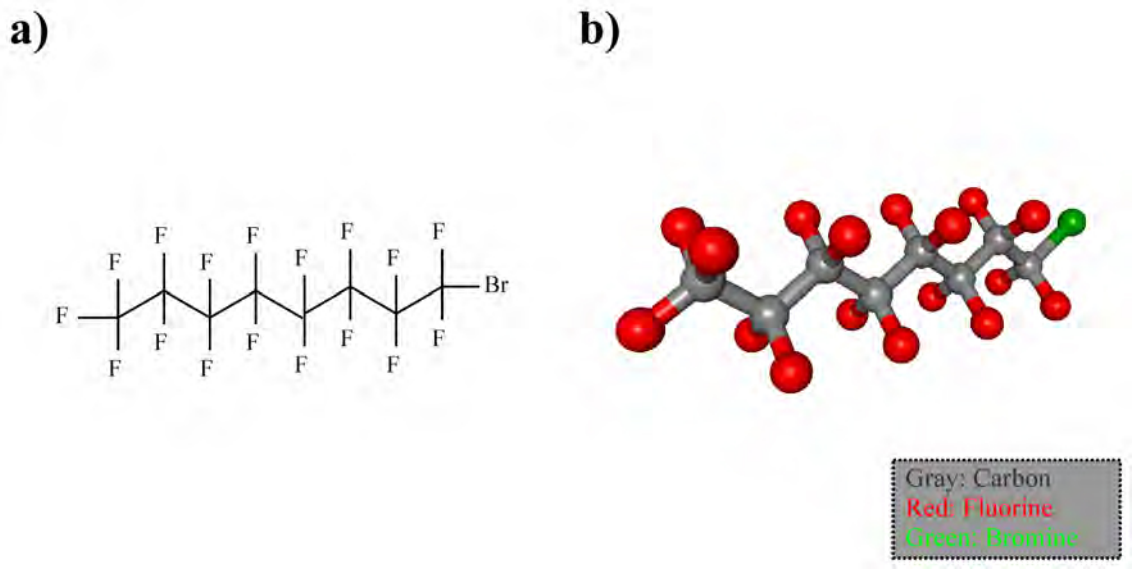


**Figure 3.8:** *a) 2D structural formula of PFOB. b) 3D structural formula of PFOB.*

Even though PFOB exhibits a more complicated fluorine spectrum than PF15C (cf. Figures 3.10a & b), it has several advantages compared to other PFC compounds. Thus, the estimated half-life for PFOB in the liver, three to four days, is relatively short [36, 72]. This unique feature of PFOB was linked to the bromide atom in the terminal position [72]. Unlike most PFC compounds, PFOB is slightly lipophilic because of its covalently bound bromide atom. This feature most likely allows faster excretion than other PFC compounds [37, 72]. Similar to other PFC compounds, the toxicity of PFOB is low ($LD_{50} \approx 40$ g/kg)

[75]. As one of the few PFC compounds PFOB, can be visualized using CT [72, 78, 80]. This is due to the bromide atom, which is radiopaque [72, 78].

Furthermore, PFOB was used as a core compound for a blood substitute PFC emulsion in several initial clinical trials [69, 73]. Although the clinical phase III trials were suspended in 2001, their resumption is still a possibility [73]. This issue further explains why PFOB is a focus in current $^{19}$F MRI research [20, 52].

#### Perfluoropolyether (PFPE)

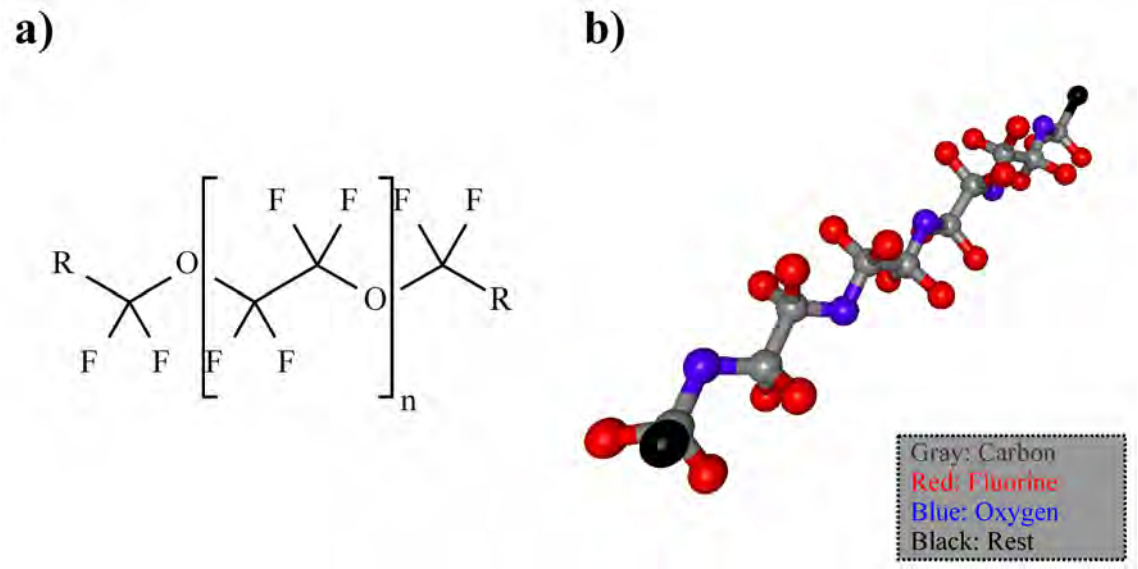


**Figure 3.9:** *a) 2D structural formula of PFPE. b) 3D structural formula of PFPE with $n = 4$.*

**P**er**F**luoro**P**oly**E**ther (PFPE) has, similar to PF15C, a relatively simple spectrum (cf. Figures 3.10a & c) with one main resonance line due to the chemically equivalent $(CF_2CF_2O)_n$ groups [37]. Unlike PF15C small side peaks can be observed since the end groups are not chemically equivalent to the $(CF_2CF_2O)_n$ groups (cf. Figure 3.10c). In fact, a slight J-coupling can be observed for the PFPE molecule [56].

Interestingly, it has been reported that the end groups of the PFPE molecules can be replaced by florescent molecules [37, 45]. This has several advantages. The fluorescence, for example, can be used for histological correlation or multi-modality *in vivo* imaging (MRI and fluorescence imaging) [37, 46]. Furthermore, both the fluorescence signal of fluorescent PFPE molecules and the $^{19}$F signal can be used for quantification studies [45, 46].

## 3.3 Quantification using $^{19}$F MRS/MRI

Since the signal of the investigated $^{19}$F marker is measured directly with $^{19}$F MRS/MRI quantification of the $^{19}$F signal can be relatively straight forward. The two most common approaches are presented in the following sections. Alternative approaches to quantify the $^{19}$F signal exist and the interested reader is referred to publications describing these techniques [45, 85].

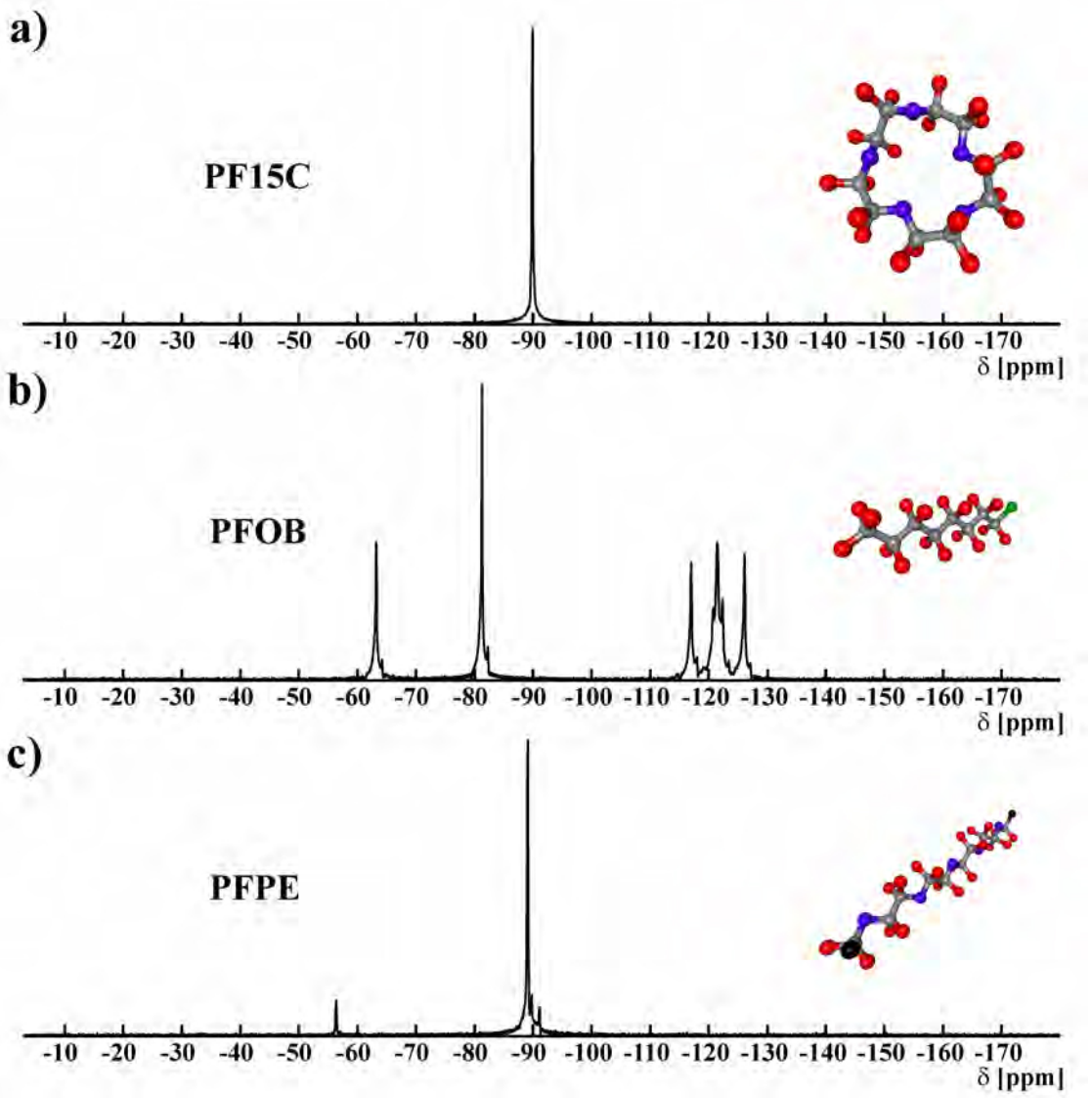


**Figure 3.10:** *a) $^{19}F$ MRS spectrum of PF15C. b) $^{19}F$ MRS spectrum of PFOB. c) $^{19}F$ MRS spectrum of PFPE. All data was normalized individually.*

### 3.3.1 Quantification using $^{19}$F MRS

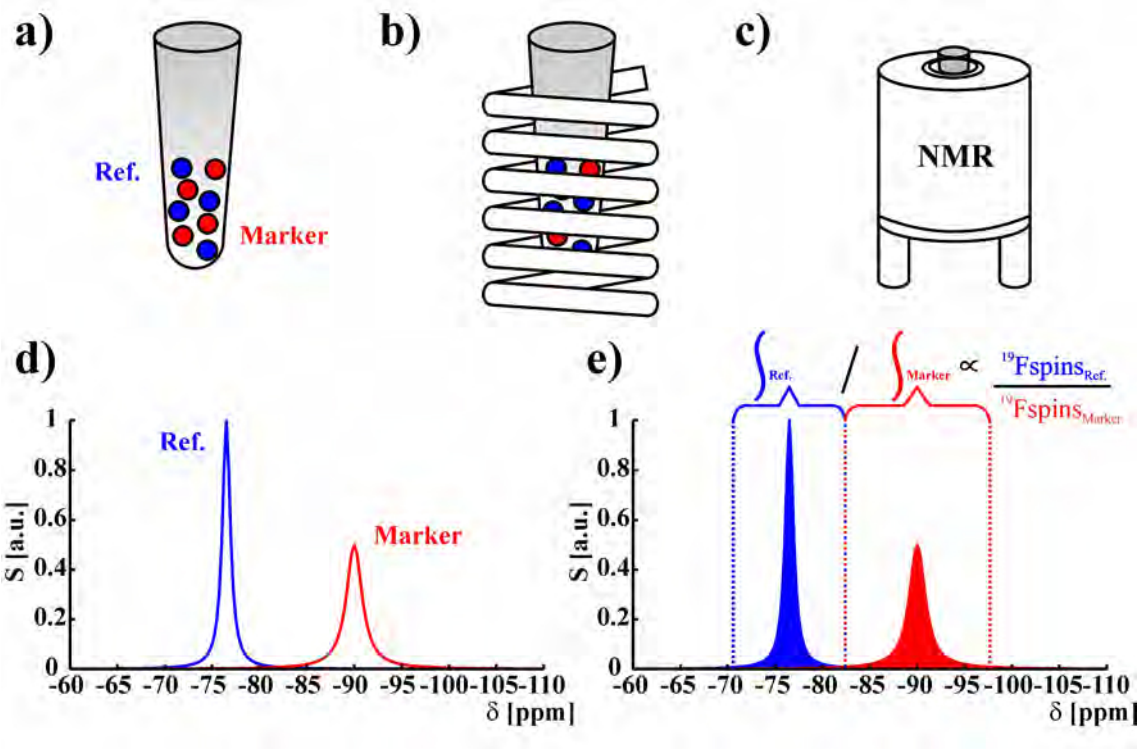


**Figure 3.11:** *Sketch showing the quantification procedure with MRS spectroscopy. a) The reference substance and the marker substance are dispensed in the same tube. b) The tube is placed into the measurement coil (normally inside the magnet). c) A global spectroscopy experiment is performed acquiring the FID after an excitation pulse. d) Simulated spectrum of the two resonance lines (reference: red, marker: blue). e) For quantification, the area under the resonance peaks is integrated. The ratio of the integrals of both resonance lines is directly proportional to the ratio of the amount of $^{19}F$ spins.*

With the help of $^{19}$F MRS, the quantification of an unknown amount of $^{19}$F marker substances is possible. To enable quantification, a $^{19}$F reference substance must be used. Importantly, the structural formula and the amount of the reference substance must be known. Additionally, the reference must exhibit its resonance peaks at a different chemical shift than the $^{19}$F marker that will be quantified.

The MRS quantification procedure is illustrated in Figure 3.11. Normally only a certain size of **N**uclear **M**agnetic **R**esonance (NMR) tubes fit a MR spectrometer without an imaging gradient system. Thus, using this type of spectrometer, the reference and marker must be dispensed in the same tube (cf. Figure 3.11a). For the measurement, the tube containing both substances is placed inside the coil mounted inside the spectrometer (cf. Figure 3.11b). The quantification experiment itself consists of an excitation pulse after which the **F**ree **I**nduction **D**ecay (FID) is acquired [44, 47]. To avoid signal differences due to $T_1$ relaxation a long enough experiment **R**epetition **T**ime (TR) must be chosen to allow full relaxation of both investigated compounds. To analyze the data, a 1D Fourier transform is performed. The resonance peaks in the obtained spectrum can be assigned to the different compounds due to their different chemical shifts (cf. Figure 3.11d). The area under the signal peaks is integrated and the ratio of the integrals of both compounds reveals the ratio of fluorine atoms present in both peaks (cf. Figure 3.11e). The amount of

atoms contributing to the reference resonance line must be known to allow quantification of the unknown marker substance. Alternatively, the weight of the marker substance can be calculated using the following formula [27]:

$$w_{marker} = w_{Ref.} \frac{N_{Ref.} A_{marker} M_{marker}}{N_{marker} A_{Ref.} M_{Ref.}} \tag{3.14}$$

with $w_{marker/Ref.}$ being the weight of the marker or reference substances, $N_{marker/Ref.}$ the number of atoms contributing to the investigated resonance lines, $A_{marker/Ref.}$ the integration areas of the resonance lines, and $M_{marker/Ref.}$ the molecular weight of the corresponding substance.

The advantage of this simple technique is its sensitivity and lack of spatial resolution, allowing it to be performed very fast. However, for *in vivo* investigations, the lack of spatial resolution often makes this simple MRS technique inapplicable.

### 3.3.2 Quantification using $^{19}F$ MRI

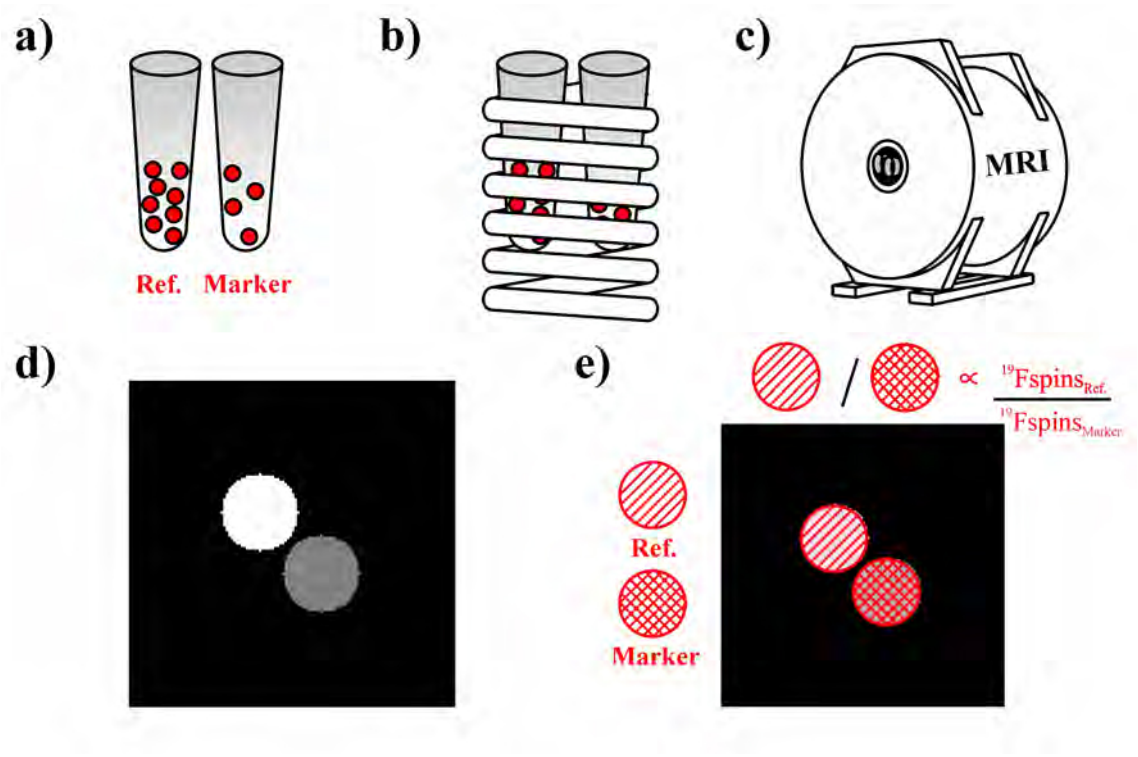


**Figure 3.12:** *Sketch showing the quantification procedure with MRI. a) The reference substance and the marker substance are dispensed in two separate tubes. b) The tubes are placed into the measurement coil. c) A spin density-weighted MRI experiment is performed. d) Sketch showing the two tubes with different intensities. e) For quantification, two ROIs are selected (reference or marker) and the signals are summed. The amount of fluorine in the ROI containing the marker can be calculated using Equation 3.15.*

An alternative, spatially resolved quantification procedure is presented in Figure 3.12. This procedure is based on spin-weighted $^{19}F$ MRI as previously presented for quantitative *in vivo* imaging [44].

First, a known amount of the reference substance is encapsulated inside a tube. The tube containing the reference is then placed next to the tube or animal containing the marker (cf. Figure 3.12a). Since the information obtained using MRI is spatially resolved, the substances are spatially separated. Thus, the same substance can be used for both, the reference and the marker. This setup minimizes signal differences due to different relaxation times. Both objects are placed together in the MR coil (cf. Figure 3.12b) and the measurement is performed in a MRI scanner with a gradient system for spatial encoding of the MRI signal (cf. Figure 3.12b). An image is obtained in which the quantitative information is encoded in the image amplitude (cf. Figure 3.12d). Two ROIs can be selected in the object containing (A) the marker signal and (B) the reference signal. The amount of fluorine spins in the ROI containing the marker can be calculated:

$$\begin{aligned} \frac{^{19}Fspins_{marker}}{^{19}Fspins_{Ref.}} &= \frac{\sum_{n_{marker}=1}^{N_{marker}} S_{n_{marker}}}{\sum_{n_{Ref.}=1}^{N_{Ref.}} S_{n_{Ref.}}} \\ \Rightarrow \; ^{19}Fspins_{marker} &= \frac{\sum_{n_{marker}=1}^{N_{marker}} S_{n_{marker}} \, ^{19}Fspins_{Ref.}}{\sum_{n_{Ref.}=1}^{N_{Ref.}} S_{n_{Ref.}}} \\ &= \frac{\sum_{n_{marker}=1}^{N_{marker}} S_{n_{marker}} C_{Ref.} N_{Ref.}}{\sum_{n_{Ref.}=1}^{N_{Ref.}} S_{n_{Ref.}}} \end{aligned} \tag{3.15}$$

with $^{19}Fspins_{marker/Ref.}$ being the fluorine spins of the marker or reference substances in the chosen ROIs, $N_{marker/Ref.}$ the number of voxels containing marker or reference $^{19}$F signal and $S_{nmarker/Ref.}$ being the signal amplitude of the individual voxels in the different ROIs. $C_{Ref.}$ is the concentration of fluorine spins per voxel in the reference tube. If cells that were labeled *ex vivo* are tracked and the intracellular amount of fluorine is known, an estimation about the number of cells in the investigated ROI can be performed [44].

Even though, in principle, this technique allows fast spatially resolved *in vivo* quantification of the investigated marker, several issues must be considered when using this technique.

As described in Section 3.1.2, a correction of the magnitude signal should be performed in low SNR images to correct for the Rician-distributed noise [44, 53].

A further issue can arise from different *ex-* and *in vivo* relaxation times. Thus, different $T_2^*$ relaxation times can be present at different spatial locations in the scanner since the homogeneity of the magnetic field is generally not the same over the entire **F**ield-**o**f-**V**iew (FOV). Thus, spin-echo-based sequences that minimize $T_2^*$-effects due to their refocusing nature should be used [86]. As mentioned in Section 3.2.2, the $T_1$ and $T_2$ relaxation times of PFC compounds can be influenced by different factors. Thus, $T_1$ and $T_2$ are functions of

the temperature and the oxygenation [36, 39]. Therefore, especially in *in vivo* experiments, it must be ensured that the reference tube has the same temperature as the animal. To minimize the influence of different $T_1$ relaxation times, a long enough sequence TR should be chosen to allow full relaxation of the fluorine spins. Furthermore, a TE that is as short as possible should be chosen to minimize the influence of different $T_2$ or $T_2^*$ relaxation times. Alternatively, quantitative experiments to correct for different relaxation times could be performed; however, those prolong the overall measurement time. The authors in [44] used a linear PFPE molecule that they claim was less sensitive to oxygenation changes than the PF15C substance. Thus, differences in the $^{19}F$ signal due to potentially different $T_1$ relaxation times *ex-* and *in vivo* were minimized [44].

A further critical point is the $B_1$ homogeneity of the used coil. Since the signal of an MR image is a function of the flip angles used, an inhomogeneous $B_1$ profile can lead to a wrong quantification [26]. In general, volume coils can be used to minimize this problem. If surface coils are used to maximize the SNR, however, the inhomogeneous $B_1$ profile will prevent quantification with the above described method when not using correction procedures. Therefore, a $B_1$ experiment should be performed to correct for this parameter. Chapter 7 describes a fast $B_1^+$ mapping procedure to allow correction of an inhomogeneous $B_1^+$ profile that can potentially be applied to quantitative $^{19}F$ MRI.

# 4 MRI & CSI sequences

The following chapter introduces different sequences used for $^{1}H/^{19}F$ MRI/CSI in the present work. Three basic MRI sequences are described: FLASH [8], TrueFISP [9] and TSE sequences [7]. Furthermore, their corresponding **C**hemical **S**hift **I**maging (CSI) counterparts are described in the respective sections: FID-CSI [87], ssfp-CSI [88] and TSE-CSI sequences [89].

As mentioned in Chapter 3, multi-resonant PFC compounds are often used in $^{19}F$ MRI. To avoid chemical shift artifacts and/or minimize J-coupling influence in $^{19}F$ MRI sequences, multiple methods have been proposed [52, 55, 57, 90]. Alternatively, CSI methods can be applied to avoid chemical shift artifacts. The basic principles of spatial encoding will be explained in the following. Furthermore, the basic principles underlying so-called gradient-echo and spin-echo sequences are presented in an additional subchapter. The last subchapter presents in more detail the different sequences used in this work. This chapter follows References [25, 26, 29, 31, 91].

## 4.1 Spatial Encoding

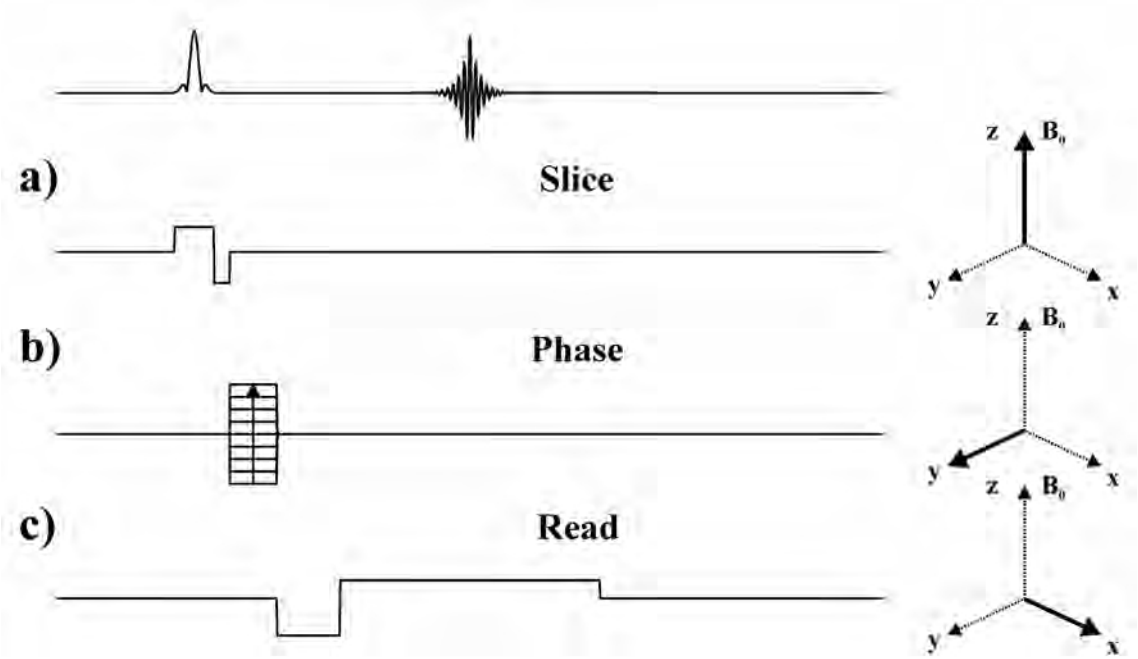


**Figure 4.13:** *Sketch to illustrate the basic components of a (2D) MRI sequence. a) For selection of a slab in the z-direction, a gradient field is turned on during excitation. b) The phase encoding gradient allows the encoding of one direction in the xy plane. c) The read gradient is turned on during the acquisition and allows encoding the second direction of the xy plane.*

To generate MR images, the MR signal must be spatially encoded. To achieve spatial encoding after or during signal excitation gradient coils integrated in the MR scanner are used. These coils produce gradient fields that are superimposed to the static $B_0$ field. A sketch of a basic MRI pulse sequence with different spatial encoding possibilities is shown in Figure 4.13. Thus, during excitation the so-called **S**lice Encoding **G**radient ($G_S$) allows excitation of only a specific slice in z direction of the object (cf. Figure 4.13a). After excitation, the **P**hase Encoding **G**radient ($G_P$) allows one direction in the xy plane to be encoded (cf. Figure 4.13b). During signal acquisition, the so-called **R**ead Encoding **G**radient ($G_R$) enables the spatial encoding of the second direction in the xy plane (cf. Figure 4.13c). The following in more detail explains the three different types of spatial encoding gradients in MR experiments.

### 4.1.1 Slice encoding

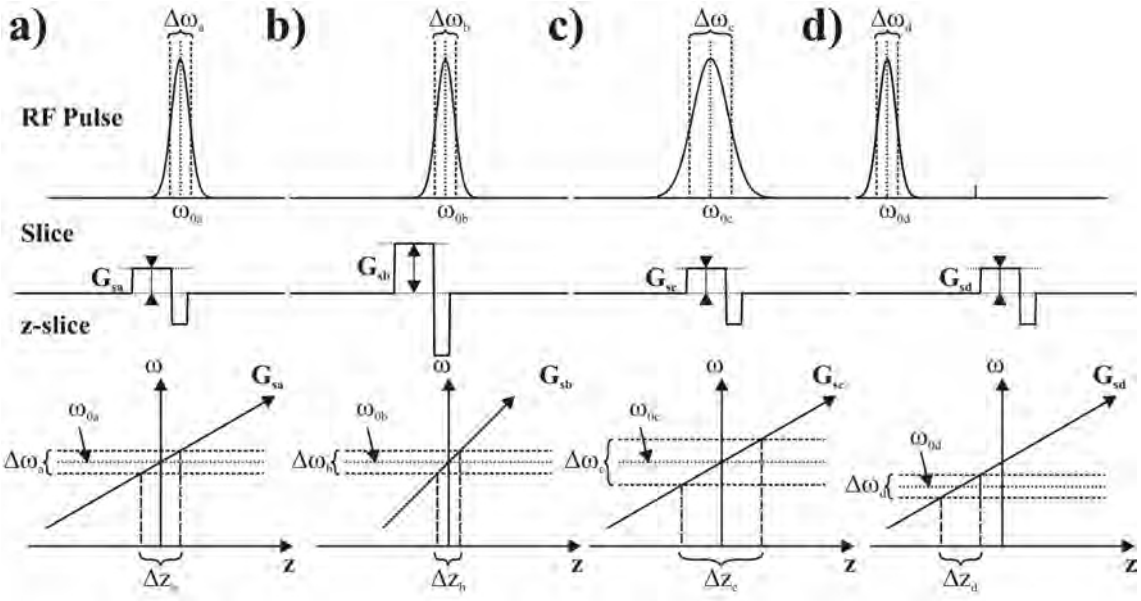


**Figure 4.14:** *Sketch illustrating the slice selection principle of 2D-MRI. The following settings are illustrated: Slice gradient magnitude; $G_{Sa} = G_{Sc} = G_{Sd} \neq G_{Sb}$; RF pulse frequency; $\omega_{0a} = \omega_{0b} = \omega_{0c} \neq \omega_{0d}$ and RF pulse bandwidth; $\Delta\omega_a = \Delta\omega_b = \Delta\omega_d \neq \Delta\omega_c$. The lowest row demonstrates that different slice widths ($\Delta z$) and locations in the probe can be excited depending on the setting of $G_S$ and the RF pulse parameters. The figure is based on a figure of Reference [91].*

For selective signal excitation from only a specific object slice, the slice gradient ($G_S(z)$) is turned on during application of a RF pulse with a certain frequency bandwidth $\Delta\omega$. Since $G_S(z)$ varies in z-direction and is superimposed to $B_0$ the Larmor frequency also varies in the z-direction:

$$\omega_0(z) = \gamma(B_0 + zG_S) \tag{4.1}$$

with $G_S(z) = zG_S$.

Figures 4.14a & b show a RF pulse with the same frequency bandwidth of $\Delta\omega$. In this case, the excited slice width $\Delta$z can be changed through altering the gradient magnitude

($G_S$). Alternatively, the bandwidth of the RF pulse $\Delta\omega$ can be changed to excite a slice with a different width, $\Delta$z (cf. Figure 4.14c).

Equation 4.1 shows that a change in the transmitter frequency $\omega_0$ allows excitation of signal at different positions along the z-direction of the object (cf. Figure 4.14d). For example, switching of the transmitter frequency is also used in 2D-multi-slice MRI to excite different slices of the 3D object.

Please note that the slice gradient is followed by a slice rephase gradient with a sign opposite to that of the slice gradient (cf. Figure 4.14). This is done to compensate for phase differences introduced in the z-direction that are due to the slice gradient. A more detailed explanation of the rephasing issue is given in the following sections.

### 4.1.2 Phase encoding

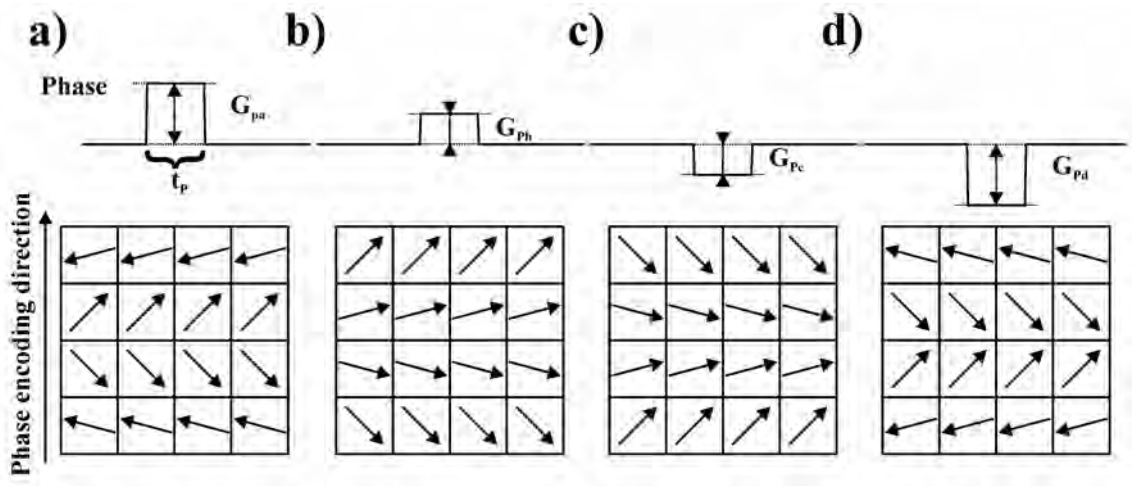


**Figure 4.15:** *Sketch illustrating the phase encoding principle of 2D/3D-MRI/CSI. The following applies: $G_{Pa} \neq G_{Pb} \neq G_{Pc} \neq G_{Pd}$. Thus, different phase states are introduced in the phase encoding direction. After acquisition, the Fourier transform reveals the spatial information of the signal distribution in the phase encoding direction. The figure is based on figures of Reference [91].*

After signal excitation and before signal acquisition, the phase gradient ($G_P(y)$) is used to achieve spatial encoding in an additional direction. Thus, for one phase step $G_P(y)$ is turned on with the magnitude $G_P$. The following applies for the resonance frequency $\omega_0(y)$ while $G_P(y)$ is turned on:

$$\omega_0(y) = \gamma(B_0 + yG_P) \tag{4.2}$$

with $G_P(y) = yG_P$.

After $G_P(y)$ is turned off, all spins again precess with $\omega_0$; however, a variation in the magnetization phase is present in the y-direction (cf. Figure 4.15):

$$\Delta\phi(y) = \gamma y \int_0^{t_P} G_P(t)dt \tag{4.3}$$

with $t_P$ being the duration of $G_P(t)$.

$G_P(t)$ and other imaging gradients are ideally constant; however, in reality each gradient needs a specific time (rise-time) to achieve the full magnitude. If the process is repeated (signal excitation - phase encoding - acquisition) n times with n different magnitudes of $G_P$, n different phase states are acquired in the y direction (cf. Figure 4.15). During acquisition the data is stored in the so-called k-space. When phase encoding is performed, a Fourier transform in the phase encoding dimension of the k-space reveals the spatial information of the signal distribution in the phase encoding direction.

Please note that, in principle, all spatial directions can be encoded using phase gradients that vary in the different spatial directions. Thus, instead of a selective RF pulse as described in Section 4.1.1, the encoding of the z-direction can also be achieved with an additional $G_P(z)$ in the z-direction (3D MRI/CSI). Furthermore, the spatial encoding in classical CSI sequences is achieved by one slice and two phase encoding gradients (2D-CSI) or three phase encoding gradients (3D-CSI). A sketch explaining the CSI post processing in greater detail is given in Appendix A on page 127.

### 4.1.3 Read encoding

In MRI, a read gradient ($G_R(x)$) is applied during the signal acquisition to achieve additional spatial encoding. Thus, the following relationship holds for the Larmor frequency in the x-direction:

$$\omega_0(x) = \gamma(B_0 + xG_R) \tag{4.4}$$

with $G_R(x) = xG_R$.

Since signal originating from different locations in the x-direction has different frequencies when $G_R(x)$ is turned on, the complete acquisition of the spatial information in the x-direction is enabled. As mentioned above, during acquisition the data is stored in the k-space. When read encoding is applied, a Fourier transform in the read encoding direction of the k-space reveals the spatial information of the signal distribution in the read encoding direction.

Since the application of any gradient has a dephasing effect on the spins, a so-called read prephase gradient is applied before the read gradient (cf. Figures 4.16a & b). After the read prephase gradient, the read gradient is applied with the opposite sign. Thus, a so-called gradient-echo is generated with maximal signal when the area under the read gradient matches the area under the read prephase gradient (cf. Figure 4.16c). To acquire the full spatial information in the x-direction, $G_R(x)$ is applied for a certain length of time, $t_R$. At its end, the signal is again dephased in the x-direction (cf. Figure 4.16d). The dephased state can be rewound by applying the initial read prephase gradient (cf. Figure 4.16f). This is necessary for balanced sequences such as TrueFISP.

Please note that the read prephase gradient, the phase encoding gradient and the slice rephase gradient can all be simultaneously applied. This application scheme allows faster sequence timing and is often used (cf. Figures 4.18, 4.20, and 4.23).

In CSI, no read encoding gradient is used for encoding a spatial direction. As mentioned above, phase encoding is instead used. Thus, no gradient is turned on during the signal acquisition. Therefore, a spectrum is obtained when a Fourier transform is applied to the spectroscopic dimension of the k-space. As mentioned above, a sketch explaining in greater detail the CSI post processing may be found in Appendix A on page 127.

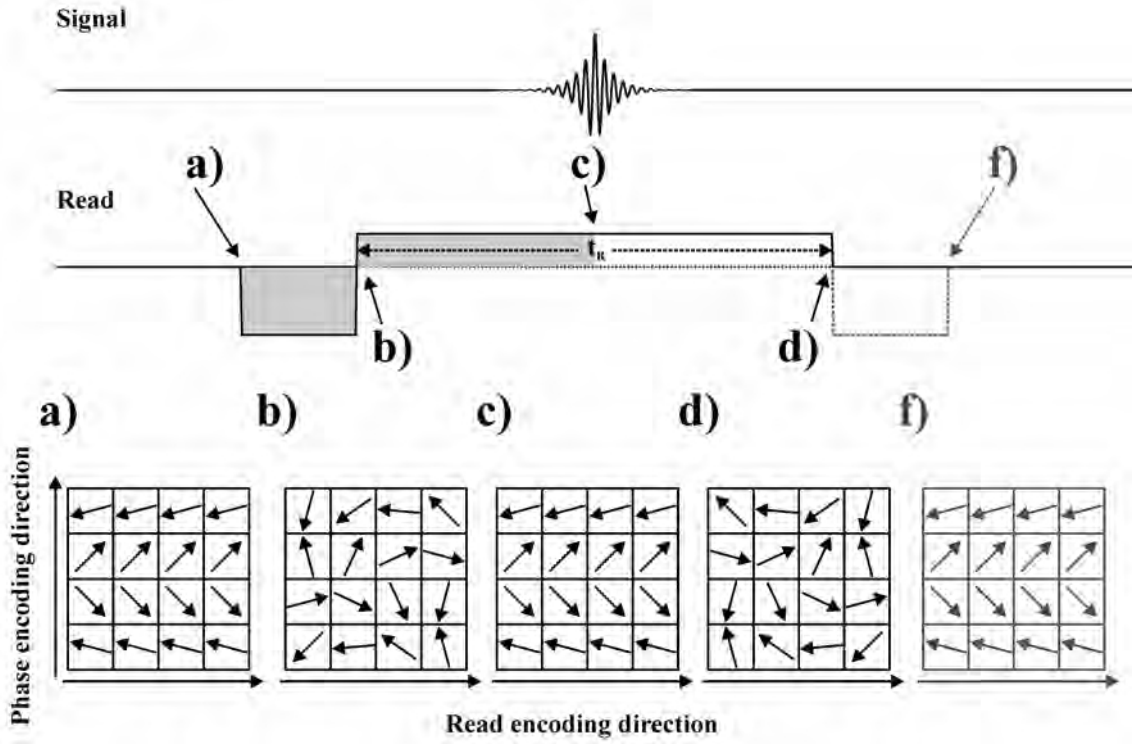


**Figure 4.16:** *Sketch illustrating the read encoding principle of a MRI experiment. Four different temporal points are regarded (a–d). a) Just before the beginning of the read gradient, the same frequency and phase is present in the read encoding direction (x-direction). b) After the so-called read prephase gradient, a different phase is present in the x-direction. After the prephase gradient, the read gradient is applied with a sign opposite to that of the prephase gradient. c) When the area under the read gradient matches the area of the read prephase gradient, the same phase is present in the x-direction. Thus, the signal is maximized and a so-called gradient-echo is generated at the TE. d) After the read gradient is turned off, a phase difference is again present in the x-direction. f) In some sequences (e.g., TrueFISP), the imaging gradients must be balanced by so-called rephase gradients to cancel any dephasing effects. Thus, the dephasing effects in the x-direction are canceled after application of the rephasing. The figure is based on figures of Reference [91].*

## 4.2 Echo Formation

### 4.2.1 Gradient-Echo

A basic gradient-echo sequence consists of an excitation pulse and spatial encoding gradients (cf. Figure 4.16). Thus, echo generation is performed using the read encoding gradient as described in Section 4.1.3. Figure 4.16 illustrates the echo formation. Two specific gradient-echo sequences are discussed in Section 4.3.1.

### 4.2.2 Spin-Echo

As mentioned in Section 2.2, the $T_2'$ decay is reversible. Contrary to the irreversible $T_2$ decay caused by microscopic magnetic field fluctuations, the $T_2'$ decay is caused by local differences (constant over time) in the external magnetic field. To compensate for the dephasing caused by these constant local magnetic field differences, spin-echo experiments can be performed.

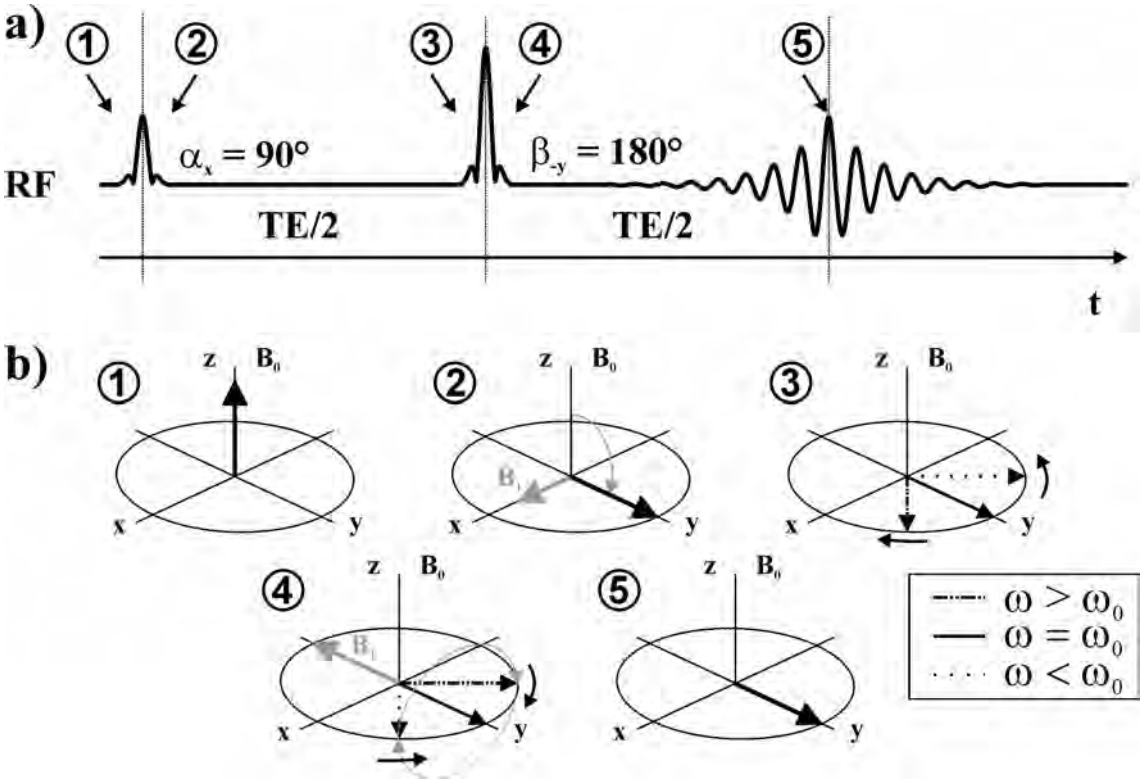


**Figure 4.17:** *Sketch showing the basic principle behind a spin-echo experiment. a) Diagram of the RF pulses and echo formation. The FIDs following the RF pulses are neglected. b) Magnetization behavior at different time points of the spin-echo experiment. Further explanations are provided in the text. The figure is based on figures of Reference [31].*

Figure 4.17 shows the basic principles of a spin-echo experiment. Here, $T_2$ relaxation and imaging gradients are ignored. A basic spin-echo experiment consists of one excitation and one refocusing pulse. Normally the excitation and refocusing pulse flip angles are set to $\alpha = 90°$ and $\beta = 180°$ (cf. Figure 4.17a). Before the excitation pulse, only longitudinal magnetization is present (cf. Figure 4.17$b_1$). Following Section 2.3, the excitation pulse rotates the magnetization vector into the transversal plane (cf. Figure 4.17$b_2$). According to Equation 2.4, spins precess with different frequencies at different spatial locations when different magnitudes of the magnetic field are present at those positions. Thus, a dephasing of the different microscopic magnetization vectors occurs over time (cf. Figure 4.17$b_3$). When a 180° refocusing pulse is played out, the magnetization vectors are rotated by 180° around the application axis of the refocusing pulse (cf. Figure 4.17$b_4$). Since all magnetization vectors still precess with the same frequency, the dephasing is compensated and an echo signal occurs at $TE$ (cf. Figure 4.17$a_5$ & $b_5$).

Two specific spin-echo sequences are regarded in Section 4.3.3.

## 4.3 Sequences

The following covers sequence diagrams, signal behavior and artifacts intrinsic to the sequences of interest for the present work.

### 4.3.1 FLASH/FID-CSI

The FLASH sequence was introduced by Haase et al. in 1986 [8]. This technique was among the first MRI sequences that allowed fast acquisition of MR images. Thus, it was a breakthrough for the clinical application of MRI. Using special techniques, a temporal resolution of 20 ms per image is currently feasible using radial FLASH sequences [92].

The FLASH sequence characteristics are described below in greater detail. Furthermore, its spectroscopic counter part (FID-CSI) is described, which was introduced by Brown et al. in 1982 [87]. In the final subsection, an artifact intrinsic to these sequences is discussed.

#### Sequence diagrams

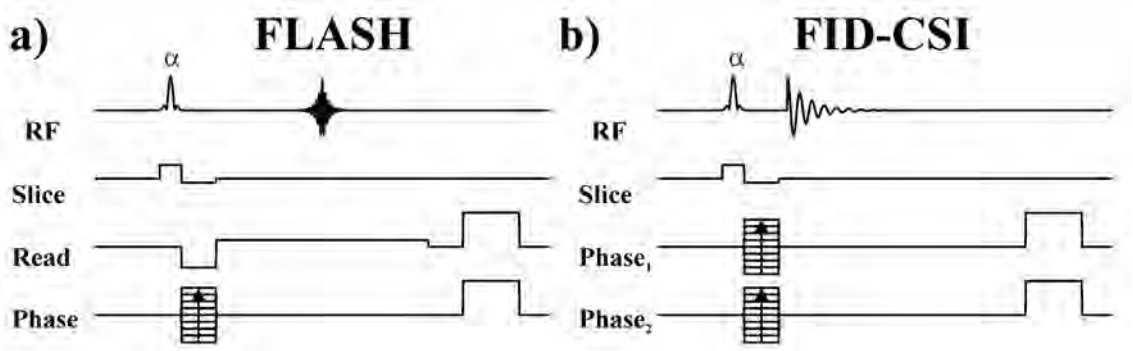


**Figure 4.18:** *Sequence diagrams of basic 2D-FLASH and 2D-FID-CSI sequences. a) Sequence diagram of a basic FLASH sequence. b) Sequence diagram of a basic FID-CSI sequence. Unlike the FLASH sequence, a second phase gradient for the spatial encoding in the x-direction is applied instead of the read gradient.*

Figure 4.18a shows a sequence diagram for a 2D-FLASH sequence similar to the one proposed by Haase et al. 1986 [8]. In principle, the FLASH sequence is a normal gradient-echo sequence. Thus, it has only one initial slice-selective pulse followed by a phase gradient and a readout gradient, which produces the gradient-echo. However, instead of using a 90° pulse for spin excitation, a pulse with a small flip angle is applied. The spoiler gradients after the readout are used to dephase the magnetization present in the transversal plane. Thus, signal contributions to the following signal acquisitions are minimized and a short $TR$ is enabled.

In spectroscopic imaging, the FID-CSI sequence [87] is often referred to as the gold standard [93]. The classical CSI sequences are intrinsically slow because only phase encoding gradients are used for spatial encoding. Thus, if the same $TR$ would be used for both the FLASH and the FID-CSI sequences, the FID-CSI sequence would be slower according to the number of phase encoding steps in the "read direction". However, compared with faster CSI methods, the FID-CSI sequence and its spin-echo counterpart

shows higher sensitivity in most measurement situations [93].

### Signal behavior

As mentioned above, the FLASH sequence is normally run with small flip angle excitation pulses. After a small flip angle excitation pulse is applied, the longitudinal magnetization is reduced by only a small amount. In the absence of relaxation, the longitudinal magnetization would vanish if a certain number of small flip angle excitation pulses would be applied in succession. Since $T_1$ relaxation is present, however, a certain part of the magnetization relaxes between the excitation pulses. Thus, a so-called steady state is reached after a number of excitation pulses. In this steady state, the same amount of longitudinal magnetization is excited, which relaxes between the excitation pulses. Consequently, the same signal is always generated by the excitation pulses:

$$M_T = M_0 \ \sin(\alpha)\frac{\left(1-e^{-TR/T_1}\right)}{\left(1-\cos(\alpha)e^{-TR/T_1}\right)}\ e^{-TE/T_2^*} \tag{4.5}$$

Equation 4.5 describes the steady state signal for a FLASH/FID-CSI sequence [91]. To achieve the steady state, a number of dummy scans in which no signal is acquired are normally performed prior to acquisition of the image information. The optimal steady state flip angle (the so-called Ernst angle) for a given $TR$ and known $T_1$ is described in Equation 4.6 [91]:

$$\alpha_{Ernst} = \arccos\left(e^{-TR/T_1}\right) \tag{4.6}$$

For quantitative FID-CSI, long $TR$ are often used to enable sufficient $T_1$ relaxation of the regarded compounds. In this case ($TR \gg T_1$), the optimal flip-angle is 90° according to Equation 4.6.

### Sequence intrinsic artifacts

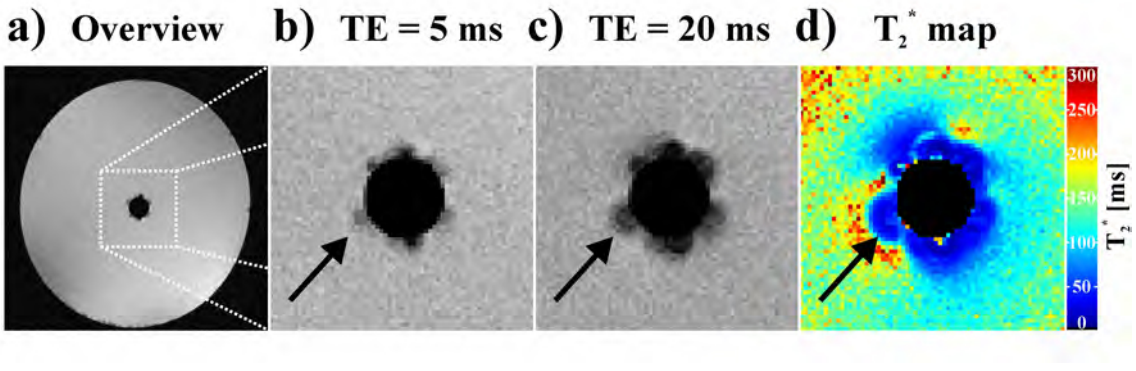


**Figure 4.19:** *$T_2^*$ problematic in FLASH sequences. a) Overview of the image with the area labeled shown in (b–d). b) FLASH image with $TE$ = 5 ms. c) FLASH image with $TE$ = 20 ms. d) $T_2^*$ map calculated from FLASH images with different $TE$ but otherwise the same parameters. Parameters underlying all images: $TR$ = 100 ms, **MaTriX** (MTX) = 256 × 256, **BandWidth** (BW) = 50 kHz, **S**lice **T**hickness (ST) = 2 mm. Measured at 7 T.*

One intrinsic artifact in FLASH/FID-CSI sequences is due to the spin dephasing in the surrounding of susceptibility differences. Thus, the $T_2^*$ time is shortened in areas with high susceptibility differences due to the faster spin dephasing. Since the FLASH/FID-CSI sequences do not contain any refocusing pulses, signal voids appear when the $T_2^*$ is short.

In a FLASH sequence, the severity of these signal voids depends on the used $TE$. Figure 4.19 shows this issue. Thus, when a long $TE$ is chosen (cf. Figure 4.19c), strong signal voids are detected in areas with short $T_2^*$ (cf. Figure 4.19d). When a shorter $TE$ is chosen, the signal voids are minimized (cf. Figure 4.19b).

$TE$ does not exist in FID-CSI sequences since read gradients are not used. Instead, after the excitation pulse and phase encoding, the FID is recorded without turning on any imaging gradients. However, when the spectral resolution is of minor importance, the **A**c**Q**uisition **T**ime ($T_{AQ}$) can be reduced to maximize the SNR of an image formed from CSI data. Alternatively, exponential filter functions based on the $T_2^*$ decay can be multiplied with the FID to maximize the sensitivity [93].

It is important to note that dephasing is more pronounced at high field strengths due to the higher frequency spread of off-resonant spins.

### 4.3.2 TrueFISP/ssfp-CSI

The so-called **F**ast **I**maging with **S**teady State **P**recession (FISP) sequence was introduced by Oppelt et al. in 1986 [9]. Due to scanner restrictions at this time, however, the proposed sequence was not feasible on routine scanners and a sequence modification was labeled with the same acronym. With the introduction of new hardware, the original proposed sequence found its way back into applications and was renamed as "**True**" **FISP** (TrueFISP) [94].

#### Sequence diagrams

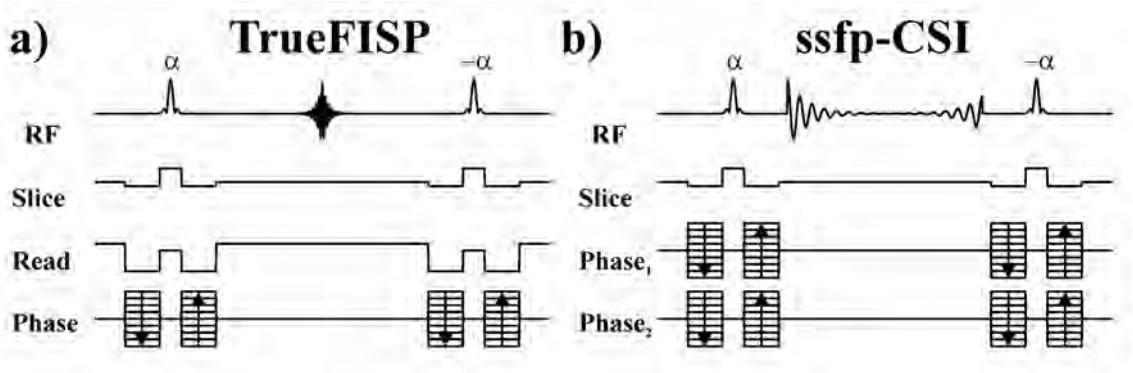


**Figure 4.20:** *Sequence diagrams of the 2D-TrueFISP and the 2D-ssfp-CSI sequences. a) Sequence diagram of the TrueFISP sequence. b) Sequence diagram of the ssfp-CSI sequence. Unlike the TrueFISP sequence, a second phase gradient is applied to achieve encoding in the x-direction.*

A sequence diagram of the TrueFISP sequence is shown in Figure 4.20a. Because the TrueFISP sequence is fully balanced, all gradient moments at the end of one cycle are zero and the sequence builds symmetrically around the echo acquisition. Furthermore, unlike

with the FLASH sequence spoiling is not performed. Thus, both the FID and the echo introduced by the preceding pulse are acquired together.

In the ssfp-CSI sequence (cf. Figure 4.20b), the read gradient is replaced by an additional phase encoding gradient before and after signal acquisition.

### Signal behavior

Normally, TrueFISP sequences are run with very short $TR$ times ($TR \ll T_2 < T_1$). The following formula can thus be used for describing the steady state signal after a number of dummy pulses:

$$S_{TrueFISP} \approx \frac{M_0 \ \sin(\alpha)}{\frac{T_1}{T_2}\big(1-\cos(\alpha)\big)+\big(1+\cos(\alpha)\big)} \ e^{-\frac{TE}{T_2}} \tag{4.7}$$

This equation holds true for an alternating sign of the excitation pulse phase [91]. Please note that for the ssfp-CSI sequence, this equation is only valid when a relatively low spectral resolution is chosen to keep $TR$ short.

Similar to the Ernst angle for FLASH imaging, an optimal angle in terms of SNR can also be found for the TrueFISP/ssfp-CSI sequences [91]:

$$\alpha_{max} = \arccos\left(\frac{T_1 - T_2}{T_1 + T_2}\right) \tag{4.8}$$

Due to the contribution of both the FID and the echo, a relatively high signal strength can be obtained. For the ideal case of $T_1 = T_2$, the reachable signal is 50% of a fully relaxed spin-echo sequence.

### Sequence intrinsic artifacts

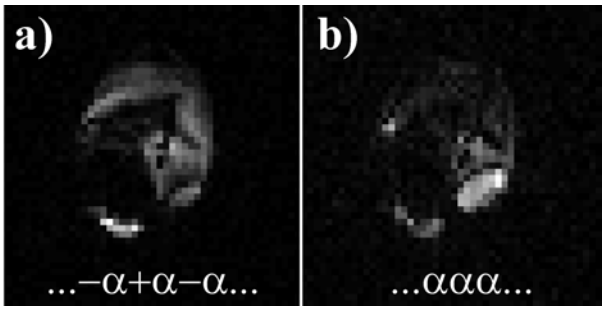


**Figure 4.21:** *Banding artifacts in $^{19}F$ TrueFISP MRI. An exemplary slice through the liver of a mouse is shown. a) TrueFISP image with sign alteration of the excitation pulse. b) TrueFISP image without sign alteration of the excitation pulse. All images are normalized to 1. Data underlying Reference [95].*

A well known artifact in TrueFISP sequences is the so-called banding artifact. Since off-resonant spins dephase between two excitation pulses, spins that are out of phase by $\Delta\theta = \pi, 3\pi, 5\pi...$ at the end of one TR cycle are not refocused. Thus, banding artifacts occur

at those regions. The dephasing of an off-resonant spin in a TrueFISP sequence is given by the following equation [96]:

$$\Delta\theta = 2\pi\Delta\nu TR \tag{4.9}$$

with $\Delta\nu$ being the off-resonance frequency. According to Equation 4.9 the spatial distribution of the artifacts is dependent on the $TR$. Thus, $TR$ times should be as short as possible are of interest for TrueFISP and ssfp-CSI imaging. Furthermore, shifting the ssfp response profile can be reached by altering the excitation pulse phase (cf. Figure 4.21).

With $^{1}$H MRI, those artifacts are easy to recognize in most image areas since proton spins are present in sufficient concentrations. As mentioned in Chapter 3, $^{19}$F MR is based on marker substances injected into the body in the absence of $^{19}$F background signal. Thus, sufficient $^{19}$F signal is only present in areas where the marker accumulates in concentrations high enough for detection. If the marker only concentrates in a small area, banding artifacts could totally suppress the necessary information. In large areas with high marker concentration (e.g., the liver) banding artifacts can easily be recognized (cf. Figures 4.21a & b).

In ssfp-CSI sequences, banding artifacts are present in the spectroscopic dimension (cf. Figures 4.22a–d upper row). When an image is formed, however, they can also translate to the image (cf. Figures 4.22a & b). If the line bandwidth is not too small, an integration of the resonance lines, however, can deliver spatial patterns with qualitatively minimized banding artifacts (cf. Figures 4.22c & d).

In both TrueFISP and ssfp-CSI sequences, banding artifacts can be minimized by combining acquisitions with different phase cycling schemes for the RF pulse. Thus, it has been shown that with the help of a specific phase cycling technique, TrueFISP imaging without banding artifacts is enabled by the combination of four acquisitions using different excitation pulse phases [97]. A longer total measurement time, however, must be take into account since additional data must be acquired.

### 4.3.3 TSE/TSE-CSI

The so-called RARE sequence was introduced by Henning et al. in 1986 [7]. As mentioned above, another common acronym for this sequence is TSE and will be used in the following.

#### Sequence diagrams

The TSE technique was introduced to allow accelerated spin-echo sequences. Figure 4.23a shows a TSE sequence diagram. In principle, the TSE sequence is similar to a **M**ulti **S**pin-**E**cho (MSE) sequence, which consists of one excitation pulse followed by a train of refocusing pulses. Contrary to a MSE sequence, however, the different echoes are differently phase encoded in a TSE sequence. Thus, a faster acquisition of the image information is possible. The acceleration factor is called the **T**urbo**F**actor (TF) and is equivalent to the number of different phase encoded echoes acquired in one echo-train.

To accelerate spectroscopic spin-echo CSI sequences, the TSE-CSI sequence presented in 4.23b can be used [89]. Again, this sequence is slower by a factor of phase encoding steps in the "read direction" than a TSE sequence having the same $TR$ and TF. Since,

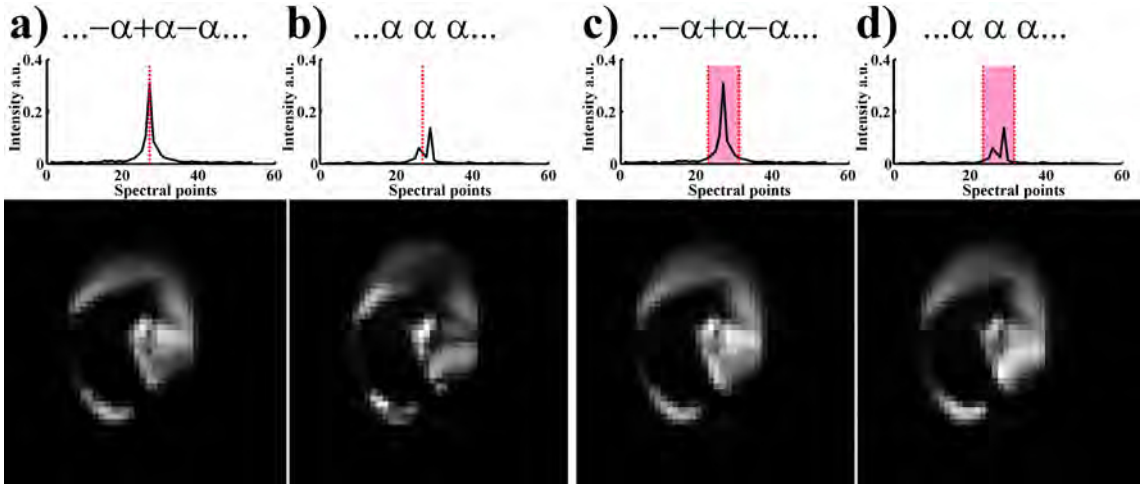


**Figure 4.22:** *Banding artifacts in $^{19}F$ ssfp-CSI. An exemplary slice through the liver of a mouse is shown. a) Pulses with sign alteration. Upper row: Spectrum obtained from one spatial point. Lower row: Image formed at the spectral position indicated with the red line in the spectrum. b) Pulses without sign alteration. Upper row: Spectrum obtained from one spatial point. Lower row: Image formed at the spectral position indicated with the red line in the spectrum. c & d) Same spectra as in (a & b), however, the images in the lower row were obtained by integrating the spectral area as indicated by the red area in the spectra. A similar image was obtained for both cases in (c & d). All images are normalized to 1. Data underlying Reference [95].*

more phase encoding gradients are used than in TSE sequences, an additional degree of freedom for the spatial acceleration direction is also given. This can result in better artifact distribution in the obtained image [56].

### Signal behavior

TSE sequences use refocusing pulses after signal excitation. Thus, susceptibility effects present in gradient-echo sequences are minimized. To achieve maximal signal, 180° pulses are used in the echo train. In this case, the following equation describes the signal of the TSE sequence [91]:

$$S_{TSE} = S_0 \ \exp\left(-\frac{k\ TIE}{T_2}\right) \tag{4.10}$$

with $k$ being the index of the echo with the lowest phase encoding gradient and the TIE the **I**nter **E**cho **T**ime. Thus, $k\ TIE$ refers to the $TE$ of a TSE sequence. Importantly, Equation 4.10 only holds true for perfect 180° pulses. Since, perfect 180° pulses are not present at every spatial point in an extended probe, the TSE sequence signal is influenced by other issues (e.g. $T_1$ relaxation) [98, 99].

However, in contrast to, for example, the FLASH sequence, $T_2^*$ effects are minimized. Thus, by using a TSE sequence, no signal voids are present even at high $TE$ (cf. Figure 4.25b) in areas with short $T_2^*$ (cf. Figure 4.19b) but long $T_2$ (cf. Figure 4.25d).

To enable stable TSE sequences when the refocusing pulse flip angle is not 180°, the so-called **C**arr **P**urcell **M**eiboom **G**ill (CPMG) conditions must be fulfilled [100, 101]. Briefly, the time between the 90° excitation pulse and the initial refocusing pulse must

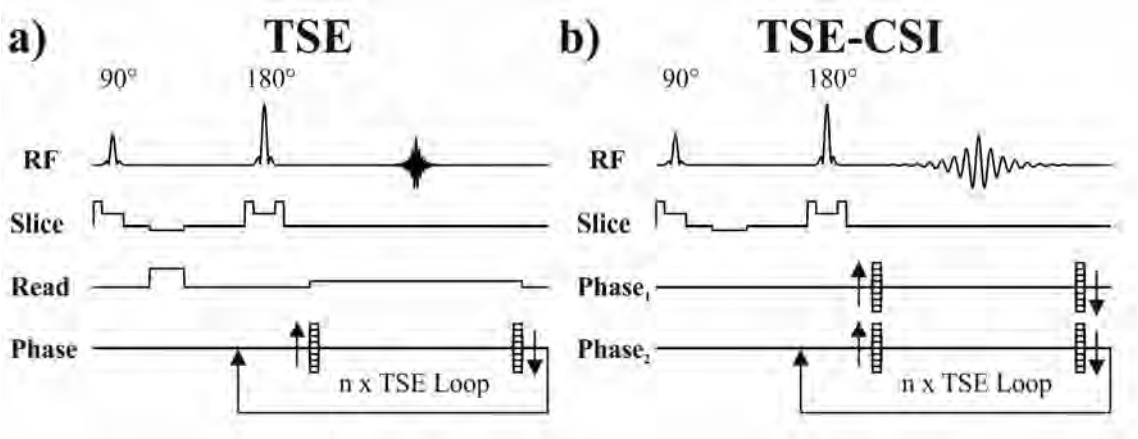


**Figure 4.23:** *Sequence diagrams of 2D-TSE and 2D-TSE-CSI sequences. a) Sequence diagram of the TSE sequence. b) Sequence diagram of the TSE-CSI sequence. Unlike the TSE sequence, a second phase gradient is applied instead of the read gradient to allow encoding of the x-direction. The factor n labels the number of echoes acquired per excitation.*

be set to $TIE/2$. The time between the following refocusing pulses must be set to $TIE$ and all refocusing pulses must be applied with 90° phase difference to the initial excitation pulse. Furthermore, a spin must accumulate the same phase between two echo spacings. Therefore, the gradients used in a CPMG-based TSE sequence must be fully balanced (cf. Figure 4.23).

In general, the considerations made for the TSE sequence are also valid for the TSE-CSI sequence.

### K-space encoding

By using a TSE sequence multiple echoes are acquired at different times after the excitation pulse. Thus, k-space segments are differently $T_2$ weighted. According to Equation 4.10, a different contrast can be achieved when different echoes after the excitation pulse are sorted into the center of the k-space (lowest phase encoding gradient).

In Figure 4.24, three so-called encoding patterns for TSE sequences are shown. Figures 4.24a & b show two typical encoding patterns for 2D-TSE sequences used in this work. As mentioned above, the echoes are differently phase encoded in a TSE echo train. Using a linear phase encoding scheme, the value of $G_P$ before signal acquisition is changed from high to low values in course of the echo train (cf. Figure 4.24a). Thereby, the k-space center is sampled at $TE = (TF \cdot TIE)/2$.

To maximize the SNR, however, a centric phase encoding scheme is often chosen for 2D-TSE sequences (cf. Figure 4.24b). Thus, the $TE$ is reduced to $TE = TIE$ by using the lowest phase encoding gradients at the beginning of the echo train. However, blurring can appear in the phase encoding direction since the outer k-space segments have a stronger $T_2$ weighting [91]. Please note that different $T_2$ weighted images can also be achieved depending on the $TE$ choice for the k-space center.

Since only phase encoding gradients are used in 2D-TSE-CSI sequences, 2D-centric phase encoding patterns can be chosen (cf. Figure 4.24c) [89]. As an advantage, this encoding strategy distributes image artifacts in two spatial directions [56].

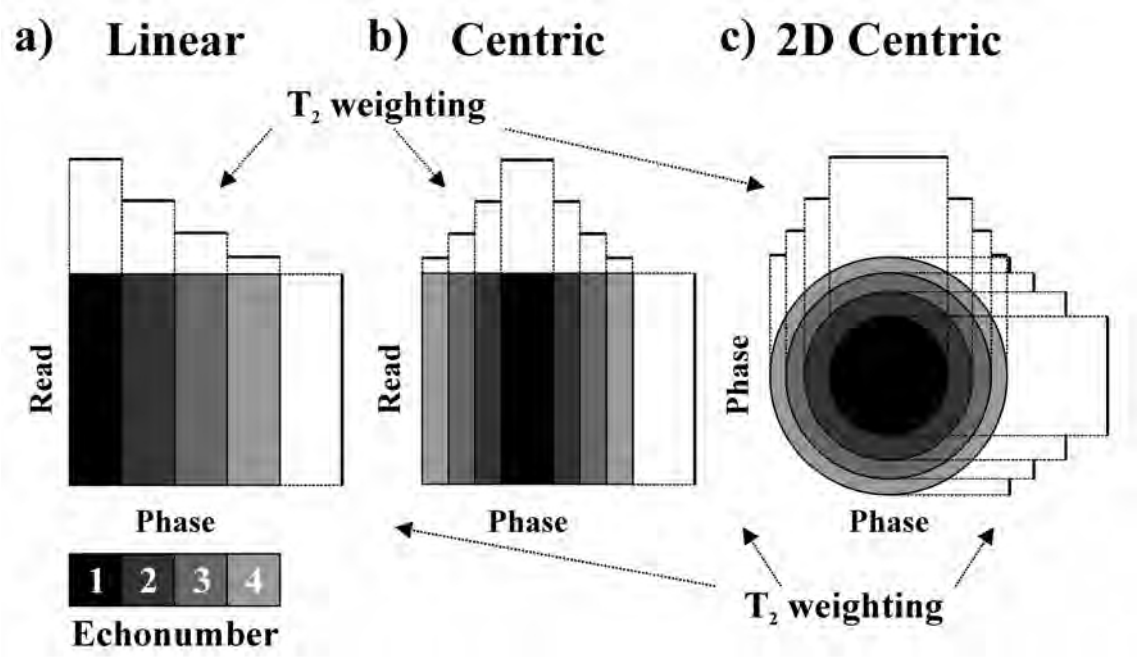


**Figure 4.24:** *Phase encoding patterns for 2D-TSE and 2D-TSE-CSI sequences. a) Linear phase encoding pattern. b) Centric phase encoding pattern. c) 2D-centric phase encoding pattern. All phase encoding patterns can be applied to 2D-TSE-CSI sequences, however, only the phase encoding patterns shown in (a) and (b) can be used for 2D-TSE sequences. An exemplary TF = 4 is shown. A dark color represents a low echo number and a light color a higher number. The surrounding step functions illustrate the $T_2$ weighting of the different k-space segments.*

### Sequence intrinsic artifacts

In Figures 4.25a & b, differences in the homogeneous phantom can be seen at the location of the arrows. The $B_1^+$ map quantitatively reveals the coil profile in this slice and shows that the flip angles differ at the position of the arrows from the mean value and thus deviations in the signal are present. As mentioned in Section 3.3.2, this issue could interfere with quantification when a volume coil is used as in the present example (double-resonant $^1H/^{19}F$ 8 leg birdcage coil). The problematic of $B_1^+$ inhomogeneity is of course not limited to TSE extends to all kinds of MRI sequences.

Another prominent artifact of TSE imaging and other multi-echo imaging sequences (e.g., BURST) is the so-called ghosting along the phase encoding direction. Ghosting artifacts are normally due to phase modulations in the k-space. An example where artificial phase-ghosting was added to a spin-echo image is presented in Figure 4.26. To create phase-ghosting in the image domain, the k-space was split into different segments in the phase encoding direction according to the chosen TF. In a second step, different phase increments were added to these k-space segments and the k-space was Fourier transformed. $T_2$ weighting of the k-space segments was neglected.

It can be observed that for higher TFs, and therefore higher k-space segmentation with a higher phase modulation frequency in the phase encoding direction, lead to lower frequency ghosts in the image (cf. Figures 4.26b–d). Contributions to phase errors can arise, for example, from eddy currents and phase errors from RF pulses.

Correcting the phase in the k-space is a simple method to correct ghosting artifacts present

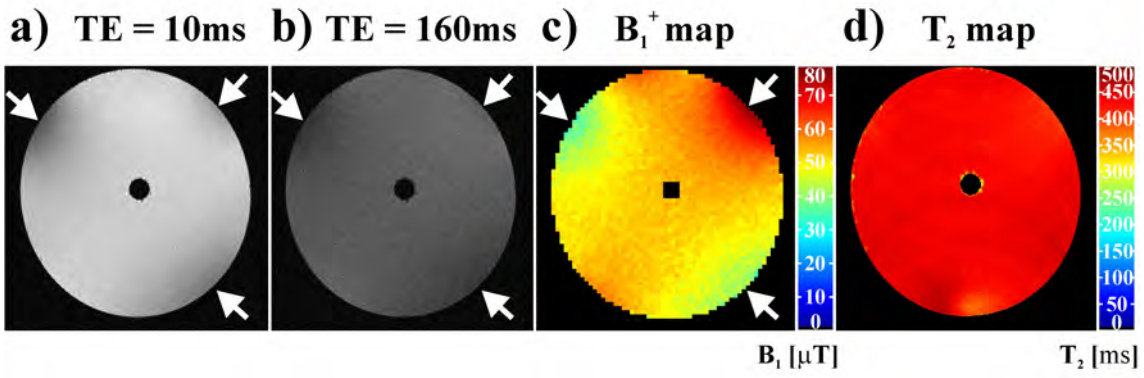


**Figure 4.25:** *Flip angle problematic for TSE sequences. a) TSE image with TE/TR = 10/1000 ms, TF = 1. b) TSE image with TE/TR = 160/1000 ms, TF = 32. c) $B_1^+$ map acquired with a BS spin-echo sequence following [102, 103]. TE/TR = 8/400 ms, MTX = 64 × 64, BS-pulse = Gaussian, Offset of BS-pulse = 16 kHz, BS-pulse duration = 1 ms. d) $T_2$ map of the phantom used for the other figures measured with a MSE sequence (TR = 2500 ms, 128 echo images, TIE = 9 ms). Parameters underlying all TSE/MSE images: MTX = 256 × 256, BW = 50 kHz, ST = 2 mm. Measured at 7 T. The arrows in (a & b) point out artifacts due to imperfect flip angles.*

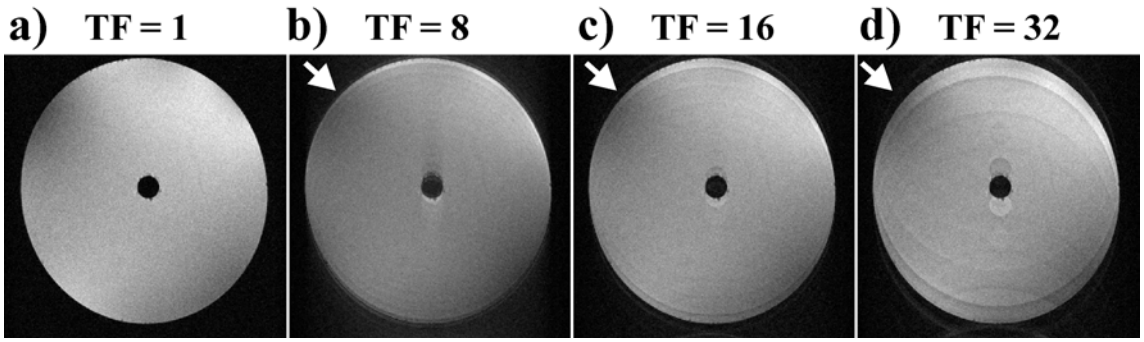


**Figure 4.26:** *Influence of phase ghosting on image quality. a) Spin-echo reference (TE/TR = 10/1000 ms, MTX: 256 × 256, BW = 50 KHz, ST = 2 mm. Measured at 7 T. b) Same image as in (a), however, a phase modulation simulating TF = 8 was added to the k-space. c) Same as (b) with TF = 16. d) Same as (b & c) with TF = 32. The arrows point out ghosting artifacts not present in the reference image.*

in the phase encoding direction. Thus, additional non-phase encoded dummy scans can be acquired with only slice and read gradients turned on. When a 1D Fourier transform is performed on this data, the phase differences of the different echoes can be obtained. With this, information the phase in the k-space can be corrected and thus the ghosting artifacts minimized [91].

# 5 Animal studies using $^{19}$F MRI

As discussed in Chapter 3, due to its unique properties, $^{19}$F MRI is a valuable tool to investigate biological processes *in vivo*. Thus, the application of $^{19}$F MRI to different preclinical models has been described in light of the possibility of future human application [16, 21, 104].

The following chapter concentrates on $^{19}$F MRI in the field of neurology. An animal model of focal cerebral ischemia as well as a model of peripheral nerve injury were investigated using $^{19}$F MRI. The first model deals with the visualization of step-wise thrombus formation in mice using $^{19}$F MRI. It further includes a qualitative comparison to SPIO-enhanced MRI and shows *in vivo* experiments of the so-called multicolor CSI technique allowing simultaneous visualization of multiple, different PFC compounds in only one animal. The second animal model focuses on the visualization of inflammation in the peripheral nervous system of rats by $^{19}$F MRI.

## 5.1 Detection of step-wise thrombus formation by $^{19}$F MRI

This section follows Reference [58].

### 5.1.1 Introduction

In 1985, a simple model of focal cerebral ischemia using **P**hoto**T**hrombosis (PT) was introduced by Watson et al. [105]. MRI studies dealing with the PT model have shown that with $T_2$-weighted MRI, PT lesions appear uniformly hyperintense in early stages of infarct development [106]. MRI studies at 1.5 T in rats further showed that, in early stages of photothrombotic lesion development, ongoing vessel occlusion can be visualized by SPIO-enhanced $^1$H-MRI [107], while delayed application of SPIO depicts neuroinflammation [106]. In 2008, Floegel et al. reported that $^{19}$F MRI can also be used to show neuroinflammation in a mouse PT model at 9.4 T [21].

Reconsideration of the PT model as study object served multiple goals:

1. Confirmation of the known effects of SPIO-enhanced $^1$H MRI on rats [106, 107] through mouse experiments
2. A comparison between SPIO-enhanced $^1$H MRI and PFC-based $^{19}$F MRI to reveal their respective limitations
3. To investigate the previously reported findings concerning *in vivo* visualization of neuroinflammation using $^{19}$F MRI [21]
4. To establish $^{19}$F imaging on the well described PT stroke model and thus to test novel $^{19}$F methodologies on an established *in vivo* animal model

The present work concentrates on a only qualitative description of the *in vivo* experiments during acute stages of the PT model. Goals one, two and four are thus of special focus. Other aspects including Goal three (e.g., quantification of occlusion volume, *ex vivo* experiments, experiments to visualize neuroinflammation and histology of the present model), are additionally regarded in [58].

### 5.1.2 Material & Methods

#### Photothrombosis

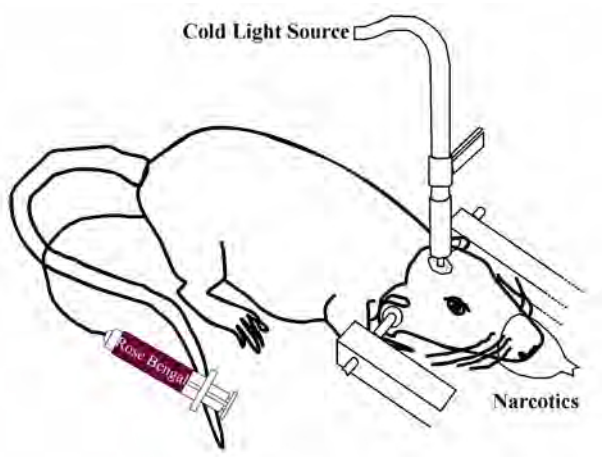


**Figure 5.27:** *Scheme of the PT operation. Figure based on a figure from Reference [108].*

*PT model*

A scheme of the PT operation is provided in Figure 5.27. In the PT model initially described by Watson et al. [105], a photosensitive dye is systemically injected into the animal. After dye injection, a specific spot of the exposed skull is illuminated. This leads to local activation of the dye and free radical formation. Disturbance of the endothelium subsequently activates platelet aggregation and the coagulation cascade, leading to thrombus formation in illuminated vessels. A more detailed description of the PT model is provided in [105].

*Surgical procedure*

Surgical procedures similar to the one presented here have been elsewhere described (e.g. [23, 24, 106, 107, 109]). Briefly, in adult C57/BL6 mice (25–30 g), the skull was exposed via a dorsal midline incision of the skin. Afterwards, 0.2 ml of sterile filtered rose Bengal solution was injected intraperitoneally. Illumination of the exposed area was performed using a fiber optic bundle of a cold light source centered stereotactically 2 mm posterior and 2.4 mm lateral from Bregma. For all animals, the illumination duration was 20 min. During the entire procedure animals were anesthesized using enflurane in a 2:1 nitrogen/oxygen atmosphere. The body temperature was kept at 37.0° C using a heating plate. After illumination, the skin was sutured and the mice were allowed to recover. The

procedure resulted in cone-shaped infarctions. Mice did not show overt clinical symptoms.

### PFC markers

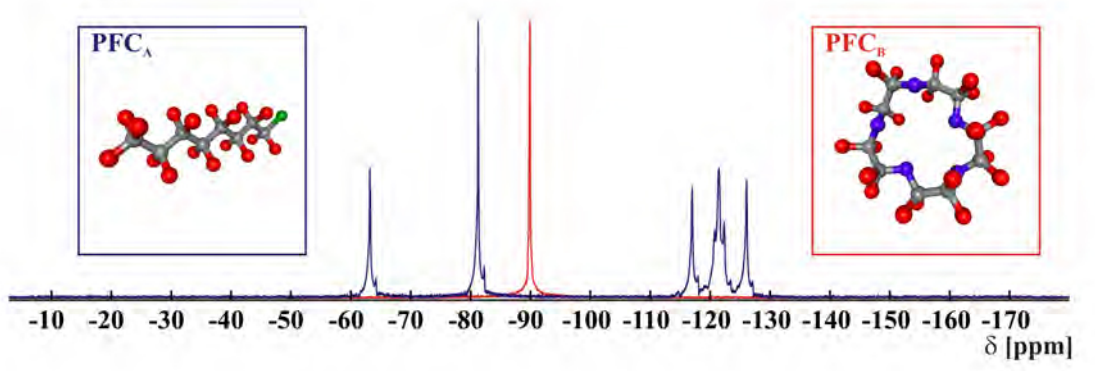


**Figure 5.28:** *Exemplary MRS spectra of the both used PFC compounds. Figure adapted from [58].*

A PF15C emulsion (10% wt/wt, Fluorochem Ltd. Glossop, UK) was used in the experiments applying only one PFC emulsion. The production and properties of this emulsion are described in more detail in Reference [21]. The emulsion was obtained from Dr. Flögel and Prof. Schrader (Uni Düsseldorf, Düsseldorf, Germany).

For experiments using two PFC compounds with different spectral signatures, an emulsion containing 40% wt/wt multi-resonant PFOB ($PFC_A$) was used. A detailed description of the production of the $PFC_A$ emulsion is provided in Reference [58]. The emulsion was obtained from Dr. Flögel and Prof. Schrader (Uni Düsseldorf, Düsseldorf, Germany). For the second PFC compound, single-resonant PF15C ($PFC_B$) was used. The 30% v/v $PFC_B$ emulsion was obtained from Celsense Inc. (VS580H, Pittsburgh, PA, USA). In Figure 5.28, the spectra of both used PFC compounds are displayed. Please refer to Section 3.2.2 for more details concerning the PFC compounds.

### SPIO contrast agents

SPIO particles (Resovist®, Bayer Schering Pharma AG, Berlin, Germany) were used as described in [106] (Application: 0.2 mmol Fe/kg body weight ).

### MRI

An overview of the different application protocols of the PFC markers or SPIO contrast agents is provided in Figure 5.29. A more detailed description of the different MR protocols is given in the following subsections.

#### *Hardware*

For $^1H$ and $^{19}F$ imaging, a home-built 20 mm diameter surface coil adjustable to both frequencies [110] was used for the experiments applying only one PFC compound.

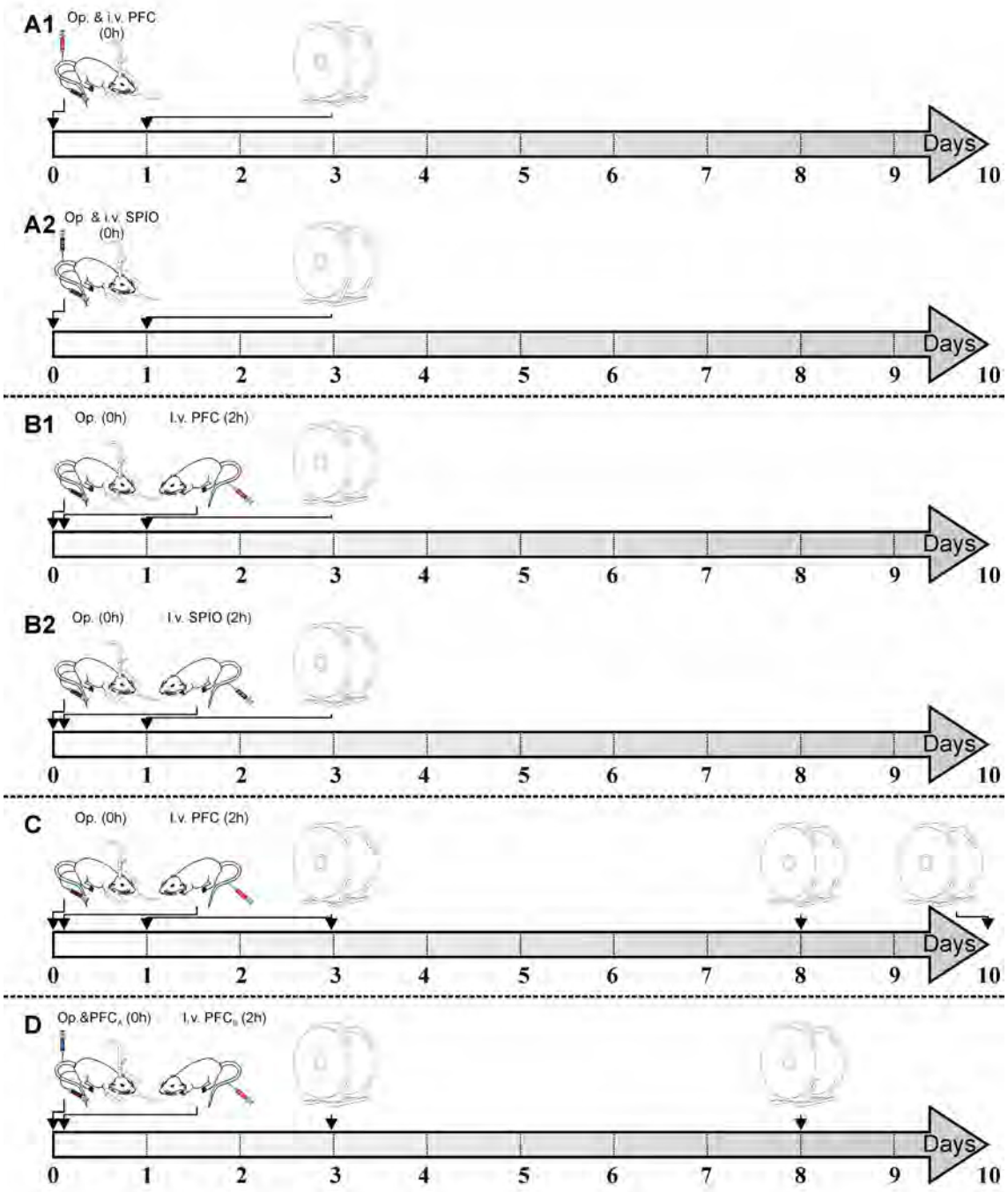


**Figure 5.29:** *Overview of the different study schemes. A) Experiments in the acute phase of PT with the application of the marker or contrast agent directly after the end of illumination (A1: PFC, A2: SPIO). B) Experiments in the acute phase of PT with the application of the marker or contrast agent 2 hours after the end of illumination (B1: PFC, B2: SPIO). C) Lesion maturation experiments with the application of the PFC marker 2 hours after the end of illumination. In contrast to the experiments in (B1), MRI was additionally performed on day three, eight and ten. D) Experiments to visualize different stages of acute "ischemic" damage in a single experiment with the application of the $PFC_A$ marker directly after the end of the illumination and the application of the $PFC_B$ marker 2 hours later. Parts of the figure are adapted from [58] and based on [108].*

Furthermore, a home-built, actively decoupled 35 mm diameter $^{19}$F birdcage coil in combination with an actively decoupled 20 mm diameter $^{19}$F receive-only surface coil was used for the experiments applying two PFC compounds [110]. Even though the birdcage/surface coil combination was optimized for $^{19}$F MRI, its performance was still sufficient to acquire $^{1}$H images for anatomical correlation of the $^{19}$F signal.

*Anesthesia*

Similar to other studies dealing with PT (e.g. [23, 24]), for all MRI measurements, mice were anesthetized using 1.5% isofluran in a 2 l/min oxygen atmosphere.

*Experiments in the acute phase of PT: A1 and B1*

To visualize different stages of acute thrombus formation with $^{19}$F MR, a PFC emulsion was applied i.v. in a dosage of 250 $\mu$l. To reveal the different affected areas of ongoing thrombus formation after illumination, two injection time points were chosen: directly after the end of illumination (cf. Figure 5.29A1, n = 4) or two hours later (cf. Figure 5.29B1, n = 4). As indicated in Figures 5.29A1 & B1 MRI scans were performed one day after PT induction.

2D single slice $^{1}$H and $^{19}$F experiments were performed, whereby, the slice was located in the middle of the infarction as depicted by $T_{2w}$ scout scans. For the acquisition of $^{1}$H reference images, a TSE sequence was used as described in Section 4.3.3 (TE/TR: 40/5000 ms; TIE: 10 ms; TF: 8; FOV: 25 × 25 mm; **Ma**a**T**ri**X** (MTX): 256 × 256; **S**lice **T**hickness (ST): 2 mm; **N**umber of **A**verages (NA): 1). The experiment time of the $^{1}$H scans was 2 min 40 s.

Regarding $^{19}$F imaging, 2D ssfp-CSI sequences as described in Section 4.3.2 were performed with the same geometry as the TSE scans (pulse shape: Hermitian; pulse bandwidth: 5400 Hz; $T_{AQ}$/TR: 10.3/13.6 ms; FOV: 25 × 25 mm; **S**pectral **P**oints (SP): 512; MTX: 41 × 41; ST: 2 mm; NA: 158). The experiment time of the $^{19}$F scans was 1 h.

The overall protocol time was $<$ 1.5 hours.

*Experiments in the acute phase of PT: A2 and B2*

To match the PFC application protocol, SPIO particles were applied in a dosage of 0.2 mmol Fe/kg body weight either directly after the end of illumination (cf. Figure 5.29A2, n = 4) or two hours later (cf. Figure 5.29B2, n = 4). As indicated in Figures 5.29A2 & B2, SPIO-enhanced $^{1}$H MRI scans were also performed one day after PT induction.

For visualization of the SPIO contrast agent, the same 2D single slice experiments were performed as the $^{1}$H reference experiments using the PFC compounds.

*Lesion maturation experiments: C*

For n = 2 mice that received the PFC marker 2 h after PT the $^{19}$F signal maturation was exemplary followed. The same MR experiments described above (A1 and B1) were

performed at days three, eight and ten after PT (cf. Figure 5.29C).

*Different stages of acute "ischemic" damage visualized in a single experiment: D*

To visualize different stages of ongoing microvascular occlusion in one experiment, a dual injection scheme was chosen for n = 3 mice. To visualize early stages, 125 $\mu$l of the $PFC_A$ emulsion were injected i.v. directly after illumination. Two hours later 125 $\mu$l of the $PFC_B$ emulsion were applied into the same animal for visualization of later stages.

3D $^1$H and $^{19}$F scans were performed three and eight days after PT (cf. Figure 5.29D). For anatomical references, multislice $^1$H TSE datasets of the mouse brain were acquired (TE/TR: 40/5000 ms; TIE: 10 ms; TF: 8; FOV: 25 × 25 mm; MTX: 256 × 256; slices: 28; ST: 1 mm; NA: 1). The experiment time of the $^1$H scans was 2 min 40 s.

3D $^{19}$F ssfp-CSI datasets were performed with the same geometry as the $^1$H TSE datasets (pulse shape: hard pulse; pulse bandwidth: 50000 Hz; $T_{AQ}$/TR: 10.3/13.6 ms; FOV: 25 × 25 × 28 mm; SP: 512; MTX: 41 × 41 × 14; NA: 6). To excite the complete spectrum of the $PFC_A$ compound, the pulse bandwidth was increased to 50000 Hz (cf. Figure 3.10b). Furthermore, to avoid chemical shift artifacts, global excitation pulses were applied without a slice gradient. The 3D ssfp-CSI scans lasted ≈ 32 min.

The total protocol time was < 1 h.

**Post Processing**

Since spectroscopic sequences were used, the $^{19}$F signal peak was integrated to generate $^{19}$F images. For the experiments using two different PFC compounds (D), the peak signals for each compound were separately integrated to generate marker specific $^{19}$F images. To reduce **P**oint **S**pread **F**unction (PSF) artifacts in the $^{19}$F 3D ssfp-CSI data, Hanning-weighting in the spatial dimensions was performed. It has been shown that such a weighting improves the PSF, which is especially critical when large voxels are used [111]. Additionally, $^{19}$F data were zero-filled in the spatial dimensions and an individually adapted threshold was applied to the $^{19}$F data to generate overlays with the $^1$H TSE data for the anatomical background. The 2D ssfp-CSI data were zero-filled to a matrix of 128 × 128 pixels and 3D ssfp-CSI data to a matrix of 128 × 128 × 28 voxels.

### 5.1.3 Results

*Experiments in the acute phase of PT: A1, A2, B1 and B2*

As mentioned above, mice received either a PFC emulsion or SPIO nanoparticles at early stages of photothrombotic stroke in initial experiments. Thus, the markers were given either directly or two hours after cessation of illumination. Importantly, under inhalation anesthesia with isoflurane, no fluorine signal was observed in the control animals that were not injected with PFC but had cortical infarctions (data not shown).

Figure 5.30A1 shows that injecting the PFC directly after the end of illumination led to a $^{19}$F signal throughout the entire infarction. In contrast, delaying the injection two hours injection resulted in a ring-like $^{19}$F signal at the outer margins of the lesions (cf. Figure 5.30B1).

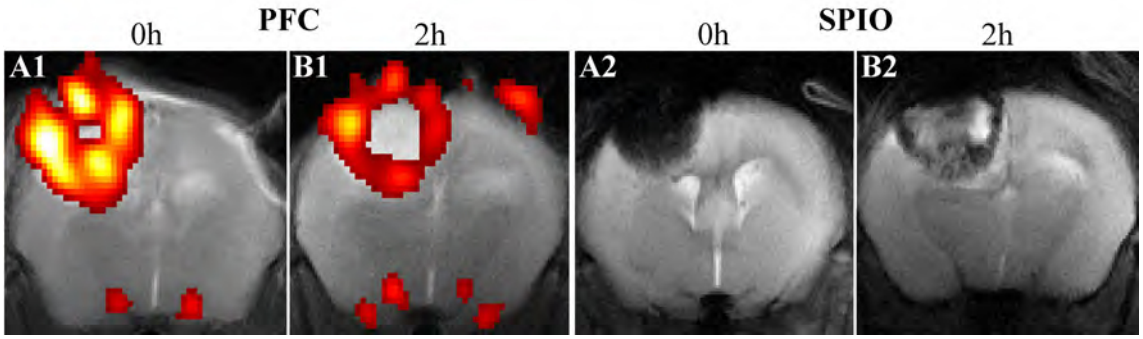


**Figure 5.30:** In vivo *imaging results of $^{19}F$ and SPIO-enhanced MRI in the acute stage of cerebral photothrombosis. A1) PFC emulsion applied immediately after illumination. B1) Delayed injection of PFC emulsion two hours later. A2) SPIO nanoparticles administered directly after illumination. B2) SPIO nanoparticles administered two hours after illumination. Figure adapted from [58].*

Similar "enhancement" patterns were observed for the signal loss with $T_{2w}$ MRI after SPIO injection at both injection time points. Thus, in animals that obtained SPIO directly after the end of illumination, cortical lesions appeared hypointense when using $T_{2w}$ MRI (cf. Figure 5.30A2). $T_{2w}$ MRI of animals that received the SPIO injection with a two hour delay showed a hyperintense infarct core surrounded by a hypointense ring at the border zone (cf. Figure 5.30B2).

*Lesion maturation experiments: C*

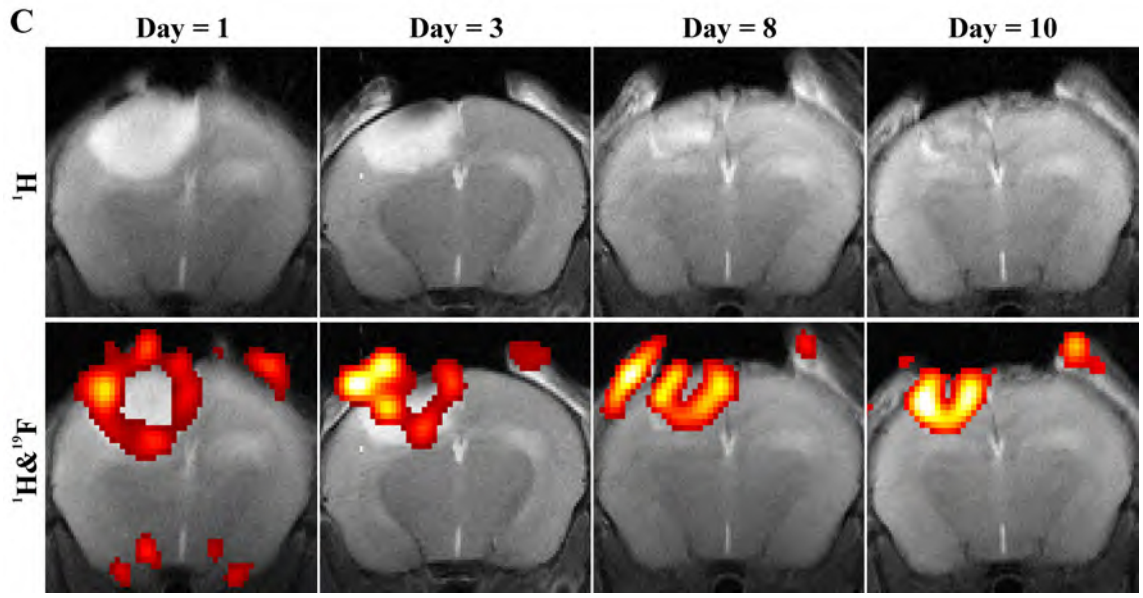


**Figure 5.31:** *Development of the $^{19}F$ signal during lesion maturation. Individual animals that received PFC two hours after photothrombotic infarction were scanned sequentially on days one, three, eight and ten. Upper row: $^{1}H$ TSE scans, lower row: $^{1}H$ & $^{19}F$ overlay images. Figure adapted from [58].*

The rim-like fluorine signal observed on the first day in animals that received the PFC emulsion 2 h after illumination (cf. Figure 5.30) persisted during further lesion maturation

(Days: 3, 8, 10; cf. Figure 5.31). During the first days following PT induction, the lesions appeared hyperintense in $T_{2w}$ $^{1}$H-TSE images. However, the hyperintense area decreased with time, leading to an almost isointense tissue signal on days eight and ten (cf. Figure 5.31). Furthermore, the allocation of the $^{19}$F signal changed over time (cf. Figure 5.31). Thus, a more "compact" distribution of the $^{19}$F signal was observable at the end of the investigation on day ten.

*Different stages of acute "ischemic" damage visualized in a single experiment: D*

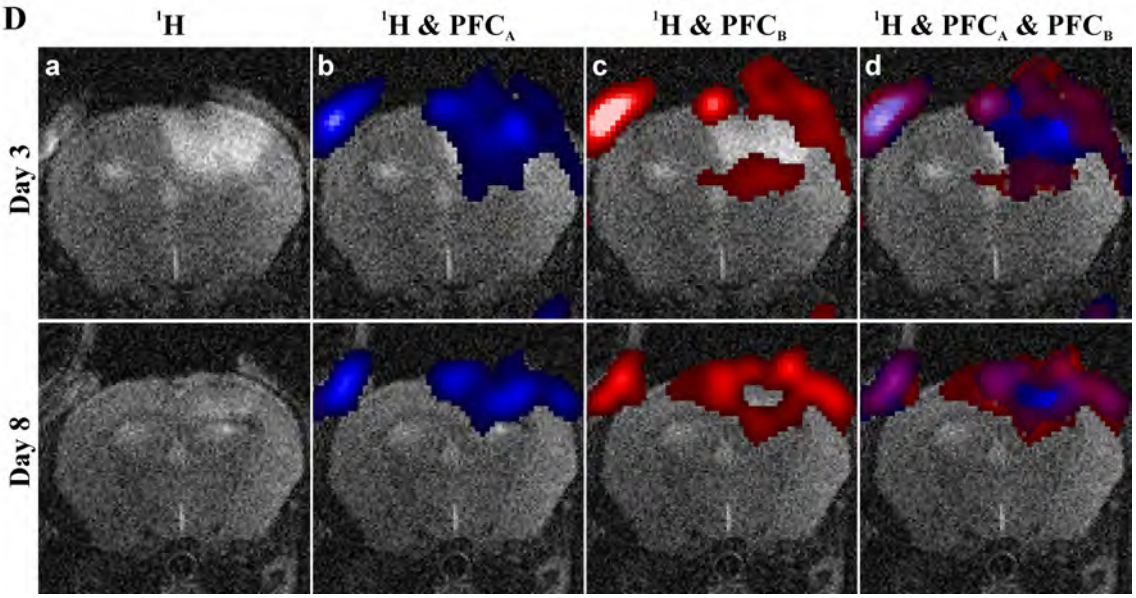


**Figure 5.32:** In vivo *visualization of ongoing thrombus formation in a single $^{19}F$ CSI experiment. Representative coronal slices of the mouse brain three and eight days after induction of PT are shown. The blue color represents the signal originating from the $PFC_A$ compound and the red color represents the $PFC_B$ signal. Figure adapted from [58].*

As described above, 3D CSI experiments visualizing two PFC compounds with different spectral profiles were performed. Thus, both markers could be spectrally discriminated, which enabled retrospective visualization of different temporal stages of ongoing thrombus formation in a single MRI measurement (cf. Figure 5.32).

Similar to the experiments using only one PFC compound, injection of the $PFC_A$ emulsion directly after cessation of illumination resulted in a fluorine signal throughout the entire cortical infarction (cf. Figure 5.32b). Consequently, delaying the injection of the second $^{19}$F marker ($PFC_B$) for two hours led to an accumulation at the outer margins without affecting the center of the infarcted zone (cf. Figure 5.32c). As described above, a more compact representation of the $^{19}$F signal was observed when imaging was repeated 8 days after PT induction (cf. Figure 5.32). The merging of the different $^{19}$F signals on the $^{1}$H background image allowed a direct comparison between the different spatial distribution of both compounds (cf. Figure 5.32d).

### 5.1.4 Discussion

As mentioned above, the purpose of this work was to qualitatively describe the possibility of visualizing ongoing vessel occlusion in the PT model with the help of $^{19}F$ MR. Thus, only issues concerning this point are discussed in the following. A more detailed discussion concerning biological and medical aspects of the PT model can be found in [58].

It was shown that $^{19}F$ MR can visualize ongoing microvascular occlusion in the PT model of focal cerebral ischemia. A similar accumulation pattern was present after injections of the $^{19}F$ marker or the SPIO contrast agent applied at the same time points (cf. Figure 5.30). Previous studies in rats demonstrated that the chosen application scheme leads to entrapment of the SPIO particles in the vessel thrombi [106] during early stage of infarct development. It is likely, that the same process underlies the findings for mice using both PFC markers and SPIO contrast agents.

Regarding the visualization of ongoing vessel occlusion, $^{19}F$-based MR has several advantages compared to SPIO-enhanced MRI:

1. The contrast in $^{1}H$ MRI is not altered when a $^{19}F$ marker is present at the ROI. In the present work, the infarctions showed the typical hyperintense signal on $T_{2w}$ $^{1}H$ reference images early after PT, which faded in follow-up measurements (cf. Figure 5.31). In contrast, SPIO-enhanced MRI showed a hypointense contrast at regions where the contrast agent accumulated (cf. Figure 5.30). Thus, $^{1}H$ image information was covered by the effect of the SPIO contrast agent. Consequently, combined $^{19}F$ & $^{1}H$ MR provides additional information that is concealed when using SPIO-enhanced $^{1}H$ MRI.
2. $^{19}F$ MR allows *in vivo* discrimination of PFC compounds with different chemical shifts in acceptable measurement times [20]. Therefore, using the PT lesion model, it was possible to monitor step-wise thrombus formation from the core of the infarction to its outer margin in a single ssfp-CSI measurement. In the future, simultaneous *in vivo* $^{19}F$ MRI of cell populations labeled with spectrally different PFC compounds might be possible
3. In general, $^{19}F$ MR is very selective compared to SPIO-enhanced MRI. Thus, false positive detection of the fluorine signal is unlikely as is possible with SPIO-enhanced MRI [16]. A false negative detection is more likely due to the often low sensitivity of $^{19}F$ MRI [16, 58]

Nevertheless, $^{19}F$-based MR has a few limitations compared to SPIO-enhanced MRI when applied to the PT model:

1. Longer measurement times than needed with $^{1}H$ MR imaging were required since only a limited amount of exogenous PFC marker was on site
2. Besides long measurement times, a low spatial $^{19}F$ MR resolution also needed to be taken into account. Thus, for $^{19}F$ MR imaging, partial volume effects were more prominent compared to the higher resolved $^{1}H$ MR imaging. Volume quantification therefore potentially leads to overestimations of areas with $^{19}F$ signal [58]

No phase alternation scheme of the excitation pulse as mentioned in Section 4.3.2 was applied. Thus, in principle, banding artifacts can occur in the CSI images. To minimize the influence of those artifacts the peak signal was summed up as shown in Figures 4.22c & d. Furthermore, only a qualitative study of the signal pattern was of interest. To further

reduce banding artifacts, different scans with phase cycling should be performed. However, this would have led to prolonged protocol times.

When 2D slice-selective CSI is to be performed, a large chemical shift between the different $^{19}$F markers may cause problems. The slice encoding gradient leads to a geometrical offset of the excited slice for each $^{19}$F marker. Since the absolute shift between different resonant lines increases with field strength, this problem becomes more severe at high field strengths. Therefore, for proper colocalization of different $^{19}$F markers at high field strengths, strong gradients or relatively small absolute shifts between different resonant lines are mandatory.

The large spectral bandwidth of $\approx$ 65 ppm for the $PFC_A$ compound ($\approx$ 18 kHz at 7 T) makes slice selective excitation difficult. Thus, a complete phase encoded 3D measurement without slice selection was chosen in this work. Those measurements, however, are difficult to acquire within an acceptable measurement time or with sufficient resolution when a volume coil is used. In this work, the problem was solved using a receive-only surface coil with a diameter of 20 mm. Thus, no fold-over artifacts from $^{19}$F signal distributed in other organs such as the liver, spleen or lungs could interfere with the measurements.

### 5.1.5 Conclusion

$^{19}$F MR provides an alternative to SPIO-enhanced MRI in visualizing ongoing vessel occlusion in the photothrombotic stroke mouse model. Additionally, different PFC markers can be visualized in a single CSI experiment. The latter approach might be of special interest in other biological models (e.g., cell tracking), especially when several different $^{19}$F targeted compounds are used.

## 5.2 Visualization of inflammation in the PNS by $^{19}$F MRI

This section follows References [47, 112].

### 5.2.1 Introduction

The present section describes the application of 3D $^{19}$F ssfp-CSI to *in vivo* imaging of inflammation in the **P**eripheral **N**ervous **S**ystem (PNS) of rats.

Using conventional $^{1}$H MRI, injured nerves show a hyperintensity on $T_{2w}$ images that fades during the healing process [113–116]. While the hyperintensity on $T_{2w}$ images reflects an increased water content caused by a variety of different events, it does not provide insight into the recruitment of inflammatory cells. Thus, to obtain more insight into the inflammatory response of injured nerves, $^{19}$F MR imaging of systemically labeled immune cells was performed. As previously described nerve injury was generated by focal lysolecithin injection into sciatic nerves [117, 118]. Higher resolved *ex vivo* imaging on the isolated nerves was used for correlation with *in vivo* results. Furthermore, *ex vivo* $^{19}$F MRS was performed to allow comparison of the inflammatory burden of lysolecithin-injured nerves to control nerves.

The following section focuses on MRI and MRS experiments of the PNS. For a description of the histological validation of the MR experiments, please refer to [47].

## 5.2.2 Material & Methods

### Lysolecithin-induced nerve injury

*Lysolecithin model*

Nerve injury was evoked by focal application of lysolecithin into the left sciatic nerve of respective animals. Specifically, lysolecithin dissolves myelin sheaths and induces demyelinating lesions with a variable axonal component [117, 118]. The myelin injury quickly attracts high numbers of inflammatory cells invading from the circulation.

The aim of this work was to label circulating immune cells with an i.v. applied PFC emulsion. In the follow-up, $^{19}$F MR was thus used to visualize the inflammation in the injured nerves.

*Surgical procedure*

For lysolecithin application, male Lewis rats weighing 150–200 g (n = 10) were deeply anesthetized by intraperitoneal injection of ketamine/xylazine (Ketavet 100; Pfizer Pharma, Karlsruhe, Germany; Rompun 2%; Bayer HealthCare, Leverkusen, Germany). In each animal, the left sciatic nerve was exposed at the height of the sciatic notch and 10 $\mu$l of 2% lysolecithin dissolved in saline were injected intraneurally with a Hamilton syringe. Afterwards the wound was closed. In a control group, three animals additionally received 10 $\mu$l of 0.9% saline into the right contralateral nerves. The operation and injection procedures were performed under sterile conditions.

### PFC markers & PFC application scheme

A single-resonant PF15C emulsion obtained from Celsense Inc. (VS580H, Pittsburgh, PA, USA) was used. Rats (n=10) received 500 $\mu$l of the PFC emulsion i.v. directly and 3 days after lysolecithin application. For details concerning the PFC compound please refer to Section 3.2.2.

### MRI & MRS

*Hardware*

Measurements were performed on the same 7 T scanner mentioned before. For *in vivo* $^{1}$H and $^{19}$F imaging, a home-built 50 mm diameter $^{1}$H/$^{19}$F surface coil was used. A home-built, 10 mm diameter solenoid coil was used for *ex vivo* imaging and MRS of the isolated sciatic nerves. Both coils are described in more detail in [110].

*Anesthesia*

For anesthesia, animals received an intraperitoneal injection of 100 mg/kg body weight propofol prior to *in vivo* MR. To retain propofol infusion of 40 mg/kg/h for the duration

of the experiments, an intravenous catheter was placed in the tail vein and connected to a syringe pump (Bioblock Scientific, Illkirch-Cedex, France). Furthermore, the animals were intubated and connected to a mechanical ventilator (Hugo-Sachs Elektronik, March-Hugstetten, Germany). The ventilator was set to deliver 3 ml air at 69 strokes per minute. *In vivo* MR imaging was performed with the animals being in prone position.

In vivo $^{1}H/^{19}F$ *imaging*

MRI was performed 5 days after surgery.

$^{1}$H reference images were obtained using a 3D FLASH sequence (TE/TR: 2.9/60 ms; FOV: 50 × 50 × 50 mm; MTX: 100 × 100 × 100; **RES**olution (Res): 0.5 mm$^3$; NA: 1). For $^{19}$F imaging, 3D ssfp-CSI sequences with the same geometry as the $^{1}$H scans were performed (pulse shape: Hermitian; pulse bandwidth: 5400 Hz; $T_{AQ}$/TR: 10.1/13.5 ms; SP: 64; MTX: 40 × 40 × 40; Res: 1.25 mm$^3$; NA: 2). In contrast to the study described in Section 5.1, two identical $^{19}$F ssfp-CSI scans were performed to enable further minimization of banding artifacts in post processing. Thus, one scan was performed with 180° alternation of the excitation pulse phase and one without phase shift alternation. The anatomical $^{1}$H reference scan lasted 10 min and both $^{19}$F ssfp-CSI scans together 1 h total. With shimming and frequency settings, the overall protocol time was ≈ 1.5 h.

Ex vivo $^{1}H/^{19}F$ *imaging*

The animals were sacrificed after the *in vivo* MR measurements. Both sciatic nerves were removed and fixed in 4% paraformaldehyde overnight. To investigate whether or not the $^{19}$F signal observed *in vivo* was located within the damaged sciatic nerves, *ex vivo* MR of the isolated nerves was performed. Therefore, both nerves together with a PFC emulsion reference tube were spatially fixed in Agar Agar (Carl Roth GmbH, Karlsruhe, Germany) placed in a 1.5 ml tube (Eppendorf AG, Hamburg Germany).

$^{1}$H reference scans were performed using a 3D TSE sequence (TE/TR: 49.12/500 ms; TIE: 6.14 ms; TF: 16; FOV: 40 × 15 × 15 mm; MTX: 256 × 96 × 96; Res: 0.156 mm$^3$; NA: 1). Using the same geometry as the TSE scans and parameters similar to those of *in vivo* measurements, $^{19}$F imaging 3D ssfp-CSI scans were acquired. To adopt to the new geometry, the matrix was changed to 128 × 48 × 48 pixels (Res: 0.312 mm$^3$). To achieve a high SNR, the NA was set to 15. The experiment time for one *ex vivo* 3D $^{19}$F ssfp-CSI scan was 16 h and 35 min. Since one additional $^{19}$F ssfp-CSI scan was performed with the same parameters but a 180° phase shift, the overall protocol time was approximately 33 h and 30 min. This includes the $^{1}$H reference scan which lasted 12 min and 30 s.

Ex vivo $^{1}H/^{19}F$ *MRS*

For each quantification experiment, sciatic nerves were placed separately in a 1.5 ml tube (Eppendorf AG, Hamburg, Germany) together with a reference tube (3 mm diameter) containing a specific amount of TFA (Sigma-Aldrich Chemie GmbH, Schnelldorf, Germany). The nerves and the reference tube were both carefully placed in the middle of the solenoid coil to minimize effects of different local $B_1$ strengths. For MRS, a spectroscopic sequence was performed applying one excitation pulse, which equally excited both resonance lines

(pulse shape: Hermitian; pulse bandwidth: 10 kHz; $T_{AQ}$/TR, 204.8/10000 ms; SP: 4096; NA: 60). Thus, the center frequency was set in the middle between the resonance frequencies of PFC15C and TFA. For each nerve, MRS lasted 10 min.

#### Post Processing

Since only small matrix sizes were used for $^{19}$F imaging, the $^{19}$F data was retrospectively weighted based on a modified Bartlett Hanning window as provided in MATLAB®. Furthermore, to retrospectively minimize banding artifacts, **S**um-**o**f-**S**quares (SOS) reconstructions of the weighted data with and without phase shift were generated. As described in Section 5.1, only the peak of the $^{19}$F signal was integrated to obtain the $^{19}$F images.

In vivo $^{1}H/^{19}F$ *imaging*

The obtained *in vivo* $^{19}$F images were zero-filled to a matrix of 100 × 100 × 100 pixels. To generate overlay data, a threshold was manually adjusted and applied to the zero-filled $^{19}$F data before overlaying it on the $^{1}$H data. For 3D reconstructions, the $^{1}$H/$^{19}$F data were zero-filled to 200 × 200 × 200 points. To enable 3D localization of the $^{19}$F into the anatomical background, a **M**inimum **I**ntensity **P**rojection (mIP) of the $^{1}$H data was generated. Thus, dark structures in the original data (e.g., bones) appeared bright in the mIP data. Thereafter, the $^{19}$F data were thresholded and overlaid on the $^{1}$H mIP data. In a final step, 3D reconstructions were generated using a MATLAB® program written by Joe Conti [119].

Ex vivo $^{1}H/^{19}F$ *imaging*

In addition to zero-filling, the same post processing steps as described for *in vivo* data were performed for the *ex vivo* data. While zero-filling was omitted for the $^{1}$H data, the $^{19}$F data were zero-filled to 256 × 96 × 96 voxels. Furthermore, $^{1}$H mIP data was generated. For easier allocation of the different components, the $^{1}$H mIP data were manually segmented using MATLAB® and an additional 3D dataset was generated.

Ex vivo $^{1}H/^{19}F$ *MRS*

The $^{19}$F MRS data were baseline corrected prior to quantification. For quantification, the area under the different signal peaks was integrated and the ratio for the value pairs obtained. Thus, the quantification was performed as described in Section 3.3.1.

### 5.2.3 Results

In vivo $^{1}H/^{19}F$ *imaging*

*In vivo* MR imaging of the animals only receiving lysolecithin into the left sciatic nerve revealed $^{19}$F marker accumulation in the left thigh. Figure 5.33a shows coronal, sagittal and axial images of the hind quarters of two exemplary animals. The $^{19}$F signal extended

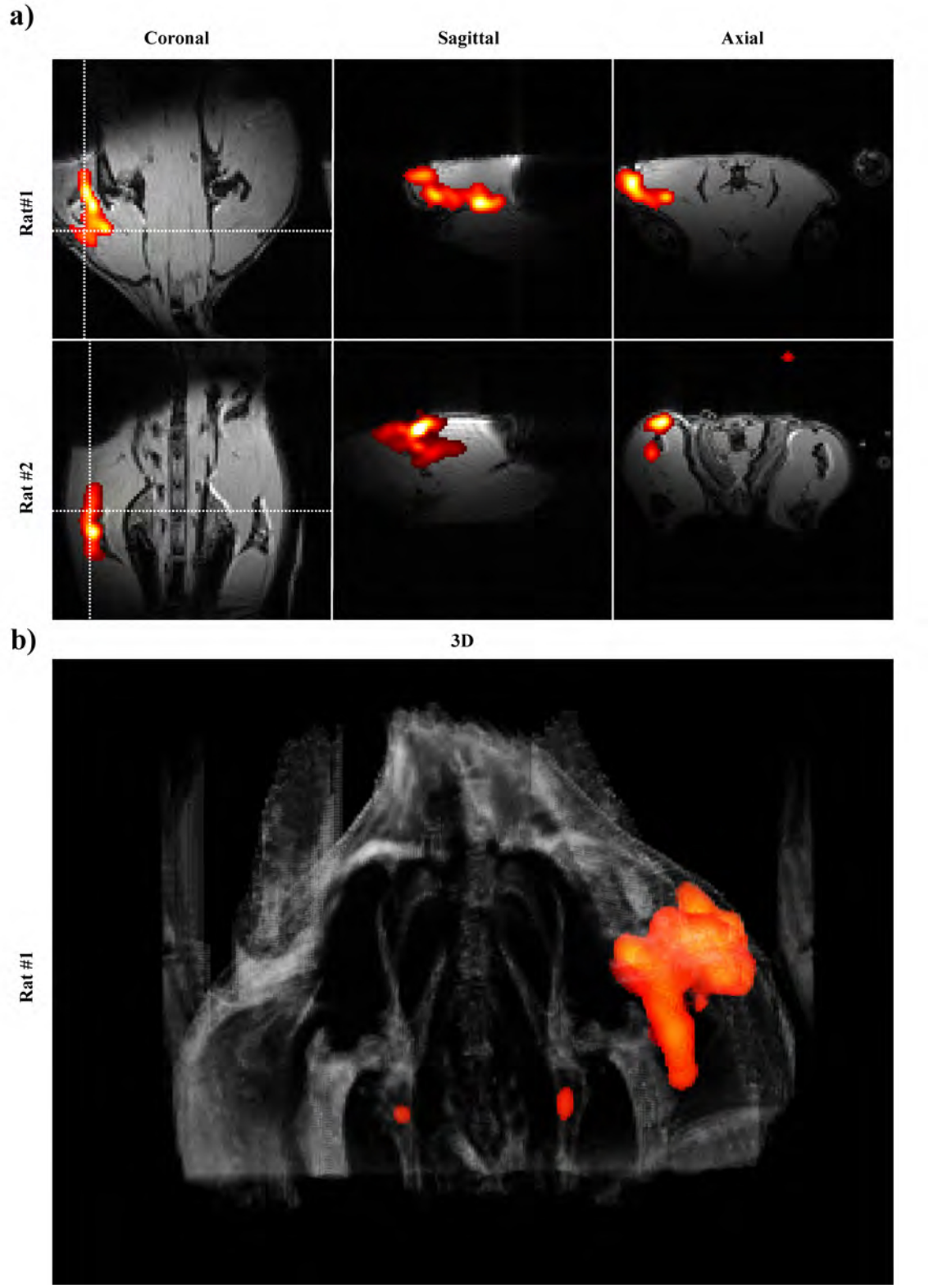


**Figure 5.33:** *Representative* in vivo *MR results obtained 5 days after lysolecithin application. a) $^{1}H/^{19}F$ overlay images showing the hind quarters of two representative animals. Both animals received lysolecithin solely in the left sciatic nerve. In addition to signal along the course of the left nerve, signal is also observable at the site of the skin incision. b) 3D $^{1}H/^{19}F$ overlay reconstruction. Figure adapted from [47, 112].*

along the proximal stretch of the left sciatic nerve. Furthermore, a strong $^{19}$F signal at the site of the skin incision was observed. Besides providing an anatomical overview with the $^{19}$F signal in the region of the left femoral head, the $^{1}$H/$^{19}$F 3D reconstruction of Rat 1 (Figure 5.33b) revealed two small $^{19}$F spots that most likely represent paraaortal lymph nodes close to the spine.

Ex vivo $^{1}H/^{19}F$ *imaging*

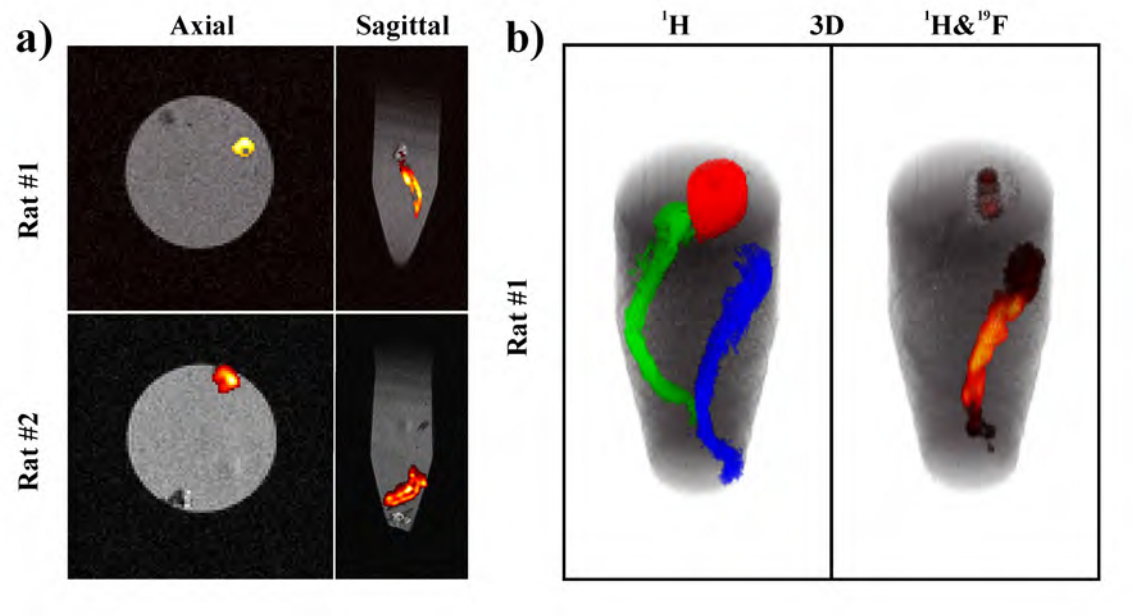


**Figure 5.34:** *Representative* ex vivo *MRI of the extracted sciatic nerves of two exemplary animals (cf. Figure 5.33). a) $^{1}H/^{19}F$ overlay images of both nerves from each animal. b) Left: Segmented 3D $^{1}H$ reconstruction of both isolated nerves from Animal 1 (reference tube: red, left sciatic nerve: blue and right sciatic nerve: green). Right: Overlay reconstruction showing $^{19}F$ signal in only the lysolecithin-injured left sciatic nerve. Figure adapted from [47, 112].*

To verify the *in vivo* results, *ex vivo* experiments on excised nerve pairs were performed as described. $^{1}$H/$^{19}$F overlay images of the isolated nerves confirmed that PFC accumulation was restricted to the left sciatic nerves, which received lysolecithin. Thus, the right untreated nerves appeared hypointense on the $^{1}$H/$^{19}$F overlay, indicating no $^{19}$F marker accumulation. In contrast, $^{19}$F signal was spread throughout the injured nerves (Figure 5.34a).

Additionally, the $^{1}$H/$^{19}$F 3D reconstruction shows the restriction of fluorine signal to the reference tube (in red, Figure 5.34b) and the left nerve (in blue, Figure 5.34b). No fluorine signal was observed in the intact right sciatic nerves (in green, Figure 5.34b).

Ex vivo $^{1}H/^{19}F$ *MRS*

The isolated peripheral nerves additionally underwent fluorine MRS to quantify and compare the intraneural $^{19}$F signal intensity. A small tube containing TFA was used as an external reference, showing a peak at -74 ppm for all MRS experiments (cf. Figure 5.35a). An additional $^{19}$F peak at -90 ppm was observed for all damaged nerves representing the

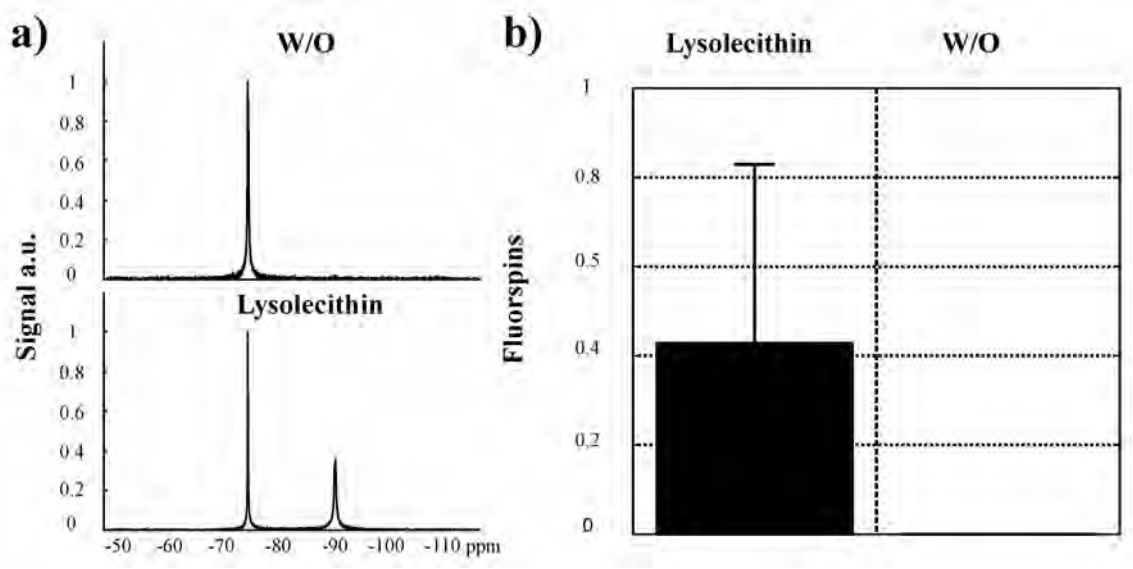


**Figure 5.35:** *Representative,* ex vivo $^{19}F$ *spectroscopy of the isolated nerves. a) Upper row: MRS spectra of the right untreated nerve of a representative animal; Lower row: MRS spectra of the left, lysolecithin injected nerve of the same animal. While both spectra show the TFA reference signal at* $\approx$ *-74 ppm, signal from the PFC marker at* $\approx$ *-90 ppm can only be observed in the spectrum of the left nerve. b) Shows a comparison between the mean fluorine amount accumulated in the injured (left) and the control nerves (right). The high standard deviation is most likely due to differing PFC emulsions labeling efficiency, depending on their age. Figure adapted from [47, 112].*

accumulation of the PF15C marker (cf. Figure 5.35a). As shown in the bar graph (cf. Figure 5.35b), the untreated right nerves did not exhibit any $^{19}F$ signal.

In the control experiments where the left sciatic nerves received lysolecithin while 0.9% saline was injected into the right nerves, a PF15C signal could be observed in both sciatic nerves at -90 ppm (cf. Figure 5.36a). The $^{19}F$ signal intensity, however, significantly differed [47]. Thus a stronger $^{19}F$ signal was observed in all lysolecithin-injured left nerves compared to their right, saline injected counterparts (Figures 5.36a & b).

### 5.2.4 Discussion

The present section describes the successful application of $^{19}F$ MR for *in vivo* visualization of inflammation in the PNS of rats. *In vivo* results were confirmed by high resolved *ex vivo* $^{19}F$ imaging. Moreover, *ex vivo* $^{19}F$ MRS enabled quantification and comparison of the $^{19}F$ signal accumulated in the differently treated sciatic nerves.

In more detail, it was possible to track inflammatory cell recruitment in acute peripheral nerve lesions using $^{19}F$ MRI. Thus, five days after intraneural lysolecithin injection, *in vivo* $^{19}F$ MRI revealed signal along the proximal stretch of the injured nerves. *Ex vivo* $^{19}F$ MRI of the isolated nerves corroborated the localization of the $^{19}F$ marker in the injured nerves while no $^{19}F$ marker accumulation was observed in the intact counterparts. Histological assessment confirmed the presence of numerous ED1-positive macrophages in the left sciatic nerve while no immune cells were observed on the untreated right side (data not shown, please refer to [47]).

When saline was additionally injected into control sciatic nerves (right), $^{19}F$ signal was bilaterally observable. However, a significant difference in $^{19}F$ signal intensity was observed

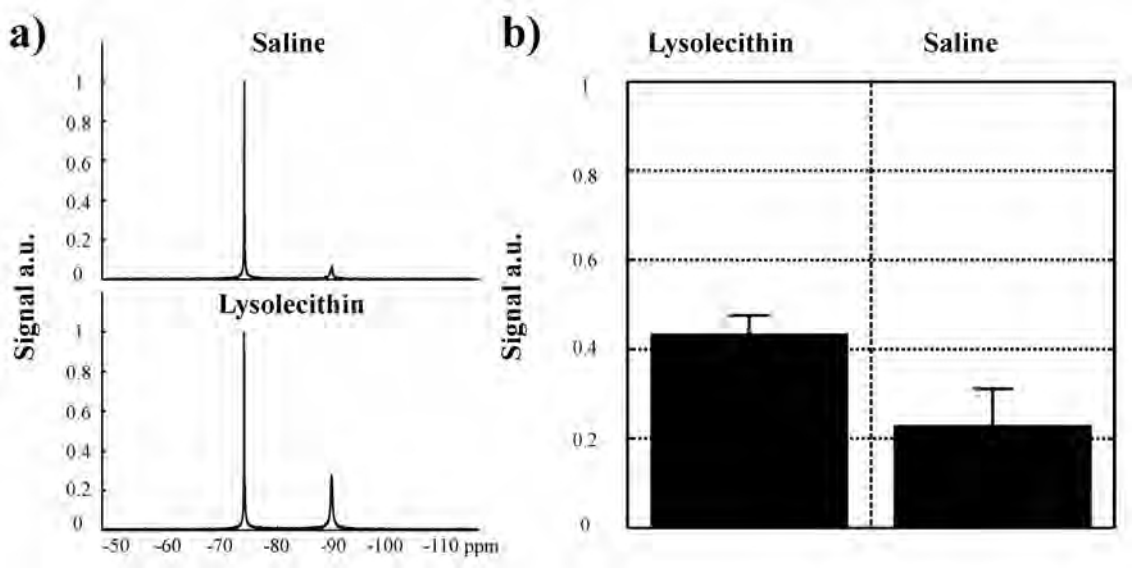


**Figure 5.36:** *Comparison between lysolecthin and saline-induced inflammation with* ex vivo $^{19}F$ *MRS of the isolated nerves. a) Upper row: MRS spectra of the right, saline injected nerve of a representative animal; Lower row: MRS spectra of the left, lysolecithin injected nerve of the same animal. Both spectra show the TFA reference signal at ≈ -74 ppm and a signal from the PFC marker at ≈ -90 ppm. b) Shows a comparison between the mean fluorine amount accumulated in the lysolecithin injected nerves and the saline injected nerves. Figure adapted from [47].*

using *ex vivo* $^{19}$F MRS. Thus, the lysolecithin injected nerves showed more signal than saline induced nerves. Importantly, immune cell recruitment in the saline injected nerves was restricted to the perineurium (data not shown, please refer to [47]). Thus, *ex vivo* $^{19}$F MRI combined with MRS might allow time efficient acquisition of information normally available only with time consuming histological techniques [120].

Regarding *ex vivo* MRS, a more precise method was proposed before that includes homogenizing the biological material and mixing it together with the spectroscopic reference [120]. Thus, differences due to an inhomogeneity $B_1$ coil profile are minimized. This procedure, however, was not an option in the present work since it inevitably leads to tissue destruction. Thus, no immunohistochemistry could have been afterwards performed to visualize local differences in immune cell recruitment [47]. To minimize differences of $B_1$ in the present work, the reference and the nerves were placed in same middle region of the coil.

Moreover, the $^{19}$F 3D ssfp-CSI sequence which was successfully applied to visualize inflammation in the present work could be used to analyze the timing of immune cell recruitment in greater detail. In this work a fixed application scheme of the PFC emulsion on days 0 and 3 after operation was used to efficiently label immune cells in the bloodstream. Applying two spectrally diverse PFC emulsions at different time points might enable a more detailed investigation of the spatiotemporal development of an inflammatory lesion. As shown in Section 5.1, the $^{19}$F 3D ssfp-CSI technique could thereby enable simultaneous acquisition of different $^{19}$F markers.

### 5.2.5 Conclusion

$^{19}$F 3D ssfp-CSI provides a tool for the visualization of inflammation in peripheral nerve lesions. Using this technique, simultaneous acquisition of multiple cell populations labeled with different $^{19}$F markers might become feasible in the future. Furthermore, in addition to histological techniques, *ex vivo* $^{19}$F imaging and MRS also provide information on the inflammatory burden.

## 5.3 Conclusion: The potential of $^{19}$F MRI to visualize biological processes

As mentioned in Chapter 3 and shown in the previous sections, $^{19}$F MRI can be used to visualize different biological processes. However, due to limited sensitivity, $^{19}$F MR cannot be applied to all biological issues. If, for example, low numbers of fluorine labeled cells are to be imaged, $^{19}$F MRI will most likely fail. While using $^{19}$F MRI, averaging is often applied to maximize the detectability of low SNR regions, thus lengthening experiment times.

These restrictions make the translation of the fluorine-based MRI technique to human applications challenging. However, as discussed in Chapter 3, a variety of PFC compounds have already been clinically evaluated as artificial blood substitutes. Furthermore, Phase 1 clinical trial studies were recently approved, which focus on *in vivo* tracking of *ex vivo* PFC labeled cells [77].

In the future additional advances in methods, hardware and instrumentation might help overcome the described sensitivity issue of $^{19}$F MRI. Thus, coil arrays might be used to improve SNR [121] as well as superconducting coils [122–124]. Besides PFCs, new, water soluble contrast agents with reduced relaxation times might facilitate biological applications [125, 126]. Furthermore, initial studies showed that hyperpolarized $^{19}$F molecules can allow a strong $^{19}$F MR signal [127], this could help overcome the sensitivity limitations of $^{19}$F-based MRI.

# 6 Application of Compressed Sensing to $^{19}$F MRI

CS is a novel mathematical method for the reconstruction of sparse, undersampled data [128, 129]. Applying CS to MR has a substantial advantage in that, theoretically the Nyquist theorem can be violated and thus the time for data acquisition can be shortened [24]. The first application to MRI was shown in 2007 by Lustig et al. [130] and several studies concentrating on CS accelerated MRI followed. Recently CS was also used to accelerate $^{19}$F CSI [22–24].

The following chapter is separated into three parts. First, a brief introduction to CS is given. The second section deals with the application of CS to accelerated $^{19}$F TSE-based CSI sequences. The last section focuses on how CS reconstructed $^{19}$F MR images can be further improved using a retrospective CS-based post processing algorithm.

## 6.1 Brief introduction to CS

Following References [23, 24], three basic requirements are mandatory for successful application of CS (cf. Figure 6.37).

1. A sparse representation of the signal (cf. Figure 6.37a)
2. An sampling pattern leading to incoherent artifacts (cf. Figure 6.37b)
3. An algorithm to reconstruct the image information from the artifact laden, undersampled image (cf. Figure 6.37c)

The first requirement is a given when using $^{19}$F MRI/CSI since the amount of fluorine in normal tissue is negligible. Furthermore, the applied exogenous $^{19}$F marker often accumulates in "hot spots". Therefore, compared to standard $^{1}$H images, $^{19}$F images are normally sparse (cf. Figure 6.37a). This allows direct application of CS in the image domain without additional sparsity transformation prior to CS reconstruction [23, 24]. As pointed out in [23, 24, 128, 129], a noisy image is unfortunately not sparse since sparsity in the strict mathematical sense only occurs in noise-free data. If the SNR is sufficient, however, the application of CS to MRI images influenced by noise is possible [23, 24, 130]. Since $^{19}$F images have often a low SNR, detailed investigations were performed in previous studies concerning this issue [23, 24].

The second requirement can be easily fulfilled using a randomly distributed sampling pattern that does not sample all points needed for the acquisition of an MRI image (cf. Figure 6.37b, inlay). To provide a good initial guess for the CS reconstruction, the **K**-space **C**enter (kc) is often fully sampled [23, 24]. Exemplary sampling patterns with different **A**cceleration **F**actors (af) and different areas of the fully sampled kc are provided in Figure 6.38.

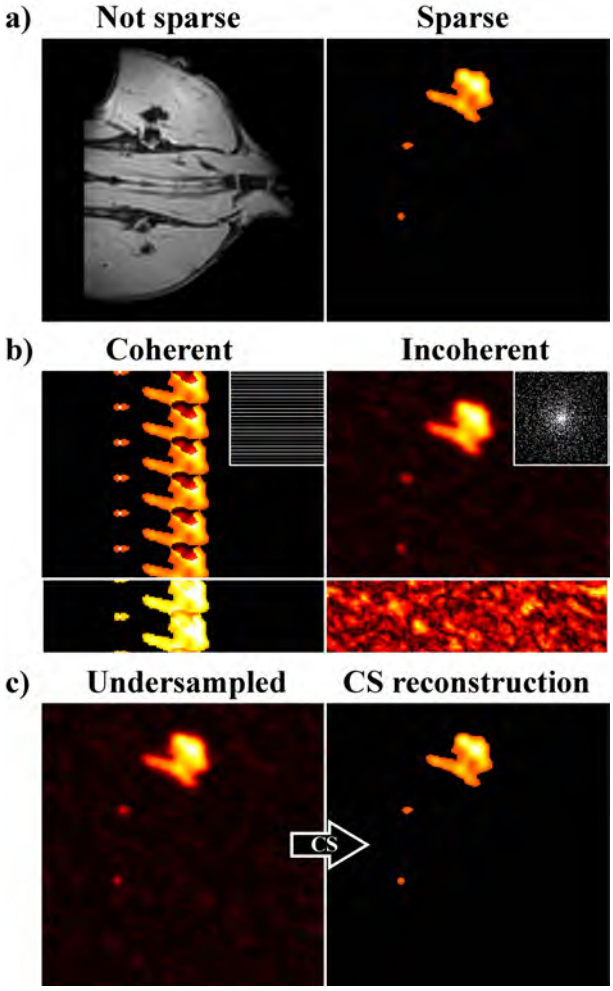


**Figure 6.37:** *Overview of the basic requirements for the application of CS. a) Illustration of a not sparse and a sparse image (thresholded* in vivo $^{19}F$ *image data from Section 5.2). b) Illustration of coherent fold-over artifacts and incoherent artifacts resulting from different undersampling strategies. The lower part of the images is differently scaled to better visualize the artifact structure. The inlays in the upper right corner show the sampling patterns of the respective k-space (af = 8). c) Demonstration of the effect of the CS reconstruction applied to the undersampled data with incoherent artifacts. Used CS parameters: af = 8, p = 1, kc = 1%. Data underlying Reference [47].*

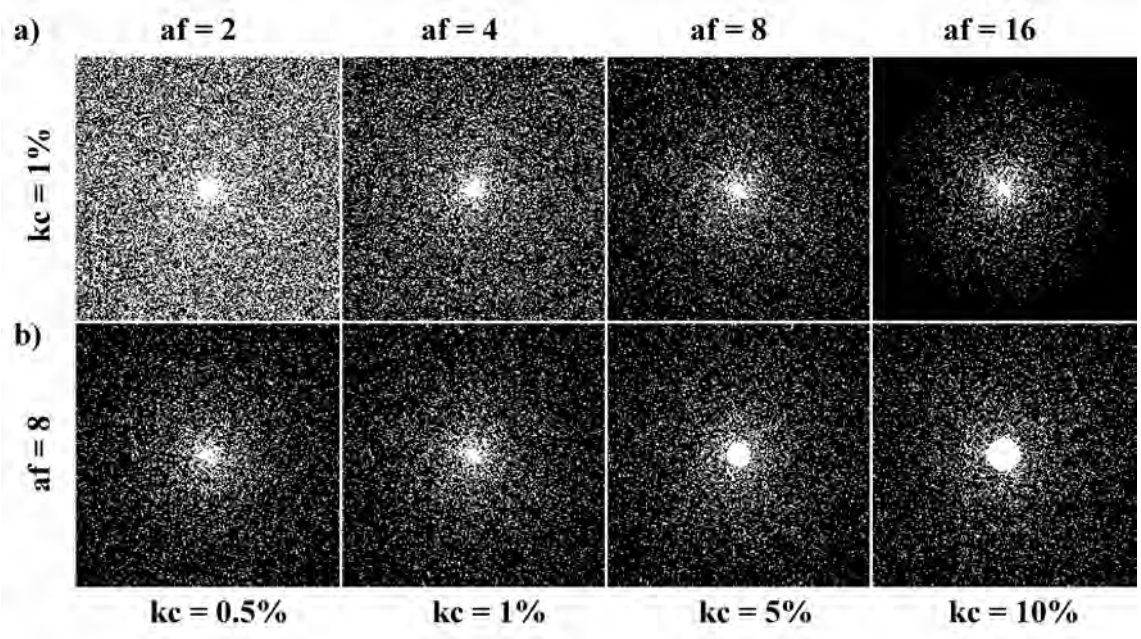


**Figure 6.38:** *a) Sampling pattern with kc = 1% and af = 2, 4, 8 and 16. b) Sampling pattern with af = 8 and kc = 0.5%, 1%, 5% and 10%. The percentage of the kc refers to the ratio between the number of sampled k-space points forming the kc and the total number of the sampled k-space points. For a description of the sampling pattern creation please refer to Section 6.3.3.*

Regarding the third requirement, different CS algorithms have been proposed to allow reconstruction of undersampled data. The algorithm used in the present work is based on the one presented in [131] and its implementation is given in more detail in [23, 24]. Briefly, strict data consistency must be fulfilled while the following reconstruction problem is solved using CS:

$$min \left\| x \right\|_p \tag{6.1}$$

where $x$ are image pixels arranged in a vector [23]. Furthermore, the norm $p$ is defined as:

$$||m||_p = (\sum_{i=1} |m_i|^p)^{\frac{1}{p}} \tag{6.2}$$

where $p \in \mathbb{R}$ and $m$ is an arbitrary vector with elements $m_i \in \mathbb{C}$ [23].

Because the algorithm was previously investigated in detail, it was solely used as "black box" algorithm in the present work with only minor modifications as described in the following sections under Material & Methods. The CS algorithm was obtained from André Fischer. A pseudo code of the used CS algorithm implementation is additionally provided in Appendix B on page 128.

## 6.2 CS-TSE-CSI

### 6.2.1 Introduction

The application of CS to $^{19}$F ssfp-CSI was described in [23, 24]. With TSE-CSI a further, spin-echo-based fast spectroscopic imaging sequence was presented in Section 4.3.3. A feature making this sequence especially interesting for $^{19}$F imaging is the often long $T_2$ relaxation time constants for multiple PFC compounds [39, 52]. Thus, this sequence might generate sufficient SNR for the application of CS to $^{19}$F imaging in different biological models. However, since multiple echoes are acquired after one excitation pulse in TSE-CSI, the CS sampling pattern is not as straightforward as in single echo methods like ssfp-CSI [23, 24].

In the present work, a 2D-centric pattern was chosen. Such a sampling scheme has some advantages compared to other encoding patterns. Thus, centric encoded sampling patterns allow an improved SNR compared to linear sampling patterns (cf. Section 4.3.3). Furthermore, by using a 2D-centric encoding pattern, artifacts are distributed more evenly along two spatial dimensions in contrast to 1D linear and centric encoding strategies (cf. Section 4.3.3). Moreover, as explained below, a fully sampled kc can be straightforwardly achieved using a 2D-centric encoding pattern for TSE-CSI.

Initial results of the **CS** accelerated **TSE CSI** (CS-TSE-CSI) sequence were promising. In this initial work, PFC containing tube phantoms inserted in a 10 mm diameter solenoid coil were imaged at 7 T [56]. This configuration, however, yielded a very high SNR that was incomparable to *in vivo* measurement situations. Thus, the CS-TSE-CSI technique was applied in the present work to an *ex vivo* mouse model with a $^{19}$F marker concentration similar to that used in *in vivo* applications. Furthermore, a coil compatible with *in vivo* measurements was used to show the possible *in vivo* application of this technique.

The following section is based on the results presented in [132].

### 6.2.2 Material & Methods

#### Mouse model

A C57/BL6-mouse with two focal cerebral ischemias induced by PT served as the *ex vivo* phantom. The PT model is described in detail in Section 5.1. This *ex vivo* phantom and application of the PFC emulsions is described in [23, 24]. Briefly, 250 $\mu$l of an PFC emulsion (PFC1) was applied i.v. directly after PT. To ensure that the PFC1 emulsion was cleared from the bloodstream, the PT procedure was repeated on the left hemisphere eight days later. Again, a second PFC emulsion (PFC2) was applied i.v. directly after the end of illumination. PFC1 and PFC2 are described in the following section in more detail. The mouse was sacrificed 14 days after the first PT. *Ex vivo* TSE-CSI experiments were performed on the animal, which was fixed in 4% paraformaldehyde.

#### $^{19}$F markers

As described in [23, 24], the animal contained two PFC emulsions with different core compounds (PFC1: VS580H, core compound: PF15C, Celsense, Inc., Pittsburgh, PA,

USA; PFC2: VS1000H, core compound: PFPE, Celsense, Inc., Pittsburgh, PA, USA). The spectral separation of the main resonance peaks of both emulsions is approximately 0.8 ppm ($\approx$ 230 Hz at 7 T).

### Hardware

The TSE-CSI sequence described in Section 4.3.3 was implemented on a 7 T scanner (Bruker BioSpin GmbH, Rheinstetten, Germany). For imaging, a home-built surface coil that was tune able to both frequencies ($^{1}$H & $^{19}$F) was used that had an inner diameter of 20 mm [110].

### Sampling pattern

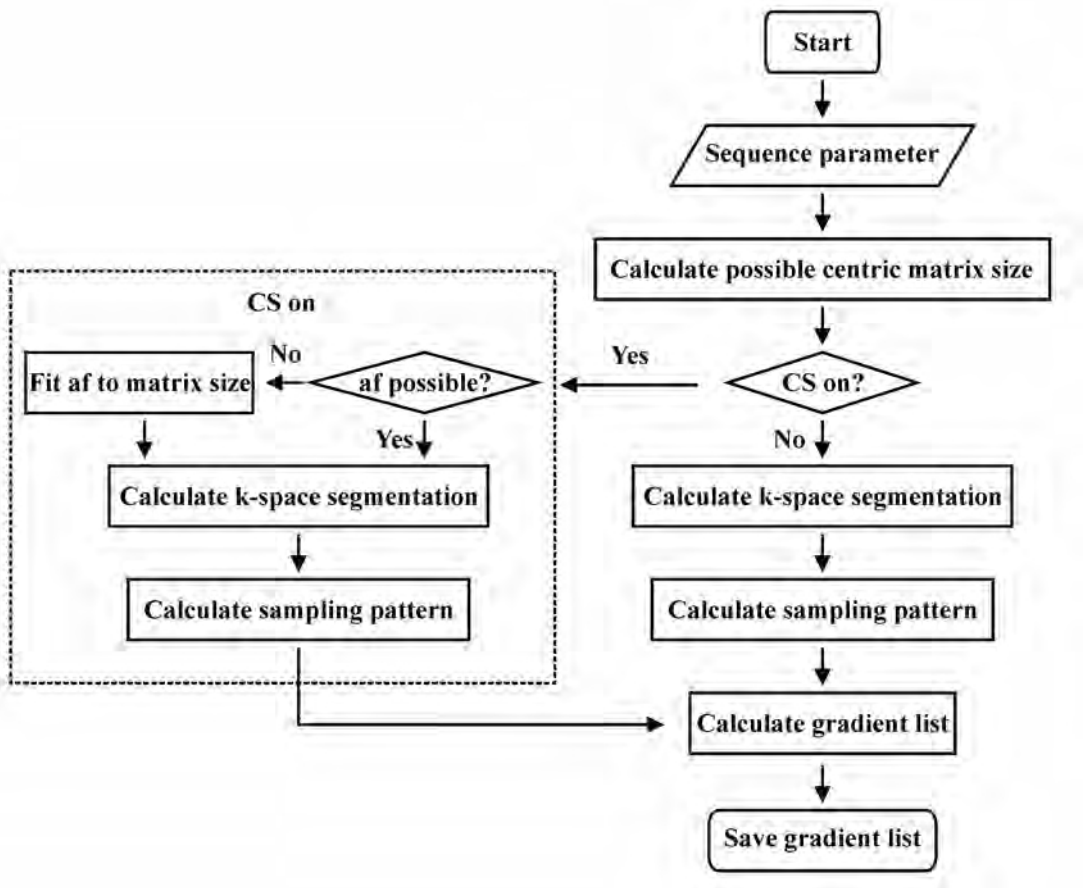


**Figure 6.39:** *Flowchart of the MATLAB® program for calculation of the fully or undersampled 2D centric sampling patterns.*

Since every spatial point is differently phase encoded in CSI, an algorithm to calculate concentric 2D encoding patterns as proposed in [89] was implemented in MATLAB®. Additionally, the possibility to undersample the encoding pattern was included in this algorithm. A flowchart showing an overview of the algorithm is presented in Figure 6.39. A brief description of the algorithm is provided in the following.

At the beginning of the calculation, different parameters must be chosen: a rectangular matrix size, TF and the af. With the help of the matrix size and the TF, a circle is calcu-

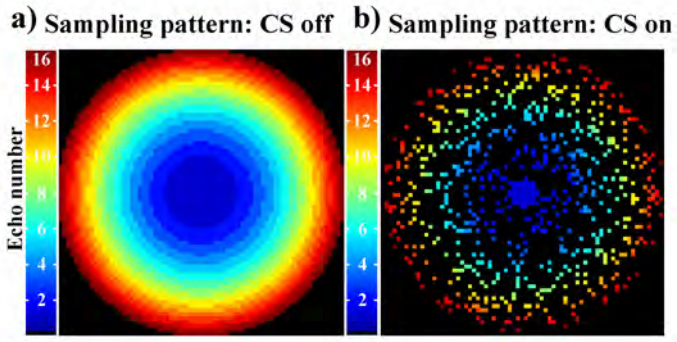


**Figure 6.40:** *a) Sampling pattern for the fully sampled data (TF = 16). b) Sampling pattern for the undersampled data (TF = 16, af = 6). The color represents the echo number in the TSE echo train from which the data point at the specific k-space position was collected. Figure adapted from Reference [132].*

lated with a similar number of points as the rectangular matrix, allowing the application of the chosen TF (cf. Figure 6.41a).

Afterwards the algorithm checks if CS is activated. If CS is not activated, the initial circle is segmented in TF concentric circles, that all have the same number of points. Thus, a circular k-space is generated, which is divided into segments containing the same number of points. The following relationship is valid: segment number = number of echoes = TF. In the next step, a sampling pattern is generated by filling all spatial points of the different segments (cf. Figure 6.40a).

If CS is activated, a first step checks if the af is possible using the calculated initial circle and chosen TF. If the af is not possible with the chosen parameter set, the af is reduced until the chosen configuration is possible. To separate the initial circle in different segments, the area of the innermost circle is first reduced by the af, since the kc is fully sampled. The other segments are accordingly adapted to take the reduced area of the inner circle into account. Afterwards, the outer segments are randomly undersampled according to the af and a sampling pattern is generated (cf. Figure 6.40b).

In a final step, gradient lists are calculated and saved. These gradient lists can be read in by the TSE-CSI sequence program, which controls the MR scanner. The parameters chosen for the algorithm were: rectangular matrix = 64 × 64 (results in a 2D centric matrix of 72 × 72), TF = 16, af = 6 (if CS activated).

To test if the signal was sufficient for the application of CS, in the present work, the k-space of the fully sampled reference was retrospectively undersampled and CS reconstructed using the same sampling pattern as the undersampled, acquired data. Besides the CS sampling pattern shown in Figures 6.41a & b, TSE-CSI experiments with a smaller matrix size were performed (cf. Figure 6.41c) as well as experiments acquired in a pseudo radial fashion (22 spokes, cf. Figure 6.41d). The latter had approximately the same measurement time as the undersampled experiment. Flowcharts and descriptions of the sampling pattern generations displayed in Figures 6.41c & d are provided in Appendix C.1 on page 129 and C.2 on page 130.

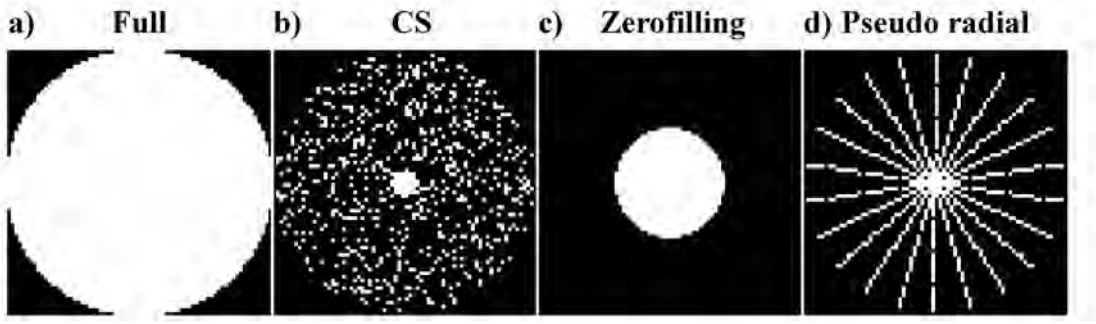


**Figure 6.41:** *Sampling pattern of the different acquisition strategies. Only sampled points are displayed. Sampling pattern for: a) fully sampled, b) CS (af = 6), c) retrospective zero-filling (af = 6) and d) pseudo radial acquisition (22 spokes, af ≈ 6 ).*

### MRI

#### $^{1}H$ *MRI*

An anatomical $^{1}$H reference was obtained with a FLASH sequence (flip angle = 30°; TE/TR = 5/50 ms; MTX = 300 × 300; FOV = 30 × 30 mm$^2$; ST = 2 mm).

#### $^{19}F$ *CSI*

The same geometry as for the $^{1}$H images was used for all $^{19}$F CSI experiments. A fully sampled reference was obtained using the described TSE-CSI sequence. Thus, a slice of the mouse brain was imaged using the 2D centric encoded sampling pattern described above (TE/$T_{AQ}$/TR = 18.6/12.9/2000 ms; SP = 64; **S**pectral **B**andwidth (SB): 5000 Hz; MTX = 72 × 72; TF = 16). Additionally, undersampled data with af = 6 were acquired using the TSE-CSI sequence. All sampling patterns are presented in Figures 6.41a – d.

#### *Post Processing*

Post processing was performed using MATLAB®. Since two spatial dimensions and one spectral dimension are available in 2D TSE-CSI, each image belonging to a specific spectral point was independently CS reconstructed as described in the following.

As mentioned before, a CS algorithm based on the one presented in [131] was used. Its implementation is provided in [23, 24]. However, in contrast to the algorithms used in [23, 24, 131], a fixed step width $t$ was used that was decreased every 30th iteration by a factor of 2. This had the advantage that no minimizing algorithm was necessary to evaluate $t$ and thus the algorithm performed faster. The value of the norm $p$ was always set to $p = 1.00$. Please note that with this parameter setting the chosen algorithm is equivalent to soft thresholding [24, 133]. Besides the step width $t$, $\epsilon$ was also decreased every 30th iteration by a factor of 2. The start values of $t$, $\epsilon = 1$, and the end values of $t$, $\epsilon = 10^{-4}$, yielded 420 iterations per CS reconstructed dataset. These parameters were used for all CS reconstructions. As mentioned above, a pseudo code of the used CS algorithm implementation is provided in Appendix B on page 128.

Experiments acquired with a smaller 2D matrix were zero-filled to a 72 × 72 point inplane matrix. For pseudo radial data, each k-space point was divided by the corresponding number of acquisitions to take into account the multiple acquisitions of the inner k-space points. CS reconstructions were not performed for these datasets. The resulted k-spaces were inverse Fourier transformed to obtain the CSI images.

### 6.2.3 Results

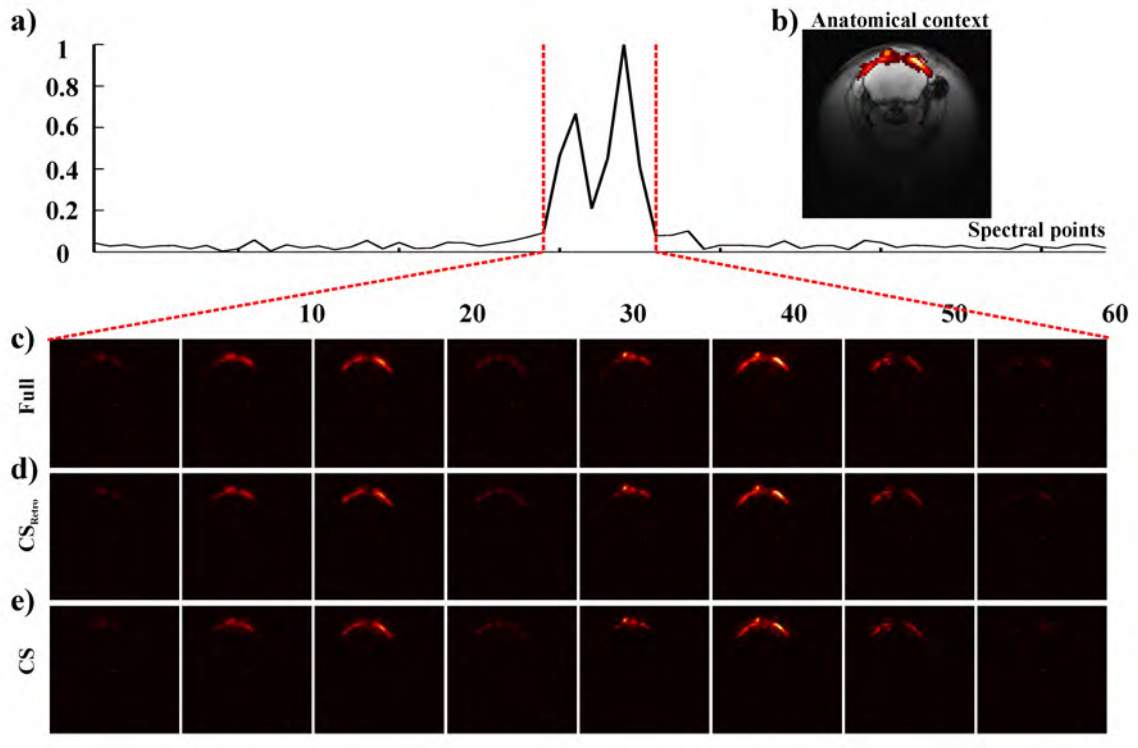


**Figure 6.42:** *Results of the fully sampled and CS reconstructed data. a) Spectrum from the fully sampled dataset showing the two main resonance peaks of the PFC1 and PFC2 compounds. To display both resonance peaks, the spectrum was obtained from the kc. b) Exemplary $^{1}H/^{19}F$ overlay for the anatomical localization of the $^{19}F$ signal. c–e) Spectral images from SP 29–36 as illustrated by the red dotted lines in (a). Spectral images of the fully sampled data (c), retrospectively undersampled and CS reconstructed data (d) and of the undersampled and CS reconstructed data (e). In general, similar signal patterns were observable for the fully sampled and the CS reconstructed data. Af = 6 was chosen when undersampling was applied. Part of the figure was adapted from a figure of Reference [132].*

Figure 6.42 shows results from the TSE-CSI experiments. In Figure 6.42a, the global spectrum from the kc shows both resonance peaks (PFC1 and PFC2). The two resonance peaks can be clearly separated. Figure 6.42b shows the $^{1}$H anatomical reference overlaid with a $^{19}$F spectral image to allow the location of the $^{19}$F signal into the anatomical context. Figure 6.42c shows the SP 29–36 of the fully sampled reference. Similar signal structures were observable when the fully sampled data were retrospectively undersampled and CS reconstructed (cf. Figure 6.42d) as well as when "real" undersampled data was acquired and CS reconstructed (cf. Figure 6.42e).

In comparison with the fully sampled data, however, the CS reconstructed images with low SNR (peak SNR = 15.7) showed a qualitative signal degradation (cf. Figures 6.43a–

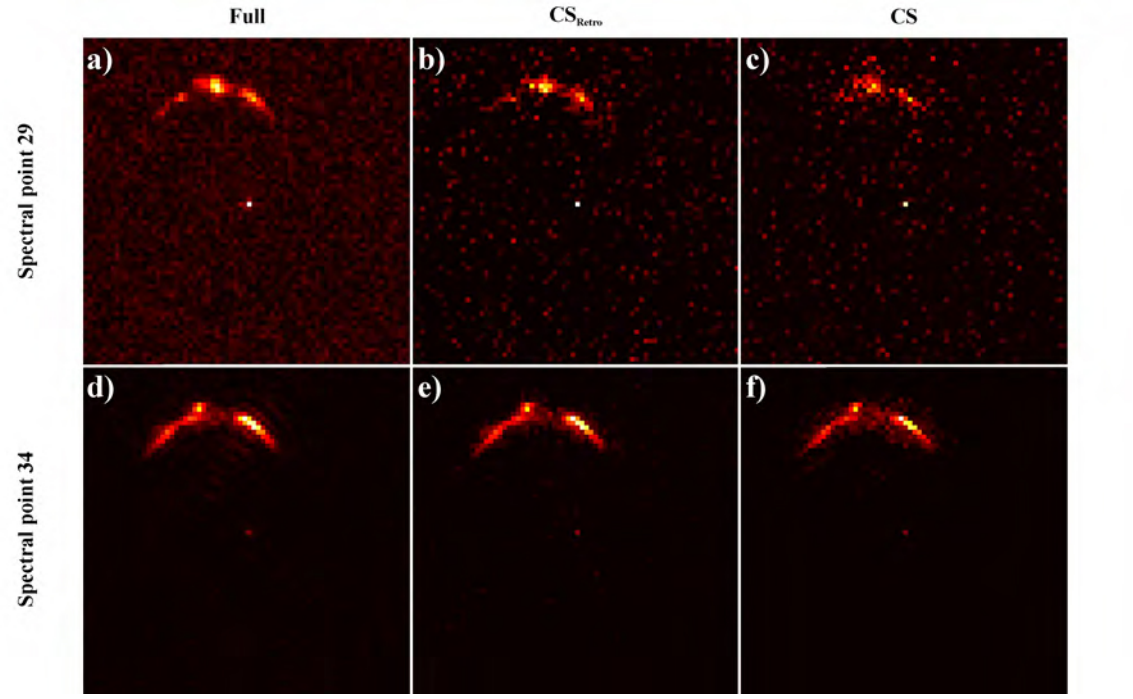


**Figure 6.43:** *a–c) Low SNR data from spectral point 29 (peak SNR = 15.7); From left to right: fully sampled data (a), retrospectively undersampled and CS reconstructed data (b) and undersampled and CS reconstructed data (c). d–f) High SNR data from spectral point 34 (peak SNR = 92.8); From left to right: fully sampled data (d), retrospectively undersampled and CS reconstructed data (e) and undersampled and CS reconstructed data (f). For better visualization the images (a–c) and (d–f) were scaled to the maximum signal of each row. Af = 6 was chosen when undersampling was applied. The bright spot in the middle of the images is most likely a baseline artifact. Part of the figure was adapted from a figure of Reference [132].*

c). Furthermore, in the case of high SNR (peak SNR = 92.8), a slight "blooming" effect could be observed for the CS reconstructions obtained from the undersampled and CS reconstructed data (cf. Figure 6.43f). This was unlike the fully sampled (cf. Figure 6.43d) and the retrospectively undersampled and CS reconstructed data (cf. Figure 6.43e).

Figures 6.44b–e show a comparison of the different TSE-CSI encoding schemes with a measurement time about six times less than the time needed for the fully sampled reference (cf. Figure 6.44a). While the undersampled but not CS reconstructed data showed strong incoherent artifacts (cf. Figure 6.44b), these artifacts were removed when CS was applied to the undersampled data (cf. Figure 6.44c). Compared to the zero-filled data (cf. Figure 6.44d) and the data acquired in a pseudo radial fashion (cf. Figure 6.44e), the CS reconstructed data appeared higher resolved. Furthermore, unlike for the zero-filled data, no Gibbs ringing artifacts [91] were observed for the CS reconstructed data (arrow Figure 6.44d). Moreover, unlike in the pseudo radial data, no streaking artifacts were observed for the CS reconstructed data (arrow Figure 6.44e).

### 6.2.4 Discussion

The successful application of CS to undersampled and thus accelerated $^{19}$F TSE-CSI was shown in the present section for data with sufficient SNR. Using an *ex vivo* PT mouse phantom, a similar situation as for *in vivo* measurements was simulated. Thus, this section

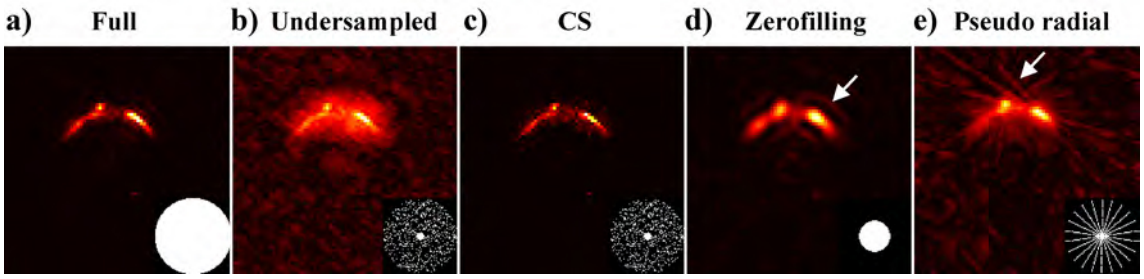


**Figure 6.44:** *Comparison of different fast TSE-CSI acquisition schemes showing spectral point 34. a) Fully sampled reference, b) undersampled data (af = 6), c) CS reconstruction of the undersampled data shown in (b), d) zero-filled dataset from data where only the inner k-space was acquired (af = 6) and e) reconstruction of data acquired in a pseudo radial fashion (af ≈ 6). The arrows in (d) and (e) point out artifacts due to the chosen acquisition scheme. Figure adapted from [132].*

provides a proof-of-principle that *in vivo* $^{19}$F TSE-CSI can possibly be accelerated using CS. However, this topic should be investigated in greater detail in the future.

A surface coil was used for the present experiments to obtain sufficient SNR, which is necessary to obtain a qualitatively good CS reconstruction [23, 24]. This was possible since the fluorine signal was distributed in close proximity to the coil. If the $^{19}$F marker is accumulated deeper in the tissue, however, a volume coil must be used due to the $B_1$ profile inherent to surface coils. Furthermore, the $B_1$ profile of the surface coil permits the application of $\sim 180°$ refocusing pulses to only a very limited area. Since the TSE-CSI sequence was CPMG-based the problem of non-180° refocusing pulses was minimized. A volume coil for excitation, however, should be applied in future studies.

The discrepancy between the CS reconstructions acquired from the undersampled k-space and the retrospectively undersampled k-space might be due to eddy current effects. This seems likely since the k-space points of the shown reconstructions were not acquired in a certain spatial order. Thus, the closest possible k-space points were not subsequently sampled. If eddy current effects are proved to be the cause for this issue, a strategy should be chosen in the future to minimize these effects [134].

The chosen 2D centric sampling pattern can be easily adapted to 3D patterns. Since 3D TSE-CSI measurements are very time consuming, CS might help to overcome this limitation.

Importantly, for *in vivo* application of this method, it must be known a priori if sufficient SNR can be expected. Scout scans could be applied in future studies to obtain a rough SNR estimation. A more detailed investigation concentrating on the application of CS in low SNR $^{19}$F data can be found in [23, 24].

### 6.2.5 Conclusion

CS accelerated TSE-CSI is feasible if sufficient SNR is present. Thus, the *in vivo* acquisition of spectrally resolved 3D $^{19}$F CSI data can be enabled using CS when sufficient SNR is given. This might be of interest for studies using several different $^{19}$F labeled markers to identify different biological processes.

## 6.3 Compressed Sensing Averaging (CSA)

### 6.3.1 Introduction

As discussed before, CS enables violating the Nyquist theorem, thus reducing the measurement time. Thereby, CS methods that enforce strict data consistency and use only one sparsity constraint, as used in the present work, provide stable and reproducible results for multiple situations [23, 24]. Unfortunately, visible spike artifacts can appear in the CS reconstructions (cf. Figures 6.45d–f) when applying these algorithms to data with high noise levels [23, 24].

To reduce those artifacts, two extensions for a CS algorithm enforcing strict data consistency [23, 24, 131] are proposed in the following. Both extensions are compared in regard to their capability to improve image quality. In order to demonstrate the benefit of this approach, simulations were performed for high noise levels on spatially sparse phantom data obtained from $^{19}$F CSI measurements.

A proof-of-principle study applying the first possible extension was previously presented [135] and is further investigated in the present work.

### 6.3.2 Motivation

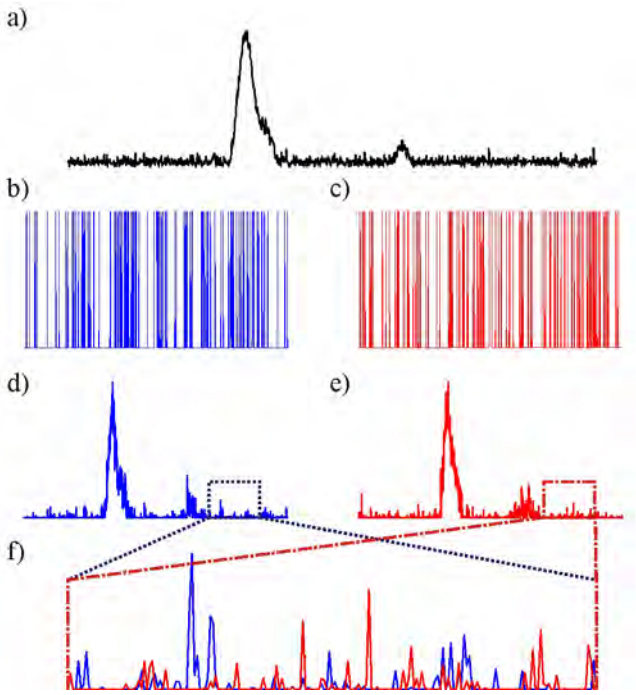


**Figure 6.45:** *Scheme illustrating the principle idea of the proposed method extensions. a) Simulated 1D spatial signal, peak SNR = 30 and 1000 points. b & c) Different 1D sampling patterns, af = 8. d & e) Corresponding CS reconstructions. f) Magnification of points 700–900 of both CS reconstructions, showing the different signal intensity and/or different position of the spike artifacts. In this example, the sampling pattern was applied to the spectral dimension. Figure based on figures from Reference [135].*

A simulated spatial 1D signal is used to illustrate the basic idea underlying the proposed extensions of the CS algorithm (Figure 6.45). When a fully acquired MR dataset (Figure

6.45a) is retrospectively undersampled using different sampling patterns (Figures 6.45b & c), the CS reconstruction leads in each case to a fully recovered image (Figures 6.45d & e). However, when a CS algorithm based on strict data consistency is used on the original data with low SNR, visible spike artifacts can appear in the reconstructions. The locations and signal intensities of these artifacts depend on the noise and the chosen sampling pattern [23] (Figure 6.45f). The proposed extensions to this CS algorithm utilize the dependency of the spike position and spike signal intensity on the chosen sampling pattern. Therefore, multiple different CS reconstructions of retrospectively undersampled data are generated to obtain an averaged CS reconstruction. Briefly, the following approach was used:

1. Initial CS reconstruction of the undersampled dataset using the initial sampling pattern
2. N additional CS reconstruction using N different sampling patterns
3. Average image of all CS reconstructions

This strategy potentially leads to improved image quality in comparison to the initial CS reconstruction and thus is investigated in greater detail in the following.

### 6.3.3 Material & Methods

#### CS algorithm and extensions

*Compressed Sensing algorithm*

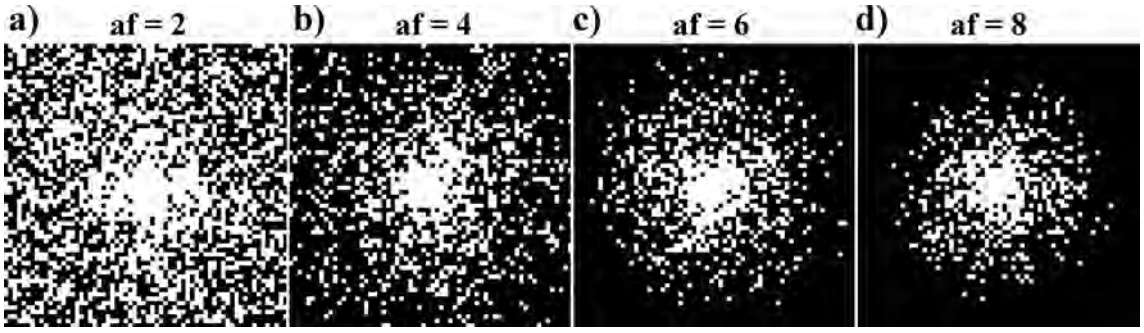


**Figure 6.46:** *Examples of sampling pattern with different afs.*

For the CS reconstructions, the same CS algorithm and parameters as described in the post procession part of Section 6.2.2 were chosen. However, since this method is a sole post processing technique, different sampling patterns were chosen than those in Section 6.2.

The chosen sampling patterns consisted of a fully sampled kc and a density-matched, randomly undersampled outer k-space (Figure 6.46). For each sampling pattern, the fully sampled kc was set to $\approx 1\%$ of the sampled points in the specific pattern. As mentioned before, this scheme was chosen since it was previously shown that a densely sampled inner k-space is well suited for CS [23, 130]. Furthermore, the following density-weighting function was used to undersample the k-space outside of the kc:

$$f(r) = e^{\frac{10}{r}} \quad , \quad r = [k_{min}, k_{max}] \tag{6.3}$$

where $r$ refers to the radius in k-space, with $k_{min}$ being the minimum and $k_{max}$ the maximum ($k_{min}$ =0.7 and $k_{max}$ = 44.5 for the chosen 64 × 64 MTX). Sampling patterns with variable density have been shown to be better suited for CS reconstructions [130]. Due to the used density-weighting function, the fully sampled kc normally contained more points than expected for 1% of the sampled points in the specific patterns (cf. Figure 6.46).

*Compressed Sensing Averaging method 1 (CSA-1)*

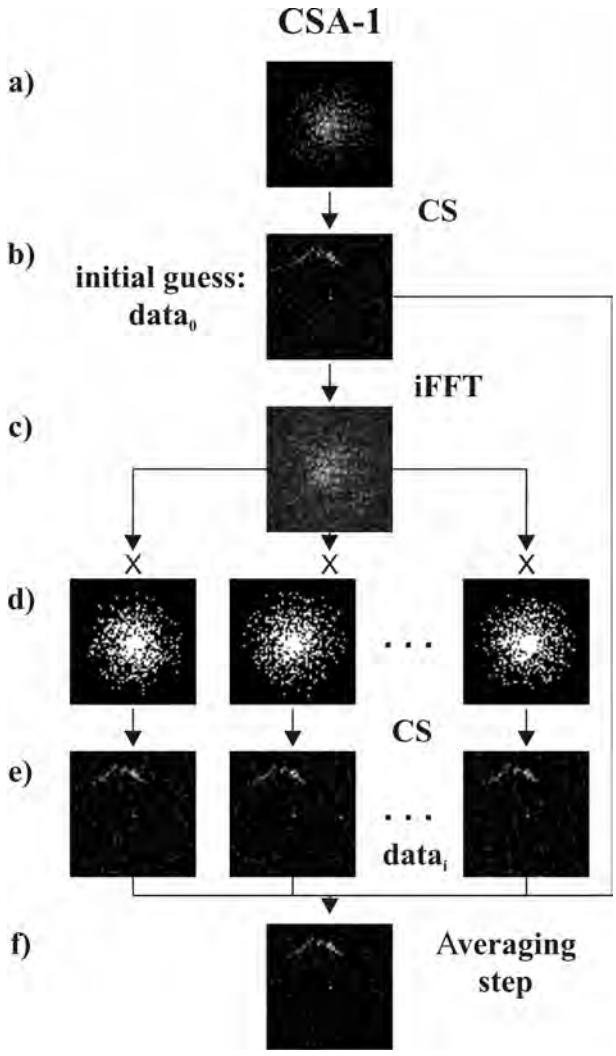


**Figure 6.47:** *Flowchart describing the CSA-1 method. a) Undersampled data is acquired. b) An initial CS reconstruction is generated from undersampled data. c) k-space data of the CS reconstructed dataset is obtained using an inverse Fourier transform. d) N different sampling patterns are applied to the k-space data to generate N new undersampled datasets. e) The undersampled datasets are CS reconstructed. f) In a final step, an average image is formed using the initial and the N reconstructed artificial datasets.*

A bootstrap-like method [135–138] was applied as the first extension. Thus, instead of only creating one CS reconstruction, additional CS reconstructions and a subsequent averaging procedure were added. In the following, this method will be referred to as the **C**ompressed **S**ensing **A**veraging 1 (CSA-1) method. Figure 6.47 shows a flowchart displaying the different steps undertaken using CSA-1. An undersampled (cf. Figure 6.47a) and CS reconstructed dataset was used as the start dataset ($data_0$, cf. Figure 6.47b). $N$

different sampling patterns with the same af as the initial sampling pattern were applied (cf. Figure 6.47d) to the k-space data of this initial CS reconstruction (cf. Figure 6.47c). These new undersampled datasets were subsequently CS reconstructed ($data_i$, cf. Figure 6.47e). A mean image was generated in a final step (cf. Figure 6.47f):

$$data_{CSA-1} = \frac{1}{N+1}\left(\sum_{i=1}^{N} data_i + data_0\right) \tag{6.4}$$

*Compressed Sensing Averaging method 2 (CSA-2)*

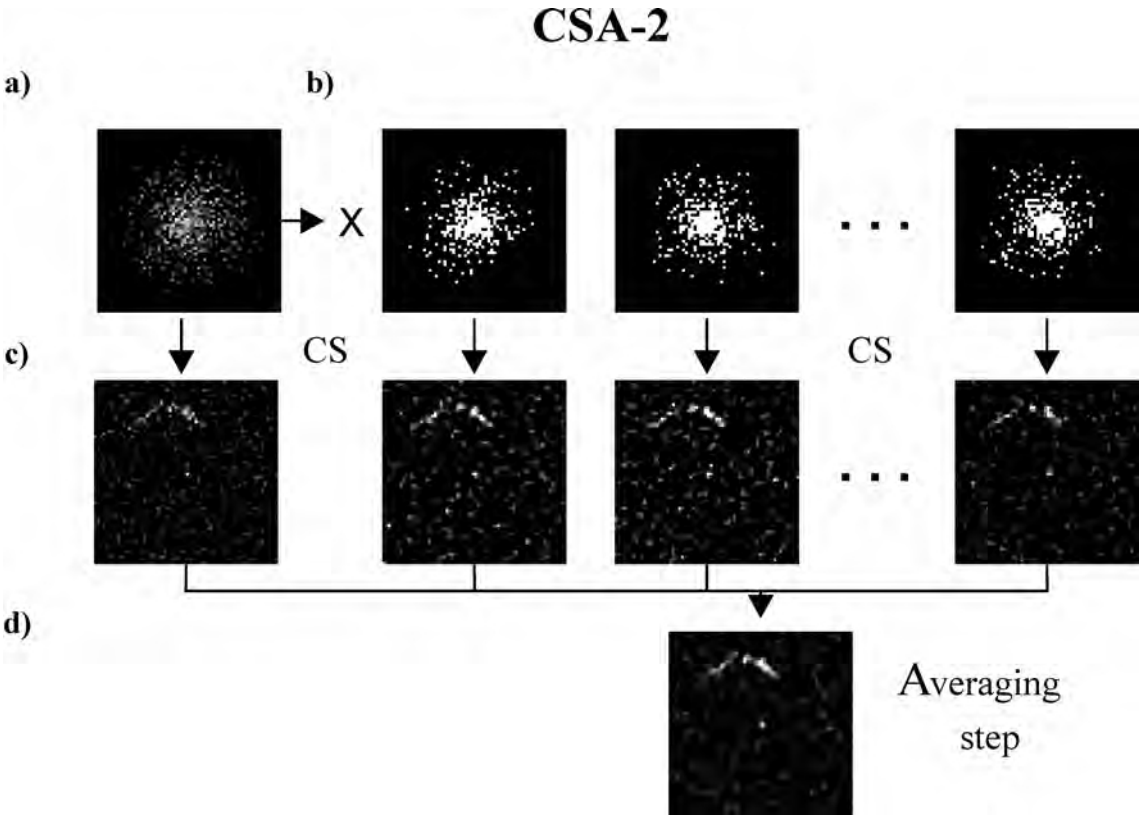


**Figure 6.48:** *Flowchart describing the CSA-2 method. a) Undersampled data is acquired. b) N different subsamples of the initial sampling pattern are applied to the k-space data to generate N artificial undersampled datasets. c) CS reconstructions are generated out of the N new undersampled datasets and the initial undersampled dataset. d) In a final step, an average image is formed using all reconstructed datasets.*

The second extension is based on the so-called jackknife method [137–140], which is closely related to the bootstrap method. Contrary to CSA-1, the second method uses only measured data. To create the CS reconstructions, the same CS algorithm as for the CSA-1 method is used. In the following, the second method will be referred to as the CSA 2 (CSA-2) method.

The flowchart in Figure 6.48 displays the different steps used with CSA-2. The original acquired data (Figure 6.48a) were further undersampled to create $N$ new, higher undersampled datasets (Figure 6.48b). For each of these $N$ datasets, different density-weighted

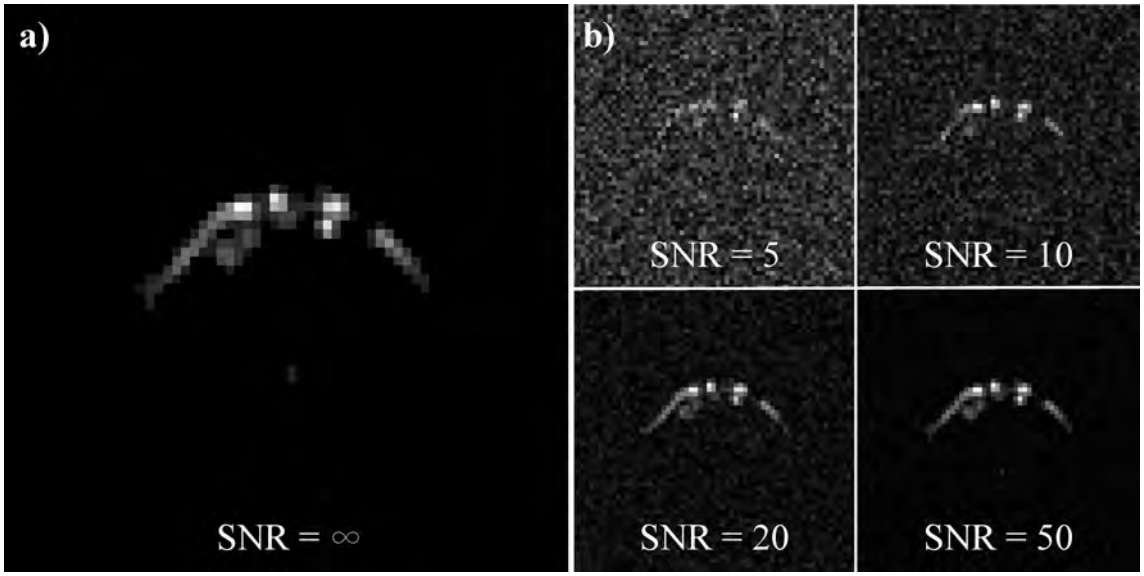


**Figure 6.49:** *a) Noise-free 2D phantom. b) Exemplary noisy 2D phantom images, peak SNR = {5, 10, 20, 50}. The numerical phantom was generated from measured data obtained from a 3D $^{19}F$ CSI experiment [23, 24].*

(cf. Equation 6.3), randomly chosen subsets (subsamples) of the initial sampling pattern were used. These $N$ additionally undersampled datasets were CS reconstructed (Figure 6.48c). An average image ($data_{CSA-2}$) was then generated from all $N$ $data_i$ datasets and from the CS reconstruction using all sampled points ($data_0$) (Figure 6.48d). Thus, Equation 6.4 also holds true for the averaging step of CSA-2.

### Numerical simulations of undersampled data

Simulations were performed in MATLAB® to study the behavior of the proposed methods. A 2D phantom was generated from a measured, normalized, and thresholded 3D $^{19}$F CSI dataset described in [23, 24]. This served as a noise-free reference. The phantom dimensions were 64 × 64 spatial points (Figure 6.49a). The number of signal containing pixels was 126, which corresponds to 3.1% of all pixels. Thus, the used phantom was considered sparse in the spatial domain and no sparsity transform was necessary prior to CS reconstruction.

*CSA-1*

Pseudo-random Gaussian white noise was independently added to the real and imaginary parts of the noise-free reference dataset (image space). The standard deviation of the Gaussian noise distribution was set to $\sigma = \{0.2, 0.1, 0.05, 0.02\}$, which corresponds to a peak SNR = {5, 10, 20, 50} (Figure 6.49b). The following afs were investigated: af = {2, 4, 6, 8}. For each noise level and af, the full dataset was undersampled and subsequently CS reconstructed to generate a start dataset ($data_0$). A total of $N = 49$ CS reconstructions ($data_{1-49}$) of the start dataset ($data_0$) were obtained. To investigate the improvement of image quality using averaging, an averaged image was generated for each $K = \{1, 2, ..., N\}$ ($data_{0-K}$). For example, $data_{0-5}$ is the averaged image of $data_0$ and the CS reconstructions

$data_1$ to $data_5$. This resulted in $K + 1 = 50$ images, $data_0$ and the 49 averaged images ($data_{0-K}$).

For each reconstruction, the sampling pattern consisted of the same fully sampled kc and a differently sampled outer k-space as described.

To investigate the robustness of the method, the simulations were repeated 100 times using the same parameters and sampling patterns but different noise corrupted data. Therefore, pseudo-random Gaussian noise with the same standard deviation values as described above was individually added to the noise-free reference for each repetition.

*CSA-2*

The same parameters and settings described for the CSA-1 method were used for the CSA-2 method. Since, unlike in the CSA-1 method, only measured data points are used for CS reconstructions with the CSA-2 method, the CS reconstruction from the full sampling pattern ($data_0$) did not serve as an initial guess. Furthermore, for all noise levels and afs, three additional **SUB A**cceleration **F**actors (subaf) were investigated: subaf = {1.25 1.5 2}. This lead to overall undersampling factors ranging from 2.5 (af = 2 × subaf = 1.25) to a maximum of 16 (af = 8 × subaf = 2). For each given noise level, af and subaf, N = 49 different subsampling patterns were generated. CS reconstructions were accordingly performed to obtain $data_{1-49}$ for each noise level, af and subaf.

### Error quantification

Since a noise-free reference image was available, the reconstruction quality of the results was quantified using the **R**oot **M**ean **S**quare **E**rror (RMSE), defined as:

$$RMSE = \sqrt{\frac{\sum_{j=1}^{M}(|R_j - O_j|)^2}{M}} \tag{6.5}$$

where $R_j$ represents the signal of the $j$-th voxel in the reconstructed image, $O_j$ represents the signal of the $j$-th voxel in the noise-free reference, and $M$ is the number of the regarded pixels calculated from the noise free reference. However, the investigated data were sparse in the spatial domain and relatively high noise levels were applied. Thus, separately regarding the background RMSE and signal fraction RMSE were imperative. This is because the RMSE of all pixels in the investigated cases was background dominated, which hampered drawing conclusions on the reconstruction quality of the few signal pixels [23]. For this reason, the RMSE of the averaged image was calculated for every averaging step regarding three different cases: (A) the total RMSE for all pixels ($RMSE_T$), (B) the RMSE for the signal containing pixels ($RMSE_S$), and (C) the RMSE regarding the pixels containing no signal (background) in the noise-free reference ($RMSE_B$). This was done for all 100 repetitions. In a final step using (A) through (C), the mean RMSE and the maximum deviation were calculated from the 100 repetitions. These calculations were performed for every averaging step.

This approach enables differentiating between the overall image reconstruction quality, the reconstruction quality of the signal fraction, and the reconstruction quality of the background.

### 6.3.4 Results

#### CSA-1

**Table 6.4:** *Relative RMSE change using the CSA-1 method ($\Delta RMSE = (RMSE_{0-49} - RMSE_0)/RMSE_0$). First/Second/Third section: Total image ($RMSE_T$)/Only signal containing pixels ($RMSE_S$)/Only background pixels ($RMSE_B$) were evaluated. A negative value represents a decrease of the relative RMSE change and a positive value stands for an increase. For calculation of the relative RMSE values, the mean RMSE values derived from the 100 different noise patterns were used.*

| $\Delta\ RMSE_T$ in % | | | | |
|---|---|---|---|---|
| SNR | af = 2 | af = 4 | af = 6 | af = 8 |
| 5 | -32.8 | -43.2 | -44.9 | -45.3 |
| 10 | -32.0 | -40.6 | -40.6 | -41.2 |
| 20 | -31.1 | -36.6 | -33.1 | -32.5 |
| 50 | -30.0 | -31.4 | -19.4 | -15.1 |
| $\Delta\ RMSE_S$ in % | | | | |
| SNR | af = 2 | af = 4 | af = 6 | af = 8 |
| 5 | -16.5 | -20.6 | -23.2 | -23.7 |
| 10 | -9.9 | -13.7 | -16.5 | -18.6 |
| 20 | -4.7 | -8.5 | -9.5 | -11.4 |
| 50 | -0.4 | -2.9 | 0.0 | 0.1 |
| $\Delta\ RMSE_B$ in % | | | | |
| SNR | af = 2 | af = 4 | af = 6 | af = 8 |
| 5 | -33.8 | -45.9 | -48.3 | -49.4 |
| 10 | -33.9 | -46.0 | -48.3 | -49.5 |
| 20 | -34.1 | -45.8 | -47.4 | -48.7 |
| 50 | -34.1 | -45.7 | -45.4 | -45.1 |

In Figure 6.50 and Table 6.4, the results of the CSA-1 method applied on the 2D phantom data are displayed.

In Figures 6.50a–c, a reference image with a peak SNR = 10, the initial CS reconstruction used as start dataset $data_0$, and the averaged image $data_{0-49}$ are shown from the left to right (af = 8). Even though spike artifacts hamper the image quality in Figure 6.50b, a background suppression is noticeable when compared to Figure 6.50a. In Figure 6.50c, the highest background suppression of all shown images is observable accompanied with a significant reduction of spike artifacts, making it possible to easily identify signal structures.

In Figures 6.50d–o, the courses of the different RMSE metrics are plotted against the number of averages.

Figurse 6.50d–g display the $RMSE_T$. For all investigated parameter settings, a decrease of the $RMSE_T$ value was achieved with an increasing number of averages. Regarding high noise levels, it can be observed that with increasing af, the $RMSE_T$ of the initial and the averaged CS reconstructions was decreased. For low noise levels, however, this trend was reversed.

Figures 6.50h–k display the course of the $RMSE_S$. Contrary to the $RMSE_T$, in two cases, a small increase of the $RMSE_S$ value with an increasing number of averages can

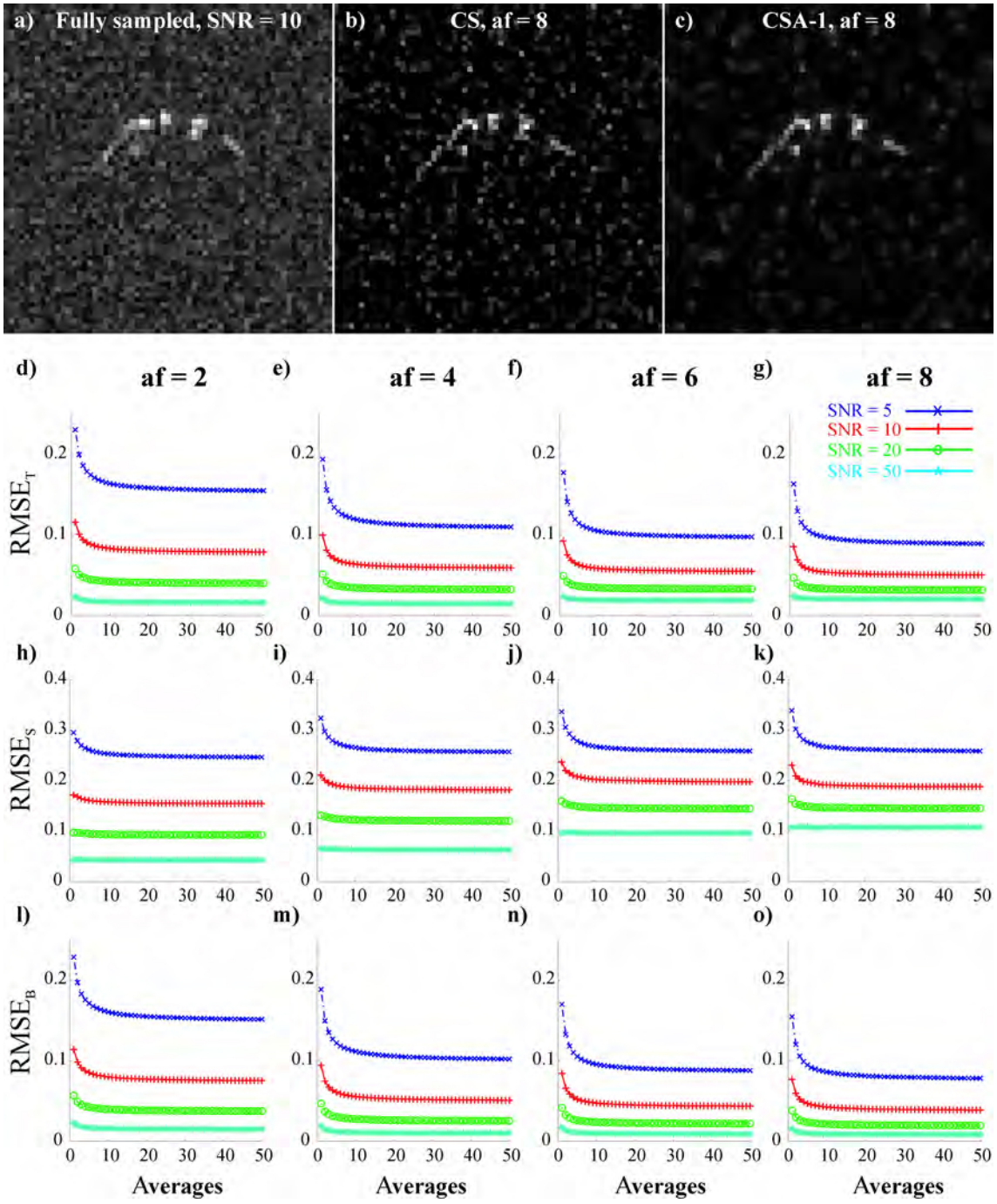


**Figure 6.50:** *Results of the CSA-1 method applied to the phantom data. a) Fully sampled image, peak SNR = 10. b) Undersampled and accordingly CS reconstructed image, af = 8. c) Undersampled and accordingly reconstructed using the CSA-1 method, af = 8 and 49 averages. For better visualization of the background all images are scaled by a factor of 0.75. d–g) $RMSE_T$ plotted against the number of averages ((d)/(e)/(f)/(g): af = 2/4/6/8). h–k) $RMSE_S$ plotted against the number of averages ((h)/(i)/(j)/(k): af = 2/4/6/8). l–o) $RMSE_B$ plotted against the number of averages ((l)/(m)/(n)/(o): af = 2/4/6/8). In the images (a–c) the results from one exemplary noise pattern are displayed. Regarding the plots, the mean RMSE derived from the 100 different noise patterns is displayed for each parameter setting.*

be observed when the CSA-1 method was used (af = 6/8, SNR = 50). For all other investigated parameters, a decrease of the $RMSE_S$ with increasing average number was achieved. For the investigated SNR levels, an increase in the af normally increased the $RMSE_S$ of the initial and the averaged CS reconstructions. Only in two cases did (SNR= 10, af = 6/8) the higher af result in a slightly lower $RMSE_S$.

Figures 6.50l–o display the $RMSE_B$ plotted against the number of averages. Regarding increasing afs, a different behavior can be observed compared to the plots displaying the $RMSE_T$ and $RMSE_S$. Thus, an increase in the af always decreased the $RMSE_B$ of the CS reconstructions. Similar to the observations for the $RMSE_T$, a decrease of the $RMSE_B$ was observed with an increasing number of averages for all applied parameter settings.

The behavior described above is reflected in Table 6.4, where the relative RMSE change between the averaged image $data_{0-49}$ and the to $data_0$ is given for the different image parts.

Regarding the $RMSE_T$, the greatest decrease for a given af was achieved with SNR = 5 (Table 6.4, first section, first row). The smallest relative decrease for a given af was achieved with SNR = 50 (Table 6.4, first section, last row). Furthermore, the first section of Table 6.4 shows that, depending on the noise level, the maximum relative decrease of the $RMSE_T$ was reached for different afs. For example, a peak SNR = 5 in the original image needed an af = 8 to reach the maximum relative decrease, while with a peak SNR = 50 it was already reached for af = 4.

In the second section of Table 6.4, the relative change of the $RMSE_S$ is displayed. Again, for a given af, the maximum relative decrease was always given for SNR = 5. Furthermore, for all investigated afs, the smallest relative decrease or highest relative increase was always given for SNR = 50. Besides SNR = 50 the maximum relative decrease of the $RMSE_S$ with a given noise level was always reached for af = 8.

In the third section of Table 6.4, only the background containing pixels are evaluated. Contrary to the other two cases, the maximum relative decrease of the $RMSE_B$ for a given af was not always given with SNR = 5. Furthermore, when each af was separately regarded, the smallest relative decrease was not always given for the same noise level. In general, however, the relative decreases of the $RMSE_B$ were less sensitive to the noise level compared to the other regarded RMSE metrics. For a given noise level, other than SNR = 50, the maximum relative decrease of the $RMSE_B$ was always reached for af = 8.

### CSA-2

In Figure 6.51 and Table 6.5 the results of the CSA-2 method applied on the 2D phantom data are displayed. The same initial CS reconstruction (af = 8) was used for the CSA-2 method as for the CSA-1 method (Figure 6.50b, Figure 6.51b).

In Figure 6.51a the same reference image with a peak SNR = 10 as in Figure 6.50a is shown. A background suppression compared to the fully sampled image (cf. Figure 6.51a) is visible in the CS reconstruction with af = 8 (cf. Figure 6.51b). In Figures 6.51c–d the corresponding averaged images ($data_{0-49}$) for two exemplary subaf are shown (Figures 6.51c & d: subaf = 1.25/2), showing an even higher background suppression. Thereby, the best results can be observed for subaf = 2 (Figure 6.51d).

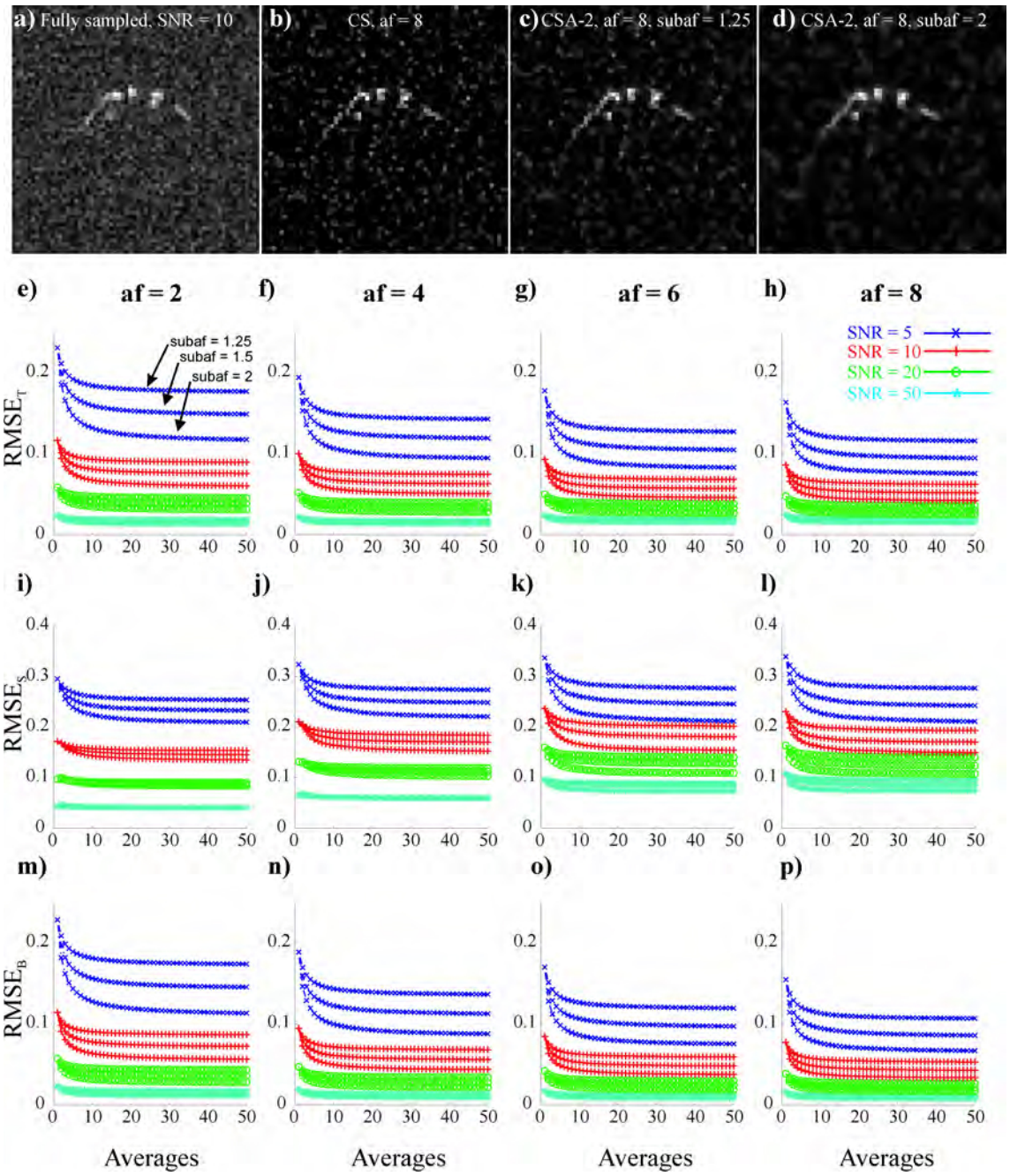


**Figure 6.51:** *Results of the CSA-2 method applied to the phantom data. a) Fully sampled image, peak SNR = 10. b) Undersampled and CS reconstructed image, af = 8. c–d) Undersampled and reconstructed images using the CSA-2 method, af = 8 and 49 averages, subaf = 1.25/2 ((d)/(f)). For better visualization of the background all images are scaled by a factor of 0.75. e–h) $RMSE_T$ plotted against the number of averages ((e)/(f)/(g)/(h): af = 2/4/6/8). i–l) $RMSE_S$ plotted against the number of averages ((i)/(j)/(k)/(l): af = 2/4/6/8). m–p) $RMSE_B$ plotted against the number of averages ((m)/(n)/(o)/(p): af = 2/4/6/8). In all plots the 3 curves displaying the different subaf are shown. Thereby, the chronological order of the curves belonging to the different subafs shown in (e) is true for all plots. In the images (a–d) the results from the same exemplary noise pattern as in Figure 6.50 are displayed. Regarding the plots, for each parameter setting, the mean RMSE derived from the 100 different noise patterns is displayed.*

**Table 6.5:** *Relative change of the RMSE using the CSA-2 method ($\Delta RMSE = (RMSE_{0-49} - RMSE_0)/RMSE_0$). First/Second/Third section: Total image ($RMSE_T$)/Only signal containing pixels ($RMSE_S$)/Only background pixels $RMSE_B$ were evaluated. In each case the values are listed for the three used subafs. A negative value represents a decrease of the relative change of the RMSE. For calculation of the relative RMSE values, the mean RMSEs derived from the 100 different noise patterns were used.*

| $\Delta\ RMSE_T$ in % | | | | |
|---|---|---|---|---|
| SNR | af = 2; subaf = 1.25/1.5/2 | af = 4; subaf = 1.25/1.5/2 | af = 6; subaf = 1.25/1.5/2 | af = 8; subaf = 1.25/1.5/2 |
| 5 | -23.4/-35.6/-49.2 | -26.5/-38.7/-51.3 | -28.4/-41.1/-53.4 | -29.2/-42.2/-53.9 |
| 10 | -23.1/-35.0/-48.2 | -25.7/-37.4/-49.4 | -26.8/-38.9/-50.8 | -27.6/-40.0/-51.0 |
| 20 | -22.8/-34.5/-46.9 | -25.0/-34.8/-45.9 | -23.8/-34.8/-46.6 | -24.6/-36.3/-46.9 |
| 50 | -22.3/-33.4/-45.0 | -21.7/-30.5/-38.0 | -17.8/-25.9/-36.3 | -18.3/-29.0/-38.6 |
| $\Delta\ RMSE_S$ in % | | | | |
| SNR | af = 2; subaf = 1.25/1.5/2 | af = 4; subaf = 1.25/1.5/2 | af = 6; subaf = 1.25/1.5/2 | af = 8; subaf = 1.25/1.5/2 |
| 5 | -14.2/-21.2/-29.1 | -15.5/-23.3/-31.9 | -17.9/-27.1/-37.1 | -18.4/-28.5/-37.8 |
| 10 | -10.4/-15.3/-21.2 | -12.7/-19.2/-27.6 | -14.8/-23.6/-34.8 | -16.2/-26.1/-35.2 |
| 20 | -7.0/-10.1/-13.3 | -9.4/-14.5/-21.5 | -11.9/-19.7/-31.7 | -14.2/-24.3/-34.6 |
| 50 | -4.3/-5.3/-4.9 | -5.8/-7.9/-8.8 | -7.6/-12.7/-23.2 | -11.3/-21.3/-31.1 |
| $\Delta\ RMSE_B$ in % | | | | |
| SNR | af = 2; subaf = 1.25/1.5/2 | af = 4; subaf = 1.25/1.5/2 | af = 6; subaf = 1.25/1.5/2 | af = 8; subaf = 1.25/1.5/2 |
| 5 | -23.9/-36.4/-50.5 | -27.7/-40.4/-53.6 | -29.8/-43.0/-55.8 | -31.0/-44.6/-56.9 |
| 10 | -24.1/-36.7/-50.8 | -28.0/-40.8/-53.8 | -30.1/-43.3/-55.8 | -31.2/-44.7/-56.6 |
| 20 | -24.4/-37.1/-51.1 | -28.2/-41.0/-53.9 | -29.9/-43.1/-55.2 | -31.4/-44.5/-55.7 |
| 50 | -24.5/-37.2/-51.3 | -28.5/-41.1/-53.3 | -29.5/-42.0/-53.2 | -29.9/-42.4/-51.7 |

In Figures 6.51e–p the course of the different RMSE metrics is plotted against the number of the averages. For all chosen parameter settings a decrease of all RMSE metrics was achieved using the CSA-2 method. Thereby, for each regarded SNR and af combination the lowest RMSE values for the averaged image can be found for the highest subaf with one exception ($RMSE_S$, SNR = 50, af = 2). If the different RMSE plots for increasing af values are regarded the CSA-2 method displays trends similar to the CSA-1 method.

The described behavior is reflected in Table 6.5, where the relative RMSE change between the averaged images $data_{0-49}$ when compared to $data_0$ is provided.

Concerning the relative change of the $RMSE_T$, the greatest decrease was achieved for all afs with SNR = 5 (Table 6.5, first section, first row). Thereby, subaf = 2 delivered the greatest decrease for each af. The smallest relative decrease was given for all afs with SNR = 50 (Table 6.5, first section, last row), whereby subaf = 1.25 gave the smallest decrease. In general, for a given af and SNR, an increase of the subaf decreased the $RMSE_T$. Similar to the results for the CSA-1 method, depending on the noise level, the maximum relative decrease of the $RMSE_T$ was reached with different afs. For example, for all subafs, a peak SNR = 5 in the original image needed af = 8 to reach the maximum relative decrease, while using a peak SNR = 50 resulted in it being reached with af = 2.

Behavior similar to the $RMSE_T$ can be observed in the relative change of the $RMSE_S$. Thus, the greatest decrease was achieved for all afs with SNR = 5 (Table 6.5, second section, first row). Again, thereby, subaf = 2 delivered the greatest decrease for each af. Furthermore, the smallest relative decrease was given for all afs for SNR = 50 (Table 6.5, second section, last row), whereby subaf = 1.25 again provided the smallest decrease. Contrary to the behavior of the $RMSE_T$, one case can be found (SNR = 50, af = 2) in which an increase of the subaf did not necessarily decrease the $RMSE_S$. Furthermore, contrary to the $RMSE_T$, the maximum relative decrease of the $RMSE_S$ for a given noise level was always reached for af = 8.

In the third section of Table 6.5, only the background containing pixels were evaluated. Contrary to the $RMSE_T$ and the $RMSE_S$, for a given af, the maximum relative decrease of the $RMSE_B$ was not always given for SNR = 5 and the minimum relative decrease not always for SNR = 50. Similar to the CSA-1 method, however, the relative decreases of the $RMSE_B$ were generally less sensitive to the noise level compared to the other regarded RMSE metrics. Similar to the $RMSE_T$ and contrary to the $RMSE_S$, an increase of the subaf led to a decrease of the relative $RMSE_B$ in all cases. Besides SNR = 50, the maximum relative decrease of the $RMSE_B$ was always reached with af = 8 for a given noise level.

### 6.3.5 Discussion

The following main results regarding the current section were found:

- The $RMSE_T$ could be decreased for all investigated parameter settings and both proposed methods
- A significant background suppression was reached in all cases, accompanied with a suppression of spike artifacts
- When only the signal containing pixels were regarded for most parameter settings (62 out of 64) a decrease of the $RMSE_S$ was observed. When only low SNR levels are regarded (SNR $\leq$ 20), which are of special interest in this work, this effect was true for all investigated parameter settings.

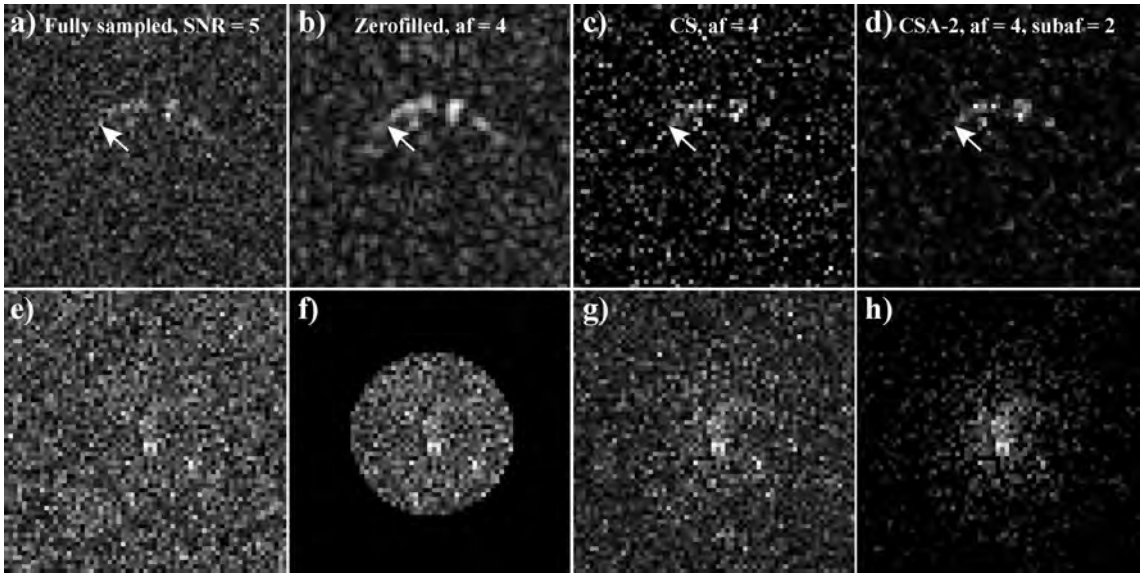


**Figure 6.52:** *Different aspects of the CSA reconstruction methods. a) Fully sampled image of the phantom with SNR = 5. b) Zero-filled image (af = 4) of the data used in (a). c) CS reconstruction (af = 4) of data underlying (a). d) Averaged image of (c) using the CSA-2 method (af = 4, subaf = 2). e) k-space of the fully sampled data (a). f) k-space of the fully zero-filled data (b). g) k-space of the CS reconstruction displayed in (c). h) k-space of the averaged CS reconstruction shown in (d). The arrows point out a difference in the signal structure that is not visible in the CS reconstructions.*

These and other issues are discussed in greater detail in the following.

### CSA-1 vs. CSA-2

*Image quality*

In all investigated cases, the $RMSE_T$ was decreased even when the $RMSE_S$ was increased. Since 96.9% of all the phantom pixels contained no signal, the decrease of the $RMSE_T$ was mainly influenced by the decrease of the $RMSE_B$.

When both methods were compared regarding the $RMSE_T$, in 25 out of 48 cases the CSA-2 method resulted in superior image quality compared to the CSA-1 method (Table 6.4 and Table 6.5). The greatest relative decrease of the $RMSE_T$ was achieved in every case with the CSA-2 method (subaf = 2).

*Signal quality*

Regarding the signal containing pixels, an increase of the $RMSE_S$ was observed with two investigated parameter settings when the CSA-1 method was used. In those cases, however, the increase of the absolute values of the $RMSE_S$ had only a minor impact on image quality since the maximum relative increase was only 0.1%. Furthermore, for high af and low SNR values, which are of special interest, the signal quality in terms of the $RMSE_S$ could be significantly improved using this method.

With the CSA-2 method, a decrease of the $RMSE_S$ was observed for all chosen parameters. In 43 out of 48 cases the CSA-2 method performed better in terms of the signal quality compared to the CSA-1 method (Table 6.4 and Table 6.5). This improved behavior was most likely because only (different) subsets of measured data points were used.

*Background suppression*

A decrease of the $RMSE_B$ was observed for all investigated parameters and both proposed methods. In all cases, the decrease of the $RMSE_B$ was higher than for the $RMSE_T$. This was due to the different behavior in the signal containing pixels, which are also included in the $RMSE_T$.

In 28 out of 48 cases the CSA-1 method decreased the $RMSE_B$ more than the CSA-2 method. Again, the greatest relative $RMSE_B$ decreases, however, were achieved in every case with the CSA-2 method (subaf = 2). The main influence for this phenomenon most likely was the higher degrees of freedom in the CS reconstructions using the CSA-2 method with a subaf = 2. Thus, the reconstructed k-space points could be modified more by the CSA-2 method since higher effective afs ($\leq 16$) were applied in this method.

*Remarks*

For the chosen parameters, the CSA-2 method normally performed better than the CSA-1 method in the present work, especially when the $RMSE_S$ was regarded. However, one must choose an additional parameter in the reconstruction process when using the CSA-2 method. Furthermore, when the chosen subaf is too high, and thus too few matrix points are sampled, the averaged image is smoothed (e.g., Figure 6.51d). Additionally, the CSA-1 method could be run with a different af as the initial CS reconstruction.

**General comments**

*Reproducibility*

In all the presented plots and tables the mean RMSE derived from the 100 different noise patterns for each parameter setting was displayed. The results of specific noise patterns can differ from the results of the mean RMSE. However, for all investigated cases the maximum deviation of the RMSE values was small (data not shown). Results similar to those presented in the current work were obtained when CSA was applied to different spatially sparse datasets (e.g., cf. Figure 6.54).

*RMSE*

As reported in other studies (e.g., [23]), the RMSE can be a problematic metric when used to describe the image quality of CS reconstructions. Unlike when a fully sampled, noise corrupted image is regarded, the RMSE is not equal for signal and background containing pixels after CS reconstruction (e.g., Figures 6.50h–o). The split of the $RMSE_T$ in the $RMSE_S$ and $RMSE_B$ avoids this problematic.

*General behavior of the RMSE*

With all methods and applications, general trends were observed in the behavior of the different RMSE metrics.

With most parameter settings, an increase of the initial $RMSE_S$ and the $RMSE_S$ of the averaged CS reconstructions was observed with increasing afs. This is most likely because a higher af increases the errors of signal containing pixels in the CS reconstructions.

However, with most parameter settings, a decrease of the initial $RMSE_B$ and the $RMSE_B$ of the averaged CS reconstructions was observed with increasing afs. With increasing af, the higher degrees of freedom in the CS reconstruction most likely allowed higher background suppression.

Since the $RMSE_T$ regards the total image, the behavior of the $RMSE_S$ and the behavior of the $RMSE_B$ are included. Thus, for high noise levels, which were of special interest in this work, increasing the af decreased the $RMSE_T$ of the averaged CS reconstructions. For low noise levels, however, this trend was reversed for some parameter settings.

*RMSE vs. CS-Averages*

The number of CS averages was arbitrarily set to 49 to enable displaying the course of the different RMSE values against the averages. For every case the RMSE values approached a limiting value with increasing averages and thus the proposed extensions proved very stable using the investigated parameter settings. Furthermore, it could be shown that by using the different methods and regarded RMSE metrics, a number of averages could be found for each investigated case for which the RMSE values did not afterwards significantly improve. Thus, the number of CS averages can generally be optimized for the given situation to minimize the computation time. To further minimize computation time, calculation of CS reconstructions can be performed parallel since every CS reconstruction is performed independently.

*Limitations of CS and CSA*

With high noise levels, the application of CS for measurement acceleration becomes challenging. Thus, acquiring a smaller amount of data with subsequent zero-filling could be used as an alternative strategy. In Figures 6.52a–d, a fully sampled, a zero-filled (af = 4), a CS reconstructed (af = 4), and a CS reconstructed image using the CSA-2 extension (af = 4, subaf = 2) are shown with a peak SNR = 5. Thereby, the zero-filled image (Figure 6.52b) provided a reduced background when compared to the fully sampled image (Figure 6.52a). This came at the cost of a blurred signal distribution. Though the CS reconstruction (Figure 6.52c) came without blurring, spike artifacts hampered the image quality. The CSA-2 method enhanced the image quality of the CS reconstruction by reducing the influence of the spike artifacts. This enabled easy identification of the signal structures (Figure 6.52d).

Figures 6.52a–d also show that CS reconstruction can fail in some pixels since the full k-space information is not available when the CSA-1 and CSA-2 method are applied on the undersampled data. Thus, the initial CS reconstruction will be inadequate when not enough or inappropriate points are sampled and a high noise level is present. For example,

the signal located next to the arrow in the reference and the zero-filled image (Figure 6.52a & b) is not present in the initial CS reconstruction (Figure 6.52c). Therefore, the signal cannot be recovered by the CSA-1 and CSA-2 methods (e.g., Figure 6.52d). However, those methods will still improve the image quality (Figure 6.52d) of the initial CS reconstruction (Figure 6.52c).

*Low frequency information*

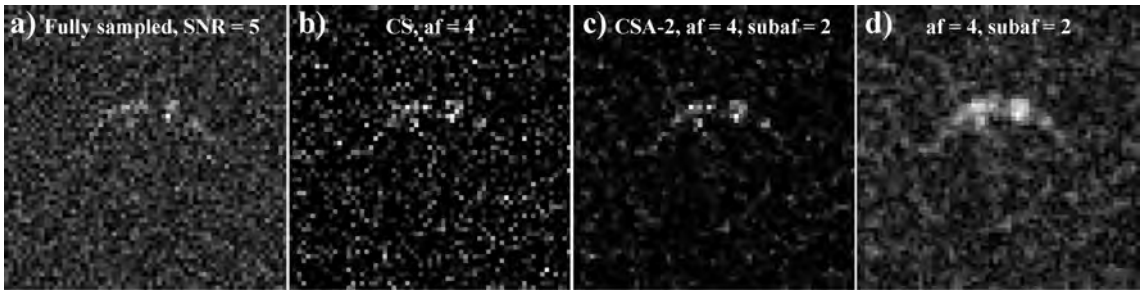


**Figure 6.53:** *Different aspects of the CSA reconstruction methods. a–c) Same data as shown in Figures 6.53a, c and d. d) Averaged image of (b) using the CSA-2 method. However, no CS reconstructions of the 49 averages were performed (af = 4, subaf = 2).*

The effect of CSA on the k-space signal distribution is shown in Figures 6.52e–h. In Figure 6.52g, the k-space of initial CS reconstruction (Figure 6.52c) is displayed. Even with high frequency components a significant signal strength is visible due to noise corruption. The signal strength is reduced, however, when compared against the fully sampled k-space (Figure 6.52e). In Figure 6.52h, the k-space of the averaged image in Figure 6.52d is shown. The signal strength is further reduced for high frequency components. Thus, the method contains features of a low pass filter because the density-weighted sampling patterns mainly contain low frequency information. However, not performing CS reconstructions on the 49 averages resulted in a blurred averaged image (Figure 6.53d). Thus, in addition to the features from the low pass filter, CS recovers additional information at unsampled high frequency k-space components in each single reconstruction. This resulted in improved reconstruction quality in the averaged image of 49 CS reconstructions (Figure 6.52d and Figure 6.53c).

*Other sampling strategies & denoising algorithms*

The investigated sampling patterns simulated CSI acquisition. Each k-space point could have thus been independently sampled. However, the proposed extensions of the CS algorithm can be easily translated to different sampling patterns. Please note that this adaption would be only mandatory for the CSA-2 method. For the CSA-1 method, modification is not necessary since it is directly applied to the initial CS reconstructed k-space.

Applying multiple reconstructions of fully sampled MRI data to generate a denoised averaged image was investigated in previous studies [141, 142]. However, instead of CS reconstructions using strict data consistency and only one sparsity constraint, a 2D **S**ingularity **F**unction **A**nalysis (SFA) model was used [141] and a CS algorithm with several regularization parameters [142].

Besides the proposed extension of the CS algorithm, several other denoising algorithms exist that could provide additional image quality improvement. This issue should be one topic of future studies.

### 6.3.6 Conclusion

The current subsection focused on enhancing the applicability of CS to noise corrupted $^{19}F$ data. It could be shown that the proposed extensions of an already existing CS algorithm were capable of improving the image quality of the CS reconstructions. Furthermore, these methods should be able to improve other noise corrupted, sparse datasets (e.g., gained through sparsity transform). Since the chosen algorithms are used solely in post processing no additional scan time is necessary.

## 6.4 Conclusion: Applicability of Compressed Sensing to $^{19}F$ MRI

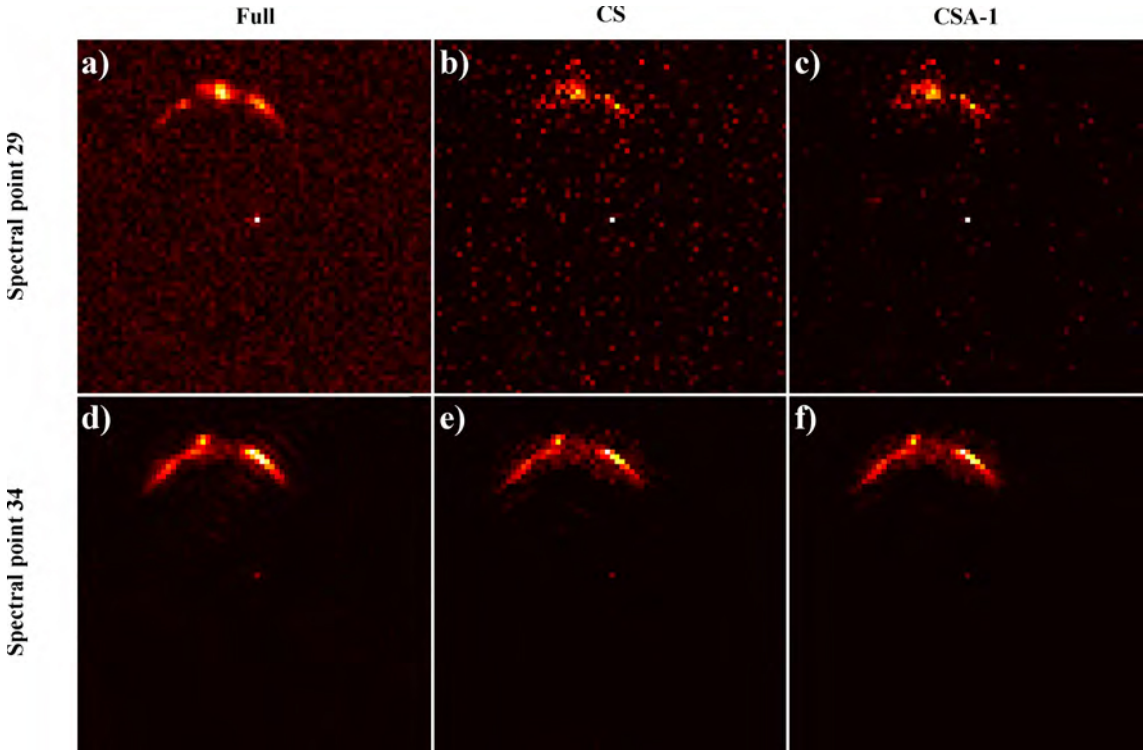


**Figure 6.54:** *Application of the CSA-1 algorithm on the CS-TSE-CSI data presented in Section 6.2, Figure 6.43. a–c) Low SNR data from spectral point 29 (peak SNR = 15.7); From left to right: fully sampled data (a), undersampled and CS reconstructed data (b) and undersampled and CS reconstructed data using the CSA-1 method with 20 iterations and additional sampling patterns corresponding to the CS-TSE-CSI original sampling pattern (c). d–f) High SNR data from spectral point 34 (peak SNR = 92.8); analog to (a–c). For better visualization, each image is scaled to its maximum. For all CS reconstructions af = 6 was chosen. The bright spot in the middle of the images is most likely a baseline artifact. Part of the figure was adapted from a figure of Reference [132].*

As shown in the last two sections (6.2 and 6.3), CS can be successfully applied to $^{19}F$ MR

data. Thus, it could be shown in Section 6.2 that TSE-CSI can be accelerated using CS. If, however, the available SNR is low, spike artifacts hamper the CS reconstruction. This has been previously shown [23, 24]. To reduce those spike artifacts, two CS-based post processing methodologies were proposed in Section 6.3.

The reduction of spike artifacts is the topic of Figure 6.54, where exemplary CSA-1 reconstructions of two spectral points in the CS-TSE-CSI data presented in Section 6.2 are shown. As described in Section 6.3, only a small effect can be observed for the high SNR data (cf. Figures 6.54d–f) when CSA is applied. However, even though the CSA-1 reconstruction cannot retrieve information lost through the initial CS reconstruction in low SNR data, less spike artifacts hampered the image quality of the CS reconstructed data when CSA-1 was applied (cf. Figure 6.54c).

In conclusion it could be shown that CS has the potential to be successfully applied to different $^{19}$F MR related issues.

# 7 Bloch-Siegert shift-based $B_1^+$ mapping

As discussed in Section 3.3.2 knowing the spatial distribution of the flip angle for *in vivo* quantification of the $^{19}$F signal is critical. The $B_1$ information is necessary for correct quantification, since the signal of an MR image is a function of the used flip angles [26]. Thus, an inhomogeneous $B_1$ profile can lead to wrong quantitative values [18]. Although this problem can be minimized using volume coils, inhomogeneous surface coils are often used to optimize the SNR of the $^{19}$F images [20, 47, 58, 143]. Therefore, a $B_1$ map should be acquired for correction purposes when quantitative $^{19}$F MRI is performed.

A new MRI method for acquiring $B_1^+$ maps was recently presented by Sacolick et al. [102]. The so-called BS method is based on the fact that an off-resonant pulse introduces a $B_1^+$-dependent phase shift to the transversal magnetization vector. Thus, $B_1^+$ information is encoded into the image phase using off-resonant pulses. Sacolick et al. showed that **BS**-based **FLASH** (BS-FLASH) and **BS**-based **S**pin-**E**cho sequences (BS-SE) allowed acquisition of quantitative $B_1^+$ data [102]. Furthermore, it was shown that the BS-shift also allows fast flip angle calibration if implemented in spectroscopic experiments [144, 145] or can be used for calculating $B_1^+$ maps in experiments using hyperpolarized $^{13}$C [146].

Importantly, its ability to be integrated into several standard MR sequences without losing the magnitude signal information is a special feature of the BS technique. Thus, BS-based $B_1^+$ mapping might improve quantification when implemented in a sensitive $^{19}$F MRI sequence. Alternatively, when the same channel is used for $^1$H and $^{19}$F MRI, $^{19}$F $B_1^+$ information could be indirectly acquired through fast $^1$H BS-$B_1^+$ mapping methods [147].

The present chapter is divided into three sections. Section 7.1 provides the basic physical principles and equations underlying the BS technique. Furthermore, it briefly reviews the initially introduced BS techniques [102]. The second section introduces a novel CPMG-based TSE $B_1^+$ mapping MRI sequence. The final section of this chapter discusses in more detail the possible application of the presented BS methods to quantitative $^{19}$F MRI.

## 7.1 Introduction to Bloch-Siegert-based MRI

This section gives a basic introduction to BS-based $B_1^+$ mapping and thereby follows [102, 148]. A more detailed theoretical description of the physical principles underlying the BS effect can be found in [102, 149, 150].

### 7.1.1 Theory

The phenomenon of the Bloch-Siegert shift was already described several decades ago [149, 150]. Briefly, the term Bloch-Siegert shift describes a shift of the on-resonant magnetization when a pulse is applied off-resonant [102, 149, 150]. According to [102] applying an off-resonant pulse causes the frequency of the on-resonant spins to shift away from the off-resonant frequency.

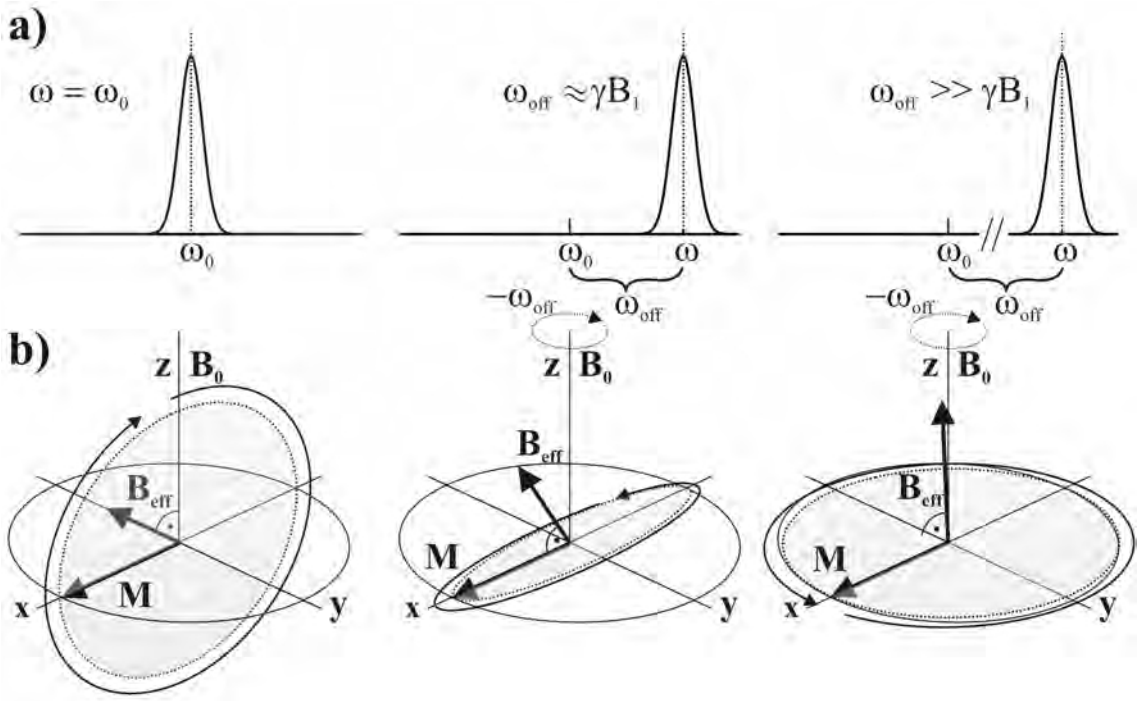


**Figure 7.55:** *Simplified sketches illustrating the effect of RF pulses applied at different frequencies relative to the magnetization vector precession frequency. a) Schemes indicating the application of a RF pulse at different frequencies. b) Corresponding sketches to (a), illustrating the effect of the different RF pulses on the magnetization vector. Thereby,* **M** *indicates the magnetization vector before the RF pulse application. The rotating frame frequency is the laboratory frequency of the RF pulse, thus* $\mathbf{B}_{eff}$ *is always a static vector. In the lower middle and right sketches, M is rotating with -*$\omega_{off}$ *before the RF pulse is applied, while M is a static vector in the lower left sketch. Please note that only a single temporal point is regarded to indicate the different rotation planes of the magnetization vector perpendicular to* $\mathbf{B}_{eff}$*. Further explanations are provided in the text.*

Equation 2.13 from Section 2.3 can be used to illustrate the effect of the off-resonant RF pulse on the magnetization vector:

$$\frac{d\mathbf{M}}{dt} = \gamma \mathbf{M} \times \mathbf{B}_{eff} \tag{7.1}$$

In the case of an off-resonant RF pulse $\omega_0 \neq \omega$ and thus the z-component of $\mathbf{B}_{eff}$ does not vanish:

$$\begin{aligned} \mathbf{B}_{eff} &= \frac{1}{\gamma}\left[(\omega_0 - \omega)\,\mathbf{e}_z + \omega_1 \mathbf{e}_x\right] \\ \Rightarrow\ \mathbf{B}_{eff} &= \frac{1}{\gamma}\left(\omega_{off}\mathbf{e}_z + \omega_1 \mathbf{e}_x\right) \end{aligned} \tag{7.2}$$

with $\omega_{off} = \omega_0 - \omega$.

This situation is the topic of Figure 7.55. In contrast to the application of an on-resonant RF pulse (cf. Figure 7.55, left), $\mathbf{B}_{eff}$ is a vector in the y-z plane (rotating frame frequency = laboratory frequency of the RF pulse). If magnetization precesses in the transversal plane before application of the off-resonant RF pulse, the magnetization vector is tilted out of the transversal plane. Thus it rotates in a plane perpendicular to $\mathbf{B}_{eff}$ (cf. Figure 7.55, middle). If, however, $\omega_{off} \gg \gamma B_1$, $\mathbf{B}_{eff}$ aligns with $\mathbf{B}_0$ and the transversal magnetization vector stays approximately in the transversal plane. However, the precession frequency of the magnetization vector shifts by a small amount of $\omega_{BS}$.

The magnitude of this effect is dependent on the magnitude of the RF-pulse $B_1(t)$, its duration ($t_{BS}$), and the $\omega_{off}$.

Under the assumption that:

$$\begin{aligned} &Assumption_I: \\ &\omega_{off} \gg \gamma B_1 \end{aligned} \tag{7.3}$$

the following equation describes the Bloch-Siegert shift [102, 148]:

$$\phi_{BS} = \int_0^{t_{BS}} \frac{(\gamma B_1(t))^2}{2(\omega_{off} + \omega_{B_0})} dt \tag{7.4}$$

with $\omega_{B_0}$ being the local off-resonance frequency due to spatial magnetic field inhomogeneities ($\omega_{B_0} = \omega_0 - \omega$). The derivation of this equation is given in more detail in References [102, 150] and Appendix D.1 on page 132.

Furthermore, if:

$$\begin{aligned} &Assumption_{II}: \\ &\omega_{off} \gg \omega_{B_0} \end{aligned} \tag{7.5}$$

Equation 7.4 can be simplified using a first order Taylor expansion in $\omega_{B_0}$ [102, 148]:

$$\phi_{BS} \approx \int_0^{t_{BS}} \frac{(\gamma B_1(t))^2}{2\omega_{off}} dt - \int_0^{t_{BS}} \frac{(\gamma B_1(t))^2 \omega_{B_0}}{2\omega_{off}^2} dt + O(\omega_{B_0}^2) \tag{7.6}$$

Using Equation 7.6, the BS-dependent phase evolution for multiple BS-based $B_1^+$ sequences is analytically described in the following subsections. For better readability, two terms are defined [148]:

$$A = \int_0^{t_{BS}} \frac{(\gamma B_1(t))^2}{2\omega_{off}} dt \tag{7.7}$$

and:

$$B = \int_0^{t_{BS}} \frac{(\gamma B_1(t))^2 \omega_{B_0}}{2\omega_{off}^2} dt \tag{7.8}$$

Thus, Equation 7.6 can be rewritten when the higher order $B_0$ terms are neglected:

$$\phi_{BS} \approx A - B \tag{7.9}$$

Thus, A is the $\omega_{B_0}$ independent term and B the $\omega_{B_0}$ dependent term. Since term B includes $\omega_{B_0}$, it is of interest to cancel this term in $B_1$ mapping experiments. Independent acquisition of additional information would otherwise be necessary to correct for this term [151]. The following subsections discuss how different BS-based sequences are performed to enable $B_1^+$ mapping without the influence of term B.

### 7.1.2 BS-FLASH

As mentioned in the introduction, BS-FLASH was introduced in 2010 by Sacolick et al. [102] for fast $B_1^+$ mapping. The following briefly reviews this sequence.

#### BS-phase evolution

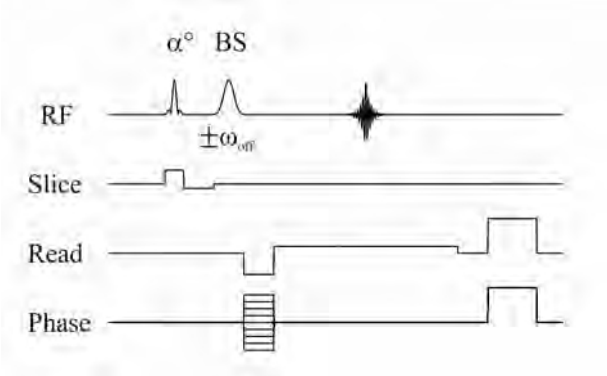


**Figure 7.56:** *BS-FLASH sequence similar to the one proposed by Sacolick et al. [102].*

A BS-sequence similar to the one proposed by Sacolick et al. [102] is shown in Figure 7.56. Using Eqs. 7.6-7.9, the phase evolution introduced by the BS-pulse applied at $+\omega_{off}$ in a BS-FLASH experiment can be written as follows:

$$\begin{aligned} &P_\alpha : \phi_{BS} = 0 \\ &P_{BS_{+\omega_{off}}} : \phi_{BS} \approx +A - B \\ &\Rightarrow \phi_{BS} \approx +A - B \end{aligned} \tag{7.10}$$

with $P_\alpha$ referring to the time after the excitation pulse and $P_{BS_{(\pm)\omega_{off}}}$ to the time after the BS-pulse. When the experiment is repeated with the same parameters and the BS-pulse is applied at -$\omega_{off}$, the BS-phase development is given by:

$$\begin{aligned} &P_\alpha : \phi_{BS} = 0 \\ &P_{BS_{-\omega_{off}}} : \phi_{BS} \approx -A - B \\ &\Rightarrow \phi_{BS} \approx -A - B \end{aligned} \tag{7.11}$$

According to Eqs. 7.10 and 7.11, the $\omega_{B_0}$ dependent term B is not annihilated in either of the two experiments. The $\omega_{B_0}$ dependent term B [102] and other scanner related phase terms, that are the same in both experiments disappear when the difference of the phase is taken [144]. The result is:

$$\Delta\phi_{BS} \approx +A - B - (-A - B) = 2A \tag{7.12}$$

Using this information, a $B_1^+$ map can be calculated [102]. A practical formula to evaluate the $B_1^+$ from the BS-phase shift for arbitrary BS-pulse shapes is provided in Section 7.2.3.

**Properties**

Although BS-FLASH sequences and other gradient-echo-based sequences [146] provide fast $B_1^+$ mapping techniques with low **S**pecific **A**bsorption **R**ates (SAR), the application of gradient-echo-based BS-$B_1^+$ mapping is limited at high field strengths. Since Assumption$_{I\&II}$ (Eqs. 7.3 and 7.5) must be fulfilled, BS-pulses are often in the order of some milliseconds [102, 103, 152] to generate a sufficient BS-phase shift (cf. Equation 7.7). The prolonged TE due to the application of the BS-pulses is critical in BS-FLASH sequences since susceptibility artifacts are enhanced (cf. Section 4.3.1). Unfortunately, this effect increases with increasing field strength.

### 7.1.3 BS-SE

In addition to BS-FLASH, BS-SE was introduced in 2010 by Sacolick et al. [102] for $B_1^+$ mapping. The following briefly reviews this sequence.

### BS-phase evolution

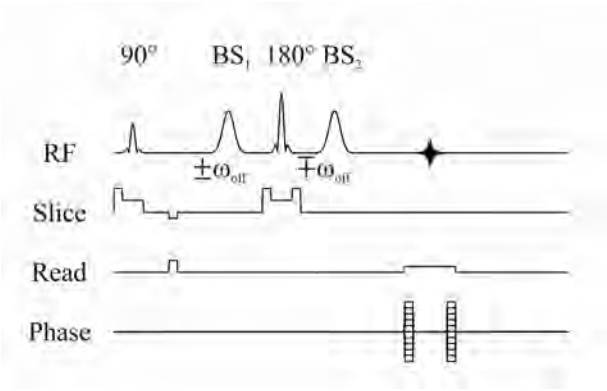


**Figure 7.57:** *BS-SE sequence similar to the one proposed by Sacolick et al. [102].*

In Figure 7.57, a BS-SE sequence similar to the one introduced in [102] is shown. In BS-SE sequences, two off-resonant BS-pulses can be applied. The first BS-pulse is applied before the refocusing pulse and the second BS-pulse after the refocusing pulse. Importantly, the sign of $\omega_{off}$ is changed. Using the same nomenclature introduced in Section 7.1.1 and Section 7.1.2, the effect of this BS-pulse scheme on the BS-phase evolution is described as follows [148]:

$$\begin{aligned} &P_{90^\circ} : \phi_{BS} = 0 \\ &P_{BS_{+\omega_{off}}} : \phi_{BS} \approx +A - B \\ &P_{180^\circ} : \phi_{BS} \approx -(+A - B) = -A + B \\ &P_{BS_{-\omega_{off}}} : \phi_{BS} \approx -A + B + (-A - B) \\ &\Rightarrow \phi_{BS} \approx -2A \end{aligned} \tag{7.13}$$

with $P_{90^\circ}$ referring to the time after the excitation pulse and $P_{180^\circ}$ to the time after the refocusing pulse. Two effects can be observed: a) The application of the second BS-pulse with inverted $\omega_{off}$ sign doubles the $\omega_{B_0}$ independent term A and b) the $\omega_{B_0}$ dependent term B is annihilated. Thus, contrary to the BS-FLASH experiment, $B_1^+$ mapping could theoretically be performed in only one experiment when no scanner dependent phase terms are present [148]. Scanner dependent phase terms, however, are normally present in MRI images (e.g., phase effects from eddy currents [144]). To cancel those effects a second experiment normally is performed with the same parameters and inverted signs of the corresponding BS-pulses [144]. Thus the following BS-phase evolution is given [148]:

$$\begin{aligned} &P_{90^\circ} : \phi_{BS} = 0 \\ &P_{BS_{-\omega_{off}}} : \phi_{BS} \approx -A - B \\ &P_{180^\circ} : \phi_{BS} \approx -(-A - B) = +A + B \\ &P_{BS_{+\omega_{off}}} : \phi_{BS} \approx +A + B + (+A - B) \\ &\Rightarrow \phi_{BS} \approx +2A \end{aligned} \tag{7.14}$$

Thus, the difference of both experiments results in:

$$\Delta\phi_{BS} \approx -2A - (+2A) = -4A \tag{7.15}$$

which is double the phase difference of a BS-FLASH experiment using the same BS-parameters. Please note that instead of performing a second BS-SE experiment, a second spin-echo experiment with the same parameters but without BS-pulses could also be performed to obtain the scanner dependent phase. This approach would minimize the total SAR at the cost of a reduced BS-phase shift [151].

#### Properties

As mentioned in Section 7.1.2, gradient-echo-based BS-sequences might not be applicable at high field strengths due to strong susceptibility artifacts. The BS-SE sequence minimizes the susceptibility artifacts at even high field strengths. Unfortunately, due to the refocusing pulses combined with the BS-pulses, the SAR is higher than sequences using low flip angles. Thus, fast standard BS-SE sequences cannot be easily applied using high field strength human scanners. An alternative spin-echo-based BS-sequence coming along with low SAR values was recently presented [152]. The same BS-considerations described above for the standard BS-SE sequence apply also to this method.

## 7.2 BS-CPMG-TSE

A CPMG-based TSE BS $B_1^+$ mapping technique is presented in the following section. It focuses on a fast acquisition of the information necessary for $B_1^+$ mapping. This section follows References [103, 153].

### 7.2.1 Introduction

In the present section, the idea of using the BS-shift for $B_1^+$ mapping is applied to TSE-based MRI. To avoid image artifacts inherent to TSE sequences, the same phase must be present before every refocusing pulse. This scenario is referred to as CPMG-based conditions [7, 100, 101]. Alternatives for avoiding image artifacts introduced by uncorrelated echoes either crush the unwanted echo pathways [154] or separate the pathways by adding an unbalanced read gradient [155, 156]. Unlike CPMG TSE imaging, however, these solutions would lead to a signal loss.

Using the proposed **BS**-based **CPMG-TSE** (BS-CPMG-TSE) method, 2D phantom and 3D *in vivo* $B_1^+$ maps were obtained. Furthermore, the high SAR inherent to BS-CPMG-TSE sequences with several refocusing and off-resonant pulses was further investigated.

### 7.2.2 BS-phase evolution

In contrast to the BS-SE sequence shown in Figure 7.58a, the proposed BS-CPMG-TSE sequence displayed in Figure 7.58b uses different BS-pulses in the refocusing train. Thus, these BS-pulses are given with the same off-resonance as the first BS-pulse but increased to $\sqrt{2}$ times the magnitude of the initial BS-pulse. When the BS-pulses are applied with

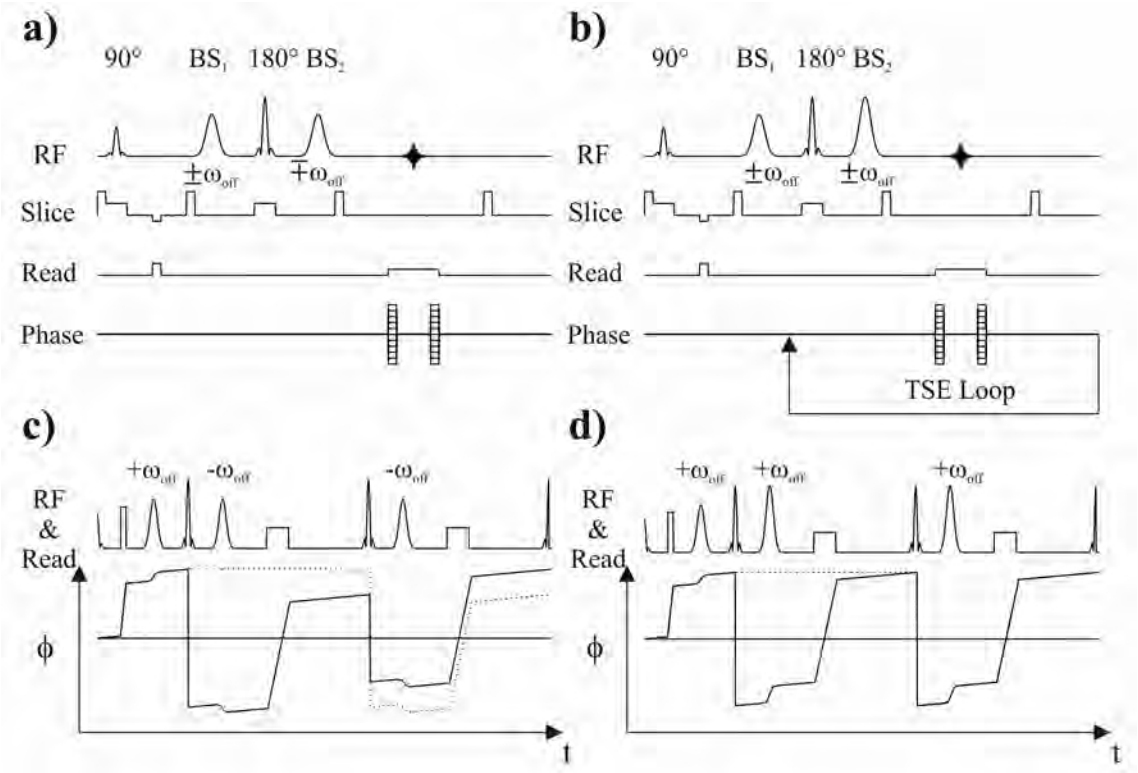


**Figure 7.58:** *Sequence diagrams and simplified phase graphs [157] of the BS-SE and BS-CPMG-TSE sequences. a) BS-SE sequence and b) BS-CPMG-TSE sequence. To fulfill CPMG conditions using the BS-CPMG-TSE sequence, in contrast to (a), the second and subsequent off-resonant pulses are applied with the same $\omega_{off}$ and a magnitude of $\sqrt{2}$ times the magnitude of the initial BS-pulse. c) Simplified phase diagram of the BS-SE sequence (assuming a second echo) and (d) Simplified phase diagram of the BS-CPMG-TSE sequences run with two echoes. The BS-phase evolution of an off-resonant spin including the effects of the read gradient are shown. The solid line represents the primary echo pathway and the dashed line represents one exemplary stimulated echo pathway. All units are arbitrary. In the RF & Read lines of (c) and (d), angular shaped objects represent the read gradients and round shaped objects the pulses. Figure adapted from Reference [103].*

$+\omega_{off}$, the following relations for the BS-phase development are given (cf. Equations 7.7 and 7.8 for the definition of terms A and B) [148]:

$$\begin{aligned} &P_{90^\circ} : \phi_{BS} = 0 \\ &P_{BS_{+\omega_{off}}} : \phi_{BS} \approx +A - B \\ &P_{180^\circ} : \phi_{BS} \approx -(+A - B) = -A + B \\ &P_{BS_{+\omega_{off}}} : \phi_{BS} \approx -A + B + (+2A - 2B) \\ &\Rightarrow \phi_{BS} \approx +A - B \end{aligned} \tag{7.16}$$

Equation 7.16 and Figure 7.58d show that when using these BS-parameters, the same phase is theoretically present before each refocusing pulse. Thus, the CPMG conditions are preserved (cf. Section 4.3.3). When, however, the BS-SE parameters are used, the CPMG conditions are broken (cf. Equation 7.13, Equation 7.14 and Figure 7.58c). Since all BS-pulses are applied with the same parameters in the refocusing train, the same BS-phase is present in all echoes.

When the BS-pulses are applied with -$\omega_{off}$, the $\phi_{BS}$ at readout is $\approx -A-B$. Thus, $\Delta\phi_{BS}$ results in:

$$\Delta\phi_{BS} \approx +A - B - (-A - B) = +2A \tag{7.17}$$

which is theoretically the same value as for the BS-FLASH experiments when the same BS-parameters are chosen (cf. Equation 7.12).

Regarding the BS-CPMG-TSE experiments, it is important to note that the BS-pulse applied in the refocusing pulse train can also be placed after the readout. A more detailed consideration of the impacts of this issue on the SAR is provided in the Material & Methods section under the point SAR considerations.

### 7.2.3 Material & Methods

$B_1^+$ mapping BS-sequences shown in Figure 7.57 and Figure 7.58 were implemented on a 7 T small animal scanner (Bruker Bio-Spin GmbH, Rheinstetten, Germany). *Ex vivo* phantom and *in vivo* animal experiments were performed to evaluate the robustness of these methods. All experiments were performed at room temperature using a home-built quadrature eight leg birdcage coil with an inner diameter of 35 mm.

#### Phantom experiments

Initial phantom experiments were performed to investigate different aspects of the BS-sequences.

*Hardware and phantoms*

Two different phantoms were used. One phantom ($P_a$) consisted of four different compartments. To create a range of different $T_1$ and $T_2$ relaxation times, different amounts of

**G**ado**F**luorine **M** (GFM) (Bayer Schering Pharma AG, Berlin, Germany) were dissolved in tap water. Afterwards, the same concentration of hydroxyethyl cellulose (Sigma-Aldrich Chemie GmbH, Steinheim, Germany) (3 g/100 ml) was added to the different GFM/water concentrates. A 50 ml tube (Greiner Bio-One GmbH, Frickenhausen, Germany) served as an outer compartment (0 mmol/L GFM). One glass NMR tube with a diameter of 10 mm (0.06 mmol/L GFM) and two glass NMR tubes with a diameter of 5 mm (0.17 mmol/L GFM) were placed inside the 50 ml tube. For quantitative evaluation on the performed experiments with $P_a$, one of the 5 mm tubes was chosen for evaluation. The other phantom ($P_b$) consisted of 1.5 g hydroxyethyl cellulose (Sigma-Aldrich Chemie GmbH, Steinheim, Germany) dissolved in 50 ml distilled water in a 50 ml tube (Greiner Bio-One GmbH, Frickenhausen, Germany).

*MR sequence parameters*

In all 2D phantom experiments, a single slice of the object was imaged with a FOV of 30 mm × 30 mm and a ST of 2 mm. Furthermore, all experiments were performed without averaging and were preceded by two dummy scans. All other sequence parameters are provided in the tables indicated in the following subsections.

*BS-pulse parameters*

All BS-experiments contained Gaussian-shaped off-resonant pulses. Initially, the unspoiled BS-SE sequence (BS-SE$_{unspoiled}$) presented in Figure 7.57 and the spoiled BS-SE sequence (BS-SE$_{spoiled}$) presented in Figure 7.58a were compared using the following BS-parameters: $t_{BS}$ = 1 ms and $\omega_{off}/2\pi$ = ±2, ±4, ±8 and ±16 kHz. For all other experiments, only the sequences presented in Figure 7.58 were used. To enable calculation of the $B_1^+$ maps, two measurements with the same $t_{BS}$ = 1 ms and $\omega_{off}/2\pi$ = ±16 kHz were always acquired. When BS-SE experiments were performed, the second BS-pulse always had an $\omega_{off}$ opposite to the initial BS-pulse. To compare BS-SE experiments with BS-CPMG experiments the same value was set for the BS-pulse magnitude of the first BS-pulse in both sequences.

*$P_a$: BS-SE$_{unspoiled}$ vs. BS-SE$_{spoiled}$*

As mentioned, initial experiments were performed to qualitatively compare the BS-SE sequences presented in Figure 7.57 (BS-SE$_{unspoiled}$) and Figure 7.58a (BS-SE$_{spoiled}$) in regard to their sensibility towards artifacts due to the interaction of the off-resonant BS-pulses with the on-resonant magnetization. For comparison, the different BS-SE sequences were acquired with the same BS-parameters and sequence parameters (cf. Table 7.6). In the following, BS-SE$_{unspoiled}$ and BS-SE$_{spoiled}$ will only be mentioned when those sequence setups are compared. The used BS-SE acronym thus always refers in the following to the BS-SE$_{spoiled}$ sequence.

*$P_b$: BS-SE vs. BS-CPMG-TSE*

To compare the BS-SE and BS-CPMG-TSE sequences, seven BS-SE and BS-CPMG-TSE experiments were performed at different BS-pulse strengths. The latter were linearly en-

**Table 7.6:** *Sequence parameters for the comparison of the BS-SE$_{unspoiled}$ and BS-SE$_{spoiled}$ experiments. Fig indicates the figure in which the experiment results are presented and P the phantom used for the experiments.*

| *Sequence* | *Fig* | *P* | *MTX* | *TE (ms)* | *TR (ms)* |
|---|---|---|---|---|---|
| BS-SE$_{unspoiled}$ | 7.59a | a | 128 × 128 | 16 | 250 |
| BS-SE$_{spoiled}$ | 7.59b | a | 128 × 128 | 16 | 250 |

coded and the TF was set to eight. To evaluate the robustness of these methods, each experiment was also performed five times. All sequence parameters are listed in Table 7.7.

**Table 7.7:** *Sequence parameters for the BS-SE and BS-CPMG-TSE experiments performed using phantom $P_b$. Fig indicates the figure in which the experiment results are presented and P the phantom used for the experiments. Table adapted from Reference [103].*

| *Sequence* | *Fig* | *P* | *MTX* | *TE (ms)* | *TR (ms)* | *TF* |
|---|---|---|---|---|---|---|
| BS-SE | 7.60a | b | 128 × 128 | 10 | 500 | N/A |
| BS-CPMG-TSE | 7.60a | b | 128 × 128 | 40 | 1000 | 8 |

Applying the highest BS-pulse magnitude, additional 2D BS-CPMG-TSE experiments were performed using both linear and centric encoding. For comparison, 2D BS-SE experiments were performed. All sequence parameters are listed in Table 7.8.

**Table 7.8:** *Sequence parameters for the BS-SE and BS-CPMG-TSE experiments performed using phantom $P_b$. Fig indicates the figure in which the experiment results are presented and P the phantom used for the experiments. The first entries in the Fig and TE columns stand for the BS-CPMG-TSE experiments with linear encoding and the second entries for those with centric encoding. Table adapted from Reference [103].*

| *Sequence* | *Fig* | *P* | *MTX* | *TE (ms)* | *TR (ms)* | *TF* |
|---|---|---|---|---|---|---|
| BS-SE | 7.60c | b | 128 × 128 | 10 | 125 | N/A |
| BS-SE | 7.60c | b | 128 × 128 | 10 | 1000 | N/A |
| BS-CPMG-TSE | 7.60b/d | b | 128 × 128 | 10/10 | 1000 | 1 |
| BS-CPMG-TSE | 7.60b/d | b | 128 × 128 | 10/10 | 1000 | 2 |
| BS-CPMG-TSE | 7.60b/d | b | 128 × 128 | 20/10 | 1000 | 4 |
| BS-CPMG-TSE | 7.60b/d | b | 128 × 128 | 40/10 | 1000 | 8 |
| BS-CPMG-TSE | 7.60b/d | b | 128 × 128 | 80/10 | 1000 | 16 |
| BS-CPMG-TSE | 7.60b/d | b | 128 × 128 | 160/10 | 1000 | 32 |

*$P_a$: BS-SE vs. BS-CPMG-TSE*

Additional experiments were performed to further compare the BS-SE and BS-CPMG-TSE sequences in regard to the achieved SNR, the obtained $B_1^+$ map quality and the SAR inherent to the sequences. Thus, BS-SE and BS-CPMG-TSE experiments with linear encoding were performed using multiple TRs and TFs. All relevant sequence parameters are provided in Table 7.9. To obtain a range of different SNR values in one image, phantom $P_a$ was imaged. All experiments were performed five times. Calculation of the different parameters is given in the section on post processing.

To evaluate the $T_1$ and $T_2$ relaxation time constants, **I**nversion **R**ecovery **S**napshot **FLASH** (IRSF) [158] (MTX: 64 × 64; inversion time: 47 ms; number of segments: 100; flip angle: 5°; TE/TR = 0.8/2.5 ms; TR$_{total}$ = 23 s) and MSE experiments (MTX: 64 × 64; number of echoes: 20; TE/TR = 40/2000 ms) were performed using the same geometry as the BS-experiments.

**Table 7.9:** *Sequence parameters for the BS-SE and linear encoded BS-CPMG-TSE experiments performed using phantom $P_a$. Fig indicates the figure in which the experiment results are presented and P the phantom used for the experiments. Table adapted from Reference [103].*

| *Sequence* | *Fig* | *P* | *MTX* | *TE (ms)* | *TR (ms)* | *TF* |
|---|---|---|---|---|---|---|
| BS-SE | 7.61/7.62 | a | 128 × 128 | 10 | 1000 | N/A |
| BS-SE | 7.61/7.62 | a | 128 × 128 | 10 | 500 | N/A |
| BS-SE | 7.61/7.62 | a | 128 × 128 | 10 | 250 | N/A |
| BS-SE | 7.61/7.62 | a | 128 × 128 | 10 | 125 | N/A |
| BS-SE | 7.61/7.62 | a | 128 × 128 | 10 | 62.5 | N/A |
| BS-CPMG-TSE | 7.61/7.62 | a | 128 × 128 | 10/10/20/40/80/160 | 1000 | 1/2/4/8/16/32 |
| BS-CPMG-TSE | 7.61/7.62 | a | 128 × 128 | 10/10/20/40/80 | 500 | 1/2/4/8/16 |
| BS-CPMG-TSE | 7.61/7.62 | a | 128 × 128 | 10/10/20/40 | 250 | 1/2/4/8 |
| BS-CPMG-TSE | 7.61/7.62 | a | 128 × 128 | 10/10/20 | 125 | 1/2/4 |
| BS-CPMG-TSE | 7.61/7.62 | a | 128 × 128 | 10/10 | 62.5 | 1/2 |

### *In vivo* experiments

For *in vivo* scanning, one mouse was anesthetized with 1.5% isoflurane in a 2 L/min oxygen atmosphere. The mouse was placed inside the same coil used for the phantom experiments.

3D BS-SE, and 3D BS-CPMG-TSE experiments were performed. The same BS-parameters were chosen as those used for the phantom experiments. Additionally, scans without phase encoding were performed to correct imperfect scaling of the BS-pulse magnitude. These scans included one scan with BS-pulses turned off; two scans ($\omega_{off}/2\pi$= +16 kHz and -16 kHz) containing one BS-pulse before the refocusing pulse pulse; and two scans ($\omega_{off}/2\pi$ = +16 kHz and -16 kHz) with an additional BS-pulse at $\sqrt{2}$ the magnitude of the first pulse (scanner setting) after the refocusing pulse (cf. Figure 7.63a).

These nonphase encoded scans were performed with otherwise the same parameters as the $B_1^+$ mapping experiments provided in Table 7.10. BS-CPMG-TSE experiments were performed with and without correction. A more detailed description of the correction procedure is given in the Section, Prospective BS-magnitude correction.

**Table 7.10:** *Sequence parameters for the* in vivo *experiments. Fig indicates the figure in which the experiment results are presented. The upper BS-CPMG-TSE row gives the parameters of the linear encoding experiments and the lower row those of the experiments with centric encoding. Table adapted from Reference [103].*

| *Sequence* | *Fig* | *FOV (mm)* | *MTX* | *TE (ms)* | *TR (ms)* | *TF* |
|---|---|---|---|---|---|---|
| BS-SE | 7.64 | 15 × 30 × 60 | 15 × 64 × 128 | 10 | 62.5/125 | N/A |
| BS-CPMG-TSE | 7.64 | 15 × 30 × 60 | 15 × 64 × 128 | 40/80/160 | 1000 | 8/16/32 |
| BS-CPMG-TSE | 7.64 | 15 × 30 × 60 | 15 × 64 × 128 | 10/10/10 | 1000 | 8/16/32 |

### Post Processing

All post processing was done in MATLAB®. $T_1$ maps were calculated pixel-wise from the IRSF experiments following [158]:

$$S(t) = C - De^{-\frac{t}{T_1^*}} \quad , \quad T_1 = T_1^* \left( \frac{D}{C} - 1 \right) \tag{7.18}$$

Thereby $C$, $D$, and $T_1^*$ were the fitting parameters of the nonlinear least square fit from which $T_1$ was calculated and $S$ was the measured signal.

$T_2$ maps were calculated for each pixel from the 2D MSE experiments using the following fit function:

$$S(t) = Ee^{-\frac{t}{T_2}} \tag{7.19}$$

with $E$ and $T_2$ being the fit parameters.

$B_1^+$ maps were calculated using the equation described in [102]. Equations 7.20-7.22 describe the conversion of the BS-phase shift difference $\Delta\phi_{BS}$ into the magnitude of a hard pulse $B_{1_{hp}}$ with the length $t_{BS}$, which serves as a reference pulse for $B_1^+$ mapping. The difference $\Delta\phi_{BS}$ was calculated from two BS-experiments with opposite $\omega_{off}$, introduced by a shaped pulse with the duration $t_{BS}$. This conversion enables comparison of different shaped pulses.

$$\Delta\phi_{BS} = \int_0^{t_{BS}} \frac{\left(\gamma B_1(t)\right)^2}{\omega_{off}} dt \quad \Rightarrow \quad B_{1_{hp}} = \sqrt{\Delta\phi_{BS} K} \tag{7.20}$$

$$K = \frac{\omega_{off}}{t_{BS}\gamma^2 K_{BSpulse}} \tag{7.21}$$

$$K_{BSpulse} = \frac{1}{N}\sum_{n=1}^{N}\left(B_{1normalized}(n)\right)^2 \tag{7.22}$$

with $\gamma$ being the relevant gyromagnetic ratio and $K = 4682.3$ ($\mu$T$^2$/radians) the pulse-specific constant in regard to a hard pulse. $K_{BSpulse} = 0.30$ was the norm factor for the chosen normalized Gaussian pulse ($B_{1normalized}$) and N refers to the number of shaped pulse elements.

When necessary, phase data were unwrapped using an algorithm described by Jenkinson [159].

For the phantom experiments, different quantitative parameters were estimated using phantom $P_a$ to allow a comparison between BS-SE and BS-CPMG-TSE experiments.

SNR calculation was performed as follows:

$$SNR = \frac{S_m}{\sigma} \tag{7.23}$$

with $S_m$ being the measured image pixel intensity and $\sigma$ the standard deviation of the noise.

To obtain a quality measure of the $B_1$ maps, the average standard deviation of the $B_1$ value ($\delta B_1$) was obtained pixel-wise from the five independent experiments.

$$\delta B_1 = \sqrt{\frac{1}{I-1}\sum_{i=1}^{I}(B_{1i} - \bar{B_1})^2} \tag{7.24}$$

Thereby, $I$ is the number of performed experiments; $i$ is the experiment index; $B_{1i}$ is the $B_1$ value of the $i$-th experiment of one specific pixel and $\bar{B_1}$ the mean $B_1$ value of this pixel.

### SAR considerations

The relative SAR of the sequences was estimated following [160–163]:

$$SAR \propto \frac{1}{TR} \sum_{j=1}^{J} \frac{\alpha_j^2}{P_{durj}} K_{Pj} \tag{7.25}$$

with $J$ being the number of pulses applied in one TR cycle; $j$ the pulse index; $\alpha_j$ the flip angle of pulse $j$; $P_{durj}$ the duration of pulse $j$; and $K_{Pj}$ the pulse shape-specific constant of pulse $j$. For SAR estimation, Hermitian-shaped excitation and refocusing pulses ($K_{Pj}$ = 5.40) and Gaussian-shaped BS-pulses ($K_{Pj}$ = 1.71) were used as provided by the scanner. Please note that the estimation of the SAR values is specific to the pulses used in this work.

Furthermore, the relative SAR was estimated for SAR-optimized BS-CPMG-TSE sequences. A SAR-optimized sequence is one in which the BS-pulses in the refocusing train are applied after the readout. Consequently, the last BS-pulse can be omitted. Thus, even if every other parameter matches that of the used BS-CPMG-TSE sequence, the calculated SAR would still be reduced. Using the SAR-optimized sequences would give a BS-phase sign opposite to that of the used BS-CPMG-TSE sequences. The SAR-optimized sequences, however, were not applied in this work since no SAR restrictions applied.

### Prospective BS-magnitude correction

In this work, phantom experiments (Figure 7.60) revealed that the CPMG conditions in BS-experiments were sometimes slightly violated. Reference experiments without BS-pulses showed that this problem was caused by the BS-pulses. Therefore, a magnitude correction of the BS-pulses in the refocusing train was performed for *in vivo* BS-CPMG experiments. As previously mentioned, two nonphase encoded scans were acquired by implementing one BS-pulse before the refocusing pulse. One scan was performed with positive $\omega_{off}$ and one with negative $\omega_{off}$ (Figure 7.63a). According to Equation 7.20, the following difference between the BS-phase $\Delta\phi_{BS1}$ of both scans is given as:

$$\Delta\phi_{BS1} = \frac{(B_{1_{hp}})^2}{K} \tag{7.26}$$

To enable BS-pulse correction two additional nonphase encoded experiments were performed. During these measurements, an additional BS-pulse was applied after the refocusing pulse. The additional BS-pulse had the same $\omega_{off}$ as the initial BS-pulse but with n = $\sqrt{2}$ more magnitude according to the scanner input (Figure 7.63). However, if, for example the hardware is not perfectly calibrated or other errors occur, the BS-pulses in the echo train will not produce the expected phase. Thus, the actual magnitude scaling (n') can differ from set n. Again, these experiments were run with $\pm\omega_{off}$. The following equation describes the measured phase difference of these two scans $\Delta\phi_{BS2}$:

$$\Delta\phi_{BS2} = \frac{(n' B_{1_{hp}})^2}{K} - \frac{(B_{1_{hp}})^2}{K} \tag{7.27}$$

If Equation 7.26 is inserted in 7.27, the factor n' can be calculated:

$$n' = \sqrt{\frac{\Delta\phi_{BS2} + \Delta\phi_{BS1}}{\Delta\phi_{BS1}}} \tag{7.28}$$

Thus, the correction factor ($BS_{Corr}$), by which the magnitude of the BS-pulses in the refocusing train must be corrected can be calculated:

$$BS_{Corr} = \frac{n}{n'} = n\sqrt{\frac{\Delta\phi_{BS1}}{\Delta\phi_{BS2} + \Delta\phi_{BS1}}} \tag{7.29}$$

An additional experiment with the BS-pulses turned off was performed before *in vivo* experiments to determine the scanner-dependent phase. The obtained scanner-dependent phase thus provided the BS-independent experiment reference phase, by which phase wraps in the nonphase encoded BS-data could be detected and corrected.

The results from phantom experiments using the described correction scheme are given in Appendix D.2 on page 133.

### 7.2.4 Results

#### Phantom experiments

*$P_a$: BS-$SE_{unspoiled}$ vs. BS-$SE_{spoiled}$*

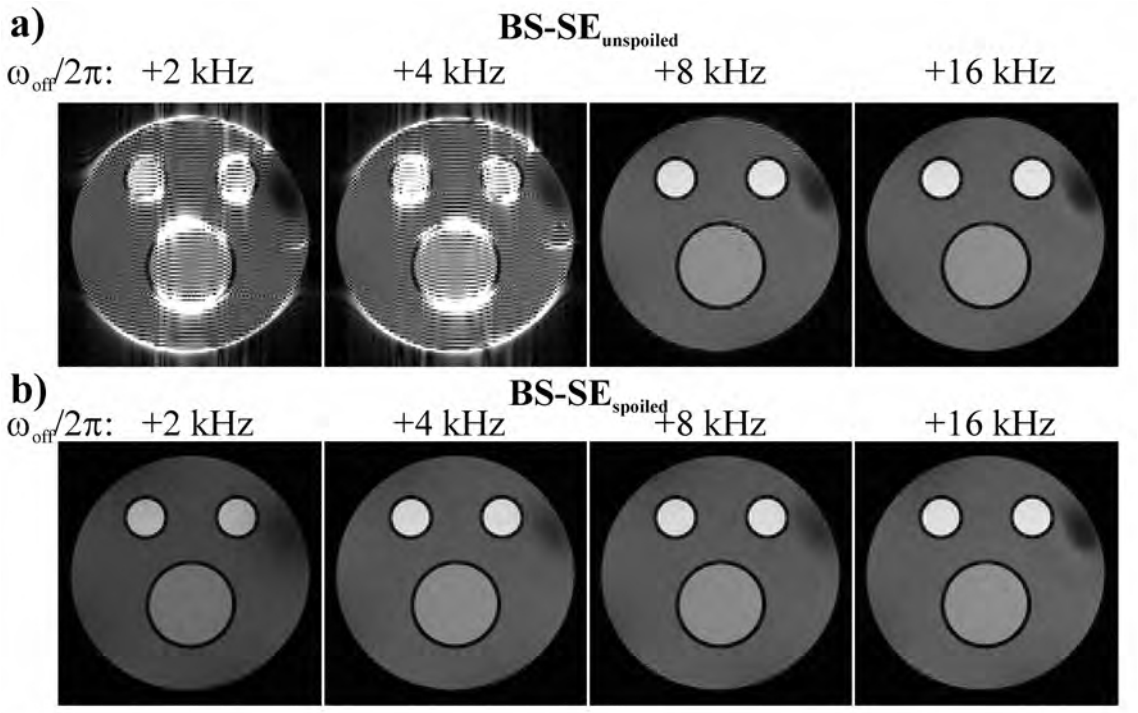


**Figure 7.59:** *Results of the comparison of the BS-$SE_{unspoiled}$ and BS-$SE_{spoiled}$ experiments. a) BS-$SE_{unspoiled}$ experiments, from left to right: $\omega_{off}/2\pi$ = +2/+4/+8+16 kHz. b) BS-$SE_{spoiled}$ experiments, from left to right: $\omega_{off}/2\pi$ = +2/+4/+8+16 kHz. All images are normalized and displayed with the same maximum set to 0.25.*

In Figure 7.59 the results from the unspoiled BS-SE (cf. Figure 7.59a) and the spoiled BS-SE (cf. Figure 7.59b) experiments are displayed. It is obvious that strong artifacts due to the non existent spoiler gradients after the BS-pulses hamper the image quality of the BS-SE$_{unspoiled}$ experiments. This effect cannot be seen for the BS-SE$_{spoiled}$ experiments. However, a signal decrease is clearly visible for the images with $\omega_{off}/2\pi = +2$ kHz. Similar results were obtained for the experiments with -$\omega_{off}$ (data not shown).

*$P_b$: BS-SE vs. BS-CPMG-TSE*

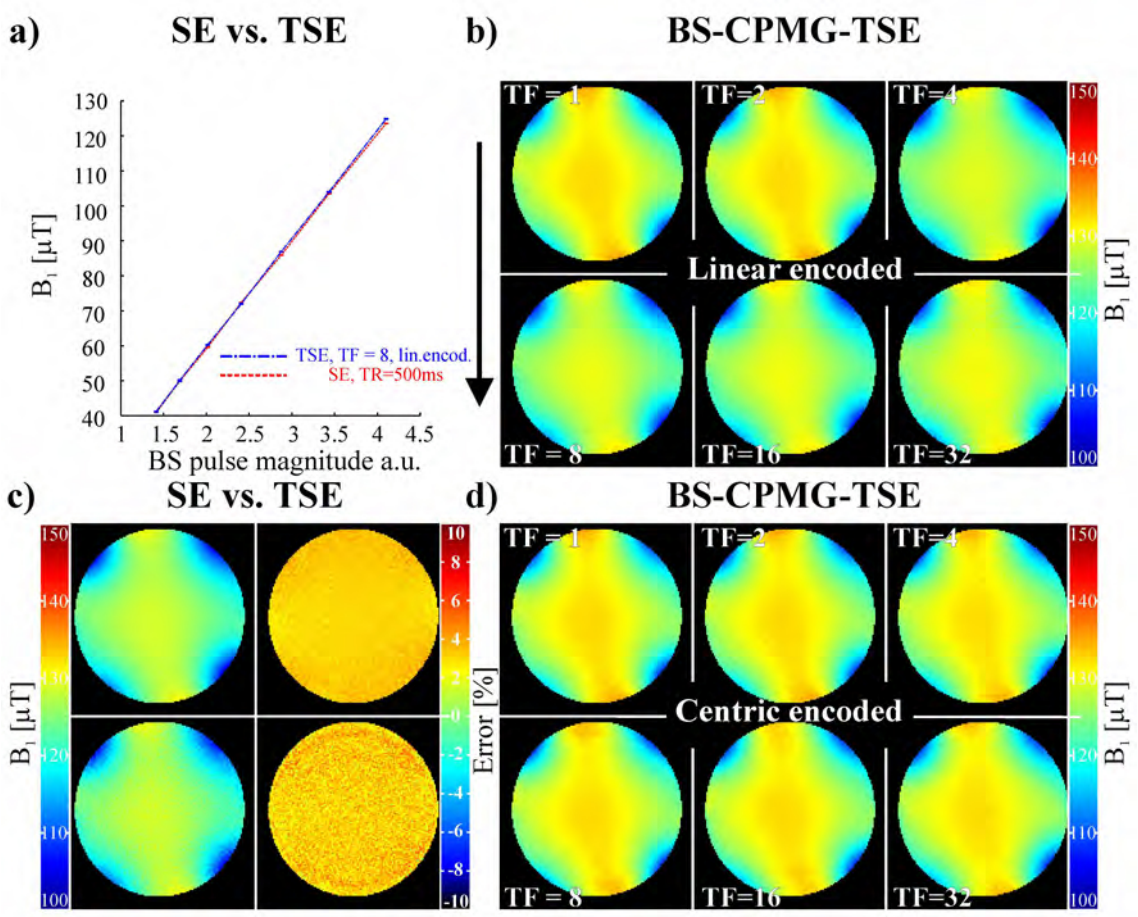


**Figure 7.60:** *Comparison of 2D phantom $B_1^+$ maps acquired with different BS-methods using phantom $P_b$. a) Mean $B_1^+$ strength calculated for seven different BS-pulse magnitudes from BS-SE and BS-CPMG-TSE experiments. b) $B_1^+$ maps acquired with the proposed BS-CPMG-TSE sequence displayed in Figure 7.58b (TR = 1000 ms; TF = 1, 2, 4, 8, 16, 32; $T_{exp}$ = 4 min 16 s, 2 min 8 s, 1 min 4 s, 32 s, 16 s, 8 s). Linear encoding was used for all acquisitions. The arrow indicates the phase encoding direction. c) Left column: $B_1^+$ maps acquired with the BS-SE sequence displayed in Figure 7.58a (upper row: TR = 1000 ms; $T_{exp}$ = 4 min 16 s; lower row: TR = 125 ms; $T_{exp}$ = 32 s). Right column: Relative error maps of the BS-SE (TR = 1000 ms/TR = 125 ms) sequence against the centric encoded BS-CPMG-TSE sequence (TF = 1/TF = 8). d) $B_1^+$ maps acquired for centric encoding with the same method and parameters as in (b). Figure from Reference [103].*

2D $B_1^+$ maps acquired with the BS-SE and the BS-CPMG-TSE methods are shown in Figure 7.60. In Figure 7.60a, the average $B_1^+$ magnitude was plotted against seven different BS-pulse strengths calculated from data acquired with the BS-SE and the BS-CPMG-TSE

methods. Both methods showed the expected linear behavior between the applied pulse magnitude and the measured $B_1^+$ values. Furthermore, it was observed that both methods were in very good agreement (Fit values for y = ax + b were BS-SE: a = 0.031, b = -0.0025, RMSE = 3.7 $10^{-4}$; BS-CPMG-TSE: a = 0.031, b = -0.0022, RMSE = 2.1 $10^{-4}$). Figure 7.60b displays the $B_1^+$ maps acquired using the BS-CPMG-TSE sequence with linear echo encoding. All maps provided similar $B_1^+$ information; however, with increasing TF came increasing noise in the $B_1^+$ maps. Furthermore, a small systematic difference between $B_1^+$ maps of low TF values (TF $\leq$ 2) and higher TF values (TF $\geq$ 4) was observed. The left column of Figure 7.60c displays two $B_1^+$ maps acquired with the BS-SE sequence. The upper was acquired with TR = 1000 ms and the lower was acquired with TR =125 ms. Both maps showed the $B_1^+$ pattern of the investigated coil. Noise influence, however, was more visible in the lower map. In the right column, two error maps are shown. The differences between the $B_1^+$ maps calculated from the BS-SE data (TR = 1000 and 125 ms) and those calculated from the BS-CPMG-TSE data (centric encoding, TF 1 and 8) are displayed. A small difference between the absolute $B_1^+$ values of both methods could be observed; however, no structure was visible. The $B_1^+$ maps shown in Figure 7.60d were acquired with centric echo encoding and the same parameters as for Figure 7.60b. Even with high TFs, the noise corruption in the maps was minimal.

*$P_a$: BS-SE vs. BS-CPMG-TSE*

Figure 7.61 provides a quantitative comparison between different parameters for the BS-SE and a linear encoded BS-CPMG-TSE sequences performed on the phantom $P_a$. In Figures 7.61a & b, the different ROIs in the phantom were separately regarded (Mean $T_1$ value ROI: 1/2/3: 2388 $\pm$ 55 ms/1472 $\pm$ 31 ms/678 $\pm$ 33 ms; Mean $T_2$ value ROI: 1/2/3: 325 $\pm$ 12 ms/290 $\pm$ 3 ms/153 $\pm$ 3 ms) (cf. Figure 7.62a).

More specifically, Figure 7.61a shows that very similar SNR values were achieved for all BS-SE experiments and the BS-CPMG-TSE experiments (TF = 1) with the same TR. Furthermore, when only experiments with the same TR value were considered, BS-SE and the BS-CPMG-TSE experiments with TF = 1–4 provided the highest SNR. By comparing sequences with the same **E**xperiment **T**ime ($T_{exp}$), Figure 7.61a shows that the BS-CPMG-TSE experiments with higher TR consistently achieved higher SNR values than the BS-SE experiments with shorter TR. Besides one exception (ROI 3: $T_{exp}$ = 8 s), for all considered $T_{exp}$, the highest SNR values could be achieved with the BS-CPMG-TSE sequence with TR = 1000 ms. Besides one exception (BS-CPMG-TSE, TR = 1000 ms, TF = 32), when sequences with the same measurement parameters were investigated, the highest SNR was always present in ROI 3 followed by ROI 2 and ROI 1.

Figure 7.61b presents the standard deviation of the $B_1^+$ maps ($\delta B_1$) calculated from the five independent measurements. Thus, the different phantom $P_a$ ROIs were separately regarded. Compared to the BS-CPMG-TSE experiments with the same TR and TF = 1, lower $\delta B_1$ values were achieved with the BS-SE sequences. The difference in the $\delta B_1$ values for those sequences was smallest for ROI 3 followed by ROI 2 and ROI 1. Furthermore, a decrease of the $T_{exp}$/TR generally increased the $\delta B_1$ values when only one type of the above described sequences was taken into account. Several cases can be found where the BS-CPMG-TSE sequences had similar or even lower $\delta B_1$ values compared to the BS-SE sequences with the same $T_{exp}$. For BS-CPMG-TSE sequences applied with TR = 62.5 ms/125 ms, the lowest $\delta B_1$ values were achieved for ROI 3 followed by ROI 2 and ROI 1. For these sequences, the $\delta B_1$ value increased with decreasing $T_{exp}$/increasing TF in all

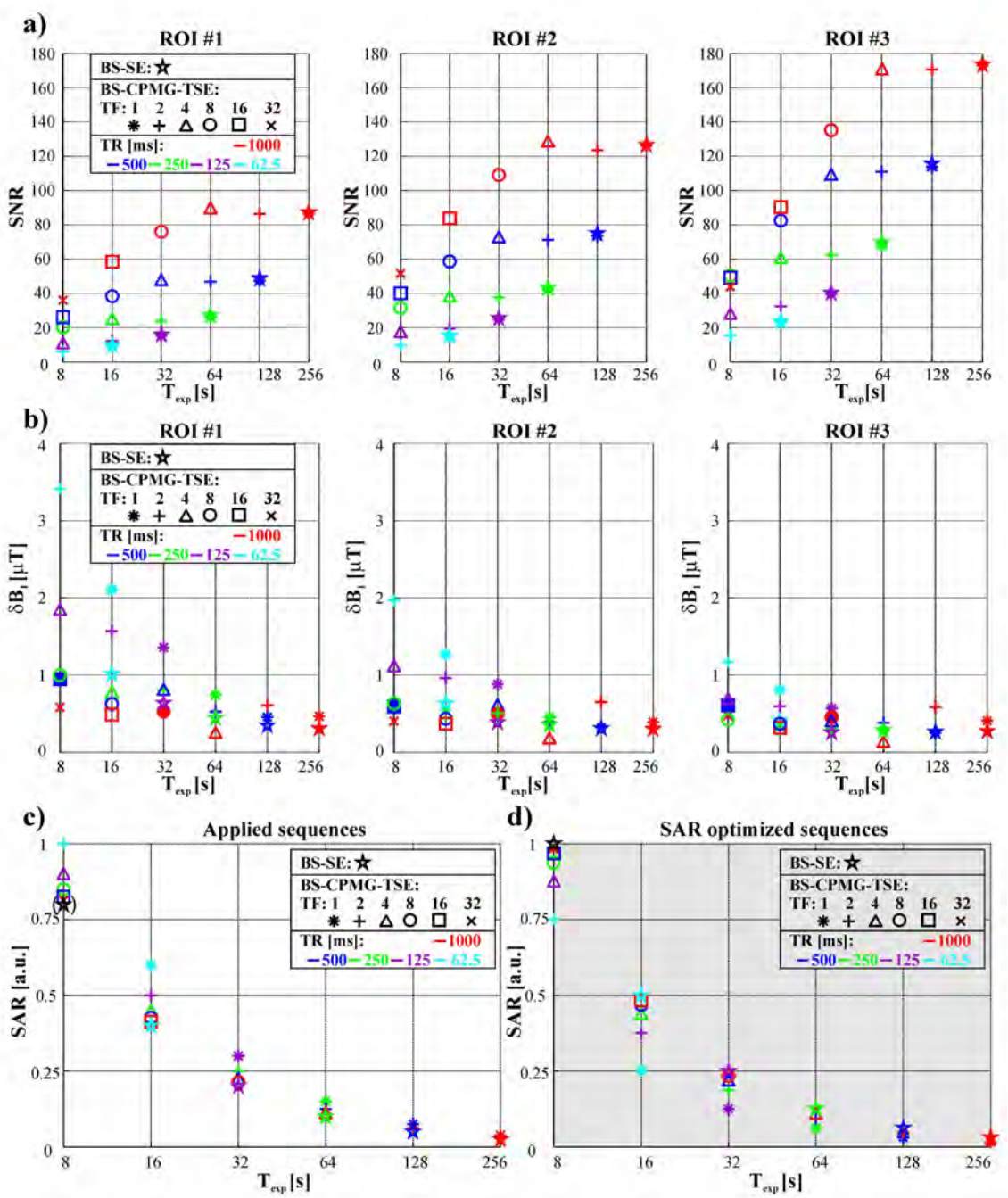


**Figure 7.61:** *Comparison of different quantitative values between the BS-SE and linear encoded BS-CPMG-TSE methods using phantom $P_a$. In (a & b), subplots for the results of the different ROIs are plotted (left: ROI 1; middle: ROI 2; right: ROI 3). The position of the ROIs can be found in Figure 7.62a. a) Mean SNR calculated separately from the different ROIs and plotted against $T_{exp}$. b) Mean $\delta B_1$ values calculated from the different ROIs plotted against $T_{exp}$. Filled symbols indicate that only four experiments were used to calculate the $\delta B_1$ values due to measurement errors. c) Estimated SAR values for the different applied sequences plotted against $T_{exp}$. The bracketed black symbol for the BS-SE sequence indicates the SAR value for a BS-SE sequence with TR = 31.25 ms. No measurement, however, could be performed using this sequence due to scanner restrictions. d) Estimated SAR values for the SAR-optimized BS-CPMG-TSE sequences compared to the BS-SE sequences. The gray background indicates that no measurements were performed using these sequences. All SAR values are given in arbitrary units and are normalized to the maximum value in each subplot. Figure from Reference [103].*

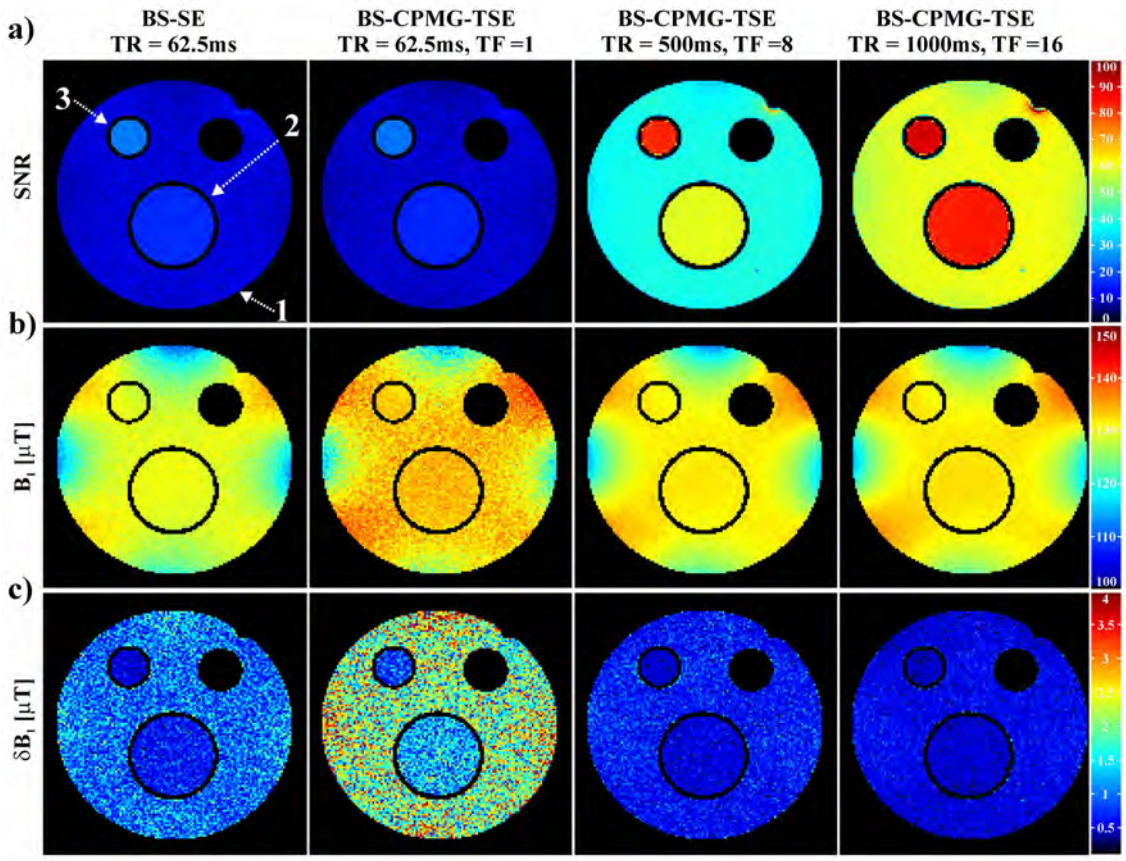


**Figure 7.62:** *Comparison of four different sequences applied on phantom $P_a$. Left to right: BS-SE: TR = 62.5 ms; BS-CPMG-TSE: TR = 62.5/500/1000 ms; TF = 1/8/16. Since only one of the NMR tubes with a concentration of 0.17 mmol/L GFM was evaluated, the other tube was excluded from the maps. The three different ROIs underlying Figure 7.61 are indicated in the left image of (a). a) SNR maps obtained from one exemplary measurement of the four different sequences. b) $B_1^+$ maps calculated from the four different sequences out of the five independent experiments. c) $\delta B_1$ maps of the four investigated sequences. Figure from Reference [103].*

investigated ROIs. These trends were not always given for BS-CPMG-TSE sequences with higher TR. For example, similar values of the $\delta B_1$ values were obvious for all parameters and ROIs of the BS-CPMG-TSE sequence with TR = 1000 ms.

In Figure 7.61c, the estimated SAR using Equation 7.25 is presented for all performed sequences. For all $T_{exp}$, the lowest values were given for the BS-SE sequences. However, when the SAR-optimized sequences were regarded (cf. Figure 7.61d), the lower SAR values were always given for the BS-CPMG-TSE sequences. In both cases, the SAR value decreased with increasing $T_{exp}$.

Figure 7.62 shows image results from four exemplary experiments (BS-SE: TR = 62.5 ms, BS-CPMG-TSE: TR = 62.5 ms/500 ms/1000 ms; TF = 1/8/16). All experiments had the same $T_{exp}$ = 16 s. In Figure 7.62a, the calculated SNR maps are presented. While similar low SNR values were achieved for both sequences with TR = 62.5 ms, higher values were obtained using the BS-CPMG-TSE sequences with TR = 500 ms/1000 ms. Figure 7.62b provides the calculated $B_1^+$ maps of those sequences. The weakest noise corruption was visible for the BS-CPMG-TSE sequences with TR = 500 ms/1000 ms followed by the BS-SE sequence with TR = 62.5 ms. The strongest noise corruption was visible for the BS-CPMG-TSE sequence with TR = 62.5 ms. This behavior is reflected by the $\delta B_1$ maps presented in Figure 7.62c.

#### *In vivo* experiments

Figures 7.63a & b presents the correction scheme used with *in vivo* experiments to adjust the magnitude of the BS-pulse in the CPMG refocusing train. Figure 7.63c shows that, without correction, the mean difference between the $B_1^+$ values obtained from the BS-CPMG experiment and those of the BS-SE experiment was $\approx$ 6.3%. As shown in Figure 7.63d, this deviation was significantly decreased when using the proposed correction scheme for the BS-pulse in the refocusing train (Mean difference = -1.3%).

*In vivo* 3D-SE and 3D-TSE data are shown in Figure 7.64. A magnitude correction of the BS-pulses was performed before BS-CPMG-TSE experiments (cf. Figure 7.63). The $B_1^+$ map calculated from the 3D BS-SE (TR = 125 ms, Figure 7.64a) experiments provided similar values as the $B_1^+$ maps calculated from the 3D BS-CPMG-TSE (Figures 7.64b & c). With linear encoding, high TFs led to a high level of noise corruption due to low *in vivo* $T_2$ values (Figure 7.64b). The same scenario increased blurring with centric encoding (Figure 7.64c).

### 7.2.5 Discussion

This work demonstrates that fast acquisition of $B_1^+$ information is enabled using BS-CPMG-TSE sequences.

To avoid artifacts from on-resonant excitation of an off-resonant BS-pulse, for all BS-sequences, the spoiler gradient after the refocusing pulse was moved behind the BS-pulse without increasing the minimal TE (cf. Figure 7.58). The improvement in the magnitude image quality using this setup could be shown by *ex vivo* experiments (cf. Figure 7.59). Alternatively, BS-pulse phase cycling [145, 164] could be applied to eliminate residual magnetization introduced by an imperfect BS-pulse. The gradient placing used in this work introduces a higher diffusion weighting [165, 166]. The data, however, can be acquired without the additional measurement necessary with phase cycling.

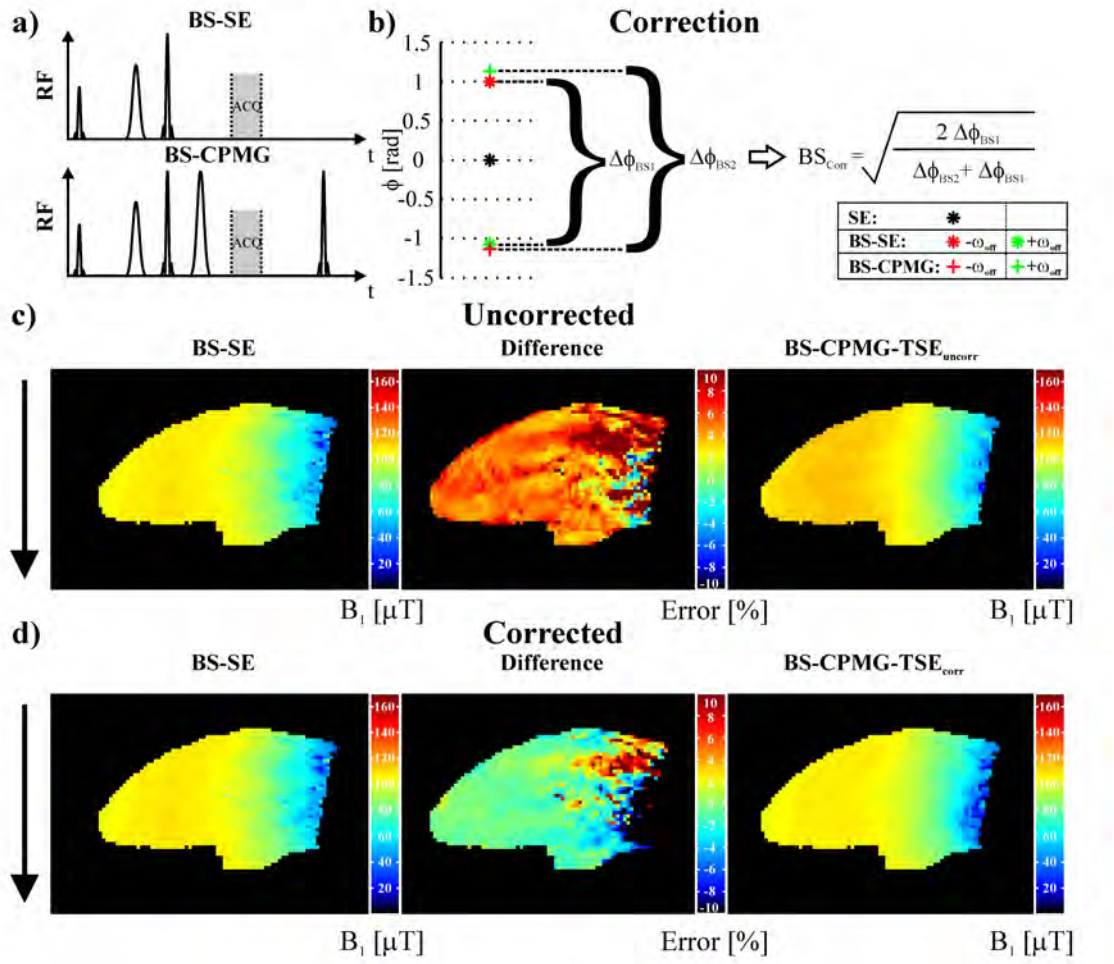


**Figure 7.63:** *Correction scheme and measurement results for the BS-pulse corrections in the BS-CPMG-TSE experiments. Arrows indicate the phase encoding direction. a) The RF pulses used in the nonphase encoded experiments are indicaded. b) Correction scheme (Eqs. 7.26–7.29) using the difference between the phases obtained from the nonphase encoded experiments shown in (a). c) $B_1^+$ map obtained from the BS-SE experiment (left); $B_1^+$ map obtained from a centric encoded BS-CPMG-TSE experiment (TF = 8, right) without BS-magnitude correction; and difference map of both experiments (middle). d) $B_1^+$ map obtained from the BS-SE experiment (left); $B_1^+$ map obtained from the centric encoded BS-CPMG-experiment (TF = 8) with corrected magnitude for the BS-pulse in the refocusing train (right) and difference map of both experiments (middle). Figure adapted from Reference [103].*

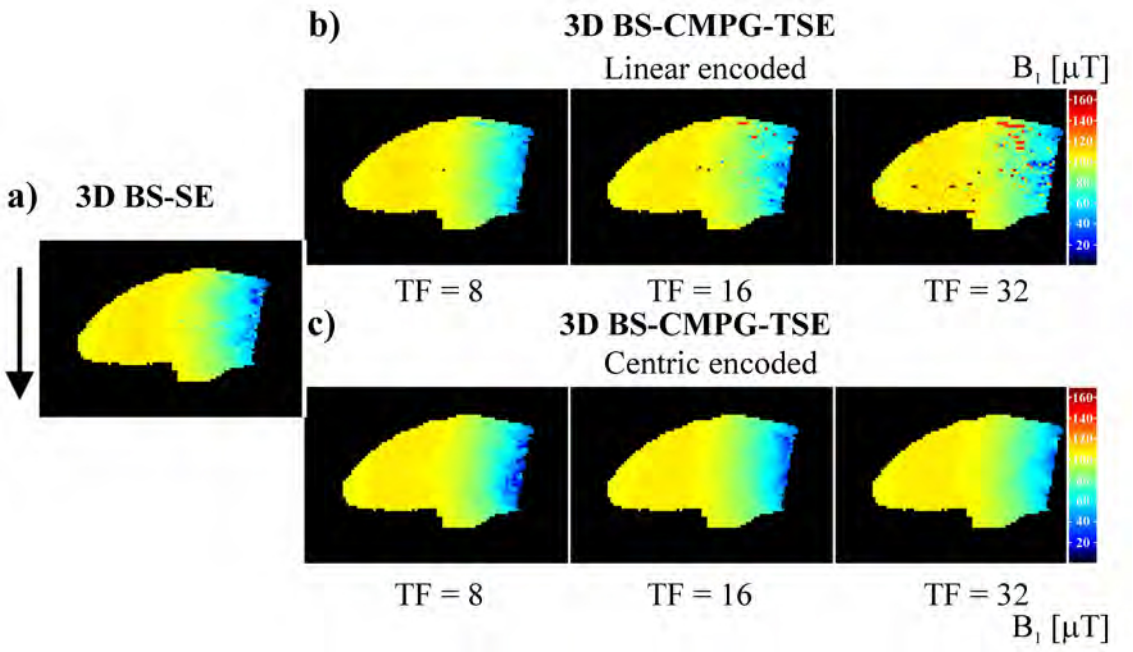


**Figure 7.64:** In vivo *3D data showing the same slice for all images. The arrow indicates the phase encoding direction. a) $B_1^+$ map from the 3D BS-SE experiment (TR = 125 ms; $T_{exp}$ = 4 min). b) Linear encoded 3D BS-CPMG-TSE data (TR = 1000 ms; TF = 8, 16, 32; $T_{exp}$ = 4 min, 2 min, 1 min). c) Centric encoded 3D BS-CPMG-TSE data (TR = 1000; TF = 8, 16, 32; $T_{exp}$ = 4 min, 2 min, 1 min). Figure adapted from Reference [103].*

Furthermore, in contrast to [102], Gaussian-shaped BS-pulses were used. Fermi pulses have a higher $K_{BSpulse}$. Compared to a Gaussian pulse, lower BS-peak magnitudes are thus needed for the same phase difference introduced by the BS-pulse. However, on-resonant excitation by the BS-pulse should be avoided. Regarding this issue, it was found that Gaussian pulses provided better results (data not shown). BS-pulses optimized for introducing a large $\phi_{BS}$ combined with minimal interference with the on-resonant magnetization might further improve BS-$B_1^+$ mapping. Studies concentrating on this issue showed promising results [164, 167].

In this work, short TE were of interest to enable BS-CPMG-TSE experiments with high TF and sufficient SNR. Thus, only short BS-pulses were inserted around the refocusing pulses. As mentioned, Equation 7.20 is only applicable for the evaluation of the $B_1^+$ maps if $\omega_{off} \gg \omega_{B_0}$ and $\omega_{off} \gg \gamma B_1$. Due to the short BS-pulses, $\omega_{off}$ was set to 16 kHz and thus $\omega_{off} \gg \omega_{B_0}$ was fulfilled. However, for the highest chosen BS-pulse magnitude, $\gamma B_1$ was smaller than $\omega_{off}$ by a factor of only $\approx 3$. Nevertheless this pulse magnitude was chosen because a linear behavior between the used pulse magnitudes and the calculated $B_1^+$ values could be shown for all investigated parameters (Figure 7.60a). Although the SAR increases using such high power BS-pulses, introducing an increased phase shift results in less noise-corrupted $B_1^+$ maps.

Compared to BS-SE experiments, in both phantom ($P_a$) and *in vivo* experiments, a shorter $T_{exp}$ was achieved using BS-CPMG-TSE experiments. Due to hardware restrictions, it was not possible to apply the TR needed (TR = 31.25 ms) using BS-SE experiments to achieve the same $T_{exp}$ as the fastest BS-CPMG-TSE experiments. The 2D BS-CPMG-TSE phantom data underlines the possible acceleration of spin-echo-based BS-$B_1^+$ mapping. Due to the long $T_2$ in phantom experiments, a TF of up to 32 still provided quantitative $B_1^+$

information for both linear and centric encoding. In general, the TF must be adapted to the $T_2$ and the TE of the chosen sequence. Regarding $B_1^+$ mapping, centric encoding might be preferable because of the $B_1^+$-data smoothness and the reduced noise corruption compared to linear encoding. However, when a high TF is chosen, blurring is introduced using centric encoding. Since, compared to the phantom, the $T_2$ relaxation time constant was reduced *in vivo*, these effects were observed for high TF.

Figures 7.60b & d display $B_1^+$ maps of different BS-CPMG-TSE experiments. The TSE sequences using the first echoes as the kc (linear encoded: TF $\leq 2$; all centric encoded sequences) show similar $B_1^+$ maps. Furthermore, similar $B_1^+$ values were obtained for linear encoded TSE sequences with TF $\geq 4$. When both cases are compared (linear encoding; TF $\leq 2$ and all centric/linear encoding: TF $\geq 4$), a small difference between the $B_1^+$ maps is obvious. The small systematic difference in Figures 7.60b & d between $B_1^+$ maps of low TF values (TF $\leq 2$) and higher TF values (TF $\geq 4$) visible for linear encoding can be explained by CPMG-like phase "jumping" at the beginning of the echo train (cf. Figure 10.71 in Appendix D.3 on page 134). For linear encoding, in contrast to TF = 1/2 and centric encoding, even echoes were used as the kc for TF $\geq 4$. Thus, the different phase values in the kc influenced the values of the phase images. This translated into a difference between the calculated $B_1^+$ maps (cf. Figure 7.60c). The initial phase "jumping", might result from amplifier inaccuracies. Since the data of Figure 7.60a show very good linear behavior, amplifier compression can most likely be excluded as a cause for the phase discrepancies. However, an incorrect linear amplifier slope would not be reflected in those graphs and can thus not be excluded. An alternative possibility could be that since Equation 7.20 is only an approximation, inaccuracies might arise. The latter issue, however, was not studied in detail in this work and should be further investigated. As a solution to minimize the mentioned phase problems, nonphase encoded scans can be obtained before $B_1^+$ mapping and then used to correct the BS-pulse magnitude (cf. Figures 7.63a & b). This procedure was applied to *in vivo* imaging (cf. Figures 7.63 and 7.64) and thus significantly reduced the deviation between the BS-SE and BS-CPMG-TSE experiments (cf. Figures 7.63c & d).

TSE sequences can generally suffer from different artifacts such as ghosting [91]. Several methods have been developed to correct those artifacts [91, 168]. However, even when ghosting artifacts were visible in absolute value phantom data (data not shown), only a small influence could be observed in the calculated $B_1^+$ maps.

The BS-SE sequence is superior to the proposed BS-CPMG sequences regarding the produced phase shift (cf. Equation 7.15 and Equation 7.17). This is due to the off-resonant BS-pulse applied after the refocusing pulse. Regarding BS-SE, the change of the BS-pulse $\omega_{off}$ sign combined with the effect of the refocusing pulse leads to summed BS-phase shifts from both BS-pulses (Equation 7.15). For the BS-CPMG-TSE sequences, the BS-pulses after the refocusing pulses are given with the same $\omega_{off}$ and with $\sqrt{2}$ times the magnitude of the initial BS-pulse. This rotates the phase through the "zero" back to the position before being mirrored by the preceding refocusing pulse. Thus, the BS-phase shift introduced by the BS-CPMG sequences is only half the phase shift introduced by a comparable BS-SE sequence (Equation 7.17). However, for BS-CPMG sequences, the encoded BS-phase information is retained and enables TSE imaging. Furthermore, as evident from Figs. 7.61 and 7.62, the needed BS-phase shift is strongly dependent on the SNR achieved by the sequence. While BS-CPMG-TSE sequences with TF = 1 always had worse $B_1^+$ map quality than that of the corresponding BS-SE experiments, several BS-CPMG-TSE sequences with other sequence parameters but the same $T_{exp}$ achieved similar or even better $B_1$

quality (cf. Figures 7.61b and 7.62c). Since only half the BS-phase shift was available in those experiments, unlike in the BS-SE experiments, this effect is due to the higher SNR achievable in BS-CPMG-TSE experiments (cf. Figures 7.61a and 7.62a).

Importantly, the proposed BS-technique should be generally possible at clinical field strength. This assumption is supported by the findings of Figures 7.61c & d, showing that the relative SAR values of the proposed sequences are in the same range as those of the BS-SE sequences with double the BS-phase. However, to stay under the SAR limit for clinical applications, long BS-pulses would be necessary. This results in relatively long $T_{esp}$ and could lead to insufficient SNR values when using linear encoding combined with large TF. This problem can be reduced by using centric encoding and/or low TF.

### 7.2.6 Conclusion

The proposed BS-CPMG-TSE sequence is a straightforward variation of the sequences described in [102] for fast $B_1^+$ mapping. At high field strengths or when spin dephasing could hamper the application of FLASH sequences with long TE, the BS-CPMG-TSE sequence provides a fast alternative for $B_1^+$ mapping. However, the SAR of BS-CPMG-based $B_1^+$ mapping must be considered for clinical applications.

## 7.3 Conclusion: Applicability of BS-based $B_1^+$ mapping to $^{19}$F MRI

As discussed in Section 3.3.2 the $B_1$ profile of the chosen coil setup is of interest for quantification purposes. When the coil for excitation is different than that used for reception, it is important to differ between the $B_1$ profile of the excitation coil ($B_1^+$) and the $B_1$ profile of the reception coil ($B_1^-$). Using BS-sequences, normally only the $B_1^+$ can be acquired. If, however, only one coil is used for both excitation and reception, the $B_1^+$ profile equals the $B_1^-$ profile. Since currently single coils are normally used in $^{19}$F MRI, BS-based $B_1^+$ mapping can be used to correct for discrepancies caused by an inhomogeneous $B_1$ profile.

As shown in the section above, the $B_1^+$ quality depends on the achievable SNR and the reached BS-phase. Regarding other nuclei besides protons, BS-based $B_1^+$ mapping has been shown for hyperpolarized $^{13}$C [146], in which the SNR issue is of less concern. Furthermore, flip angle calibration was shown for x-nuclei ($^3$He and $^{13}$C) using spectroscopic BS-methods [144]. In this case averaging was applied when the SNR was insufficient. Since the SNR is often low in $^{19}$F MRI, this issue must be taken into account in $^{19}$F BS-$B_1^+$ mapping. If insufficient SNR is present averaging can be used to improve the SNR; however, increased $T_{exp}$ must be taken into account. Furthermore, a sensitive $B_1^+$ mapping method should be used. As discussed in Chapter 3, PFC compounds often have a long $T_2$, thus TSE-based $B_1^+$ mapping such as that presented in the present work could enable sensitive $^{19}$F $B_1^+$ mapping. Alternatively, coils have been presented that use the same channel for both $^1$H and $^{19}$F MRI [169–171]. For example, as described in [170], the sensitivity profile for both channels was inherently the same in this double-resonant coil. Thus, when it can be ensured that sufficient $^1$H signal is present at the locations where the $^{19}$F signal can be found, such a coil would enable the correction of $^{19}$F MRI data with a $B_1^+$ map acquired using a $^1$H $B_1^+$ mapping sequence. An initial study dealing with this idea showed promising results [147].

# 8 Discussion & Conclusion

The present work dealt with different aspects and techniques concerning $^{19}$F MR. In the following, a short discussion of each different aspect is provided. Thereby, only the experimental Chapters 5, 6 and 7 of this work are regarded.

In Chapter 5, the successful application of $^{19}$F MR to visualize biological processes *in vivo* could be shown. Therefore, two different animal models were used. Ongoing vessel occlusion was visualized in a PT mouse model in addition to visualization of the inflammatory response after intra neural induction of lysolecithin in a rat model. These completely different models underline the wide applicability of $^{19}$F MR in preclinical research. Thus there have been numerous publications in the field of $^{19}$F MR dealing with different aspects of this topic [16, 20, 21, 36–39, 43–47]. Thereby, $^{19}$F MR-based cell tracking is of high interest due to the unique properties of $^{19}$F MRI [16, 18, 19, 37, 50]. Unfortunately, often only a low number of $^{19}$F-labeled cells must be visualized, providing only low numbers of $^{19}$F spins, which ultimately results in low SNR. Therefore, concepts for maximizing the SNR in $^{19}$F MR imaging for future studies have been proposed [18, 19, 37, 42, 50]. Briefly, these concepts include the choice of the $^{19}$F marker, adapted MR sequence parameters, optimized cell labeling strategies, and customized hardware (MR-coils).

A subsection of Chapter 6 investigated whether or not time consuming $^{19}$F TSE-CSI experiments can be accelerated using CS. Thus, it was shown that $^{19}$F TSE-CSI experiments can be significantly accelerated. CS, however, can only be successfully applied when sufficient SNR is available. When the SNR is low, so-called spike artifacts occur with the CS algorithm used in the present work. However, in an additional subsection it was shown that these artifacts can be reduced using a CS-based post processing algorithm. Thus, CS might help overcome limitations with time consuming $^{19}$F CSI experiments. This was previously shown for 3D $^{19}$F ssfp-CSI experiments [23, 24].

Chapter 7, the last experimental chapter, dealt with a novel technique to quantify the $B_1^+$ profile of an MR coil. It was shown that using a specific application scheme of off-resonant pulses, BS-based $B_1^+$ mapping can be enabled using a CPMG-based TSE sequence. Thus, a fast acquisition of the data necessary for $B_1^+$ mapping was enabled. Furthermore, susceptibility artifacts that are especially problematic at high field strengths, such as those used in the present work, were minimized due to the spin-echo nature of the presented sequence. In the future, BS-CPMG-TSE $B_1^+$ mapping could possibly be applied to improve quantification using $^{19}$F MRI. Thus, the coil profile could be corrected when the data are acquired with a $^{19}$F BS-CPMG-TSE sequence. This might be necessary since often external references are used that might be in the inhomogeneous area of the coil. The application of the TSE sequence is especially interesting for $^{19}$F MRI since often PFC markers have a long $T_2$ and thus the SNR can be maximized. Although the presented BS-sequence entails a high SAR, making the application to human scanners with high field strength questionable, other spin-echo-based BS-techniques might overcome this issue [152, 172].

Finally, it is important to note that first clinical trials using $^{19}$F cell tracking have been approved [77]. This is a further step toward $^{19}$F cellular MRI in humans. Besides safety

concerns, the translation of this technique to human applications, however, remains challenging due to sensitivity issues of this technique. Therefore, the medical issue must be well known to predict whether or not $^{19}$F MR can help answer medical questions. Further improvements in methods, hardware, and instrumentation, however, might help overcome these limitations.

# 9 Diskussion & Zusammenfassung

Diese Arbeit handelt von verschiedenen Aspekten und Techniken der $^{19}$F MR Bildgebung. Im Folgenden wird jeder dieser Aspekte kurz diskutiert. Dabei werden nur die experimentellen Kapitel 5, 6 und 7 der Arbeit betrachtet.

Im Kapitel 5 wurde gezeigt, dass die $^{19}$F **M**agnet**R**esonanz**T**omographie (MRT) erfolgreich zur Visualisierung von biologischen Prozessen angewendet werden kann. Dazu wurden zwei verschiedene Tiermodelle benützt. An einem PT Mausmodell wurde ein stattfindender Gefäßverschluss dargestellt, und in einem Rattenmodell konnte zusätzlich die inflammatorische Antwort nach intraneuraler Einbringung von Lysolecithin visualisiert werden. Diese stark unterschiedlichen Modelle stellen die breite Anwendungsmöglichkeit der $^{19}$F MR Bildgebung in der präklinischen Forschung heraus. Daher gibt es bereits verschiedene Publikationen auf dem Feld der $^{19}$F MR Bildgebung, die sich mit verschiedensten Aspekten dieses Themengebietes beschäftigten [16, 20, 21, 36–39, 43–47]. Dabei ist, wegen der speziellen Eigenschaften der $^{19}$F MRT, die $^{19}$F MR Bildgebung von Zellen von großem Interesse [16, 18, 19, 37, 50]. Bedauerlicherweise muss oftmals eine kleine Menge von $^{19}$F markierten Zellen bildgegeben werden, die wiederum nur wenige $^{19}$F Spins beinhalten. Dies führt schlussendlich zu einem schlechten SNR. In der Vergangenheit wurden deshalb, für zukünftige Studien, verschieden Konzepte zur SNR Maximierung der $^{19}$F MR Bildgebung vorgeschlagen [18, 19, 37, 42, 50]. Diese Konzepte betreffen die Wahl der $^{19}$F Substanz, die Optimierung der Sequenzparameter, die Optimierung der Strategien zur Zellmarkierung und die Angepassung der Geräte (MR-Spulen).

In einem Unterabschnitt des Kapitels 6 wurde untersucht, ob die Anwendung von CS es ermöglicht zeitaufwändige $^{19}$F TSE-CSI Experimente zu beschleunigen. Dabei konnte gezeigt werden, dass $^{19}$F TSE-CSI Experimente signifikant beschleunigt werden können. Allerdings kann CS nur erfolgreich angewendet werden, wenn ausreichend SNR vorhanden ist. Denn ist das nicht der Fall und wird der CS Algorithmus dieser Arbeit verwendet, dann entstehen sogenannte spike Artefakte. Es konnte aber in einem weiteren Unterabschnitt gezeigt werden, dass diese Artefakte mit einem CS basierten Algorithmus in der Nachbearbeitung der Daten reduziert werden können. Zusammenfassend lässt sich sagen, dass CS es ermöglicht, Limitationen von zeitaufwändigen $^{19}$F CSI Experimenten zu überwinden. Für 3D $^{19}$F ssfp-CSI Experimente wurde dies bereits gezeigt [23, 24].

Kapitel 7, das letzte experimentelle Kapitel, handelt von einer neuartigen Technik um das $B_1^+$ Profil einer MR Spule quantitativ auszumessen. Es wurde gezeigt, dass mit einem bestimmten Anwendungsschema von offresonanten Pulsen, BS-basiertes $B_1^+$ Mapping mit Hilfe einer CPMG basierten TSE Sequenz betrieben werden kann. Somit wurde eine schnelle Aufnahme der Daten, welche für das $B_1^+$ Mapping benötigt werden, ermöglicht. Darüberhinaus wurden Suszeptibilitäts Artefakte durch die Spin-Echo Natur dieser Sequenz minimiert. Diese Artefakte sind vor allem bei hohen Magnetfeldern, die auch in dieser Arbeit verwendet wurden, problematisch. In der Zukunft könnte das BS-CPMG-TSE $B_1^+$ Mapping möglicherweise dazu beitragen, die Quantifizierung mittels $^{19}$F MRI zu verbessern. So könnte zum Beispiel das Spulenprofil korrigiert werden, wenn Daten mit einer $^{19}$F BS-CPMG-TSE Sequenz aufgenommen werden. Dies wird möglicherweise nötig sein, da

oftmals externe Referenzen zur Quantifizierung benutzt werden die wiederum in dem inhomogenen Gebiet der Spule platziert sein könnten. Die Anwendung der TSE Sequenz ist sehr interessant für die $^{19}$F MRI, da PFC Substanzen oftmals lange $T_2$ Zeiten haben und somit das SNR maximiert werden kann. Auch wenn die präsentierte BS-Sequenz ein hohes SAR beinhaltet, was die Anwendung an Humanscannern in Frage stellt, so könnten doch andere Spin-Echo basierte BS-Techniken dieses Problem überwinden [152, 172].

Abschließend lässt sich sagen, dass erste klinische Studien, welche sich auf die Verfolgung von $^{19}$F markierten Zellen konzentrieren, bereits genehmigt wurden [77]. Dies ist ein wichtiger Schritt in Richtung der Humananwendung der zellulären $^{19}$F MRT. Die Übertragung dieser Technik auf Humananwendungen bleibt allerdings wegen Sicherheitsbedenken und der Sensitivitätsprobleme schwierig. Darum muss über die spezifische medizinische Fragestellung sehr viel gewusst werden, um vorhersagen zu können, ob die $^{19}$F MR eine Hilfe bei der Beantwortung dieser sein kann. Weiterentwicklungen von Methoden und Geräten könnten allerdings dazu beitragen diese Einschränkugen zu überwinden.

# 10 Appendix

## A: CSI data processing

The following sketch describes the post processing of the CSI data.

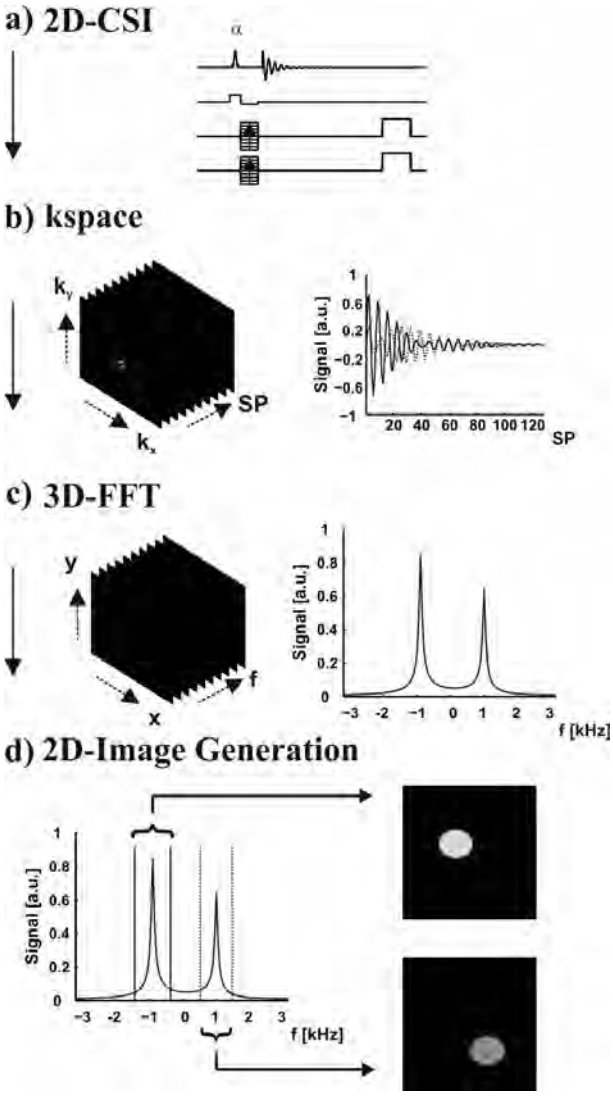


**Figure 10.65:** *Sketch illustrating the reconstruction of the CSI data. a) 2D-CSI sequence as described in Section 4.3.1. b) Left side: 3D k-space containing two so-called k dimensions and one time dimension (FID). The FID from the k-space center is illustrated on the right. c) Left side: 3D dataset after a Fourier transform containing two spatial dimensions and one spectral dimension. The spectral dimension is illustrated on the right. d) Spectrally selective images, each covering one of the two main peaks, are shown.*

Figure 10.65 illustrates the CSI post processing process for a 2D-CSI sequence. First, the

data is acquired using a CSI-based sequence without read gradient (cf. Figure 10.65a). The acquired data is stored in a 3D k-space as illustrated on the left side of Figure 10.65b. Thus, depending on the phase encoding strength, the signal is stored at different so-called k locations in the k-space, while the corresponding time domain signal (FID) is stored in the third dimension (cf. 10.65b, right side). Consequently, after a 3D Fourier transform, the 3D data contains two spatial dimensions and one spectral dimension (cf. Figure 10.65c). To obtain spectrally selective images, the data can be summed along the spectral dimension (cf. Figure 10.65d, left side). Thus, the desired spectrally selective images are generated by including the relevant spectral positions (cf. Figure 10.65d, right side). Please note that additional post processing techniques can be applied in the reconstruction process (e.g. zero-filling, application of filter functions). Further note that for 3D-CSI techniques a 4D k-space is generated (one time dimension, three k dimensions). For a more detailed description of the k-space please refer to [91]. Please note that ssfp-CSI data can be processed as described, thus including the FID and the echo signal (cf. Figure 4.20b).

## B: CS algorithm

The presented pseudo code follows References [23, 24]. As mentioned in Section 6.2, instead of a minimizing algorithm, a fixed step width $t$ was used that was decreased every 30th iteration by a factor of 2. This allowed faster execution of the CS algorithm:

**Input**
$x$: Image
$y$: Undersampled k-space data
FFT: Fast Fourier Transform (image space → k-space)
IFFT: Inverse FFT (k-space → image space)

**Initialize**
$x_0$ = IFFT(y), normalize $x_0$ to 1, $n = 1$, $\epsilon = 1$, $t = 1$, $p = 1$

**Iterations**
*while* $\epsilon > 10^{-4}$
$d = \left(\sqrt{(|x_{n-1}|^2 + \epsilon^2)}\right)^{p-2} \cdot x_{n-1}$
$x_n = x_{n-1} - t \cdot d$
$y_n$ = FFT($x_n$)
Reinsert acquired k-space points at respective positions
in $y_n \rightarrow y_{n,SDC}$ (**S**trict **D**ata **C**onsistency)
$x_n$ = IFFT($y_{n,SDC}$)
*if* n is multiple of 30
$\epsilon = \epsilon \cdot 0.5$
$t = t \cdot 0.5$
*end*
n = n + 1
*end*

# C: CS-TSE-CSI

The following flowcharts describe the calculation of the reduced and pseudo radial CS-TSE-CSI sampling patterns.

## C.1: Reduced 2D centric sampling pattern

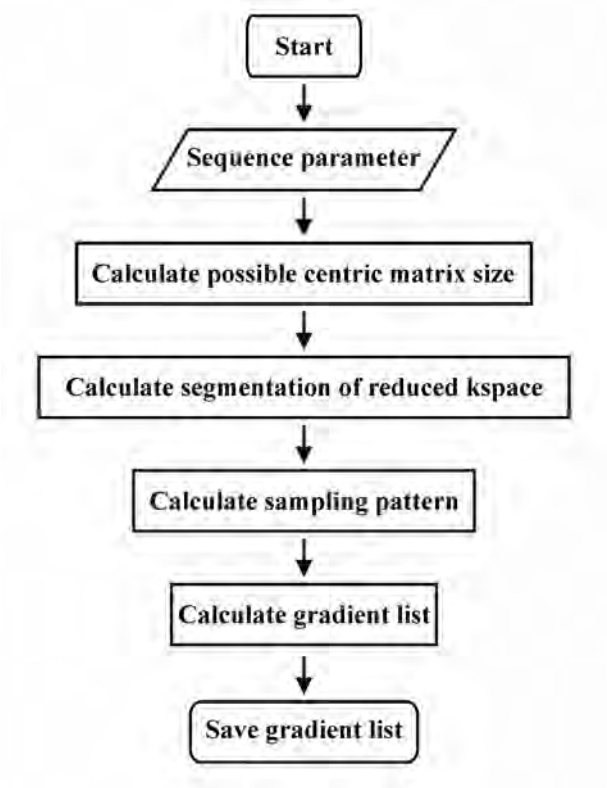


**Figure 10.66:** *Flowchart of the MATLAB® program for calculating the reduced 2D centric sampling patterns.*

Figure 10.66 provides the flowchart describing the calculation of the reduced 2D centric pattern.

As described in Section 6.2.2, different parameters had to be provided at the beginning of the calculation: a rectangular matrix size, TF, and the af. The chosen parameters for the reduced 2D centric sampling pattern were the same as described in Section 6.2.2: rectangular matrix = 64 × 64 (resulted in a 2D centric matrix of: 72 × 72), TF = 16, af = 6.

With the help of the matrix size and the TF, a circle allowing the chosen TF was calculated with a similar number of points as the rectangular matrix (cf. Figure 6.41a). This initial calculation was chosen for all different sampling strategies. Thus, for the reduced data, it was possible to zero-fill to the same matrix size as the fully sampled and the CS reconstructed data directly after data acquisition. This was because the k-space data was sorted into the same matrix size (72 × 72).

To enable filling the reduced matrix size according to the chosen af, TF concentric circles, each with the same reduced number of points, were calculated. The sampling pattern was

generated by filling all spatial points of the different segments (cf. Figure 10.67b). In a final step, gradient lists were calculated and saved.

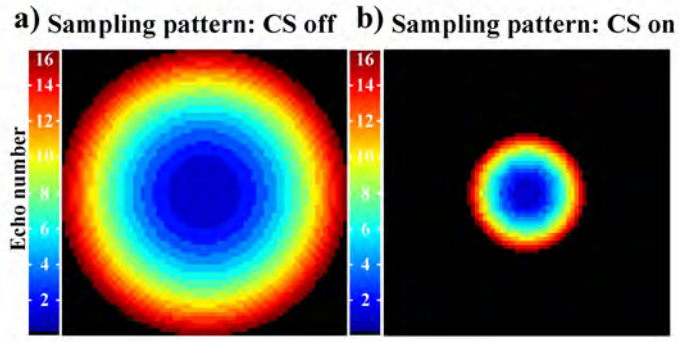


**Figure 10.67:** *a) Sampling pattern for the fully sampled data. b) Sampling pattern for the data with reduced matrix size according to af (af = 6). The color represents the echo number in the TSE echo train for which the data point at the specific k-space position was collected. Part of the figure was adapted from a figure of Reference [132].*

Please note that if af = 1 would have been chosen, the reduced 2D sampling pattern would have been equal to the fully sampled pattern described in Section 6.2.2.

## C.2: 2D centric pseudo radial sampling pattern

Figure 10.68 provides a flowchart displaying the procedure to calculate pseudo radial TSE-CSI patterns.

As mentioned before, the parameter setup and calculation of the initial circle was the same as for the other sampling strategies.

A second step calculated the number of spokes needed to fill the circle with a number of points similar to that of the corresponding 2D centric encoded sampling pattern and which furthermore allowed application of the chosen TF and af (if applicable). Afterwards, the coordinates of the spokes and thus the radial distribution were calculated. Since in TSE-CSI experiments each k-space point is independently acquired, the radial coordinates were re-gridded onto a Cartesian grid and thus a pseudo radial trajectory was generated. This allowed fast Fourier transforms to be directly used to generate the TSE-CSI images from the acquired k-space data.

The sampling patterns were again used to generate a gradient list and were saved in a final step. In Figure 10.69 two radial patterns are shown.

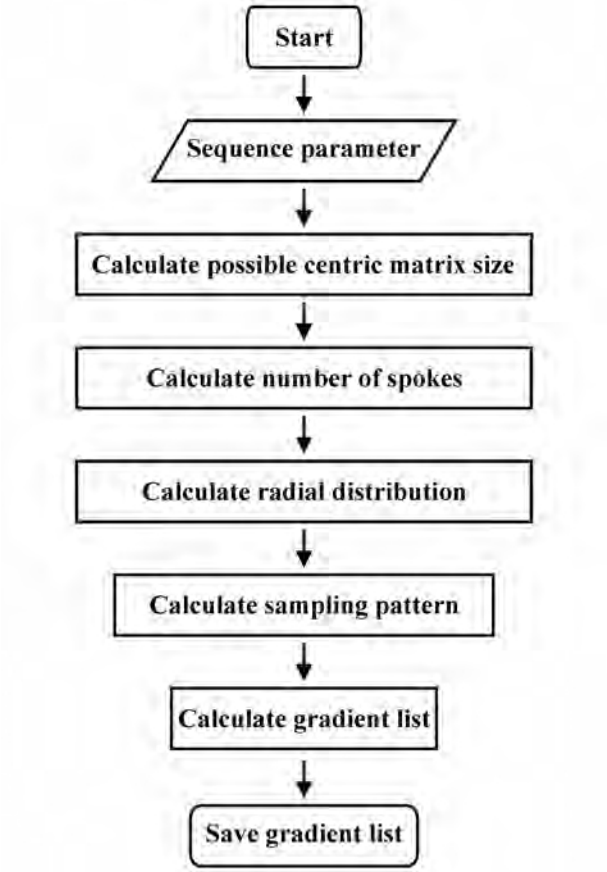


**Figure 10.68:** *Flowchart of the MATLAB® program for calculating the 2D centric pseudo radial sampling patterns.*

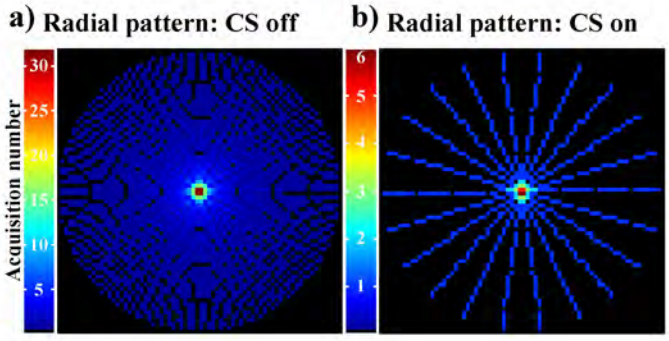


**Figure 10.69:** *a) Radial pattern for the fully sampled data. b) Radial pattern for the data with reduced matrix size according to the af = 6. The color represents the number of k-space point samplings.*

# D: Bloch-Siegert-shift

## D.1: Derivation of the Bloch-Siegert-shift equation

In this subsection, starting with Equation 7.2, the derivation of Equation 7.4 is shown following Reference [102, 150].

$$\mathbf{B}_{eff} = \frac{1}{\gamma}\left(\omega_{off}\mathbf{e}_z + \omega_1\mathbf{e}_x\right) \tag{10.1}$$

Thus the magnitude of $\mathbf{B}_{eff}$ is given by:

$$\begin{aligned} (\gamma B_{eff})^2 &= \omega_{off}^2 + \omega_1^2 \\ \Rightarrow\ (\omega_{BS} + \omega_{off})^2 &= \omega_{off}^2 + \omega_1^2 \end{aligned} \tag{10.2}$$

Equation 10.2 can be rewritten:

$$\begin{aligned} \omega_{BS} + \omega_{off} &= \sqrt{\left(\omega_{off}^2 + \omega_1^2\right)} \\ \Rightarrow\ \omega_{BS} + \omega_{off} &= \sqrt{\left(\omega_{off}^2 + \omega_1^2\right)} + 1 - 1 \\ \Rightarrow\ \omega_{BS} + \omega_{off} &= \sqrt{\left(\omega_{off}^2 + \omega_1^2\right)} + \omega_{off} - \omega_{off} \\ \Rightarrow\ \omega_{BS} + \omega_{off} &= \omega_{off} + \omega_{off}\left[\sqrt{\left(1 + \frac{\omega_1^2}{\omega_{off}^2}\right)} - 1\right] \\ \Rightarrow\ \omega_{BS} &= \omega_{off}\left[\sqrt{\left(1 + \frac{\omega_1^2}{\omega_{off}^2}\right)} - 1\right] \end{aligned} \tag{10.3}$$

Using Assumption$_I$ ($\omega_{off} \gg \gamma B_1 = \omega_1$), the square-root term of Equation 10.3 can be developed using a Taylor expansion. With:

$$\begin{aligned} f(x) &= \sqrt{(1+x)} \\ and\ x &= \frac{\omega_1^2}{\omega_{off}^2} \end{aligned} \tag{10.4}$$

$f(x)$ can be developed for x $\to$ 0:

$$\begin{aligned} f(x) &\approx 1 + \frac{1}{2}\cdot x + O^2 \\ \Rightarrow\ f(x) &\approx 1 + \frac{1}{2}\cdot x \\ \Leftrightarrow\ \sqrt{(1+x)} &\approx 1 + \frac{1}{2}\frac{\omega_1^2}{\omega_{off}^2} \end{aligned} \tag{10.5}$$

Equation 10.5 reinserted in Equation 10.3 yields:

$$\begin{aligned} \omega_{BS} &\approx \omega_{off}\left[1+\frac{1}{2}\frac{\omega_1^2}{\omega_{off}^2}-1\right] \\ \Rightarrow\ \omega_{BS} &\approx \frac{1}{2}\frac{\omega_1^2}{\omega_{off}} \end{aligned} \tag{10.6}$$

Since $\omega_1 = \gamma B_1$, Equation 10.6 can be rewritten:

$$\omega_{BS} \approx \frac{1}{2}\frac{(\gamma B_1)^2}{\omega_{off}} \tag{10.7}$$

Equation 10.7 provides the BS-shift frequency introduced by the off-resonant BS pulse. As described in Section 7.1.1, the off-resonant BS pulse has the duration $t_{BS}$. Thus, the following BS-phase shift is introduced to on-resonant spins:

$$\phi_{BS} \approx \int_0^{t_{BS}} \frac{(\gamma B_1(t))^2}{2(\omega_{off})} dt \tag{10.8}$$

If additionally local off-resonance frequencies ($\omega_{B_0}$) are regarded, Equation 10.8 becomes Equation 7.4 from Section 7.1.1:

$$\phi_{BS} \approx \int_0^{t_{BS}} \frac{(\gamma B_1(t))^2}{2(\omega_{off}+\omega_{B_0})} dt \tag{10.9}$$

## D.2: Phantom phase correction

This section deals with phantom experiments concentrating on the described magnitude correction scheme (Section 7.2.3) for the second BS-pulse of the BS-CPMG technique.

In Figure 10.70, the relative error maps of the $B_1^+$ maps acquired with the BS-CPMG-TSE sequence on $P_a$ are displayed. The obtained $B_1^+$ map from a comparable BS-SE experiment was used as a reference. The absolute value of the relative error is plotted for better comparison. In general, a smaller relative error is apparent for the BS-CPMG-TSE experiments performed with $B_1$ magnitude correction of the BS-pulses. The parameters used for the BS-SE and TSE-CPMG-TSE experiments are provided in Table 10.11.

**Table 10.11:** *Sequence parameters for the phantom experiments dealing with the BS-pulse corrections for the BS- CPMG-TSE experiments.*

| *Sequence* | *Fig* | *P* | *FOV (mm)* | *MTX* | *TE (ms)* | *TR (ms)* | TF |
|---|---|---|---|---|---|---|---|
| BS-SE | N/A | a | 15 × 30 × 60 | 15 × 64 × 128 | 10 | 125 | N/A |
| BS-TSE | 10.70 | a | 15 × 30 × 60 | 15 × 64 × 128 | 40 | 1000 | 8 |

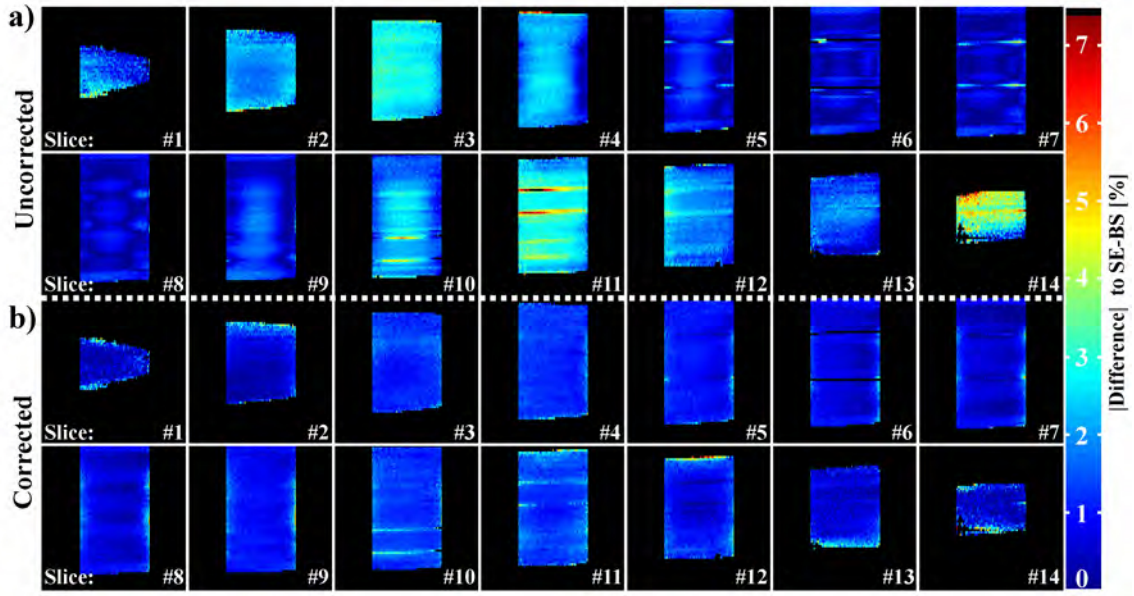


**Figure 10.70:** *Absolute value of the relative error maps obtained from BS phantom experiments. a) Relative error maps of the uncorrected BS-CPMG-TSE experiments. b) Relative error maps of the corrected BS-CPMG-TSE experiments. Contrary to the other phantom experiments, a sagittal view was chosen. The error maps were calculated against the $B_1^+$ maps obtained from the BS-SE experiments.*

## D.3: Phase plots of the BS-CPMG sequence

As described in Chapter 7, $B_1^+$ values obtained from BS-CPMG-TSE experiments without corrected magnitudes of the second BS-pulse slightly differed from the $B_1^+$ values obtained from comparable BS-SE sequences. This was most likely due to imperfect scaling of the BS-pulse magnitude. Additional experiments dealing with this problematic are presented in the following two subsections.

The present Section follows parts of Reference [103] and deals with experiments showing initial "phase jumping" in uncorrected BS-CPMG experiments as mentioned in Section 7.2.5. The experiments were performed on phantom $P_b$.

Figure 10.71 shows plots of the phase evolution during BS-CPMG sequences with multiple echoes (same phase encoding for all echoes). Thereby, the mean phase with standard deviation derived from the used multi-echo sequences is plotted. Compared to the reference sequence without BS-pulses, a slight "phase jumping" at the beginning of the BS-CPMG echo trains can be observed (cf. arrows Figure 10.71). Table 10.12 shows the parameters used for these experiments according to the nomenclature introduced in Chapter 7.

**Table 10.12:** *Sequence parameters for the experiments concentrating on the initial phase problematic of the used BS-CPMG methodology. Fig indicates the figure in which the experiment results are presented and P the phantom used for the experiments. Table adapted from Reference [103].*

| *Fig* | *P* | *MTX* | *TE (ms)* | *TR (ms)* | Number of echoes |
|---|---|---|---|---|---|
| 10.71 | b | 64 × 64 | 40 | 2000 | 20 |

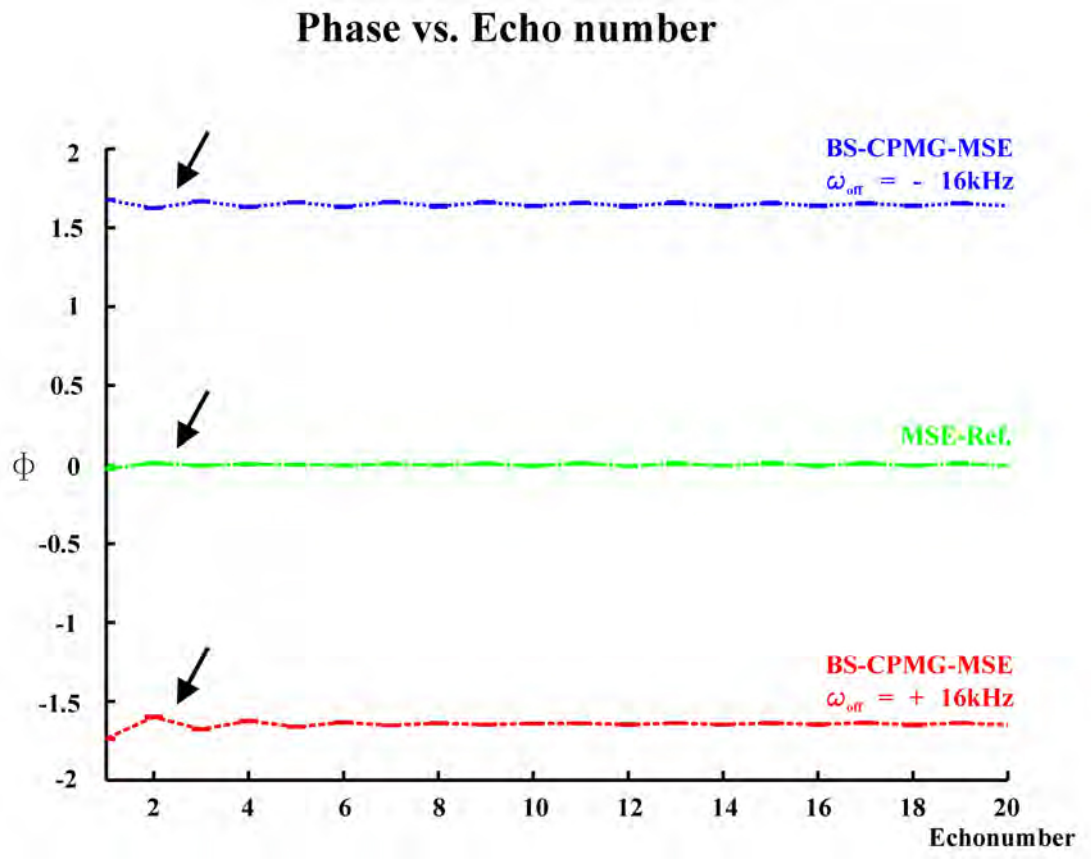


**Figure 10.71:** *Figure dealing with the phase problematic of the presented BS-CPMG setup. The phase is centered around the phase obtained from the reference scan without BS-pulses. The arrows point out visible "phase jumping" at the beginning of the BS-CPMG echo trains. Figure adapted from Reference [103].*

# Bibliography


[1] F. Bloch, W.W. Hansen, and M. Packard. Nuclear induction. *Physical review*, 70 (7-8):460–474, 1946.

[2] E.M. Purcell, H.C. Torrey, and R.V. Pound. Resonance absorption by nuclear magnetic moments in a solid. *Physical review*, 69(1-2):37, 1946.

[3] P.C. Lauterbur. Image formation by induced local interactions: examples employing nuclear magnetic resonance. *Nature*, 242(5394):190–191, 1973.

[4] A. Kumar, D. Welti, and R.R. Ernst. NMR Fourier zeugmatography. *Journal of Magnetic Resonance (1969)*, 18(1):69–83, 1975.

[5] W.A. Edelstein, J.M.S. Hutchison, G. Johnson, and T.W. Redpath. Spin warp NMR imaging and applications to human whole-body imaging. *Physics in Medicine and Biology*, 25:751, 1980.

[6] P. Mansfield. Multi-planar image formation using NMR spin echoes. *Journal of Physics C: Solid State Physics*, 10:L55, 1977.

[7] J. Hennig, A. Nauerth, and H. Friedburg. RARE imaging: a fast imaging method for clinical MR. *Magnetic Resonance in Medicine*, 3(6):823–833, 1986.

[8] A. Haase, J. Frahm, D. Matthaei, W. Hanicke, and K.D. Merboldt. FLASH imaging. Rapid NMR imaging using low flip-angle pulses. *Journal of Magnetic Resonance (1969)*, 67(2):258–266, 1986.

[9] A. Oppelt, R. Graumann, H. Barfuss, H. ans Fischer, W. Hartl, and W. Schajor. FISP-a new fast MRI sequence. *Electromedica*, 54:15–18, 1986.

[10] T.D. Henning, O. Saborowski, D. Golovko, S. Boddington, J.S. Bauer, Y. Fu, R. Meier, H. Pietsch, B. Sennino, D.M. McDonald, and H.E. Daldrup-Link. Cell labeling with the positive MR contrast agent Gadofluorine M. *European radiology*, 17(5):1226–1234, 2007.

[11] F.L. Giesel, M. Stroick, M. Griebe, H. Tröster, C.W. von der Lieth, M. Requardt, M. Rius, M. Essig, H.U. Kauczor, M.G. Hennerici, and M. Fatar. Gadofluorine m uptake in stem cells as a new magnetic resonance imaging tracking method: an in vitro and in vivo study. *Investigative radiology*, 41(12):868, 2006.

[12] D.D. Stark, R. Weissleder, G. Elizondo, P.F. Hahn, S. Saini, L.E. Todd, J. Wittenberg, and J.T. Ferrucci. Superparamagnetic iron oxide: clinical application as a contrast agent for MR imaging of the liver. *Radiology*, 168(2):297–301, 1988.

[13] R. Weissleder. Liver MR imaging with iron oxides: toward consensus and clinical practice. *Radiology*, 193(3):593–595, 1994.

[14] J.W.M. Bulte and D.L. Kraitchman. Iron oxide MR contrast agents for molecular and cellular imaging. *NMR in Biomedicine*, 17(7):484–499, 2004.

[15] A. Stroh, C. Faber, T. Neuberger, P. Lorenz, K. Sieland, P.M. Jakob, A. Webb, H. Pilgrimm, R. Schober, E.E. Pohl, and C. Zimmer. In vivo detection limits of magnetically labeled embryonic stem cells in the rat brain using high-field (17.6 T) magnetic resonance imaging. *Neuroimage*, 24(3):635–645, 2005.

[16] E.T. Ahrens, R. Flores, H. Xu, and P.A. Morel. In vivo imaging platform for tracking immunotherapeutic cells. *Nature biotechnology*, 23(8):983–987, 2005.

[17] Y-X. Ye, T.C. Basse-Luesebrink, P. Arias, K. Hu, T. Kampf, V. Kocoski, X. Helluy, P.M. Jakob, K-H. Hiller, R. Jahns, and W.R. Bauer. MR Cell tracking in reperfused myocardial infarction with microvascular obstruction: Fluorine-19 MR could be a better solution. In *Proceedings of the 18th Annual Meeting of the International Society for Magnetic Resonance in Medicine*, number 2718. ISMRM, 2010.

[18] G. Stoll, T. Basse-Lüsebrink, G. Weise, and P. Jakob. Visualization of inflammation using 19F-magnetic resonance imaging and perfluorocarbons. *Wiley Interdisciplinary Reviews: Nanomedicine and Nanobiotechnology*, 2012. doi: 10.1002/wnan.1168.

[19] M. Srinivas, A. Heerschap, E.T. Ahrens, C.G. Figdor, and I.J.M. Vries. 19F MRI for quantitative in vivo cell tracking. *Trends in biotechnology*, 28(7):363–370, 2010.

[20] K.C. Partlow, J. Chen, J.A. Brant, A.M. Neubauer, T.E. Meyerrose, M.H. Creer, J.A. Nolta, S.D. Caruthers, G.M. Lanza, and S.A. Wickline. 19F magnetic resonance imaging for stem/progenitor cell tracking with multiple unique perfluorocarbon nanobeacons. *The FASEB Journal*, 21(8):1647–1654, 2007.

[21] U. Flögel, Z. Ding, H. Hardung, S. Jander, G. Reichmann, C. Jacoby, R. Schubert, and J. Schrader. In vivo monitoring of inflammation after cardiac and cerebral ischemia by fluorine magnetic resonance imaging. *Circulation*, 118(2):140–148, 2008.

[22] A. Fischer, T.C. Basse-Lüsebrink, T. Kampf, G. Ladewig, M. Blaimer, F.A. Breuer, G. Stoll, W.R. Bauer, and P.M. Jakob. Improved sensitivity in 19F cellular imaging using nonconvex compressed sensing. In *Proceedings of the 17th Annual Meeting of the International Society for Magnetic Resonance in Medicine*, number 3154. ISMRM, 2009.

[23] T. Kampf, A. Fischer, T.C. Basse-Lüsebrink, G. Ladewig, F. Breuer, G. Stoll, P.M. Jakob, and W.R. Bauer. Application of compressed sensing to in vivo 3D 19F CSI. *Journal of Magnetic Resonance*, 207(2):262–273, 2010.

[24] A. Fischer. *On the Application of Compressed Sensing to Magnetic Resonance Imaging.* PhD thesis, University of Würzburg, 2011.

[25] D. Weishaupt, V.D. Köchli, and B. Marinecek. *Wie funktioniert MRT?* Springer, 2009.

[26] E.M. Haacke, R.W. Brown, M.R. Thompson, and R. Venkatesan. *Magnetic resonance imaging: physical principles and sequence design.* New York: A John Wiley and Sons, 1999.

[27] H. Günther. *NMR-Spektroskopie.* Thieme, 1992.

[28] H. Friebolin. *Ein-und zweidimensionale NMR-Spektroskopie.* VCH, 1999.

[29] T.C. Basse-Lüsebrink. Einsatz der MR-Bildgebung zur Darstellung 19F-markierter Zellen in-vitro. Diplomarbeit, University of Würzburg, 2007.

[30] T. Lanz. *Bau und Charakterisierung von NMR-Meßspulen.* PhD thesis, University of Würzburg, 2001.

[31] M.H. Levitt. *Spin dynamics*. John Wiley & Sons, 2001.

[32] I.I. Rabi, N.F. Ramsey, and J. Schwinger. Use of Rotating Coordinates in Magnetic Resonance Problems. *Rev. Mod. Phys.*, 26(2):167–171, 1954.

[33] D.I. Hoult and RE Richards. The signal-to-noise ratio of the nuclear magnetic resonance experiment. *Journal of Magnetic Resonance*, 24(1):71–85, 1976.

[34] G.N. Holland, P.A. Bottomley, and W.S. Hinshaw. 19F magnetic resonance imaging. *Journal of Magnetic Resonance (1969)*, 28(1):133–136, 1977.

[35] G.P. Biro, P. Blais, and A.L. Rosen. Perfluorocarbon blood substitutes. *Critical reviews in oncology/hematology*, 6(4):311–374, 1987.

[36] Y. Jian-xin, V.D. Kodibagkar, C. Weina, and R.P. Mason. 19F: a versatile reporter for non-invasive physiology and pharmacology using magnetic resonance. *Current medicinal chemistry*, 12(7):819–848, 2005.

[37] J.M. Janjic and E.T. Ahrens. Fluorine-containing nanoemulsions for MRI cell tracking. *Wiley Interdisciplinary Reviews: Nanomedicine and Nanobiotechnology*, 1(5): 492–501, 2009.

[38] P. Parhami and B.M. Fung. Fluorine-19 relaxation study of perfluoro chemicals as oxygen carriers. *The Journal of Physical Chemistry*, 87(11):1928–1931, 1983.

[39] B.J. Dardzinski and C.H. Sotak. Rapid tissue oxygen tension mapping using 19F inversion-recovery echo-planar imaging of Perfluoro-15-crown-5-ether. *Magnetic resonance in medicine*, 32(1):88–97, 1994.

[40] J. Lutz and P. Metzenauer. Effects of potential blood substitutes (perfluorochemicals) on rat liver and spleen. *Pflügers Archiv European Journal of Physiology*, 387(2):175–181, 1980.

[41] J. Lutz and M. Stark. Half life and changes in the composition of a perfluorochemical emulsion within the vascular system of rats. *Pflügers Archiv European Journal of Physiology*, 410(1):181–184, 1987.

[42] S. Temme, F. Bönner, J. Schrader, and U. Flögel. 19F magnetic resonance imaging of endogenous macrophages in inflammation. *Wiley Interdisciplinary Reviews: Nanomedicine and Nanobiotechnology*, 2012. doi: 10.1002/wnan.1163.

[43] U. Nöth, S.P. Morrissey, R. Deichmann, S. Jung, H. Adolf, A. Haase, and J. Lutz. Perfluoro-15-crown-5-ether labelled macrophages in adoptive transfer experimental allergic encephalomyelitis. *Artif Cells Blood Substit Immobil Biotechnol*, 25:243–254, 1997.

[44] M. Srinivas, P.A. Morel, L.A. Ernst, D.H. Laidlaw, and E.T. Ahrens. Fluorine-19 MRI for visualization and quantification of cell migration in a diabetes model. *Magnetic Resonance in Medicine*, 58(4):725–734, 2007.

[45] J.M. Janjic, M. Srinivas, D.K.K. Kadayakkara, and E.T. Ahrens. Self-delivering nanoemulsions for dual fluorine-19 MRI and fluorescence detection. *Journal of the American Chemical Society*, 130(9):2832–2841, 2008.

[46] M. Srinivas, M.S. Turner, J.M. Janjic, P.A. Morel, D.H. Laidlaw, and E.T. Ahrens. In vivo cytometry of antigen-specific t cells using 19F MRI. *Magnetic Resonance in Medicine*, 62(3):747–753, 2009.

[47] G. Weise, T.C. Basse-Luesebrink, C. Wessig, P.M. Jakob, and G. Stoll. In vivo imaging of inflammation in the peripheral nervous system by 19F MRI. *Experimental neurology*, 229(2):494–501, 2011.

[48] T. Hertlein, V. Sturm, S. Kircher, T. Basse-Lüsebrink, D. Haddad, K. Ohlsen, and P. Jakob. Visualization of abscess formation in a murine thigh infection model of Staphylococcus aureus by 19F-magnetic resonance imaging (MRI). *PLoS One*, 6(3): e18246, 2011.

[49] H. Waiczies, S. Lepore, N. Janitzek, U. Hagen, F. Seifert, B. Ittermann, B. Purfürst, A. Pezzutto, F. Paul, T. Niendorf, and W. Sonia. Perfluorocarbon particle size influences magnetic resonance signal and immunological properties of dendritic cells. *PloS one*, 6(7):e21981, 2011.

[50] J. Ruiz-Cabello, B.P. Barnett, P.A. Bottomley, and J.W.M. Bulte. Fluorine (19F) MRS and MRI in biomedicine. *NMR in Biomedicine*, 24(2):114–129, 2011.

[51] Philips Medical Systems. *Prinzipien der MR-Tomographie*.

[52] C. Giraudeau, J. Flament, B. Marty, F. Boumezbeur, S. Mériaux, C. Robic, M. Port, N. Tsapis, E. Fattal, E. Giacomini, F. Lethimonnier, D. Le Bihan, and J. Valette. A new paradigm for high-sensitivity 19F magnetic resonance imaging of perfluorooctylbromide. *Magnetic Resonance in Medicine*, 63(4):1119–1124, 2010.

[53] H. Gudbjartsson and S. Patz. The Rician distribution of noisy MRI data. *Magnetic Resonance in Medicine*, 34(6):910–914, 1995.

[54] L. Brateman. Chemical shift imaging: a review. *American Journal of Roentgenology*, 146(5):971–980, 1986.

[55] E.E. Babcock, R.P. Mason, and P.P. Antich. Effect of homonuclear J modulation on 19F spin-echo images. *Magnetic resonance in medicine*, 17(1):179–188, 1991.

[56] J. Beck. Selektive 19F-MR-Spektroskopie und-Bildgebung. Diplomarbeit, University of Würzburg, 2010.

[57] B. Özdemirel and O. Nalcioglu. Correction of chemical-shift artifacts in multislice F-19 imaging with perfluorooctyl bromide. *Magn Reson Med*, 23:324–332, 1992.

[58] G. Weise, T.C. Basse-Lüsebrink, C. Kleinschnitz, T. Kampf, P.M. Jakob, and G. Stoll. In Vivo Imaging of Stepwise Vessel Occlusion in Cerebral Photothrombosis of Mice by 19F MRI. *PloS one*, 6(12):e28143, 2011.

[59] B. Kosata. BKchem version 0.13.0, 2009. Available online at `http://bkchem.zirael.org/`; downloaded on may 22nd 2011.

[60] A. Moll, A. Hildebrandt, H.P. Lenhof, and O. Kohlbacher. BALLView: a tool for research and education in molecular modeling. *Bioinformatics*, 22(3):365–366, 2006.

[61] A. Hildebrandt, A.K. Dehof, A. Rurainski, A. Bertsch, M. Schumann, N.C. Toussaint, A. Moll, D. Stockel, S. Nickels, S.C. Mueller, H.P. Lenhof, and O. Kohlbacher. BALL-biochemical algorithms library 1.3. *BMC Bioinformatics*, 11:531, 2010.

[62] Sigma-Aldrich. Material and Safety Data Sheet: Trifluoressigsäure, 2011. Available online at `www.sigmaaldrich.com`; downloaded on june 6th 2011.

[63] M. Paxian. Künstliche Sauerstoffträger als Alternative zur Fremdbluttransfusion. *Der Anaesthesist*, 50(13):43–49, 2001.

[64] G.E. Gerhardt and R.J. Lagow. Synthesis of the perfluoropoly (ethylene glycol) ethers by direct fluorination. *The Journal of Organic Chemistry*, 43(23):4505–4509, 1978.

[65] T.R. Bierschenk, T. Juhlke, H. Kawa, and R.J. Lagow. Fluorination of acetals, ketals and orthoesters, 1991. U.S. Pat. No. 5053536.

[66] A. Rebel, T. Frietsch, M. Quintel, C. Lenz, and K.F. Waschke. Zerebrale Effekte von Perfluorcarbonen. *Der Nervenarzt*, 70(8):679–687, 1999.

[67] M.P. Krafft. Fluorocarbons and fluorinated amphiphiles in drug delivery and biomedical research. *Advanced drug delivery reviews*, 47(2-3):209–228, 2001.

[68] R.P. Mason, P.P. Antich, E.E. Babcock, J.L. Gerberich, and R.L. Nunnally. Perfluorocarbon imaging in vivo: A 19F MRI study in tumor-bearing mice. *Magnetic resonance imaging*, 7(5):475–485, 1989.

[69] P.T. Leese, R.J. Noveck, J.S. Shorr, C.M. Woods, K.E. Flaim, and P.E. Keipert. Randomized safety studies of intravenous perflubron emulsion. I. Effects on coagulation function in healthy volunteers. *Anesthesia & Analgesia*, 91(4):804–811, 2000.

[70] M. Srinivas, L.J. Cruz, F. Bonetto, A. Heerschap, C.G. Figdor, and I.J.M. De Vries. Customizable, multi-functional fluorocarbon nanoparticles for quantitative in vivo imaging using 19F MRI and optical imaging. *Biomaterials*, 31(27):7070–7077, 2010.

[71] F. Bonetto, M. Srinivas, B. Weigelin, L.J. Cruz, A. Heerschap, P. Friedl, C.G. Figdor, and I.J.M. Vries. A large-scale 19F MRI-based cell migration assay to optimize cell therapy. *NMR in Biomedicine*, 2012. doi: 10.1002/nbm.2774.

[72] J.G. Riess. Overview of progress in the fluorocarbon approach to in vivo oxygen delivery. *Artificial Cells, Blood Substitutes and Biotechnology*, 20(2-4):183–202, 1992.

[73] C.I. Castro and J.C. Briceno. Perfluorocarbon-Based Oxygen Carriers: Review of Products and Trials. *Artificial organs*, 34(8):622–634, 2010.

[74] U. Nöth, P. Groehn, A. Jork, U. Zimmermann, A. Haase, and J. Lutz. 19F-MRI in vivo determination of the partial oxygen pressure in perfluorocarbon-loaded alginate capsules implanted into the peritoneal cavity and different tissues. *Magnetic resonance in medicine*, 42(6):1039–1047, 1999.

[75] A.V. Ratner, R. Hurd, H.H. Muller, B. Bradley-Simpson, W. Pitts, J.D. Shibata, C. Sotak, and S.W. Young. 19F magnetic resonance imaging of the reticuloendothelial system. *Magnetic resonance in medicine*, 5(6):548–554, 1987.

[76] N.S. Faithfull. Mechanisms and efficacy of fluorochemical oxygen transport and delivery. *Artificial Cells, Blood Substitutes and Biotechnology*, 22(2):181–197, 1994.

[77] Celsense Inc. Celsense, Inc. Announces First Clinical Trial Authorization by the US Food and Drug Administration (FDA) for Use of Its Cell Tracking Imaging Product Cell Sense, 2011. Available online at `http://www.celsense.com/june27_first_clinical_trial.html`; viewed on august 18th 2011.

[78] R.F. Mattrey. Perfluorocarbons in computed tomography. *Investigative Radiology*, 19(4):S129–S130, 1984.

[79] R.F. Mattrey. Perfluorocarbons in Ultrasound. *Investigative Radiology*, 19(4):S131–S132, 1984.

[80] R.F. Mattrey and D.C. Long. Potential role of PFOB in diagnostic imaging. *Investigative radiology*, 23:S298–S301, 1988.

[81] E.G. Schutt, D.H. Klein, R.M. Mattrey, and J.G. Riess. Mikrobläschen als Kontrastmittel für die diagnostische Ultraschall-Bildgebung: die Schlüsselrolle von Perfluorverbindungen. *Angewandte Chemie*, 115(28):3336–3355, 2003.

[82] Y. Fu, D.A. Kedziorek, R. Ouwerkerk, S.M. Shea, N. Azene, A. Arepally, J.W. Bulte, R. Krieg, F. Wacker, and D.L. Kraitchman. Multifunctional Perfluorinated Microcapsules for Mesenchymal Stem Cell Delivery and Engraftment Tracking using 19F MRI, X-ray, and Ultrasound. In *Proceedings of the 17th Annual Meeting of the International Society for Magnetic Resonance in Medicine*, number 528. ISMRM, 2009.

[83] D.A. Kedziorek, P. Walczak, Y. Fu, T. Ehtiati, A.B. Brost, N. Azene, G. Huang, J.W. Bulte, S.M. Shea, R. Krieg, R. Ouwerkerk, F.K. Wacker, and D.L. Kraitchman. 19F MRI and C-arm CT Guiding of Reporter Probe Injection to Microencapsulated Mesenchymal Stem Cells for in vivo Cell Viability Assessment with Bioluminescence Imaging. In *Proceedings of the 17th Annual Meeting of the International Society for Magnetic Resonance in Medicine*, number 918. ISMRM, 2009.

[84] F.K. Schweighardt and J.A. Rubertone. Perfluoro-crown ethers in fluorine magnetic resonance imaging, 1989. U.S. Pat. No. 4838274.

[85] D. Lee, K. Marro, E. Shankland, and M. Mathis. Quantitative 19F imaging using inductively coupled reference signal injection. *Magnetic Resonance in Medicine*, 63 (3):570–573, 2010.

[86] A.M. Abduljalil, A. Kangarlu, Y. Yu, and P.M.L. Robitaille. Macroscopic susceptibility in ultra high field MRI. II: acquisition of spin echo images from the human head. *Journal of computer assisted tomography*, 23(6):842, 1999.

[87] T.R. Brown, B.M. Kincaid, and K. Ugurbil. NMR chemical shift imaging in three dimensions. *Proceedings of the National Academy of Sciences*, 79(11):3523–3526, 1982.

[88] O. Speck, K. Scheffler, and J. Hennig. Fast 31P chemical shift imaging using SSFP methods. *Magnetic resonance in medicine*, 48(4):633–639, 2002.

[89] J.H. Duyn and C.T.W. Moonen. Fast proton spectroscopic imaging of human brain using multiple spin-echoes. *Magnetic resonance in medicine*, 30(4):409–414, 1993.

[90] H.K. Lee and O. Nalcioglu. Reblurred deconvolution method for chemical shift removal in F-19 (PFOB) MR imaging. *Journal of Magnetic Resonance Imaging*, 2(1): 53–61, 1992.

[91] M.A. Bernstein, K.E. King, X.J. Zhou, and W. Fong. *Handbook of MRI pulse sequences*. Elsevier, 2004.

[92] M. Uecker, S. Zhang, D. Voit, A. Karaus, K.D. Merboldt, and J. Frahm. Real-time MRI at a resolution of 20 ms. *NMR in Biomedicine*, 23(8):986–994, 2010.

[93] R. Pohmann, M. Von Kienlin, and A. Haase. Theoretical evaluation and comparison of fast chemical shift imaging methods. *Journal of Magnetic Resonance*, 129(2): 145–160, 1997.

[94] W.R. Nitz. Magnetresonanztomographie Sequenzakronyme und weitere Kürzel in der MR-Bildgebung. *Der Radiologe*, 43(9):745–766, 2003.

[95] T.C. Basse-Luesebrink, A. Fischer, T. Kampf, V. Sturm, G. Ladewig, G. Stoll, and P.M. Jakob. 19F-Compressed-Sensing-CISS: Elimination of banding artifacts in 19F bssfp MRI/CSI without sacrificing time. In *Proceedings of the 18th Annual Meeting of the International Society for Magnetic Resonance in Medicine*, number 4888. ISMRM, 2010.

[96] K. Scheffler and S. Lehnhardt. Principles and applications of balanced SSFP techniques. *European radiology*, 13(11):2409–2418, 2003.

[97] Q-S. Xiang and M.N. Hoff. Simple Cross-Solution for Banding Artifact Removal in bSSFP Imaging. In *Proceedings of the 18th Annual Meeting of the International Society for Magnetic Resonance in Medicine*, number 74. ISMRM, 2010.

[98] J. Hennig. Multiecho imaging sequences with low refocusing flip angles. *Journal of Magnetic Resonance*, 78(3):397–407, 1988.

[99] J. Hennig, M. Weigel, and K. Scheffler. Multiecho sequences with variable refocusing flip angles: optimization of signal behavior using smooth transitions between pseudo steady states (TRAPS). *Magnetic resonance in medicine*, 49(3):527–535, 2003.

[100] H.Y. Carr and E.M. Purcell. Effects of Diffusion on Free Precession in Nuclear Magnetic Resonance Experiments. *Phys. Rev.*, 94(3):630–638, 1954.

[101] S. Meiboom and D. Gill. Modified spin-echo method for measuring nuclear relaxation times. *Review of Scientific Instruments*, 29(8):688–691, 1958.

[102] L.I. Sacolick, F. Wiesinger, I. Hancu, and M.W. Vogel. B1 mapping by Bloch-Siegert shift. *Magnetic Resonance in Medicine*, 63(5):1315–1322, 2010.

[103] T.C. Basse-Lüsebrink, V.J.F. Sturm, T. Kampf, G. Stoll, and P.M. Jakob. Fast CPMG-based Bloch-Siegert B1+ mapping. *Magnetic Resonance in Medicine*, 67(2): 405–418, 2011.

[104] J. Schwitter. Extending the frontiers of cardiac magnetic resonance. *Circulation*, 118 (2):109–112, 2008.

[105] B.D. Watson, W.D. Dietrich, R. Busto, M.S. Wachtel, and M.D. Ginsberg. Induction of reproducible brain infarction by photochemically initiated thrombosis. *Annals of neurology*, 17(5):497–504, 1985.

[106] C. Kleinschnitz, M. Bendszus, M. Frank, L. Solymosi, K.V. Toyka, and G. Stoll. In vivo monitoring of macrophage infiltration in experimental ischemic brain lesions by magnetic resonance imaging. *Journal of Cerebral Blood Flow & Metabolism*, 23(11): 1356–1361, 2003.

[107] C. Kleinschnitz, A. Schütz, I. Nölte, T. Horn, M. Frank, L. Solymosi, G. Stoll, and M. Bendszus. In vivo detection of developing vessel occlusion in photothrombotic ischemic brain lesions in the rat by iron particle enhanced MRI. *Journal of Cerebral Blood Flow & Metabolism*, 25(11):1548–1555, 2005.

[108] F. Wurm. *Einfluss aktivitätsabhängiger Prozesse aufendogene neurale Stammzellen im Gyrus dentatus nach photochemisch induzierten Hirninfarkten*. PhD thesis, University of Jena, 2006.

[109] M. Schroeter, S. Jander, and G. Stoll. Non-invasive induction of focal cerebral ischemia in mice by photothrombosis of cortical microvessels: characterization of inflammatory responses. *Journal of neuroscience methods*, 117(1):43–49, 2002.

[110] S. Fiedler. Hochfrequenzspulen für die 19F MR-Bildgebung bei 7T. Diplomarbeit, University of Würzburg, 2009.

[111] R. Pohmann and M. von Kienlin. Accurate phosphorus metabolite images of the human heart by 3D acquisition-weighted CSI. *Magnetic resonance in medicine*, 45 (5):817–826, 2001.

[112] T.C. Basse-Luesebrink, G. Weise, C. Wessig, P.M. Jakob, and G. Stoll. Imaging of inflammation in the peripheral nervous system by 19F MRI. In *Proceedings of the 19th Annual Meeting of the International Society for Magnetic Resonance in Medicine*, number 3710. ISMRM, 2011.

[113] M.J. Kuhn, K.A. Johnson, and K.R. Davis. Wallerian degeneration: evaluation with MR imaging. *Radiology*, 168(1):199–202, 1988.

[114] D.S. Titelbaum, J.L. Frazier, R.I. Grossman, P.M. Joseph, L.T. Yu, E.A. Kassab, W.F. Hickey, D. LaRossa, and M.J. Brown. Wallerian degeneration and inflammation in rat peripheral nerve detected by in vivo MR imaging. *American journal of neuroradiology*, 10(4):741–746, 1989.

[115] A.T. Dailey, J.S. Tsuruda, A.G. Filler, K.R. Maravilla, R. Goodkin, and M. Kliot. Magnetic resonance neurography of peripheral nerve degeneration and regeneration. *The Lancet*, 350(9086):1221–1222, 1997.

[116] G.A. Grant, G.W. Britz, R. Goodkin, J.G. Jarvik, K. Maravilla, and M. Kliot. The utility of magnetic resonance imaging in evaluating peripheral nerve disorders. *Muscle & nerve*, 25(3):314–331, 2002.

[117] K.J. Smith and S.M. Hall. Nerve conduction during peripheral demyelination and remyelination. *Journal of the neurological sciences*, 48(2):201–219, 1980.

[118] J.W. Griffin, E.A. Stocks, K. Fahnestock, A. Van Praagh, and B.D. Trapp. Schwann cell proliferation following lysolecithin-induced demyelination. *Journal of neurocytology*, 19(3):367, 1990.

[119] J. Conti. vol3D, 2004. Available online at `http://www.mathworks.com/`; downloaded on february 15th 2010.

[120] E.T. Ahrens, W.B. Young, H. Xu, and L.K. Pusateri. Rapid quantification of inflammation in tissue samples using perfluorocarbon emulsion and fluorine-19 nuclear magnetic resonance. *BioTechniques*, 50:229–234, 2011.

[121] P.B. Roemer, W.A. Edelstein, C.E. Hayes, S.P. Souza, and O.M. Mueller. The NMR phased array. *Magn. Reson. Med.*, 16(2):192–225, 1990.

[122] P. Styles, N.F. Soffe, C.A. Scott, D.A. Cragg, F. Row, D.J. White, and P.C. White. A high-resolution NMR probe in which the coil and preamplifier are cooled with liquid helium. *JMR*, 60(3):397–404, 1984.

[123] R.D. Black, T.A. Early, P.B. Roemer, O.M. Mueller, A. Mogro-Campero, L.G. Turner, and G.A. Johnson. A High-Temperature Superconducting Receiver for Nuclear Magnetic Resonance. *Science*, 259(5096):793–795, 1993.

[124] F. Odoj, E. Rommel, M. v. Kienlin, and A. Haase. A superconducting probehead applicable for nuclear magnetic resonance microscopy at 7 T. *Rev. Sci. Instrum.*, 69 (7):2708–2712, 1998.

[125] K.H. Chalmers, M. Botta, and D. Parker. Strategies to enhance signal intensity with paramagnetic fluorine-labelled lanthanide complexes as probes for 19F magnetic resonance. *Dalton Trans.*, 40(4):904–913, 2011.

[126] K.H. Chalmers, A.M. Kenwright, D. Parker, and A.M. Blamire. 19F-lanthanide complexes with increased sensitivity for 19F-MRI: Optimization of the MR acquisition. *Magnetic Resonance in Medicine*, 66(4):931–936, 2011.

[127] U. Bommerich, T. Trantzschel, S. Mulla-Osman, G. Buntkowsky, J. Bargon, and J. Bernarding. Hyperpolarized 19F-MRI: parahydrogen-induced polarization and field variation enable 19F-MRI at low spin density. *Phys. Chem. Chem. Phys.*, 12 (35):10309–10312, 2010.

[128] D.L. Donoho. Compressed sensing. *Information Theory, IEEE Transactions on*, 52 (4):1289–1306, 2006.

[129] E.J. Candès, J. Romberg, and T. Tao. Robust uncertainty principles: Exact signal reconstruction from highly incomplete frequency information. *Information Theory, IEEE Transactions on*, 52(2):489–509, 2006.

[130] M. Lustig, D. Donoho, and J.M. Pauly. Sparse MRI: The application of compressed sensing for rapid MR imaging. *Magnetic Resonance in Medicine*, 58(6):1182–1195, 2007.

[131] R. Chartrand. Exact reconstruction of sparse signals via nonconvex minimization. *Signal Processing Letters, IEEE*, 14(10):707–710, 2007.

[132] T.C. Basse-Luesebrink, J. Beck, T. Kampf, A. Fischer, G. Weise, G. Stoll, and P.M. Jakob. Application of Compressed Sensing to 19F turbo spin echo chemical shift imaging. In *Proceedings of the 19th Annual Meeting of the International Society for Magnetic Resonance in Medicine*, number 1502. ISMRM, 2011.

[133] A.S. Stern, D.L. Donoho, and J.C. Hoch. NMR data processing using iterative thresholding and minimum l1-norm reconstruction. *Journal of Magnetic Resonance*, 188(2):295–300, 2007.

[134] O. Bieri, M. Markl, and K. Scheffler. Analysis and compensation of eddy currents in balanced SSFP. *Magnetic resonance in medicine*, 54(1):129–137, 2005.

[135] T.C. Basse-Luesebrink, T. Kampf, A. Fischer, G. Ladewig, G. Stoll, and P.M. Jakob. Spike artifact reduction in nonconvex Compressed Sensing. In *Proceedings of the 18th Annual Meeting of the International Society for Magnetic Resonance in Medicine*, number 4886. ISMRM, 2010.

[136] B. Efron. *The jackknife, the bootstrap, and other resampling plans.* Society for Industrial and Applied Mathematics Philadelphia, 1982.

[137] B. Efron and R. Tibshirani. Bootstrap methods for standard errors, confidence intervals, and other measures of statistical accuracy. *Statistical science*, 1(1):54–75, 1986.

[138] W.H. Press, B.P. Flannery, S.A. Teukolsky, and W.T. Vetterling. *Numerical recipes in C.* Cambridge Univ Press, 1992.

[139] J. Singer and M. Berger. The Jackknife applied to incomplete blood sampling models. *Pharmaceutical Statistics*, 2(3):161–166, 2003.

[140] C.F.J. Wu. Jackknife, bootstrap and other resampling methods in regression analysis. *The Annals of Statistics*, 14(4):1261–1295, 1986.

[141] J. Luo, Y. Zhu, and I.E. Magnin. Denoising by averaging reconstructed images: application to magnetic resonance images. *IEEE Trans Biomed Eng*, 56:666–674, 2009.

[142] J. Miao, W. Li, S. Narayan, X. Yu, and D.L. Wilson. MR Rician Noise Reduction in Diffusion Tensor Imaging using Compressed Sensing by Sampling Decomposition. In *Proceedings of the 18th Annual Meeting of the International Society for Magnetic Resonance in Medicine*, number 4890. ISMRM, 2010.

[143] P. Boehm-Sturm, L. Mengler, S. Wecker, M. Hoehn, and T. Kallur. In Vivo Tracking of Human Neural Stem Cells with 19F Magnetic Resonance Imaging. *PloS one*, 6 (12):e29040, 2011.

[144] R.F. Schulte, L. Sacolick, M.H. Deppe, M.A. Janich, M. Schwaiger, J.M. Wild, and F. Wiesinger. Transmit gain calibration for nonproton MR using the Bloch–Siegert shift. *NMR in Biomedicine*, 24(9):1068–1072, 2011.

[145] L.I. Sacolick, L. Sun, M.W. Vogel, W.T. Dixon, and I. Hancu. Fast radiofrequency flip angle calibration by Bloch-Siegert shift. *Magnetic Resonance in Medicine*, 66(5): 1333–1338, 2011.

[146] A.Z. Lau, A.P. Chen, and C.H. Cunningham. Integrated Bloch-Siegert B1 mapping and multislice imaging of hyperpolarized 13C pyruvate and bicarbonate in the heart. *Magnetic Resonance in Medicine*, 67(1):62–71, 2011.

[147] T.C. Basse-Lüsebrink, V.J.F. Sturm, A. Vilter, T. Kampf, V.C. Behr, and P.M. Jakob. Fast, indirect assessment of the 19F B1 profile by 1H Bloch-Siegert B1 mapping using double-resonant 1H/19F coils. In *Proceedings of the 20th Annual Meeting of the International Society for Magnetic Resonance in Medicine*, number 3367. ISMRM, 2012.

[148] V.J.F. Sturm, T.C. Basse-Lüsebrink, T. Kampf, G. Stoll, and P.M. Jakob. Improved encoding strategy for CPMG-based Bloch-Siegert B1+ mapping. *Magnetic Resonance in Medicine*, 2011. doi: 10.1002/mrm.23232.

[149] F. Bloch and A. Siegert. Magnetic resonance for nonrotating fields. *Physical Review*, 57(6):522, 1940.

[150] N.F. Ramsey. Resonance transitions induced by perturbations at two or more different frequencies. *Physical Review*, 100(4):1191, 1955.

[151] M. Saranathan, M.M. Khalighi, A.B. Kerr, and B.K. Rutt. Fast 3D B1+ mapping using an optimized, asymmetric Bloch-Siegert method. In *Proceedings of the 19th Annual Meeting of the International Society for Magnetic Resonance in Medicine*, number 577. ISMRM, 2011.

[152] T.C. Basse-Lüsebrink, T. Kampf, A. Fischer, V.J.F. Sturm, D. Neumann, H. Köstler, D. Hahn, G. Stoll, and P.M. Jakob. SAR-reduced spin-echo-based Bloch–Siegert B1+ mapping: BS-SE-BURST. *Magnetic Resonance in Medicine*, 2011. doi: 10.1002/mrm.23259.

[153] T.C. Basse-Luesebrink, V. Sturm, T. Kampf, G. Stoll, and P.M. Jakob. Turbo Spin Echo Bloch Siegert Shift B1+ Mapping. In *Proceedings of the 19th Annual Meeting of the International Society for Magnetic Resonance in Medicine*, number 2929. ISMRM, 2011.

[154] C.S. Poon and R.M. Henkelman. Practical T2 quantitation for clinical applications. *Journal of Magnetic Resonance Imaging*, 2(5):541–553, 1992.

[155] Y. Zur and S. Stokar. A phase-cycling technique for canceling spurious echoes in NMR imaging. *Journal of Magnetic Resonance (1969)*, 71(2):212–228, 1987.

[156] F. Schick. SPLICE: Sub-second diffusion-sensitive MR imaging using a modified fast spin-echo acquisition mode. *Magnetic resonance in medicine*, 38(4):638–644, 1997.

[157] M. Weigel. *Entwicklung, Optimierung und klinische Erprobung von T2-gewichteten Meßverfahren mit reduzierter Hochfrequenzleistung für die Kernspintomographie*. PhD thesis, University of Freiburg, 2007.

[158] R. Deichmann and A. Haase. Quantification of T1 values by SNAPSHOT-FLASH NMR imaging. *Journal of magnetic resonance*, 96(3):608–612, 1992.

[159] M. Jenkinson. Fast, automated, N-dimensional phase-unwrapping algorithm. *Magnetic resonance in medicine*, 49(1):193–197, 2003.

[160] D.I. Hoult and P.C. Lauterbur. The sensitivity of the zeugmatographic experiment involving human samples. *Journal of Magnetic Resonance (1969)*, 34(2):425–433, 1979.

[161] P.A. Bottomley, R.W. Redington, W.A. Edelstein, and J.F. Schenck. Estimating radiofrequency power deposition in body NMR imaging. *Magnetic Resonance in Medicine*, 2(4):336–349, 1985.

[162] D.I. Hoult. Sensitivity and Power Deposition in a High-Field Imaging Experiment. *Journal of Magnetic Resonance Imaging*, 12(1):46–67, 2000.

[163] P.A. Bottomley and E.R. Andrew. RF magnetic field penetration, phase shift and power dissipation in biological tissue: implications for NMR imaging. *Physics in Medicine and biology*, 23:630–643, 1978.

[164] M.M. Khalighi, B.K. Rutt, and A.B. Kerr. RF pulse optimization for Bloch-Siegert B1+ mapping. *Magnetic Resonance in Medicine*, 2011. doi: 10.1002/mrm.23271.

[165] E.O. Stejskal. Use of Spin Echoes in a Pulsed Magnetic-Field Gradient to Study Anisotropic, Restricted Diffusion and Flow. *The Journal of Chemical Physics*, 43: 3597–3603, 1965.

[166] J.E. Tanner and E.O. Stejskal. Restricted Self-Diffusion of Protons in Colloidal Systems by the Pulsed-Gradient, Spin-Echo Method. *The Journal of Chemical Physics*, 49:1768–1777, 1968.

[167] M.M. Khalighi, B.K. Rutt, M. Saranathan, and A.B. Kerr. RF Pulse optimization for Bloch-Siegert B1+ Mapping. In *Proceedings of the 19th Annual Meeting of the International Society for Magnetic Resonance in Medicine*, number 4431. ISMRM, 2011.

[168] X. Zhou, Z.P. Liang, G.P. Cofer, C.F. Beaulieu, S.A. Suddarth, and G.A. Johnson. Reduction of ringing and blurring artifacts in fast spin-echo imaging. *Journal of Magnetic Resonance Imaging*, 3(5):803–807, 1993.

[169] P. Mazurkewitz and C. Leussler. Double resonant transmit receive solenoid coil for MRI, 2007. International Pat. No. WO 2007/117853 A1.

[170] L. Hu, F.D. Hockett, J. Chen, G.M. Lanza, and S.A. Wickline. Single-input double-tuned birdcage coil with identical B1 field profile for 1H and 19F imaging. In *Proceedings of the 18th Annual Meeting of the International Society for Magnetic Resonance in Medicine*, number 1502. ISMRM, 2010.

[171] S. Fiedler, T.C. Basse-Lüsebrink, M.A. Lopez, and P.M. Jakob. Solenoids for combined 1H and 19F MRI at 7 Tesla. In *Proceedings of the German Section of the ISMRM*. DSISMRM, 2009.

[172] A. Gotschy, U.C. Hölscher, T. Basse-Lüsebrink, A. Fischer, M. Choli, T. Kampf, V. Sturm, D. Neumann, V. Herold, H. Köstler, D. Hahn, G. Stoll, W.R. Bauer, and P.M. Jakob. Rapid and low SAR B1-Mapping using a BURST-based Bloch-Siegert-Shift Sequence. In *Proceedings of the 20th Annual Meeting of the International Society for Magnetic Resonance in Medicine*, number 3365. ISMRM, 2012.

# Publications

**Paper**

- T. Kampf[1], A. Fischer[1], **T.C. Basse-Lüsebrink**[1], G. Ladewig, F. Breuer, G. Stoll, P.M. Jakob, and W.R. Bauer. Application of compressed sensing to in vivo 3D 19F CSI. *Journal of Magnetic Resonance*, 207(2):262–273, 2010.
- T. Hertlein[1], V. Sturm[1], S. Kircher, **T. Basse-Lüsebrink**, D. Haddad, K. Ohlsen, and P. Jakob. Visualization of Abscess Formation in a Murine Thigh Infection Model of Staphylococcus aureus by 19F-magnetic resonance imaging (MRI). *PLoS One*, 6(3):e18246, 2011.
- G. Weise, **T.C. Basse-Luesebrink**, C. Wessig, P.M. Jakob, and G. Stoll. In vivo imaging of inflammation in the peripheral nervous system by 19F MRI. *Experimental Neurology*, 229(2):494–501, 2011.
- **T.C. Basse-Lüsebrink**[1], V.J.F. Sturm[1], T. Kampf[1], G. Stoll, and P.M. Jakob. Fast CPMG-based Bloch-Siegert B1+ Mapping. *Magnetic Resonance in Medicine*, 67(2):405–418, 2011.
- P.J. Hill[1], J. Stritzker[1], M. Scadeng, U. Geissinger, D. Haddad, **T.C. Basse-Lüsebrink**, U. Gbureck, P. Jakob, and A.A. Szalay. Magnetic Resonance Imaging of Tumors Colonized with Bacterial Ferritin-Expressing Escherichia coli. *PLoS One*, 6(10):e25409, 2011.
- **T.C. Basse-Lüsebrink**[1], T. Kampf[1], A. Fischer[1], V.J.F. Sturm[1], D. Neumann, H. Köstler, D. Hahn, G. Stoll, and P.M. Jakob. SAR-Reduced Spin-Echo-Based Bloch-Siegert B1+ Mapping: BS-SE-BURST. *Magnetic Resonance in Medicine*, 2011. doi: 10.1002/mrm.23259.
- G. Weise[1], **T.C. Basse-Luesebrink**[1], C. Kleinschnitz, T. Kampf, P.M. Jakob, and G. Stoll. In vivo imaging of stepwise vessel occlusion in cerebral photothrombosis of mice by 19F MRI. *PLoS One*, 6(12):e28143, 2011.
- V.J.F. Sturm[1], **T.C. Basse-Lüsebrink**[1], T. Kampf[1], G. Stoll, and P.M. Jakob. Improved Encoding Strategy for CPMG-Based Bloch-Siegert B1+ Mapping. *Magnetic Resonance in Medicine*, 2011. doi: 10.1002/mrm.23232.
- G. Stoll, **T. Basse-Lüsebrink**, G. Weise, and P. Jakob. Visualization of inflammation using 19F-MRI and perfluorocarbons. *Wiley Interdisciplinary Reviews: Nanomedicine and Nanobiotechnology*, 2012. doi: 10.1002/wnan.1168.

[1] Authors contributed equally

## Conference Talks

- **T.C. Basse-Luesebrink**, T. Kampf, M. Weber, A. Heymer, R. Ebert, U. Noeth, W.R. Bauer, P.M. Jakob, and D. Haddad. Double-labeled mesenchymal stem cells for 1H-/19F-MR imaging. In *Proceedings of the Deutsche Gesellschaft für Stammzellforschung Jahrestagung*. GSZ, 2007.

- Y. Ye, **T. Basse-Luesebrink**, V. Kocoski, T. Kampf, K. Hu, P. Arias, P.M. Jakob, K. Hiller, R. Jahns, and W.R. Bauer. Cellular Fluorine 19-MR: a potential clinically translational method to monitor inflammatory responce in reperfused myocardial infarction - preliminary studies in a small rodent model. In *Proceedings of the 26th annual scientific meeting of the European Society for Magnetic Resonance in Medicine and Biology*, number 346. ESMRMB, 2009.

- **T.C. Basse-Luesebrink**, G. Ladewig, T. Kampf, G. Melkus, D. Haddad, W.R. Bauer, P.M. Jakob, and G. Stoll. Multi-color 19F CSI: Simultaneous detection of differently labeled cells in vivo. In *Proceedings of the 17th Annual Meeting of the International Society for Magnetic Resonance in Medicine*, number 806. ISMRM, 2009.

- V. Sturm, T. Hertlein, **T. Basse-Lüsebrink**, D. Haddad, K. Ohlsen, and P. Jakob. In vivo monitoring of bacterial infections using high-field MR microscopy. In *Proceedings of the 18th Annual Meeting of the International Society for Magnetic Resonance in Medicine*, number 215. ISMRM, 2010.

- G. Ladewig, **T.C. Basse-Luesebrink**, C. Wessig, P.M. Jakob, and G. Stoll. Imaging of inflammation in the peripheral nervous system by 1H/19F MRI: a pilot study. In *Proceedings of the 20th Meeting of the European Neurological Society*, number O132. ENS, 2010.

- Y-X. Ye, **T.C. Basse-Luesebrink**, P. Arias, T. Kampf, V. Kocoski, E. Bauer, K. Hu, V. Jahns, P.M. Jakob, K-H. Hiller, R. Jahns, and W.R. Bauer. In vivo monitoring of anti-inflammatory Atorvastatin-effects in reperfused myocardial infarction using integrated cellular fluorine 19F-MRI and 1H-cardiac MRI. In *Proceedings of the 19th Annual Meeting of the International Society for Magnetic Resonance in Medicine*, number 669. ISMRM, 2011.

- Y. Ye, **T. Basse-Luesebrink**, P.-A. Arias-Loza, V. Kocoski, T. Kampf, Q. Gan, E. Bauer, S. Sparka, X. Helluy, K. Hu, V. Biovin, K.-H. Hiller, P.M. Jakob, R. Jahns, and W.R. Bauer. Blood Monocyte Recruitment in Microvascular Obstruction and Intramyocardial Hemorrhage: New Insights from Fluorine-19 Cellular Magnetic Resonance Imaging in Experimental Reperfused Myocardial Infarction. *Circulation*, 124(21):A538, 2011. *Winner: 2011 Melvin Judkins Young Investigator Award.*

- **T.C. Basse-Lüsebrink**, S. Weibel, E. Hofmann, J. Langbein, V.J.F. Sturm, T. Kampf, P.M. Jakob, and A. Szalay. Imaging tumor colonization with an oncolytic Vaccinia virus strain (GLV-1h68) in a melanoma model by 19F MRI. In *Proceedings of the 20th Annual Meeting of the International Society for Magnetic Resonance in Medicine*, number 676. ISMRM, 2012. *Award: ISMRM Merit Award, Summa Cum Laude.*

- Y.-X. Ye, M. Sauter, **T.C. Basse-Luesebrink**, T. Kampf, X. Helluy, K.-H. Hiller, A. Yilmaz, U. Sechtem, W.R. Bauer, R. Kandolf, K. Klingel, and P.M. Jakob. Non-invasive in vivo imaging of inflammation in experimental viral myocarditis by 19F cellular MRI. In *Proceedings of the 20th Annual Meeting of the International Society for Magnetic Resonance in Medicine*, number 389. ISMRM, 2012.

---

**Electronic and Traditional Poster**

---

- D. Haddad, **T.C. Basse-Lüsebrink**, T. Kampf, M. Weber, A. Heymer, U. Nöth, W.R. Bauer, and P. Jakob. 1H/19F MR Imaging of SPIO and PFC double-labeled Mesenchymal Stem Cells. In *Proceedings of the Joint Molecular Imaging Conference*, number 1041. AMI, 2007.
- A. Wilms, M. Weber, D. Haddad, A. Heymer, **T. Basse-Lüsebrink**, A. Steinert, P. Jakob, F. Gohlke, O. Rolf, and U. Nöth. Cell-Based Therapy of Fatty Degeneration after Rotator Cuff Tears. In *Proceedings of the Deutsche Gesellschaft für Stammzellforschung Jahrestagung*. GSZ, 2007.
- T. Kampf, **T.C. Basse-Lüsebrink**, M. Weber, A. Heymer, R. Ebert, C. Stoetzel, U. Gbureck, U. Noeth, P.M. Jakob, W.R. Bauer, and D. Haddad. In vitro /in vivo MRI visualization of PFC/VSOP double-labeled mesenchymal stem cells. In *Proceedings of the 16th Annual Meeting of the International Society for Magnetic Resonance in Medicine*, number 1692. ISMRM, 2008.
- **T.C. Basse-Lüsebrink**, T. Kampf, C.H. Ziener, G. Klug, W.R. Bauer, P.M. Jakob, and D. Haddad. Evaluation of sensitivity increase by T1 and T2 contrast agents in 19F MRI of PF15C. In *Proceedings of the 16th Annual Meeting of the International Society for Magnetic Resonance in Medicine*, number 1655. ISMRM, 2008.
- S.C. Sparka, A. Werner, T. Kampf, **T.C. Basse-Luesebrink**, D. Haddad, W.R. Bauer, P.M. Jakob, and W.A. Schenk. Novel Type of 19F MRI Contrast Agent. In *Proceedings of the 16th Annual Meeting of the International Society for Magnetic Resonance in Medicine*, number 1670. ISMRM, 2008.
- J. Stritzker, P.J. Hill, P. Brader, S. Weibel, Y.A. Yu, M. Scadeng, D. Haddad, **T. Basse-Lüsebrink**, Y. Fong, R. Blasberg, P. Jakob, and A.A. Szalay. Bacterial Tumor Colonization and Its Use for Tumor Imaging Modalities. In *Proceedings of the World Molecular Imaging Congress*, number 1199. WMIC, 2008.
- S. Sparka, **T.C. Basse-Luesebrink**, T. Kampf, G. Klug, W.R. Bauer, D. Haddad, P.M. Jakob, and W.A. Schenk. Synthesis and Characterisation of a novel bimodal 1H-/19F-MR Contrast Agent. In *Proceedings of the World Molecular Imaging Congress*, number 1509. WMIC, 2008.
- **T.C. Basse-Lüsebrink**, T. Kampf, G. Melkus, G. Ladewig, M. Weber, G. Stoll, P.M. Jakob, W.R. Bauer, and D. Haddad. A fast approach to distinguish between cells labeled with different PFCs in a single MR measurement. In *Proceedings of the 25th annual scientific meeting of the European Society for Magnetic Resonance in Medicine and Biology*, number 599. ESMRMB, 2008.
- T. Kampf, **T.C. Basse-Lüsebrink**, G. Melkus, U. Flögel, J. Schrader, P.M. Jakob, D. Haddad, and W.R. Bauer. sFADE: a fast and sensitive CSI method for multi resonant 19F MRI. In *Proceedings of the 25th annual scientific meeting of the European*

*Society for Magnetic Resonance in Medicine and Biology*, number 958. ESMRMB, 2008.

- J. Bremicker, G. Klug, T. Kampf, E. Bauer, **T. Basse-Lüsebrink**, M. Weber, U. Gbureck, U. Nöth, P. Jakob, and W.R. Bauer. Detection limits of Very Small Iron Oxide Nanoparticles in labeled cells: a quantitative evaluation of histochemistry and MR-relaxometry. In *Proceedings of the Deutsche Gesellschaft für Kardiologie Jahrungstagung*, number 1043. DGK, 2009.
- G. Klug, **T.C. Basse-Lüsebrink**, C. Schnell, T. Kampf, E. Bauer, V. Herold, M. Parczyk, E. Rommel, G. Stoll, P.M. Jakob, and W.R. Bauer. 1H/19F molecular MR-imaging in mouse models of acute and chronic inflammation. In *Proceedings of the 17th Annual Meeting of the International Society for Magnetic Resonance in Medicine*, number 3172. ISMRM, 2009.
- A. Fischer, **T.C. Basse-Lüsebrink**, T. Kampf, G. Ladewig, M. Blaimer, F.A. Breuer, G. Stoll, W.R. Bauer, and P.M. Jakob. Improved sensitivity in 19F cellular imaging using nonconvex compressed sensing. In *Proceedings of the 17th Annual Meeting of the International Society for Magnetic Resonance in Medicine*, number 3154. ISMRM, 2009.
- G. Klug, J. Bremicker, T. Kampf, E. Bauer, **T.C. Basse-Lüsebrink**, M. Weber, U. Gbureck, U. Nöth, P.M. Jakob, and W.R. Bauer. Detection Limits of Very Small Iron Oxide Nanoparticles in Labeled Cells: A Quantitative Evaluation of Histochemistry and MR-Relaxometry. In *Proceedings of the 17th Annual Meeting of the International Society for Magnetic Resonance in Medicine*, number 906. ISMRM, 2009.
- S. Fiedler, **T.C. Basse-Lüsebrink**, M.A. Lopez, and P.M. Jakob. Solenoids for combined 1H and 19F MRI at 7 Tesla. In *Proceedings of the German Section of the ISMRM*. DSISMRM, 2009.
- **T.C. Basse-Luesebrink**, T. Kampf, G. Stoll, and P.M. Jakob. Dixon and Chimera: Two methods for fast separation of PFC compounds with small chemical shift difference. In *Proceedings of the 18th Annual Meeting of the International Society for Magnetic Resonance in Medicine*, number 3196. ISMRM, 2010.
- **T.C. Basse-Luesebrink**, T. Kampf, A. Fischer, G. Ladewig, G. Stoll, and P.M. Jakob. Spike artifact reduction in nonconvex Compressed Sensing. In *Proceedings of the 18th Annual Meeting of the International Society for Magnetic Resonance in Medicine*, number 4886. ISMRM, 2010.
- **T.C. Basse-Luesebrink**, A. Fischer, T. Kampf, V. Sturm, G. Ladewig, G. Stoll, and P.M. Jakob. 19F-Compressed-Sensing-CISS: Elimination of banding artifacts in 19F bssfp MRI/CSI without sacrificing time. In *Proceedings of the 18th Annual Meeting of the International Society for Magnetic Resonance in Medicine*, number 4888. ISMRM, 2010.
- Y-X. Ye, **T.C. Basse-Luesebrink**, P. Arias, K. Hu, T. Kampf, V. Kocoski, X. Helluy, P.M. Jakob, K.-H. Hiller, R. Jahns, and W.R. Bauer. MR Cell tracking in reperfused myocardial infarction with microvascular obstruction: Fluorine-19 MR could be a better solution. In *Proceedings of the 18th Annual Meeting of the International Society for Magnetic Resonance in Medicine*, number 2718. ISMRM, 2010.
- **T.C. Basse-Luesebrink**, J. Beck, T. Kampf, A. Fischer, G. Weise, G. Stoll, and P.M. Jakob. Application of Compressed Sensing to 19F turbo spin echo chemical

shift imaging. In *Proceedings of the 19th Annual Meeting of the International Society for Magnetic Resonance in Medicine*, number 1502. ISMRM, 2011.

- **T.C. Basse-Luesebrink**, V. Sturm, T. Kampf, G. Stoll, and P.M. Jakob. Turbo Spin Echo Bloch Siegert Shift B1+ Mapping. In *Proceedings of the 19th Annual Meeting of the International Society for Magnetic Resonance in Medicine*, number 2929. ISMRM, 2011.
- **T.C. Basse-Luesebrink**, G. Weise, C. Wessig, P.M. Jakob, and G. Stoll. Imaging of inflammation in the peripheral nervous system by 19F MRI. In *Proceedings of the 19th Annual Meeting of the International Society for Magnetic Resonance in Medicine*, number 3710. ISMRM, 2011.
- V. Sturm, **T.C. Basse-Lüsebrink**, T. Kampf, G. Stoll, and P.M. Jakob. Simultaneous Bloch Siegert B1+ and T2 mapping in one experiment using a multi spin echo sequence. In *Proceedings of the 19th Annual Meeting of the International Society for Magnetic Resonance in Medicine*, number 4413. ISMRM, 2011.
- V. Sturm, T. Hertlein, **T.C. Basse-Lüsebrink**, K. Ohlsen, and P.M. Jakob. In-vivo monitoring of therapeutic effects on bacterial infection using high-field 19F-MRI. In *Proceedings of the 19th Annual Meeting of the International Society for Magnetic Resonance in Medicine*, number 3709. ISMRM, 2011.
- G. Weise, **T.C. Basse-Luesebrink**, C. Wessig, P.M. Jakob, and G. Stoll. Imaging of inflammation in the peripheral nervous system by 1H/19F MRI: a pilot study. In *Journal of the Peripheral Nervous System, Proceedings*, 16:149–150. PNS, 2011.
- **T.C. Basse-Lüsebrink**, V.J.F. Sturm, A. Vilter, T. Kampf, V.C. Behr, and P.M. Jakob. Fast, indirect assessment of the 19F B1 profile by 1H Bloch-Siegert B1 mapping using double-resonant 1H/19F coils. In *Proceedings of the 20th Annual Meeting of the International Society for Magnetic Resonance in Medicine*, number 3367. ISMRM, 2012.
- V.J.F. Sturm, **T.C. Basse-Lüsebrink**, T. Kampf, and P.M. Jakob. Multi Bloch-Siegert B1+ mapping in a single experiment. In *Proceedings of the 20th Annual Meeting of the International Society for Magnetic Resonance in Medicine*, number 3364. ISMRM, 2012.
- A. Gotschy, U.C. Hölscher, **T. Basse-Lüsebrink**, A. Fischer, M. Choli, T. Kampf, V. Sturm, D. Neumann, V. Herold, H. Köstler, D. Hahn, G. Stoll, W.R. Bauer, and P.M. Jakob. Rapid and low SAR B1-Mapping using a BURST-based Bloch-Siegert-Shift Sequence. In *Proceedings of the 20th Annual Meeting of the International Society for Magnetic Resonance in Medicine*, number 3365. ISMRM, 2012.